DISS. ETH NO. 28651

BED STABILIZATION OF STEEP MOUNTAIN STREAMS WITH STEP-POOL SEQUENCES

A thesis submitted to attain the degree of

DOCTOR OF SCIENCES of ETH ZURICH

(Dr. sc. ETH Zurich)

presented by

FIONA EVELYNE MAAGER

MSc ETH Env Eng, ETH Zurich

born on *24.09.1990*

citizen of St.Gallen, Switzerland

accepted on the recommendation of

Prof. Dr. Robert M. Boes
Prof. Dr. Francesco Comiti
Prof. Dr. Peter Molnar
Dr. Benjamin Hohermuth
Dr. Volker Weitbrecht

2022

Acknowledgements

- Anja Adamov, Camille Girod, Dea Wehrli, and Luzia Meier, for their friendship, the positive energy, and the moral support.

- My family and in particular my parents, Evelyne and Rolf, for the unconditional encouragement and motivation way beyond the past four years.

- My partner Sebastian Gabriel for his infinite support and the amazing skill of surprising me over and over again.

Zurich, October 2022   Fiona Maager

Table of contents

Abstract

Steep mountain streams in pre-Alpine and Alpine regions may pose a high risk to the often densely populated regions located in downstream valleys. While in the upper reach of a mountain stream sediment enters the channel either through bed and bank erosion or due to hillslope processes (e.g. landslides), sediment is deposited on the alluvial fan due to a reduction in channel slope. These sediment deposits reduce the channel discharge capacity potentially resulting in overbank flow and inundations. In the past centuries, concrete check dams have been used to stabilize the channel bed to avoid bed and bank erosion. However, many of these concrete structures require costly refurbishment, they have low ecological value, do not integrate well into the landscape, and may fail abruptly during an overload scenario. Artificial step-pool systems, imitating the typical natural step-pool morphology of steep streams, are a promising alternative to these rigid concrete works. The present thesis is divided into Part A investigating natural step-pool systems and Part B focusing on artificial step-pool systems.

A step-pool morphology is common in steep streams with bed slopes exceeding ~4%. These streams typically have macrorough sidewalls induced by large boulders, vegetation, or logs protruding into the flow. Within this study, physical flume experiments were conducted at the Laboratory of Hydraulics, Hydrology and Glaciology (VAW) at ETH Zurich. Part A addresses the effect of macrorough sidewalls on flow resistance, bed stability, and step formation of natural, self-organizing step-pool systems. Existing studies showed that bed stability increases in steep streams with macrorough sidewalls but the responsible processes had not yet been identified. The main objective of Part A was to quantify the contribution of hydraulic and granular effects to this stability increase by macrorough sidewalls. The former is related to the decrease of bed shear stress due to sidewall friction and the latter to grain-sidewall interlocking. Initially, an existing sidewall correction procedure was extended to estimate bed shear stress in steep rough channels with macrorough sidewalls. Bed shear stress decreased by 5% to 40% in mobile bed experiments with macrorough sidewall highlighting the importance of sidewall friction. The increase in bed stability was fully explained by hydraulic effects in moderately rough sidewall experiments. However, granular effects became important in the roughest sidewall experiments as the steps preferentially formed in the narrowing sections upstream of the roughness elements and they also sustained higher bed shear stress. The present study provides novel insights into

the processes shaping the typical step-pool morphology in steep streams with macrorough sidewalls thereby contributing to a better management of these systems.

Knowledge of natural, self-organizing step-pool streams is crucial for the design of artificial step-pool sequences representing nature-based bed stabilization works. Similarly to self-organizing streams, artificial step-pool sequences were hypothesized to have a self-stabilizing character. The overall goal of Part B of this study was to investigate the relevant processes occurring in these systems and to translate the results into design recommendations for practitioners. Therefore, physical flume experiments were conducted to systematically investigate the effects of bed slope, channel width, sediment supply conditions, and the composition of the base materials on bed stability, failure mechanisms, and scour depths. Furthermore, various step-pool geometries were tested by changing the step-forming block size, varying step spacing, and modifying block arrangement. The step-forming block size, sediment supply conditions, bed slope, and block arrangement were found to be sensitive parameters regarding bed stability. Moreover, the majority of the failure mechanisms were related to block tilting (46%) or to a destabilization of the step toe due to scouring (45%). Contrary to the expectations, the step-pool sequences failed abruptly in ~70% of the experiments, as an initial step failure led to an upstream propagating erosion pattern destroying all upstream steps. A new stable condition after such an integral system failure was associated with a substantial decrease in bed slope. Lastly, an empirical relation was developed to estimate the resulting step height for both clear-water and sediment supply conditions, which is particularly important to design bank protection measures. Finally, all these results regarding bed stability, failure mechanisms, and scour depth estimation were integrated into design recommendations for artificial step-pool sequences which can be used in the future in grade-control and restoration projects.

Kurzfassung

Steile Gebirgsbäche in den Voralpen und Alpen stellen potenziell eine Gefahr für die unterhalb liegenden, oftmals dicht besiedelten Gebiete dar. Geschiebe wird infolge von Sohlen- und Seitenerosion in den Bach eingetragen und lagert sich aufgrund der abnehmenden Sohlschubspannung weiter unten auf dem Schwemmkegel ab. Dadurch wird die Gerinnekapazität reduziert, was zu Ausuferungen und Überschwemmungen führen kann. Um den Geschiebeeintrag zu verhindern bzw. zu reduzieren, wurden Gebirgsbäche in den vergangenen Jahrzehnten insbesondere mit Wildbachsperren stabilisiert. Diese verursachen hohe Kosten, sind aus ökologischer Sicht wenig wertvoll, gliedern sich schlecht ins Landschaftsbild ein und weisen ein abruptes Versagen im Überlastfall auf. Eine vielversprechende Alternative stellen gebaute Stufen-Becken-Sequenzen dar, welche nach dem Vorbild natürlicher Stufen-Becken-Sequenzen gebaut werden. Im Teil A dieser Arbeit werden die natürlichen Stufen-Becken-Sequenzen untersucht, und im Teil B liegt der Fokus auf den gebauten Stufen-Becken-Sequenzen.

Stufen-Becken-Sequenzen entstehen typischerweise in Gebirgsbächen mit einem Sohlgefälle grösser als ~4%. Üblicherweise sind die Ufer sehr rau, da Felsriegel, grosse Blöcke, Vegetation oder Schwemmholz in die Strömung hineinragen. Im Rahmen dieser Arbeit wurden physikalische Modellversuche an der Versuchsanstalt für Wasserbau, Hydrologie und Glaziologie (VAW) an der ETH Zürich durchgeführt. Teil A befasst sich mit makrorauen Ufern und deren Einfluss auf den Fliesswiderstand sowie mit der Stabilität von eigendynamischen Stufen-Becken-Sequenzen. In früheren Studien wurde gezeigt, dass die Sohlstabilität in steilen Gerinnen mit zunehmender Uferrauheit zunimmt, die massgebenden Prozesse wurden bisher aber noch nicht quantifiziert. In dieser Arbeit galt es herauszufinden, ob die Abnahme der Sohlschubspannung durch den erhöhten Widerstand der Ufer (hydraulische Effekte) oder das Verkeilen der Blöcke mit den Ufern (granulare Effekte) zu einer zusätzlichen Stabilität beitragen. Zunächst wurde ein bestehendes Rauigkeitsüberlagerungsmodell erweitert, um den Einfluss der rauen Ufer auf den Fliesswiderstand zu quantifizieren. Es wurde gezeigt, dass die Sohlschubspannung in Versuchen mit makrorauen Ufern und beweglicher Sohle um 5% bis 40% reduziert wurde. Ausserdem zeigten die Versuche, dass die Zunahme der Sohlstabilität in den Versuchen mit wenig bis mittelrauen Seitenwänden hauptsächlich durch die hydraulischen Effekte erklärt werden konnte. In den Experimenten mit sehr rauen Ufern spielten granulare Effekte zusätzlich

eine Rolle. Zum einen bildeten sich die Stufen bevorzugt in den Engstellen, welche durch die Rauheitselemente induziert wurden. Zum anderen waren die Stufen deutlich stabiler als in Versuchen mit glatten Ufern, was auf ein Verkeilen der Blöcke mit den makrorauen Ufern hindeutet. Im Allgemeinen trägt diese Arbeit zum Prozessverständnis bezüglich Enstehung und Stabilität von Stufen-Becken-Sequenzen bei, welche typisch in steilen Gebirgsbächen sind.

Das Prozessverständnis der natürlichen Stufen-Becken-Sequenzen ist wichtig für die Dimensionierung von gebauten Stufen-Becken-Sequenzen. Es wurde angenommen, dass diese Systeme, analog zu den natürlichen Systemen, einen selbststabilisierenden Charakter aufweisen. Allerdings sind bisher nur wenige Bemessungskriterien für gebaute Stufen-Becken-Sequenzen vorhanden. Ziel der vorliegenden Arbiet war es, die wichtigsten Prozesse solcher Systeme zu identifizieren und die Ergebnisse in einer ersten Bemessungsgrundlage zusammenzufassen. Physikalische Modellversuche wurden durchgeführt, um den Einfluss der Sohlneigung, der Gerinnebreite, der Zusammensetzung des Sohlmaterials und unterschiedlicher Geschiebezugaberaten auf die Stabilität, die Versagensmechanismen und die zu erwartenden Kolktiefen systematisch zu untersuchen. Ausserdem wurden verschiedene Stufen-Becken-Geometrien untersucht, wobei dazu das Blockgewicht, die Stufenlänge und die Blockanordnung variiert wurden. Dabei waren das Blockgewicht der stufenbildenden Blöcke, die Geschiebezufuhr, das Sohlgefälle sowie die Blockanordnung die wichtigsten Parameter hinsichtlich Stabilität. In einem weiteren Schritt wurden die Versagensmechanismen identifiziert, wobei die meisten Stufenversagen auf ein Kippen der Blöcke (46%) oder auf eine Destabilisierung des Stufenfusses infolge Unterkolkung (45%) zurückzuführen waren. Entgegen den Erwartungen wurde in ~70% der Versuche ein abruptes Systemversagen beobachtet. Dabei verursachte das Versagen einer einzelnen Stufe eine rückwärtsschreitende Erosion, welche zur Zerstörung aller oberhalb liegenden Stufen führte. Ein neuer stabiler Zustand nach einem solchen integralen Systemversagen war mit einer erheblichen Abnahme der Sohlneigung verbunden. Als letzter Punkt wurde eine empirische Gleichung entwickelt, um die resultierende Stufenhöhe bei Reinwasserbedingungen und mit Geschiebezugabe abzuschätzen, was insbesondere für die Bemessung des Uferschutzes von Bedeutung ist. Abschliessend wurden die Ergebnisse zu einer Bemessungsgrundlage für die Dimensionierung solcher gebauten Stufen-Becken-Sequenzen zusammengefasst.

1   Introduction

1.1   Motivation

First and second order streams account for about 60 to 80% of the total length of the river network worldwide (Strahler 1957; Benda *et al.* 2005; Downing *et al.* 2012). These headwater streams have steep slopes and highly variable conditions in terms of runoff, bed grain size distribution, and bedload transport (Comiti and Mao 2012; Rickenmann 2016). In these headwater streams, i.e., steep mountain streams, discharge increases rapidly during flood events, which is associated with an increase in bedload transport. These steep mountain streams are typically characterized by single step-pool units emerging in channels with bed slopes exceeding ~4% and continuous step-pool sequences for bed slopes higher than 6% to 7% (Montgomery and Buffington 1997; Church and Zimmermann 2007; Recking *et al.* 2012). A great amount of research exists on these natural, self-organizing step-pool systems focusing on step formation mechanisms (e.g., Whittaker and Jäggi 1982; Abrahams *et al.* 1995; Comiti *et al.* 2005; Church and Zimmermann 2007; Golly *et al.* 2019), step stability (e.g., Weichert 2006; Zimmermann *et al.* 2010), geometric relations (e.g., Curran and Wilcox 2005; Chin and Wohl 2005; Chartrand *et al.* 2011; Richardson and Carling 2021), and failure mechanisms (e.g., Crowe 2002). The typical near-critical flow regime is referred to as tumbling flow attributed to the oscillation between supercritical flow over the steps and subcritical flow in the pools (Peterson and Mohanty 1960; Ganz 2003). The emerging hydraulic jumps are highly efficient in dissipating energy that would otherwise be available to erode the channel bed (e.g., Wilcox *et al.* 2011).

Steep streams are schematically divided into upper, middle, and lower reaches (Figure 1.1, Weichert 2006). While sediment enters the channel either through hillslope processes (e.g., landslides) in the upper reach and through bed and bank erosion in both, upper and middle reaches, the sediment is deposited at the transition from the middle reach to the lower reaches (i.e., alluvial fan) due to the significant reduction in channel slope and transport capacity (Badoux *et al.* 2013). Sediment deposition on the alluvial fan decreases the channel discharge capacity potentially leading to overbank flow and inundations causing high damages to the often densely populated areas in the valleys below. As a consequence, these mountain streams can be hazardous to the human population in pre-Alpine and Alpine regions in Europe and other mountainous regions worldwide. Bed stabilization
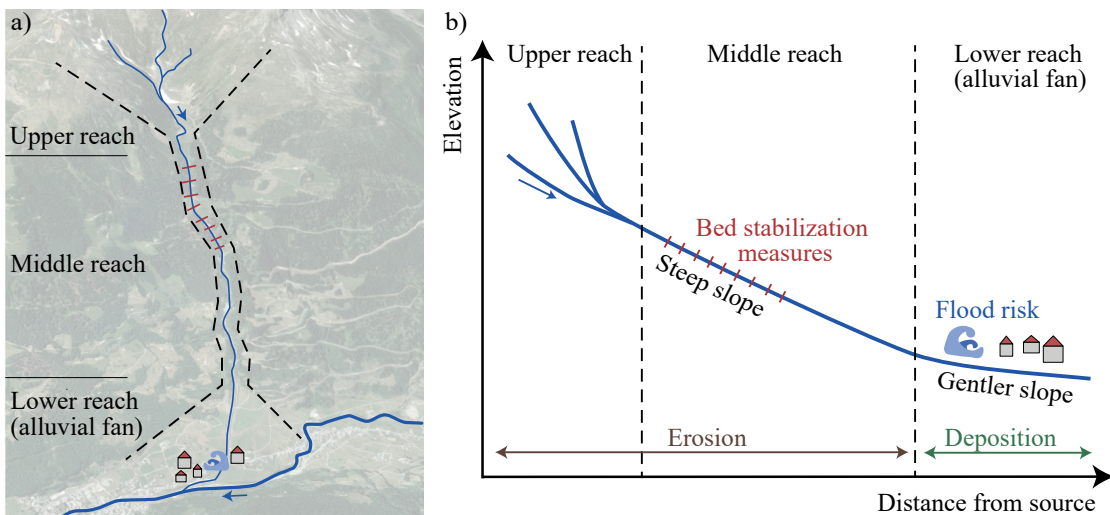
Figure 1.1 a) Plan view of a steep stream (swisstopo 2020); b) corresponding longitudinal profile

measures are required to avoid channel bed incision and to control bank erosion particularly in the upper and middle reaches.

In the past decades, mainly concrete check dams have been used to control channel bed and bank incision (Figure 1.2a). However, these bed stabilization works have high construction, maintenance, and refurbishment costs, may fail instantaneously in an overload scenario, and are related to ecological disadvantages as the longitudinal river continuum is interrupted (Monaghan *et al.* 2005). A promising approach is to replace these concrete check dams with artificial step-pool sequences (i.e., boulder check dams) imitating the natural step-pool morphology of steep mountain streams (Figure 1.2b). Ideally, these step-pool systems have a self-stabilizing character as they adapt to a flood by rearranging the step-forming blocks in a way that another stable step-pool system emerges (Smith *et al.* 2020).

Artificial step-pool sequences have been used in river restoration projects to enhance habitat diversity (Chin *et al.* 2009; Comiti *et al.* 2009b; Yu *et al.* 2010). However, only few studies are available quantifying the ecological impacts of such artificial step-pool systems. For instance, Comiti *et al.* (2009b) found macroinvertebrate richness and diversity to increase in a reach comprising artificial step-pool units compared to a reach with concrete check dams. Furthermore, Chin *et al.* (2021) investigated the co-evolution of a step-pool morphology and biological communities in a self-organized step-pool system where the river itself arranged the randomly placed large boulders into step-pool units. They found that benthic macroinvertebrate communities became more diverse as the step-

Figure 1.2 a) Section of concrete check dams in Gürbe Stream, Switzerland, $S \approx 0.07$ (Photo: SWV 2021); b) Artificial step-pool sequence in Betelriedgraben Stream, Switzerland, $S = 0.15$, right after construction in August 2022 at low discharge (Photo: VAW)

pool morphology developed which was associated with the formation of distinct habitat types. Moreover, Wang *et al.* (2009) found macroinvertebrate density to be considerably higher in a step-pool stream compared to a neighbouring natural stream without step-pool morphology. Even though the ecological benefits of artificial step-pool systems, in particular regarding fish passage, remains unclear, it is reasonable to assume that artificial step-pool systems are a promising alternative to concrete check dams as the habitat is more diverse and they are much better integrated into the landscape (Comiti *et al.* 2009b). In addition, artificial step-pool sequences have proven to be cost-effective in comparison with traditional grade-control structures such as concrete check dam sequences (Lenzi 2002; Beffa 2016).

1.2 Research gaps

The present study aims at contributing to a better understanding of the processes shaping the typical step-pool morphology in steep streams. The channel banks of these steep streams typically contain macrorough elements caused by bedrock, larger boulders, vegetation, or large logs protruding into the flow. These macrorough banks or sidewalls have been proven to increase bed stability in steep mountain streams (Zimmermann *et al.* 2010) but the responsible processes have not been untangled yet. Bed stability is assumed to increase either because sidewall friction reduces bed shear stress (hydraulic effects), because the larger boulders interlock with the rough sidewalls creating extraordinary stable steps (granular effects), or both. Previous investigations demonstrated that granular effects related to grain-grain interlocking, also referred to as jamming, substantially affect bed stability (Zimmermann *et al.* 2010). Steps occurred more frequently in narrow or nar-

rowing sections and also sustained higher hydraulic loads in channels with small channel width to step-forming boulder size ratios, i.e., jamming ratios (Golly *et al.* 2019; Saletti and Hassan 2020). Nevertheless, a sidewall correction is required to quantify bed shear stress in a channel with macrorough sidewalls to properly account for hydraulic effects. Up to now, no such sidewall correction procedure exists for steep streams with macrorough sidewalls, prohibiting to untangle hydraulic and granular effects.

Knowledge of natural, self-organizing step-pool streams is crucial for the design of artificial step-pool sequences representing a nature-based bed stabilization measure. However, only few and inconsistent design recommendations are available for these artificial step-pool sequences (e.g. Thomas *et al.* 2000; Lenzi 2002; Mooney *et al.* 2007). In particular, a procedure linking step-pool geometry (i.e., step spacing and the resulting scour depths) to the system's stability is lacking. Moreover, the failure modes of artificial step-pool systems, which are directly related to the self-stabilizing character of these systems, have not been investigated, yet. The present study aims at providing a consistent design aid for practitioners planning such step-pool sequences as bed stabilization measures or in restoration projects.

1.3   Objectives

Physical flume experiments were conducted at the Laboratory of Hydraulics, Hydrology and Glaciology (VAW) at ETH Zurich to address the above presented research gaps. The thesis was divided into Part A investigating self-organizing step-pool systems (A1 and A2) and Part B addressing artificial step-pool systems (B1 to B5). The following research questions were aimed at being answered:

A1: *To what extent does sidewall friction caused by the macrorough sidewalls reduce the bed shear stress in steep channels?*
It was hypothesized that the bed shear stress decreases significantly in channels with macrorough sidewalls. The research question was addressed by modifying an existing sidewall correction procedure to steep rough channels with macrorough sidewalls allowing a bed shear stress quantification.

A2: *To what extent is the increase in bed stability in channels with macrorough sidewalls related to hydraulic and granular effects, respectively?*

Knowledge of bed shear stress in channels with macrorough sidewalls was used in the bed stability assessment to untangle hydraulic and granular effects contributing to bed stability. It was hypothesized that a significant part of the increase in stability is attributed to hydraulic effects.

B1: *What are the relevant failure mechanisms leading to the destruction of artificial step-pool sequences?*

Step failure mechanisms were assumed to be comparable to those in self-organizing systems, i.e., mechanisms related to scouring are most prominent while destruction by collision and step burial are less frequent.

B2: *Do artificial step-pool systems have a self-stabilizing character in terms of adapting to a flood by rearranging into another stable system?*

It was hypothesized that artificial step-pool systems do have a self-stabilizing character ensuring a more gradual failure in case of an overload scenario.

B3: *Does the experimental procedure (steady and unsteady hydrographs) affect the geometric relations, stability, and failure mechanisms of artificial step-pool sequences?*

It was hypothesized that stationary conditions lead to a collapse at smaller discharges attributed to the longer duration of the peak discharge. Moreover, the descending limb of a hydrograph was assumed to lead to larger scour depths compared to stationary conditions as the free falling jet impinges more vertically on the channel bed in the vicinity of the step toe, potentially triggering step failure.

B4: *How does sediment supply affect scour dimensions and stability of artificial step-pool systems?*

It was hypothesized that clear-water conditions represent a critical condition regarding step stability as scour depths were assumed to be smaller compared to sediment supply conditions. This question was addressed by comparing flume experiments with and without sediment supply for different bed slope, channel width, and step-geometry parameters.

B5: *Which parameters are decisive for the structural stability of such artificial step-pool systems?*

A parameter study was conducted to determine the effect of the channel bed parameters, i.e., bed slope, channel width, and base material composition, and the step-geometry parameters, i.e., step-forming block size, drop height, step spacing, and block arrangement, on the stability of artificial step-pool systems. Moreover, it was hypothesized that jamming effects contribute to step stability.

The main findings of Part A were published in Water Resources Research (Maager *et al.* 2022a,c). The results of Part B are compiled to a design aid for artificial step-pool sequences which is outlined at the end of the present thesis. This research was funded by the Federal Office for the Environment (FOEN) and the Laboratory of Hydraulics, Hydrology and Glaciology (VAW) at ETH Zurich.

1.4   Outline

The present work is subdivided into eight chapters. The hydraulic fundamentals regarding flow resistance, bed shear stress estimation, incipient sediment particle motion, and sediment transport are summarized in Chapter 2 followed by a literature review on steep streams with a step-pool morphology in Chapter 3. Chapter 4 presents the experimental setup for both self-organizing and artificial step-pool systems. The main results regarding the effects of macrorough sidewalls on flow resistance and stability of step-pool channels are compiled in Chapter 5. Moreover, the results on the artificial step-pool systems are presented in Chapter 6 focusing on hydraulic conditions, geometric relations, bed stability, and failure mechanisms. Chapter 7 provides recommendations for practitioners regarding the design of artificial step-pool systems in steep mountain streams. Finally, the conclusions and an outlook are presented in Chapter 8 followed by the Appendix A.

2   Fundamentals

2.1   Overview

This chapter provides an overview of the fundamentals regarding flow resistance, channel stability, sediment transport estimation in (steep) open channels. It does not aim at a comprehensive presentation of each topic but rather focuses on the basic principles applied in the present work. Section 2.2 summarizes approaches to quantify flow resistance in steep open channels. Section 2.3 presents different methods to quantify bed shear stress in particular when accounting for sidewall roughness. Furthermore, Section 2.4 elaborates on the fundamentals regarding channel stability and presents commonly used sediment transport equations. The flow over macrorough surfaces is elaborated in Section 2.5, which is used in Part A with the self-organizing step-pool systems with macrorough sidewalls.

2.2   Flow resistance

Flow resistance originates from the interaction with a solid boundary resulting in shear and pressure forces acting on the flow. Shear forces are a consequence of the wall normal velocity gradient and fluid viscosity. They are often referred to as skin friction, because they arise from the contact with the boundary's surface or skin. Pressure forces arise due to pressure differences at the upstream and downstream end of large roughness elements, which are exposed to the flow. They are referred to as form drag, because the pressure forces acting on these roughness elements highly depend on their shape and geometry and on the flow Reynolds number. Form drag increases substantially if the flow separates from the surface boundary and a wake region is formed, which is characterized by high turbulence and formation of large eddies. Powell (2014) summarizes the following sources contributing to the flow resistance in alluvial rivers:

- Boundary resistance (skin friction)
- Channel resistance (geometry of channel cross-section, planform geometry and presence of bed forms, longitudinal variations of bed slope, i.e., form drag)
- Vegetation resistance (caused by drag of flora and large wood)
- Spill resistance (energy dissipation due to hydraulic jumps emerging at rough structures, e.g., in step-pool systems)
- Sediment transport resistance (energy used to move sediments)

Within the scope of the present study, vegetation and sediment transport resistance are not considered and spill resistance is incorporated into the channel resistance. Flow resistance controls the parameters flow velocity v, flow depth h (or hydraulic radius R), energy slope S_f, and boundary shear stress τ. The Darcy-Weisbach Equation (2.1), Chézy Equation (2.2), and Gaukler-Manning-Strickler Equation (2.3) are most commonly used to relate flow resistance to these flow parameters:

$$v = \sqrt{\frac{8\,g\,R\,S_f}{f}} \tag{2.1}$$

with f = Darcy-Weisbach friction factor,

$$v = C\sqrt{R\,S_f} \tag{2.2}$$

with C = Chézy roughness coefficient, and

$$v = \frac{1}{n_M}R^{2/3}S_f^{1/2} \tag{2.3}$$

with n_M = Manning roughness coefficient. The ratio between mean flow velocity and shear velocity $u_* = \sqrt{g\,R\,S_f}$ describes flow resistance. The following relation interrelates the above described coefficients of common flow resistance equations:

$$\frac{v}{u_*} = \sqrt{\frac{8}{f}} = \frac{C}{\sqrt{g}} = \frac{R^{1/6}}{n_M\sqrt{g}} \tag{2.4}$$

These equations are based on the assumption of steady, uniform flow conditions. In most cases, the assumption of steady flow conditions is reasonable, while uniform flow conditions are rarely attained (Powell 2014). Natural channels have a high spatial variability resulting in non-uniform flow conditions. The above described equations can be applied without considerable error if the flow non-uniformity is not too high (Powell 2014).

Many flow resistance equations for open channel flow are based on the previous findings of pipe flow experiments conducted by Colebrook (1939). However, flow resistance estimation is particularly difficult if the size, shape, and distribution of the bed material is heterogeneous, because the form drag increases when large cobbles and boulders are present (Bray and Davar 1987). Thus, the equations developed for gravel-bed rivers might

not be applicable in steep streams with heterogeneous and widely graded bed material. Bray and Davar (1987) classified gravel-bed channels into three categories of energy dissipation using the relative submergence h/d (or R/d) with d = size of bed material as a criterion (Figure 2.1). The main energy dissipation originates from shear forces at a relative submergence larger than 20. However, the lower the relative submergence is, the more important the drag forces become, which are increased by flow separation at the surface of large boulders and the resulting formation of macro-scale eddies. Consequently, energy dissipation in channels with $h/D_{50} \leq 3$ are dominated by drag forces. The regime is referred to as the jet and wake regime. The flow regime between a relative submergence of $3 < h/D_{50} < 20$ is called transitional, where both shear forces and drag forces are contributing similarly. The following sections present separate approaches for channels with high and low relative submergence, respectively.
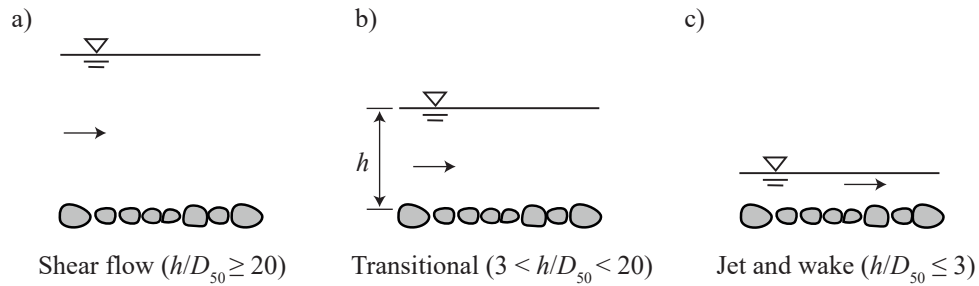
Figure 2.1 Classification of gravel-bed channels in terms of the relative submergence h/D_{50} with D_{50} = median bed surface particle size; a) shear flow, b) transitional flow, and c) jet and wake flow (after Bray and Davar 1987)

2.2.1 High relative submergence

Flow resistance equations for high relative submergence were developed assuming that the grains on the surface act as a compact boundary and the interaction of the flow with the surface leads to a logarithmic velocity profile. Keulegan (1938) developed Equation (2.5) for the Darcy-Weisbach friction factor f for open channels and found the coefficients $c_1 = 2.03$ and $c_3 = 12.2$. According to Bray and Davar (1987), these coefficients correspond to a rectangular channel with aspect ratio $W/h \approx 7$. The equivalent sand roughness in Equation (2.5) may be replaced with $k = (1...4)\, d_{90}$ in natural channels depending on the gravel arrangement at the bed surface (Bezzola 2021).

$$\frac{1}{\sqrt{f}} = c_1 \log_{10}\left(\frac{c_3\, R}{k}\right) \tag{2.5}$$

The coefficient c_3 depends on the cross-section shape; Bathurst (1982) found the following relation:

$$c_3 = 11.1 \left(\frac{R}{h_{max}} \right)^{-0.314} \tag{2.6}$$

with h_{max} = maximum depth of cross-section. Therewith, a value of $c_3 = 11.1$ is obtained for infinitely wide channels and $c_3 = 13.46$ for a circular pipe.

2.2.2 Low relative submergence

The grains protrude into the flow and they do not necessarily form a compact boundary layer in steep channels with low relative submergence. Bed forms such as riffle-pools or step-pools further contribute to flow resistance often referred to as spill resistance (Curran and Wohl 2003; Wilcox *et al.* 2006; Church and Zimmermann 2007; Comiti *et al.* 2009a; Comiti and Mao 2012). Flow resistance is commonly underestimated using Equation (2.5) in channels with low relative submergence and the resistance equations need modifications. Similarly to the approaches for high relative submergence, a characteristic grain diameter d_x is used as a roughness parameter. Thompson and Campbell (1979), for example, accounted for the drag of large grains protruding into the flow by incorporating an extra term:

$$\frac{1}{\sqrt{f}} = 2.03 \log_{10} \left(\frac{12.2\,R}{k} \right) \left(1 - \frac{0.1\,k}{R} \right) \tag{2.7}$$

with a hydraulic roughness $k = 4.5\,d_{50} = 2.37\,d_{84}$. Furthermore, Ferguson (2007) developed the variable power equation (VPE) combining the roughness-layer relation $(8/f)^{0.5} \propto h/d$ for low relative submergence and the Manning-Strickler relation $(8/f)^{0.5} \propto (h/d)^{1/6}$, commonly used for high relative submergence. The VPE is linear at $h/d < 1$ and asymptotic to a 1/6 power relation for $h/d \gg 1$:

$$\sqrt{\frac{8}{f}} = \frac{m_1\,m_2 \left(\frac{h}{d_{84}} \right)}{\sqrt{m_1^2 + m_2^2 \left(\frac{h}{d_{84}} \right)^{5/3}}} \tag{2.8}$$

with coefficients $m_1 = 6.5$ and $m_2 = 2.5$ suggested by Rickenmann and Recking (2011). Aberle and Smart (2003) introduced the standard deviation of the bed elevations σ_z as a

bed roughness parameter to estimate flow resistance:

$$\sqrt{\frac{8}{f}} = 3.86 \ln\left(\frac{h}{\sigma_z}\right) - 1.19 \tag{2.9}$$

Moreover, they proposed a linear relation performing similarly well compared to the logarithmic approach:

$$\sqrt{\frac{8}{f}} = 0.91 \frac{h}{\sigma_z} \tag{2.10}$$

Chen *et al.* (2020) analyzed a large set of flume and field data covering various bed morphologies to compare the performance of using d_i or σ_z as roughness parameters. They found approaches using σ_z to outperform approaches using d_i particularly in steep rough channels.

Hydraulic geometry approaches

Power law equations relate the mean flow velocity to the discharge $v = c\,Q^m$ with c, m = coefficients for a given cross-section being referred to as at-a-site hydraulic geometry concepts (Leopold and Maddock 1953). These equations may be extended to in-between-sites or regime equations expanding the relation with bed slope S and a measure for hydraulic bed roughness k (e.g., d_{90} or σ_z). The following general relationship results for the mean flow velocity in a rectangular channel with unit discharge $q = Q/W$:

$$v = c\,g^{\frac{1-m_1}{2}} S^{m_2} q^{m_1} k^{\frac{1-3m_1}{2}} \tag{2.11}$$

with c, m_1, m_2 = coefficients and g = gravitational acceleration. Rickenmann (1990) approximated the hydraulic bed roughness k with d_{90} of the bed material leading to:

$$v = 1.3\,g^{0.20} S^{0.20} q^{0.60} d_{90}^{-0.40} \tag{2.12}$$

for flume experiments with channel bed slopes $0.03 \leq S \leq 0.20$. Similarly, Aberle and Smart (2003) analyzed flume data and found the following equation using $k = \sigma_z$:

$$v = 0.96\,g^{0.20} S^{0.20} q^{0.60} \sigma_z^{-0.40} \tag{2.13}$$

for bed slopes ranging between $0.02 \leq S \leq 0.10$.

Dimensionless approaches

Rickenmann and Recking (2011) evaluated a large field data set consisting of 2'980 measurements and developed a novel approach to model flow resistance. They defined dimensionless variables q^{**} and v^{**} as follows:

$$q^{**} = \frac{q}{\sqrt{g\,S\,d_{84}^3}} \tag{2.14}$$

$$v^{**} = \frac{v}{\sqrt{g\,S\,d_{84}}} \tag{2.15}$$

and the relation between the two variables is the power function:

$$v^{**} = c\,q^{**\,m} \tag{2.16}$$

with the parameters c and m. They found three pairs of coefficients for the three domains $q^{**} \leq 1$ (large-scale roughness), $1 < q^{**} < 100$ (intermediate-scale roughness), and $q^{**} \geq 100$ (small-scale roughness). They proposed a flow resistance equation for each domain:

$$v^{**} = 1.55\,q^{**\,0.706}; \qquad (q^{**} \leq 1) \tag{2.17}$$

$$v^{**} = 1.60\,q^{**\,0.545}; \qquad (1 < q^{**} < 100) \tag{2.18}$$

$$v^{**} = 3.20\,q^{**\,0.395}; \qquad (q^{**} \geq 100) \tag{2.19}$$

2.3   Bed shear stress estimation

Sidewalls substantially affect flow conditions in physical flume experiments especially in narrow flumes with small widths W and high flow depths h, leading to small aspect ratios W/h. On the one hand, sidewalls affect the flow conditions directly by the sidewall shear stress and on the other hand also indirectly by secondary flows and the resulting velocity-dip phenomenon (Guo 2015). A sidewall correction is required to obtain the bed shear stress. Guo (2015) summarized the often used flow depth method (FDM), hydraulic radius method (HRM), and the Generalized Einstein-Johnson (GEJ) sidewall correction procedure to predict bed shear stress. The bed shear stress τ_b is the force exerted on a river bed by a water column per unit area vice versa the resisting force of the river bed pointing to the opposite direction. The three methods are described in the following sections.
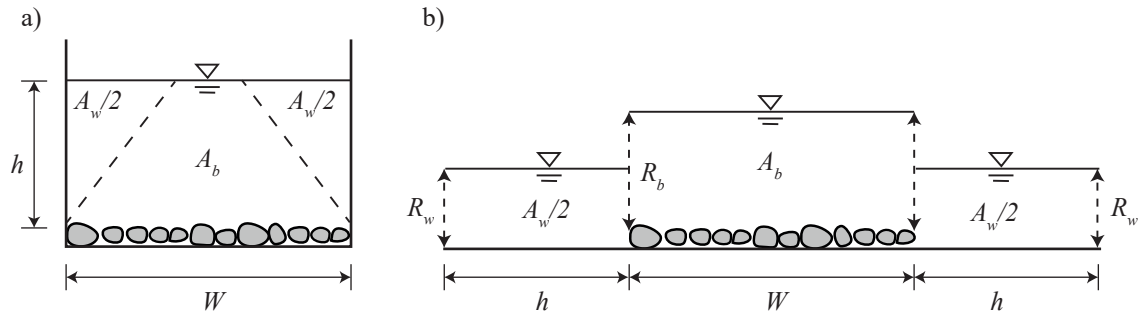
Figure 2.2 Illustration of Einstein's sidewall correction method: a) channel cross-section and b) subareas A_b and A_w of the bed and the sidewalls, respectively (adapted from Guo 2015)

2.3.1 Flow depth method

The bed shear stress $\tau_{b,h}$ is calculated with the following equation according to the FDM:

$$\tau_{b,h} = \rho\, g\, h\, S_f, \tag{2.20}$$

where h = flow depth and S_f = energy slope. Estimating the bed shear stress with the FDM leads to an upper bound for τ_b, i.e., the maximum bed shear stress. The sidewall shear stress acting on both sidewalls of the channels over two times the flow depth is neglected. Thus, the flow depth method is only applicable to wide channels, where the influence of the sidewalls is negligible.

2.3.2 Hydraulic radius method

A lower bound for $\tau_{b,R}$ is specified for narrow channels with small aspect ratios using the HRM. The flow depth in Equation (2.20) is replaced by the hydraulic radius R leading to:

$$\tau_{b,R} = \rho\, g\, R\, S_f \tag{2.21}$$

This method assumes that the total shear stress is distributed equally over the bed width and both sidewalls. The underlying assumption is that bed and sidewalls are equally rough. However, the hydraulic radius method underestimates the bed shear stress in a channel with a rough bed and smooth sidewalls. On the contrary, bed shear stress might be overestimated if the sidewalls are much rougher compared to the channel bed.

2.3.3   Sidewall correction procedures

The channel is commonly divided into the subareas A_b and A_w corresponding to the bed and sidewalls, respectively, when applying a sidewall correction procedure (Einstein 1934; Johnson 1942; Vanoni and Brooks 1957). The interfaces between the subareas (dashed lines in Figure 2.2) are perpendicular to the velocity isolines, thus, no mass and momentum exchange occurs between A_w and A_b. The interfaces do not contribute to the wetted perimeter of the subareas, which are assumed to be independent parallel channels with the same mean flow velocity v and energy slope S_f but with different boundary roughness. The following geometric relations are derived from Figure 2.2 for A_w, A_b, and the hydraulic bed radius R_b:

$$A_w = 2\,h\,R_w; \qquad A_b = (W\,h) - A_w = h\,(W - 2\,R_w) \tag{2.22}$$

$$R_b = \frac{A_b}{W} = h\left(1 - \frac{2\,R_w}{W}\right) \tag{2.23}$$

Einstein (1934) calculated the hydraulic radius of the sidewalls using the Manning coefficient $n_{M,w}$ to describe the sidewall roughness:

$$R_w = \left(\frac{n_{M,w}\,v}{\sqrt{S_f}}\right)^{3/2} \tag{2.24}$$

However, Einstein's approach using the Manning coefficient $n_{M,w}$ is only valid for hydraulically rough conditions. Johnson (1942) modified the Einstein sidewall correction procedure and replaced Equation (2.24) with the von Karman friction law for hydraulically smooth conditions, because such conditions often prevail for the sidewall sub-channels A_w in experimental flumes. The generalized Einstein-Johnson (GEJ) sidewall correction procedure uses the Colebrook (1939) equation, which is valid for smooth, transitional, and rough turbulent flows:

$$\frac{1}{\sqrt{f_w}} = -2\log_{10}\left(\frac{2.51\,f}{\mathsf{Re}\,f_w^{3/2}} + \frac{1}{3.71\,f_w}\frac{f\,k_w}{4\,R}\right) \tag{2.25}$$

where f and R are the total friction factor and hydraulic radius, f_w, R_w, and k_w are the sidewall friction factor, hydraulic radius, and equivalent sand roughness. The Reynolds number is defined as $\mathsf{Re} = (4\,R_w\,v)/v$ with v = kinematic water viscosity. The following

relations are valid following Einstein's hypothesis of equal mean flow velocity v in all sub-channels:

$$v = \sqrt{\frac{8\,g\,R\,S_f}{f}} = \sqrt{\frac{8\,g\,R_w\,S_f}{f_w}} = \sqrt{\frac{8\,g\,R_b\,S_f}{f_b}}, \tag{2.26}$$

thus:

$$R_w = \frac{f_w}{f}\,R; \qquad R_b = \frac{f_b}{f}\,R \tag{2.27}$$

For rectangular channels, the bed friction factor f_b is calculated with:

$$f_b = f + \frac{2\,h}{W}\,(f - f_w) \tag{2.28}$$

Equation (2.28) results from the relation of the total boundary shear stress τ, distributed over the total wetted area $W + 2\,h$ divided into the bed shear stress τ_b acting over the channel width W plus the sidewall shear stress τ_w, distributed over two times the flow depth: $\tau\,(W + 2\,h) = W\,\tau_b + 2\,h\,\tau_w$. Sidewall shear stress τ_w and bed shear stress τ_b are defined as:

$$\tau_w = \rho\,g\,R_w\,S_f; \qquad \tau_b = \rho\,g\,R_b\,S_f; \tag{2.29}$$

and the corresponding dimensionless bed shear stress θ_b is defined as:

$$\theta_b = \frac{R_b\,S}{(s-1)\,d} \tag{2.30}$$

with $s = \rho_s/\rho$ = relative sediment density, and d = grain diameter.

2.4   Incipient motion and sediment transport

The present section elaborates on the incipient motion of single grains and sediment mixtures. First, a force balance is presented for a single grain to assess the driving and resisting forces. Second, the incipient motion of a bed with uniform grain sizes and sediment mixtures is summarized and approaches to assess sediment transport are introduced.

2.4.1   Single grain force balance

Figure 2.3 gives an overview of the driving and resisting forces on a single grain by applying a force balance which was adapted for a step-forming boulder. The gravity force F_G acts in vertical direction and is divided into a destabilizing component $F_G\,\sin\alpha$ and a resisting component $F_G\,\cos\alpha$, where α = angle of the reference plane compared to the
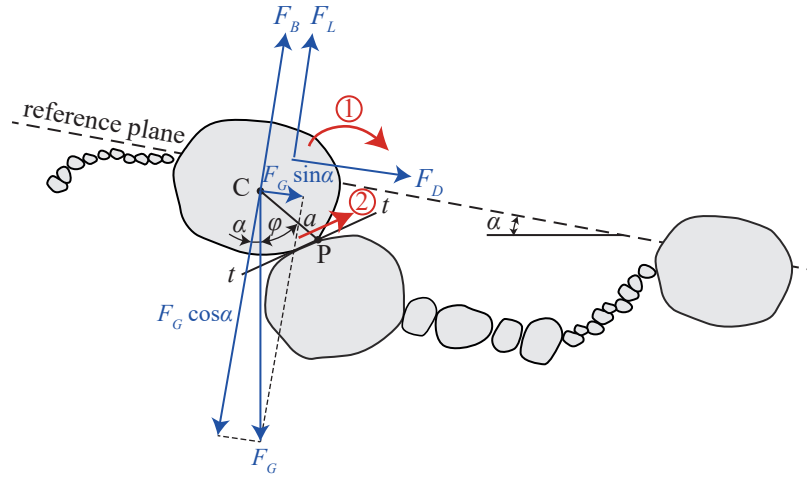
Figure 2.3 Acting forces on a (step-forming) boulder (adapted from Bezzola 2002); boulder size is exaggerated; entrainment mechanisms: ①: tilting around pivot point P, ②: sliding along the tangential plane *t-t*

horizontal plane. The gravity force of the boulder is defined as:

$$F_G = M_B\, g = \frac{\pi}{6} D^3 \rho_s\, g \qquad (2.31)$$

with M_B = block weight, ρ_s = sediment density, and D = equivalent spherical boulder diameter. Furthermore, the buoyancy force F_B is defined according to Equation (2.32) and acts perpendicular to the reference plane:

$$F_B = \frac{M_B}{\rho_s} \rho\, g\, \cos\alpha = \frac{\pi}{6} D^3 \rho\, g \cos\alpha \qquad (2.32)$$

with ρ = water density. The drag F_D and lift forces F_L act parallel and perpendicular to the flow, respectively. They are expressed as:

$$F_D = \frac{1}{2}\rho\, v_{ref}^2\, C_D\, A_D; \qquad F_L = \frac{1}{2}\rho\, v_{ref}^2\, C_L\, A_L \qquad (2.33)$$

with v_{ref} = reference velocity, C_D, C_L = drag and lift coefficients, A_D = area of the boulder perpendicular to the reference plane, and A_L = base area projected on the reference plane. Note that v_{ref} is often approximated by a mean flow velocity estimate. However, the highly turbulent flow leads to considerable velocity deviations both in space and time (e.g., Wilcox and Wohl 2007). Assuming boulders with an ellipsoidal shape with *a-* , *b-*, and *c*-axis, with the longest *a*-axis oriented parallel to the flow, the following equations

describe A_D and A_L:

$$A_D = \frac{\pi}{4} D_b D_c; \qquad A_L = \frac{\pi}{4} D_a D_b \qquad (2.34)$$

with D_a, D_b, and D_c corresponding to the diameter of the a-, b-, and c-axis of the boulder. The drag and lift coefficients have to be determined empirically.

Lamb *et al.* (2017) measured drag and lift coefficients for shallowly submerged cobbles in steep streams with bed slopes ranging from $0.004 < S < 0.3$. They found drag coefficients ranging from $C_{D,sub} = 0.4$ to 0.7 for submerged grains ($h/D \geq 1$) with the lower end corresponding to supercritical flow and the higher end to subcritical flow. The following relation was established for partially submerged particles ($h/D < 1$):

$$C_D = C_{D,sub} \left(\frac{h}{D}\right)^{-1.5} \qquad (2.35)$$

A lift coefficient of $C_{L,sub} = 0.7$ and 1.0 was found for well submerged particles ($h/D > 3$). However, the lift coefficients decreased to zero as h/D decreased and became even negative for partially submerged particles ($C_L = -1$ for $h/D = 0.5$). The following equation relates the lift coefficient to the relative submergence and can be applied to $h/D > 0.5$:

$$C_L = C_{L,sub} \tanh\left[0.7 \ln\left(\frac{h}{D}\right)\right] \qquad (2.36)$$

The equation may not be applied to partial submergence $h/D < 0.5$ as the lift coefficients are even more negative and not well predicted. Lamb *et al.* (2017) assumed that the observed increase in the critical Shields parameter in steep channels with low relative submergence may be associated with the decrease in lift force or even becoming negative, pulling the particles towards the bed.

Two entrainment mechanisms may lead to a destabilization of the boulder (Figure 2.3). On the one hand, the boulder may tilt or roll into the downstream pool (mechanism ①). The ratio of driving and resisting moments around pivot point P equaling unity represents the critical condition. On the other hand, the boulder may slide along the tangential plane indicated as *t*-*t* line in Figure 2.3 (mechanism ②). This mechanism occurs when the static friction between the considered boulder and its neighbouring boulder is smaller than the driving forces. Overall, both entrainment mechanisms are equally important and their occurrence depends on the bed structure, the grain shape, and the grain orientation (Li and Komar 1986).

Table 2.1 Force components and lever arms regarding pivot point P, a = distance between center of gravity C and pivot point P (see Figure 2.3), k_1 and k_2 take the shift with regard to C into account)

Force	Force component	Lever arm regarding P
Gravity force	$F_G \sin \alpha$	$a \cos(\phi + \alpha)$
	$F_G \cos \alpha$	$a \sin(\phi + \alpha)$
Buoyancy force	F_B	$a \sin(\phi + \alpha)$
Hydrodynamic drag force	F_D	$a \cos(\phi + \alpha) + k_1 D$
Hydrodynamic lift force	F_L	$a \sin(\phi + \alpha) + k_2 D$

A force balance is provided to describe the critical condition for tilting. Table 2.1 summarizes the force components and the lever arm regarding pivot point P. Note that a is the distance between the center of gravity (C) and the pivot point P indicated in Figure 2.3. The grain pivot angle ϕ is the angle at which the center of gravity C tilts around point P, where a tilting back to its initial position is not possible. Li and Komar (1986) conducted experiments to determine pivot angles for grains with different sizes and shapes. The following relations are proposed for the tilting of ellipsoids:

$$\phi = 42.0° \left(\frac{D}{d}\right)^{-0.32} \quad \text{for} \quad \frac{D}{d} < 1 \tag{2.37}$$

$$\phi = 36.8° \left(\frac{D}{d}\right)^{-0.52} \quad \text{for} \quad \frac{D}{d} > 1 \tag{2.38}$$

where D is the equivalent spherical diameter of the large grain and d is the grain diameter of the base material. While for angular grains:

$$\phi = 51.3° \left(\frac{D}{d}\right)^{-0.33} \tag{2.39}$$

With regard to the gliding mechanism, a simplification of the static friction law may be applied using the following relation:

$$(F_G \cos \alpha - F_B - F_L) \, \mu = F_G \sin \alpha + F_D \tag{2.40}$$

with μ = coefficient of static friction approached by $\mu = \tan \psi$, where ψ = angle of repose. According to Lane (1955), the angle of repose ψ depends on the grain diameter and values between 36° and 41° are obtained for equivalent spherical grain diameters $D > 5$ cm.

2.4.2   Stability of uniform bed material

Shields (1936) conducted pioneering work regarding the stability of uniform grain material. He conducted flume experiments investigating incipient motion in a tilting flume with bed slopes below $S < 0.005$ and with large relative submergence ($R_b/d > 25$ with R_b = hydraulic bed radius, d = grain diameter of the base material). He found the dimensionless critical bed shear stress θ_c to be a function of the grain Reynolds number $\mathrm{Re}_* = (u_* d)/\nu$ with u_* = shear velocity and ν = kinematic fluid viscosity. The critical dimensionless bed shear stress is defined as:

$$\theta_c = \frac{\tau_{b,c}}{g\,(\rho_s - \rho)\,d} = \frac{R_b\,S}{(s-1)\,d} \tag{2.41}$$

with $\tau_{b,c}$ = bed shear stress for incipient motion and $s = \rho_s/\rho$ = relative sediment density. For $\mathrm{Re}_* > 10^3$, Shields (1936) found the dimensionless critical bed shear stress to be constant $\theta_c \approx 0.06$. Buffington and Montgomery (1997) reanalyzed incipient motion data from the past decades and found the critical bed shear stress normalized with the median grain diameter ranging between $\theta_{c,50} = 0.030$ to 0.073, determined from visual observations, and 0.052 to 0.086, determined from reference bedload transport rates.
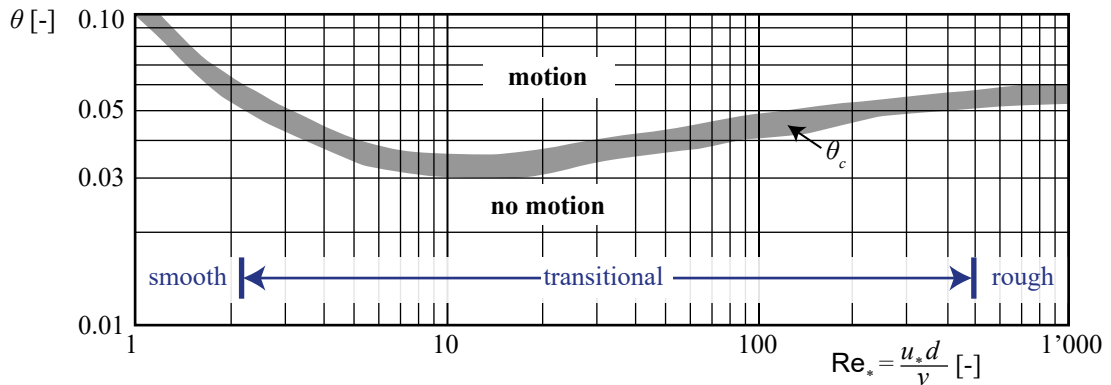
Figure 2.4 Shields diagram (modified after Bezzola 2021)

Meyer-Peter and Müller (1948) conducted flume experiments investigating sediment transport using uniform grain material in a channel with bed slopes $0.0007 < S < 0.015$ and relative submergence $7.5 < R_b/d < 67.5$. They observed movement of single grains at $\theta_c \approx 0.03$ and general sediment transport at $\theta_c = 0.047$. The Shields diagram is used to assess the stability of uniform grain material and has been reproduced by many others (e.g. summarized in Montgomery and Buffington 1997). However, the application is restricted

to conditions with a geometrical standard deviation of the bed material of $\sigma_g = \sqrt{d_{84}/d_{16}}$
< 1.5 and relative submergence $R_b/d > (8...10)$. The Shields diagram can not be directly
applied to steep mountain streams which are characterized by low relative submergence
and widely graded bed material.

2.4.3 Effects of bed slope and relative submergence

Neill (1967) found the Shields parameter θ_c to increase with increasing bed slope,
which has been reproduced by many others (e.g., Ashida and Bayazit 1973; Mizuyama
1977; Bathurst 1987; Lenzi *et al.* 2006). Theoretical considerations following the force
balance of a single grain lead to the opposite, as the destabilizing gravity component in-
creases with increasing bed slope. As a consequence, the increased grain stability in steep
streams was attributed to the increase of relative roughness d/h at which form drag and
spill resistance increased leading to a decrease in bed shear stress (e.g., Ashida and Bayazit
1973; Montgomery and Buffington 1997).

In order to analyze the slope dependency of the critical bed shear stress, Lamb *et al.*
(2008) compiled a tremendous amount of flume and field data and found θ_c to increase
with bed slope:

$$\theta_c = 0.15\, S^{0.25} \tag{2.42}$$

which is valid for $0.001 < S < 0.10$. Data for channels with $S < 0.001$, i.e., mostly for
sand-bed rivers, lack, because Lamb *et al.* (2008) excluded data with $\mathrm{Re}_* \leq 100$ from the
analysis to ensure hydraulically rough conditions. Steep stream data with bed slope ex-
ceeding $S \geq 0.10$ are generally lacking. Note that the median grain diameter d_{50} was used
to calculate the dimensionless critical bed shear stress in studies using sediment mixtures.

2.4.4 Bedload transport equations for heterogeneous sediment mixtures

Sorting processes lead to the formation of an armor layer for widely graded sediment
mixtures ($\sigma_g > 1.5$, Little and Mayer 1972). The smaller grain sizes are transported first
leading to a coarsening of the bed surface. During this phase, partial sediment transport
of the smaller grain size fractions occurs which either originated from the bed or were
supplied from upstream. The armor layer breaks up and the bulk sediment mixture under-
neath is exposed to the flow if the applied bed shear stress exceeds the critical bed shear
stress of the grains forming the armor layer. As a consequence, all grain size fractions are
mobilized and transported leading to full sediment transport conditions.

The bedload transport equation by Meyer-Peter and Müller (1948) relates the effective bed shear stress θ to the critical shear stress θ_c and sediment transport is initiated when $\theta > \theta_c$. This equation is not presented herein, because it should ideally be applied for $S < 0.005$ as transport capacity is overestimated at higher slopes (Bezzola 2021). Rickenmann (1990) developed a sediment transport equation for steeper streams with $0.002 < S < 0.20$:

$$q_s = 3.1 \, \rho_s \, \sqrt{g} \, d_m^{3/2} \left(\frac{d_{90}}{d_{30}} \right)^{0.2} \sqrt{\theta}(\theta - \theta_c) \, \mathsf{F}^{1.1} \tag{2.43}$$

with q_s = unit bedload transport rate [kg/(sm)], ρ_s = sediment density, d_m = mean grain size diameter, d_{90} and d_{30} = grain size diameter for which 90% and 30% are finer, respectively, θ = dimensionless bed shear stress, $\theta_c = 0.05$, and $\mathsf{F} = v/\sqrt{g\,h}$ = Froude number for rectangular cross-sections. The reach-averaged flow velocity was estimated with Equation (2.12). Kaspar (2017) found the equation to be suitable for artificial step-pool sequences using the equivalent spherical grain diameter D_{eq} of the step-forming blocks as a roughness parameter instead of the d_{90} of the base material.

2.4.5 Bimodal sediment mixtures

Bimodal sediment mixtures contain fine bed material with diameter d and coarse material with diameter D but intermediate grain fractions are mostly lacking. According to Raudkivi and Ettema (1982), two mechanisms may occur in case the coarser material is located at the surface and loosely packed: i) The grains protruding into the flow are mobilized at critical bed shear stress much smaller than determined with the Shields diagram being as low as $\theta_c = 0.01$ due to their exposure (Fenton and Abbot 1977). As a consequence, the large fraction is mobilized prior to the mobilization of the fine fraction (overpassing); ii) the fine fraction may be mobilized first leading to an embedding of the large fraction. Raudkivi and Ettema (1982) observed overpassing at ratios $1 < D/d < 6$ and embedding at ratios $D/d > 17$.

2.5 Flow over surfaces with macrorough elements

Perry *et al.* (1969) experimentally investigated different sidewall roughness geometries in a wind tunnel and distinguished two types of roughness (Figure 2.5a,c) following the concepts originating from pipe flow experiments. Therein, k-type flow resistance

a) k-type flow (RAF)   b) transition (NRF)   c) d-type flow (SGF)
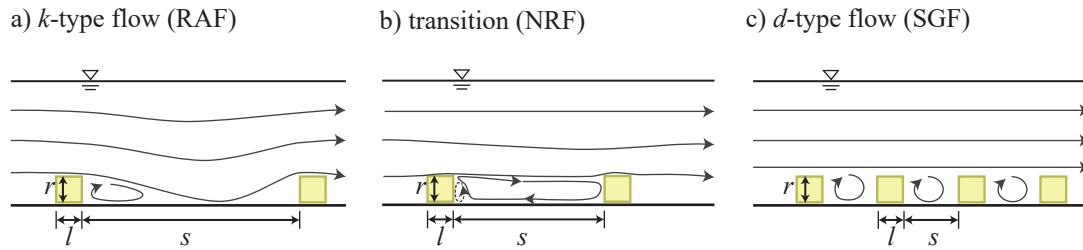
Figure 2.5 Characterization of flow over rectangular elements with RAF = reattachment flow, NRF = normal recirculating flow, and SGF = square-grooved flow (according to Perry *et al.* 1969; Meile *et al.* 2011)

mainly depends on the roughness element size k and d-type flow resistance on the diameter d of the pipe. Similarly, Leonardi *et al.* (2003) performed direct numerical simulations of turbulent channel flows with square bars on one side of the channel wall. They tested different roughness densities r/s, i.e., the ratio between the macroroughness element thickness r protruding into the flow to the element spacing s in flow direction, ranging from 0.053 to 3. For simulations with roughness densities smaller than ~0.14, the flow around each element was unaffected by the corresponding downstream element. Consequently, the flow reattached to the walls before reaching the downstream element (k-type flow) and the flow around an element remained unchanged (Leonardi *et al.* 2003). A roughness density around 0.10 to 0.14 was also reported in other studies to represent the transition between k-type and d-type flow (Adachi 1964; Liu *et al.* 1966).

Similarly, Meile *et al.* (2011) distinguished the flow types reattachment flow (RAF), normal recirculating flow (NRF), and square-grooved flow (SGF) in a channel with macro-rough sidewalls and a small bed slope. Therein, the RAF type corresponds to the k-type flow, the SGF to the d-type flow and the NRF is a transitional regime in between. Meile *et al.* (2011) found the roughness density $r/s \approx 0.10$ to 0.15 to represent the threshold between the RAF and NRF regimes. Flow resistance is maximal when the recirculating wakes behind the roughness elements expand approximately to the downstream roughness element and the flow is about to reattach to the sidewalls, i.e., for ratios $r/s \approx 0.10$ to 0.15. However, at $r/s \geq 0.10$ the jet impinges on the downstream element before reattaching to the sidewalls leading to a decrease in flow resistance despite a higher density of roughness elements.

3 Literature review on step-pool systems

3.1 Overview

This chapter gives an overview of the research conducted on step-pool systems in steep streams. Section 3.2 presents the channel characteristics, morphological classification, and sediment transport regimes of steep streams in general. Section 3.3 summarizes the main findings on the formation processes, typical flow conditions, geometry, bed stability, and failure mechanisms of self-organizing step-pool systems. Section 3.4 provides an overview of existing design recommendations regarding step-pool geometry, scouring processes, stability, and failure mechanisms of artificial step-pool systems. Finally, selected case studies of artificial step-pool systems are presented.

3.2 Steep mountain streams

Headwater streams, accounting for 60 to 80% of the cumulative drainage network worldwide (Strahler 1957; Benda *et al.* 2005; Downing *et al.* 2012), are characterized by steep bed slopes and differ fundamentally from lowland rivers in terms of hydrodynamics, bed morphology, and sediment transport processes (Grant *et al.* 1990; Comiti and Mao 2012). Steep mountain streams feature very high variability in the spatial and temporal domains (Rickenmann 2016). Runoff, for instance, rapidly increases during convective rainstorm events due to the small catchment areas, i.e., CA < 25 km² (Rickenmann 2016). Sediment supply and transport are also highly variable. The presence of relatively large cobbles and boulders compared to the channel width are characteristic for steep streams, which are therefore referred to as cobble- or boulder-bed rivers (Comiti and Mao 2012). The grain size distribution (GSD) of the stream bed is very heterogeneous and varies considerably along the reach. Hydraulic parameters such as flow depth or flow velocity vary not only temporally during low and high flow periods but also spatially due to extremely heterogeneous river bed (Rickenmann 2016).

According to the definition of Montgomery and Buffington (1997), mountain rivers are channels with bed slopes $S > 0.002$ and steep streams are a subset of these mountain streams with bed slopes $S > 0.04$ (Comiti and Mao 2012). The channel morphology of steep streams is, besides fluvial processes, greatly affected by hillslope processes such as debris flows and landslides (Comiti and Mao 2012). Rickenmann (2016) distinguished mountain rivers and torrents depending on the predominant processes, bed slope, bed mor-

Table 3.1 Characterization of steep streams according to Rickenmann (2016)

	Mountain river	**Torrent**
Processes:	Fluvial sediment transport	Debris flow Fluvial sediment transport
Bed slope:	$S = 0.01$ to 0.10	$S > 0.05$ to 0.10
Bed morphology:	More uniform geometry, armor layer, residual blocks Rapids, riffles, pools, bars	Irregular geometry, boulders, bedrock, cascade, step-pools
Lateral sediment input:	low	high
Sediment storage:	high	low

phology, and sediment supply and storage (Table 3.1). Torrents have steep bed slopes at which debris flows become likely, leading to an abundance of large, generally immobile boulders. Torrents are characterized by a more irregular geometry compared to mountain rivers. Contrary, mountain rivers are mainly influenced by fluvial sediment transport and have a more uniform geometry. No clear bed slope threshold exists distinguishing torrents from mountain rivers.

Table 3.2 summarizes the channel parameters catchment area (CA), bed slope S, bankfull channel width W, grain diameter d_i of the bed material for which $i\%$ is finer, and unit discharge q_{RI} corresponding to the indicated recurrence interval (RI) of various Alpine streams. The Alpine mountain rivers and torrents presented herein have CAs between 0.5 and 170 km^2, bed slopes ranging from 0.02 to 0.19, channel widths of 4.7 to 23.5 m, and d_{84} ranging from 0.08 to 0.96 m. The mean unit discharge (±standard deviation) of the flood with RI smaller than 30 years, 30 to 50 years, and 100 years are $q_{<30} = 2.2$ (±2.0) m^2/s, $q_{30-50} = 3.9$ (±2.7) m^2/s, and $q_{100} = 4.9$ (±2.5) m^2/s. Channel and hydraulic parameters vary not only from catchment to catchment but also within the stream.

The bed slope of the streams presented in Table 3.2 negatively correlates with the CA (Pearson's correlation coefficient $p_{Pear} = -0.45$) and unit discharge q ($p_{Pear} = -0.55$, Figure 3.1). Higher unit discharges are expected in streams with lower bed slope (i.e., larger CAs). The indicated RI serve as a rough guidance only due to the high uncertainty attributed to the heterogeneity of steep streams but also to the low availability of long term measurements.

Table 3.2 Hydrological and reach parameters of Alpine mountain rivers and torrents (S = mean bed slope, W = channel width, CA = catchment area, RI = recurrence interval, q_{RI} = unit discharge corresponding to the indicated RI)

Stream name	CA [km^2]	S [-]	W [m]	d_{50} [m]	d_{84} [m]	RI [y]	q_{RI} [m^2/s]
Sperbelgraben[a]	0.5	0.10	5.4	0.04	0.08	20-30	0.2
Rappengraben[a]	0.6	0.11	5	0.03	0.08	50-80	0.5
	0.7	0.06	5	0.03	0.08	30-40	0.4
Erlenbach[a,b]	0.7	0.15-0.17	4.7	0.07	0.29	20	2.3
						50	3.1
Melera[a]	1.1	0.17	5.6	0.04	0.16	80-100	1.4
Schwändlibach[a]	1.4	0.10	5	0.03	0.16	40-50	1.7
Rotenbach[a]	1.7	0.05	5.6	0.05	0.18	40-50	3.2
Rio Cordon (I)[c,d]	5	0.17	5.3	0.11	0.36	12	1.0
						100	2.0
Betelriedgraben[e]	11.5	0.08-0.15	5	0.02	0.20	30	3.4
						100	4.6
						300	6.0
Steinibach[a]	12.2	0.19	8	0.12	0.92	100	5.0
						300	6.3
Buoholzbach[a]	13.9	0.17	9.8	0.07	0.23	30-100	4.1
Kleine Schliere[f]	21	0.03	13	0.06	0.30	30	3.7
						100	6.6
						300	10.4
Mattenbach[a]	31	0.15	13.5	0.07	0.45	30	3.3
Gamsa[a]	38	0.17	11.8	0.05	0.14	?	5.9
Baltschieder[a]	43	0.14	11.7	0.07	0.18	?	8.5
Maso di Spinelle (I)[a]	45	0.14	23.5	-	-	20-25	2.2
						100	3.6
Saltina[a]	78	2	0.14	0.06	0.16	80	8.5
Weisse Lütschine[g]	165	0.04-0.06	12	0.06	0.11	5	5.3
						30	7.1
						100	8.2
Lonza[a]	170	0.06	12.4	0.05	0.20	100	7.7

[a]Nitsche *et al.* (2011), [b]Turowski *et al.* (2013), [c]Rainato *et al.* (2017), [d]Rainato *et al.* (2020), [e]VAW (2015), [f]VAW (2014),[g]HSR (2017)
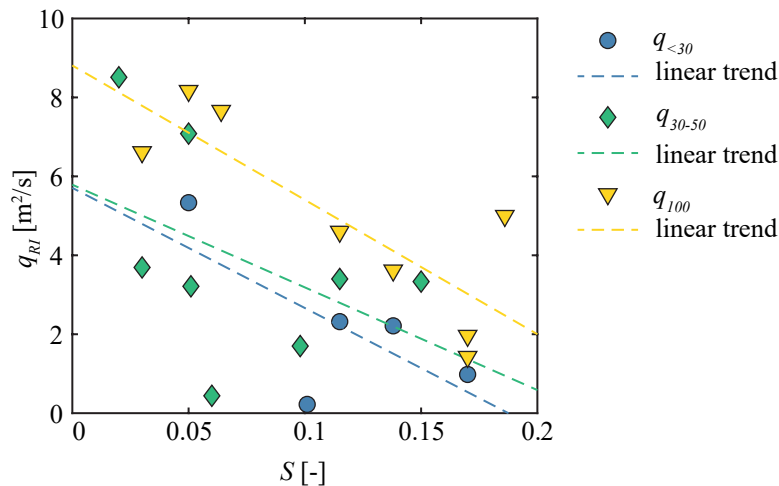
Figure 3.1 Unit discharge q_{RI} for RI smaller 30 years, 30 to 50 years, and 100 years as a function of bed slope S and the corresponding linear trends (data according to Table 3.2)

3.2.1   Morphological classifications

Montgomery and Buffington (1997) distinguished the following channel morphologies: cascade channels, step-pool channels, plane-bed channels, and pool-riffle channels (Figure 3.2).

Cascade channels

Cascade channels are typical in torrents ($S > 0.10$) with narrow channel widths, often confined by the valley flanks. The bed material consists of larger cobbles and boulders which are laterally and longitudinally disorganized. Pool spacing is assumed to be smaller than one channel width. The large grains remain immobile and are only mobilized during infrequent floods with RI = 50 to 100 years (Grant *et al.* 1990). Fluvial processes are dominated by debris flow processes in cascade reaches (Palucis and Lamb 2017).

Step-pool channels

The typical features of step-pool channels are longitudinal channel-spanning steps which form due to the accumulation of cobbles and boulders. Step-pool morphologies develop in streams with bed slopes $0.02 < S < 0.20$ (Abrahams *et al.* 1995; Palucis and Lamb 2017) and the downstream pools have a spacing of about one to four times the channel width (Montgomery and Buffington 1997; Chin *et al.* 2009). The flow alternates between supercritical flow over the step crests and subcritical flow in the pools leading to high energy dissipation (Chin 1989). Similarly to cascade channels, step-pool sequences form
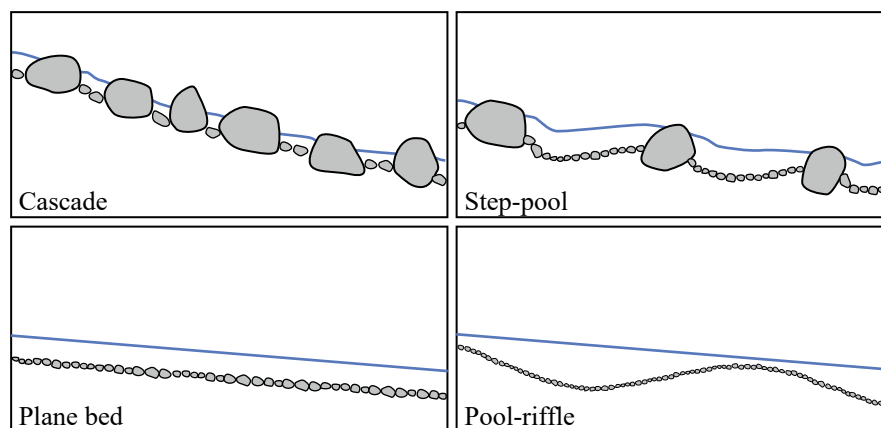
Figure 3.2 Longitudinal profile sketch of the channel morphology of mountain streams at low flow conditions (adapted from Montgomery and Buffington 1997)

in narrow, often confined, channels with small aspect ratios. Church and Zimmermann (2007) found that steps form at low jamming ratios $W/D_{84} < 15$. The definition of Montgomery and Buffington (1997) distinguishes the disorganized cascade morphology and the well-organized step-pool morphology. However, the occurrence of highly organized step-pool morphology with channel-spanning steps is very unusual in mountain streams (Zimmermann 2009). A more detailed review on the self-organizing step-pool morphology is presented in the subsequent Section 3.3.

Plane-bed reaches

Plane-bed reaches form in streams with moderate to high bed slopes, low aspect ratios $W/h < 12$, and bed material consisting of gravels and cobbles (Montgomery and Buffington 1997; Palucis and Lamb 2017). They differ from the other morphologies due to their lack of distinguished bed forms.

Pool-riffle channels

The undulating bed of pool-riffle channels consists of sequences of bars, pools, and riffles. Pool-riffle channels form in unconfined channels with low to moderate bed slopes ($S < 0.03$), width-to-depth ratios $W/h > 12$, and a pool spacing of about five to seven times the channel width (Montgomery and Buffington 1997; Palucis and Lamb 2017).

3.2.2   Macrorough sidewalls

Steep channels feature macrorough bed forms but also macrorough banks or sidewalls. Whereas the former is caused by larger boulders, the latter is attributed to constrictions

caused by bedrock, large boulders, vegetation, or large wood laterally protruding into the flow. The terms banks and sidewalls are used synonymously in the present study. The standard deviation of the mean bank position σ_w is a measure for sidewall roughness introduced by Zimmermann (2009). He found sidewall roughness $\sigma_w \approx 0.43$ m for Giveout and Shatford Creek in Canada. At the base of the channel, these creeks have a mean channel with of $W_m = 5$ and 6 m, respectively, resulting in a relative sidewall roughness of $\sigma_w/W_m \approx 0.08$.

Figure 3.3 illustrates the bank positions obtained from field data (beffa tognacca GmbH 2020), where the dots represent the bank points determined visually from drone footage and the lines represent the mean bank positions fitted to the data following Zimmermann (2009). Herein, σ_w is the standard deviation of the euclidean distance between bankline points and mean bank position. The obtained relative sidewall roughness $\sigma_w/W_m \approx 0.06$ to 0.09 of the reach presented in Figure 3.3 was in the range of the values obtained by Zimmermann *et al.* (2010). However, a precise procedure to estimate σ_w is still lacking.
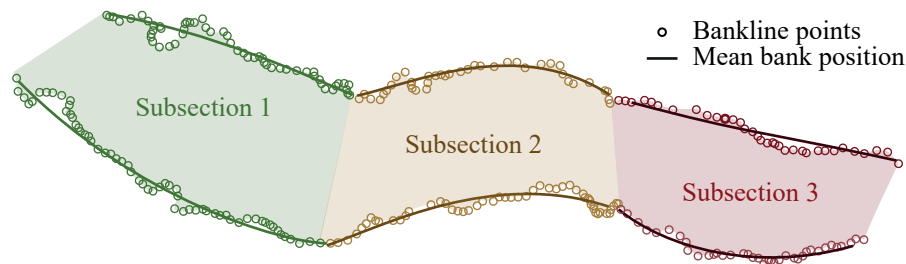
Figure 3.3 Illustration of macrorough sidewalls in a reach of the Verzasca River (data from beffa tognacca GmbH 2020); the reach was divided into Subsections 1 to 3

3.2.3   Sediment transport regimes

The sediment transport regimes, i.e., the relative magnitude of transport capacity $Q_{s,TC}$ to sediment supply $Q_{s,in}$, differ for steep streams with small catchment areas (CAs) compared to streams with gentler bed slopes and larger CAs (Montgomery and Buffington 1997). Sediment transport is supply limited in steep streams as $Q_{s,in}/Q_{s,TC}$ is generally small (Figure 3.4). On the contrary, sediment transport is transport limited in streams with gentler bed slopes because sediment supply exceeds the transport capacity.

Sediment is provided by hillslope processes (e.g., landslides), debris flows, and bed and bank erosion in steep streams and the sediment moving through the system at high flow stages often moves periodically (Whittaker 1987). There are two phases of sediment
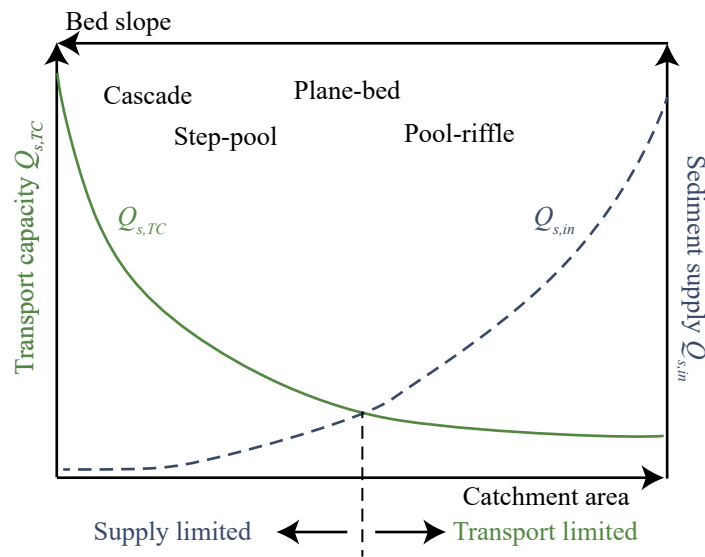
Figure 3.4 Illustration of sediment capacity ($Q_{s,TC}$) and sediment supply ($Q_{s,in}$) in mountainous catchments (modified after Montgomery and Buffington 1997)

transport, i.e., sediment transport over an armor layer and sediment transport at flows capable of breaking the armor layer (Whittaker 1987). Because the grains of the armor layer are only mobilized during infrequent, high-intensity floods, sediment transport over a stable armor layer is more likely to occur. These conditions are also common in channelized lowland rivers with a sediment deficit.

3.3 Self-organizing step-pool systems

Alternating channel-spanning steps and pools are the main features of the step-pool channel morphology (Montgomery and Buffington 1997; Church and Zimmermann 2007). These step-pool units consist of large cobbles or boulders, but also large wooden elements (logs) and bedrock may trigger step formation. Only the former are investigated within the scope of the present study. Single step-pool units have been observed in channels with bed slopes $S > 0.04$ and a continuous step-pool morphology develops in channels with $S > 0.06$ to 0.07 (Church and Zimmermann 2007; Recking *et al.* 2012). This bed slope threshold of continuous step-pool morphology depends on the channel width and the size of the step-forming grains and cannot be precisely defined. Furthermore, typical step-pool channels with regularly spaced channel-spanning steps have rarely been reported from field observations (Milzow *et al.* 2006; Church and Zimmermann 2007). Even though step-pool channels have been reported on bed slopes up to 0.40 (Grant *et al.* 1990), Church and Zimmermann (2007) assume that unbroken step-pool sequences form in channels with

bed slopes $0.07 < S < 0.20$ as steeper channels are dominated by debris flows leading to a cascade morphology.

Figure 3.5 shows a longitudinal profile sketch of a step-pool sequence, where S = bed slope, L_d = step spacing, Λ = step wavelength, H_d = drop height, and H = step height. As the present study investigates bed slopes $S \leq 0.10$, the difference between step spacing L_d and step wavelength Λ is smaller than 0.5%. Thus, the step wavelength is approximated by the step spacing ($\Lambda \approx L_d$) throughout the study. The following sections elaborate on different theories regarding the formation mechanisms (Section 3.3.1), typical flow conditions (Section 3.3.2), step-pool geometry (Section 3.3.3), stability (Section 3.3.4), and step destruction mechanisms (Section 3.3.5) of self-organizing step-pool systems.
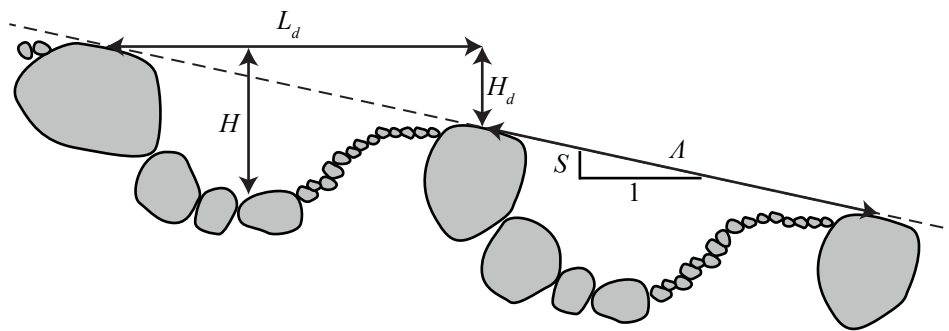
Figure 3.5 Longitudinal profile sketch of a step-pool sequence with S = bed slope, L_d = step spacing, Λ = step wavelength, H_d = drop height, and H = step height

3.3.1   Step-pool formation

The formation of step-pool sequences depends on the following conditions and requirements (Grant *et al.* 1990; Lenzi 2001; Molnar *et al.* 2010):

- Local conditions of the channel (slope, width, ...)

- Heterogeneous bed material

- High floods capable of mobilizing the step-forming grains (RI $\geq$ 20-50 years)

- Near-critical to supercritical flow conditions

- Low sediment supply ($Q_{s,in} \ll Q_{s,TC}$)

Various step-pool formation models have emerged over the past decades. Recently, Golly *et al.* (2019) summarized the three major concepts *hydraulic controls*, *granular interac-*

tion, and *random drivers*. An overview of these step formation concepts is presented in Table 3.3.

The *hydraulic control* class includes approaches linking step formation to hydraulic conditions. The antidune formation theory, for instance, states that the largest grains, transported during high flow conditions, form an initial step as they are deposited under the crest of the standing waves (Whittaker and Jäggi 1982). Smaller grains are sheltered by large grains during the falling limb of the hydrograph leading to the formation of a channel-spanning step. The maximum flow resistance approach by Abrahams *et al.* (1995) assumes that the channel arranges its geometry to maximize energy dissipation, i.e., into a state of maximum flow resistance. The large grains form step-pool units being highly efficient in terms of energy dissipation. Moreover, the pool-scour model relates step formation to scouring mechanisms (Comiti *et al.* 2005). Large grains come to rest at the depositional berm located downstream of the pool forming the next downstream step. Consequently, step spacing is indirectly controlled by the height of the upstream step. Regularly spaced steps are expected when step formation is driven by hydraulic controls (Golly *et al.* 2019) and they dominate in streams with gentler bed slopes (i.e., $S < 0.075$, Chin and Wohl 2005; Zimmermann 2009; Comiti and Mao 2012).

The most prominent theory regarding the second concept of *granular interactions* is the jammed state hypothesis (Church and Zimmermann 2007). It emerged from observations in which steps were much more stable than expected. This additional stability is related to the interlocking of the large boulders forming stable, channel-spanning force

Table 3.3 Overview of important step-pool formation models (adapted from Golly *et al.* 2019)

Class	Concept	Implications
Hydraulic controls	Antidune[a]	Analogy to antidune formation in gravel-bed rivers
	Maximum flow resistance[b]	Energy dissipation (and flow resistance) is at its maximum
	Pool-scour[c]	Scouring processes control step formation
Granular interactions	Jammed state hypothesis[d]	Interlocking of grains, stable force chains
Random drivers	Keystone concept[e]	Steps form at random location of large, immobile boulders

[a]Whittaker and Jäggi (1982),[b]Abrahams *et al.* (1995), [c]Comiti *et al.* (2005), [d] Church and Zimmermann (2007), [e]Zimmermann and Church (2001)

chains. Force chains are particle assemblies transmitting the force in lateral direction and requiring an external force pointing into the opposite direction (Campbell 2003). In steep channels, the external force is applied by the sidewalls (channel banks). Thus, the hydraulic force applied to a large step-forming boulder is not only transmitted vertically into the ground but also horizontally into the channel sidewall. The local constrictions caused by the macrorough sidewalls (Section 3.2.2) may trigger step formation as the large grains transported in clusters deposit upstream of these constriction due to jamming. Jamming is more likely to occur when channel width is small compared to the step-forming blocks ($W/D \leq 6$). Consequently, jamming is assumed to be an important control in narrow (steep) channels owing to the inverse relation between width and bed slope (e.g., Judd 1964; Grant *et al.* 1990). Moreover, steps are more likely to form in narrow or narrowing sections caused by local constrictions (Zimmermann *et al.* 2010; Golly *et al.* 2019; Saletti and Hassan 2020).

The third concept of step formation is associated with *random drivers*. Steps are hypothesized to form at keystone locations comprising immobile large grains resulting from glacial deposits, debris flows, landslides, tributaries, or antecedent transport (Zimmermann and Church 2001). This formation mechanism is more likely to control step formation in steep streams as large blocks are abundant. Golly *et al.* (2019) pointed out that all formation processes somehow depend on sediment transport and hydraulic conditions. Nevertheless, different formative processes lead to different expectations where steps form and how regular their geometry will be.

Curran and Wilcox (2005) identified three mechanisms of step formation in flume experiments. The most common mechanism, accounting for 60% of all step formations, was associated with an initial deposition of the large step-forming grains either on a rough patch of the bed surface or when the grains encountered an obstacle in the channel bed. Therein, hydraulic controls may be decisive as the blocks deposited at regions with lower bed shear stress. However, large particles coming to rest in the vicinity of bed obstacles (keystones) points to random drivers. The second mechanism included excavation of step-forming grains already present in the sediment bed and accounted for 24% of the observed step-pool formations. It remains unclear, whether they were previously deposited due to a hydraulically controlled mechanisms or if these grains represent random keystones. The third mechanisms, accounting for the remaining 16% of all step formations, was related to

symmetrical dunes that periodically formed in the channel similar to the antidune theory. These observations demonstrate that a clear distinction between hydraulic control, granular interactions, and random drivers is difficult. Multiple step formation controls may be important in a single mountain stream mainly depending on the local conditions (Golly *et al.* 2019).

3.3.2   Flow conditions

Flow conditions in step-pool reaches are very complex and greatly differ from flow conditions in gravel-bed rivers (Comiti and Mao 2012). This complexity is attributed to the high bed slopes, low flow depths, poorly sorted and heterogeneous bed material, and the resulting low relative submergence h/d (Comiti and Mao 2012).

A comparison to flow conditions of regular drop structures is worthwhile despite the irregular bed morphology of step-pool channels. Church and Zimmermann (2007) compiled the typical flow regimes for regularly stepped-bed channels (Figure 3.6). The flow is affected by the downstream tailwater (i.e., submerged jet flow) at mild slopes and subcritical flow conditions with reach-averaged Froude numbers $F < 1$. Impinging jets point towards the channel bed at low discharges (Wu and Rajaratnam 1996). Surface jets occur at higher discharges and point towards the downstream step rather than directly on the channel bed. Uniform, subcritical flow is attained when discharge further increases, but is not likely to occur in step-pool channels (Church and Zimmermann 2007). Steep
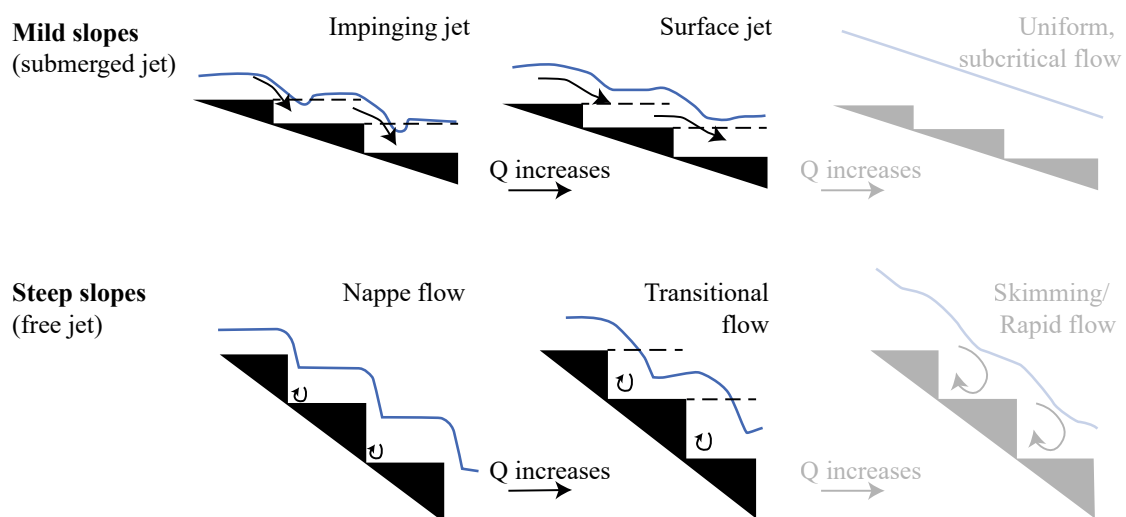
Figure 3.6 Flow regime over stepped-bed channels, the grayish flow regimes are not expected to occur in natural step-pool systems (adapted from Church and Zimmermann 2007)

stepped-bed channels usually feature supercritical flow ($F > 1$) leading to free falling jets. The free flow conditions at low discharge is referred to as nappe flow (Chanson 1994). An increase in discharge results first in a transitional flow regime and then in skimming flow conditions, where the entire flow becomes supercritical and is characterized by a smooth free-surface and recirculating eddies at the step corners (Chanson 1994; Boes and Hager 2003).

It is assumed that nappe flow conditions are predominant at low flow stages for both mild and steep slopes when transferring these flow regimes to a natural step-pool system. With an increase in discharge in milder sloped channels, the impinging jet emerges first followed by the surface jet regime at higher discharges. The transitional flow regime emerges in channels with steeper slopes as discharge increases. The flow hardly reaches a supercritical state, i.e., skimming flow conditions, in natural step-pool systems as the large grains would likely be destabilized under such conditions (Church and Zimmermann 2007; Comiti and Mao 2012). Similarly, Piton and Recking (2019) demonstrated that flows with a transport stage higher than unity ($\theta/\theta_c > 1$) reworking the entire channel, were near-critical and rarely exceeded $F > 1.3$ to 1.5. Hydraulic features observed at near-critical flow like standing waves, lateral shock waves, or hydraulic jumps are very efficient energy dissipating features (Piton and Recking 2019). The oscillation between sub- and supercritical flow leading to the emergence of hydraulic jumps is a key control in natural step-pool systems (Church and Zimmermann 2007).

3.3.3   Step-pool geometry

A great number of approaches exist to correlate the main geometric parameters H = step height, L_d = step spacing or L = step length with channel variables like S = bed slope, W = channel width, or d = characteristic grain diameter (Figure 3.5). Step spacing L_d is the distance between two step crests and step length L is the length of a single step-pool unit. Consequently, step length is generally smaller than step spacing ($L < L_d$) or equals step spacing in case the pool expands to the downstream step. A brief summary is provided below, for an extensive review on geometric relations in step-pool channels see Richardson and Carling (2021).

Step length and height

Many researchers described an inverse relationship of step length and bed slope (Judd 1964; Whittaker 1987; Grant *et al.* 1990; Wohl and Grodek 1994; Chin 1999; Wooldridge and Hickin 2002; Chin and Wohl 2005; Zimmermann *et al.* 2010). Moreover, several authors found a positive relation between step spacing and channel width (Wohl *et al.* 1997; Chin 1999; Chartrand and Whiting 2000) while others were not able to find a clear relation (Wooldridge and Hickin 2002). For example, Chin *et al.* (2009) condensed findings from various field studies and found:

$$L = (1...4)\, W \tag{3.1}$$

Similarly, Okazaki *et al.* (2006) analyzed eight small catchments in Japan with bed slopes ranging from $S = 0.016$ to 0.20 and found

$$L = (1...2)\, W \tag{3.2}$$

Several authors found step height and bed slope to be positively correlated (Wohl and Grodek 1994; Chin 1999), i.e., step height is generally higher in steep streams. Furthermore, step height is controlled by the size of the step-forming boulders (Ashida *et al.* 1984; Wohl *et al.* 1997; Chin 1999; Chartrand and Whiting 2000). According to Chin (1999), boulder diameter D controlled drop height H_d in streams of the Santa Monica Mountains, USA:

$$\frac{H_d}{D} = 1.2 \tag{3.3}$$

Similarly, Ashida *et al.* (1984) in Chin (1999) found a relation for flume experiments:

$$\frac{H_d}{D_m} \approx 1 \tag{3.4}$$

with D_m = mean boulder diameter of the armor layer. Maxwell and Papanicolaou (2001) conducted flume experiments with bed slopes $S = 0.03$ to 0.07 and relative submergence $h/d_{84} = 0.5$ to 2.5. They developed Equation (3.5) to predict step height H and Equation (3.6) to predict step length L:

$$\frac{H}{h}\,\sigma_g^{0.5} = 2.0 \left[\frac{Q}{\sqrt{g\,h^5}} \left(\frac{d_{50}}{h} \right)^{1.5} \right]^{0.31} \tag{3.5}$$

$$L = 7.39 \ln\left(\frac{H}{S}\right) - 5.52 \tag{3.6}$$

where h = flow depth, Q = water discharge, $\sigma_g = \sqrt{d_{84}/d_{16}}$ = geometrical standard deviation, and d_i = grain size for which $i\%$ are finer. The experiments were conducted in a 0.91 m wide channel using three different grain size distributions (GSDs) with $d_{50} = 25$ to 130 mm and $d_{84} = 59$ to 176 mm resulting in jamming ratios $W/d_{84} \approx 5$ to 15, and $\sigma_g \approx 2.5$ to 3.5.

Relative steepness

Abrahams *et al.* (1995) defined the relative steepness $c = (H/L)/S$ by relating step steepness H/L to the bed slope S. A relative steepness of one indicates that step steepness equals the channel slope and the step-pool morphology resembles a staircase. Step-pools sequences with $(H/L)/S > 1$ are inversely sloped, i.e., the lowest point of the pool is lower than the crest of the downstream step. Maximum flow resistance occurred for relative steepness ratios:

$$1 < \frac{H/L}{S} < 2 \tag{3.7}$$

according to the flume experiments of Abrahams *et al.* (1995). The same authors found this relation to hold for field data, in which average values of relative steepness $c \approx 1.5$ were observed. Streams need to experience some *ordinary* floods to obtain a relative steepness above unity (Lenzi 2001). They observed $c < 1$ in field investigation on step-pool systems in the Italian Alps. Relative steepness decreased when fine material was deposited in the pools during low flow conditions and increased when the fine material was eroded during subsequent floods (Comiti *et al.* 2005).

Nevertheless, ratios $c > 2$ were found in streams with bed slopes below 0.05 to 0.07 in subsequent field investigations (Wohl *et al.* 1997; Chartrand and Whiting 2000; Zimmermann and Church 2001). The rise of c for lower bed slope streams was confirmed by Comiti *et al.* (2005) for both natural step-pool systems and for artificial scour pools of grade-control works, i.e., check dams. Comiti *et al.* (2005) developed Equation (3.8) with m_1 being a geometrical parameter ranging between 6 and 8. The equation takes this increase of c for lower bed slopes into account and tends to $c \approx 1.5$ for high bed slopes.

$$c = \frac{m_1 S + 1}{m_1 S} \tag{3.8}$$

The equation was derived with the assumption of an ideal regular staircase-like step-pool architecture and might not hold for natural step-pool systems that are highly variable (Comiti *et al.* 2005). Data of Zimmermann and Church (2001), for example, are below the relative steepness proposed by Comiti *et al.* (2005).

Temporal scale

The geometric relations developed from field and laboratory studies are only a snapshot at a given time. The observed step-pool geometry resulted from different floods in the past (Molnar *et al.* 2010). Lenzi (2001) conducted long-term field surveys of the stream bed of the Rio Cordon, Italy, recording discharge and bed load transport rates. A steep stream modifies its channel geometry during exceptional floods with RI ≥ 30 to 50 years (Grant *et al.* 1990; Lenzi 2001). The large, otherwise immobile, boulders are mobilized, leading to the formation of steps. Ordinary floods with RI ranging from one to ten years are subsequently forming the stream bed as pools emerge due to scouring (Lenzi 2001). The average steepness factor *c* of the Rio Cordon stream was measured before and after the September 1994 flood with a RI between 30 and 50 years and being considered to be an exceptional flood (Lenzi 2001). The steepness factor decreased from *c* = 1.3 before to *c* = 0.79 after the flood due to the breakdown of the step-pool structure and/or the filling of pools. The newly formed steps and pools did not follow the idea of Abrahams *et al.* (1995) that flow resistance was maximized during the 1994 flood. However, the channel seems to gradually evolve towards this state of maximum flow resistance after a couple of ordinary floods. After the ordinary flood in October 1998, a value of *c* = 1.33 was determined.

3.3.4   Bed stability

Church and Zimmermann (2007) defined three key controls of step stability in steep channels. The first control is the *hydraulic load* acting on the grains on the channel bed (θ/θ_c). Second, the ratio between sediment supply and discharge Q_s/Q, i.e., *sediment concentration*, controls bed stability. High sediment supply can lead to the filling of pools which then leads to a decrease in flow resistance and an increase in near-bed flow velocity, i.e., an overall decrease of bed stability (Hohermuth and Weitbrecht 2018). The third key control is the *jamming ratio W/D* with *W* = channel width and *D* = diameter of the step forming blocks. Channels with small jamming ratio, i.e., narrow channels containing large boulders, are more stable due to interlocking of grains (see Section 3.3.1).

Zimmermann *et al.* (2010) connected channel stability to the sediment transport rate measured at the flume outlet to distinguish stable and unstable states and defined four stability classes. Class 0 included data at the end of an experimental test run where the bed adjusted to the flow and little to no changes occurred. In class 0, sediment transport rates were low (runs without sediment feed) and velocity measurements remained constant. In class 1, only little change was observed visually as only small grains were mobilized. In class 2, the bed was significantly modified at least locally, i.e., new steps and pools formed or were destroyed. Moreover, class 3 included conditions during which the bed heavily changed throughout the entire flume length leading to a destruction of the bed structures. In this case, a progressive upstream erosion (PUE) pattern was observed where the destruction of a step triggered the step failure in the upstream. Comiti *et al.* (2009a) observed a similar erosion pattern during their flume experiments.

Zimmermann *et al.* (2010) explicitly tested the jammed state hypothesis by conducting flume experiments. Therein, $D_{84,step}$ = diameter of the step-forming blocks was used to express the jamming ratio $W/D_{84,step}$. Bed stability was described by the Shields ratio between applied dimensionless shear stress and critical dimensionless bed shear stress $\theta_c = 0.045$:

$$\frac{\theta}{\theta_c} = \frac{R\,S}{(s-1)\,d_{50}} \frac{1}{0.045} \tag{3.9}$$

Bed topography was scanned after the discharge was lowered to zero for the stable bed experiments of class 0. For these experiment, Zimmermann *et al.* (2010) found that the Shields ratio significantly increased for jamming ratios $W/D_{84,step} \leq 6$ (dashed line in Figure 3.7) and they obtained a nonlinear fit predicting the Shields ratio as:

$$\frac{\theta}{\theta_c} = 6.7 \left(\frac{W}{D_{84,step}} \right)^{-0.57} \tag{3.10}$$

The scatter was rather large resulting in a predictive power $R^2 = 0.27$ for the above presented Equation (3.10). As a consequence, Zimmermann *et al.* (2010) analyzed data of stability classes 2 and 3 representing unstable bed conditions. No clear threshold was defined as the data of stable and unstable bed conditions overlap. Consequently, they quantified the probability p of a parameter combination θ/θ_c and $W/D_{84,step}$ to result in unstable condition (Figure 3.7).
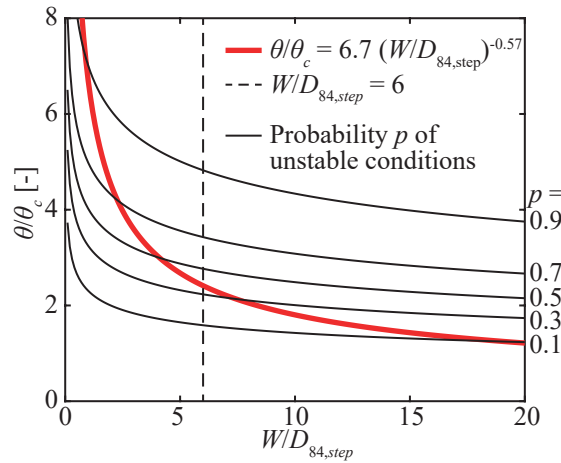
Figure 3.7 Stability assessment according to Zimmermann *et al.* (2010) with Shields ratio θ/θ_c as a function of the jamming ratio $W/D_{84,Step}$ (red line: Equation (3.10), dashed line: $W/D_{84,Step} = 6$, solid lines: data plotting above are unstable with probability p

Zimmermann *et al.* (2010) conducted experiments with both smooth and rough sidewalls. They glued plywood slabs to the flume sidewalls reproducing the same standard deviation of the mean banks position σ_w, as observed in Shatford Creek, Canada (Zimmermann *et al.* 2010, Section 3.2.2). The bed was more stable in tests with rough sidewalls and Zimmermann *et al.* (2010) concluded that grain-sidewall interactions increased step stability. However, they did not account for hydraulic effects of the rough sidewalls potentially reducing bed shear stress, as no appropriate sidewall correction procedure was available.

The self-stabilization processes in steep channels are associated with bed rearrangement, i.e., bed erosion (Weichert *et al.* 2008). Among others, Weichert *et al.* (2009) defined different scales at which self-stabilization mechanisms occur in steep-channels:

- *Micro-scale* (~0.01-0.1 *W*): Bed armoring as key process

- *Meso-scale* (~ 1 *W*): Formation of steps and pools

- *Macro-scale* (~10 *W*): Formation of riffle and pools

- *Reach-scale* (> 100 *W*): Rotational erosion around a pivot point reducing bed slope

Aberle (2000) analyzed flume data of natural step-pool channels and found the threshold between stable and unstable channel beds to be given by:

$$q_{stab} = \frac{0.20 \sqrt{g \, \sigma_z^3}}{S^{1.3}} \tag{3.11}$$
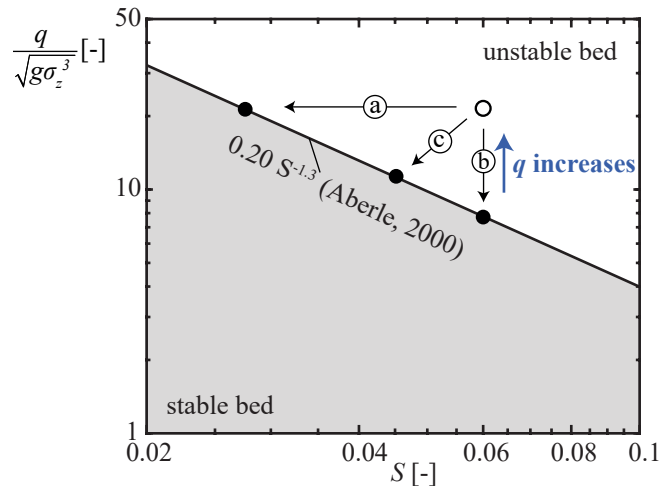
Figure 3.8 Self-stabilization through (a): reduction of bed slope, (b): increase of channel roughness, or (c): a mixture of both (adapted from Weichert *et al.* 2008)

A discharge increase leads to a short-term destabilization of the channel bed (Figure 3.8). Self-stabilization occurs either through (a) a reduction in slope, (b) an increase of bed roughness in terms of the standard deviation of the bed elevations σ_z, or (c) a combination of both (Figure 3.8).

3.3.5   Step failure

Monitoring step failure in the field has hardly been achieved, because high flows are infrequent and observations would be difficult if not dangerous. Most of the data on step failure has been obtained from laboratory investigations. Crowe (2002) observed three step failure mechanisms during flume experiments with sediment feed. The majority of the steps (77%) collapsed due to the *downstream scour*. The step failure caused by scouring processes was divided into *keystone tumbling* (39%) and *aggregate slumping* (38%). The former process included step failure where the top keystone tumbled into the downstream pool because of undermining by downstream scour. The latter process was associated with an overall collapse of the step. *Step failure by collision* of large grains with the keystones accounted for 10% of all step failures. The third process was the *burial of the step-pool units* with fine sediments, accounting for the remaining 13%. Even though the step remains stable, the pool filling reduces flow resistance and the associated increase in near-bed flow velocity may lead to the destabilization of the step (Hohermuth and Weitbrecht 2018). These buried steps may be excavated during a subsequent flood. Steps may also be destroyed by *debris flow events* (Church and Zimmermann 2007).

3.4   Artificial step-pool systems

Design recommendations for artificial step-pool sequences are reviewed herein. Lenzi (2002) defines the following prerequisites for the use of boulder check dams (i.e., step-pool sequences) as grade-control structures:

- Bed slopes ranging from 0.05 to 0.20

- Abundance of large boulders

- Possibility to place the boulders on large boulders already present in the stream

- Step-pool morphology existing in the stream or its tributaries

Stabilization works with large boulders comprise concrete check dams covered with boulders, boulders reinforced with a concrete framework, boulder check dams strengthened with cement, or boulder check dams without any reinforcement (Lenzi 2002, Table 3.4). Check dams with *reinforced concrete frameworks* include structures containing large boulders being firmly tied to each other and anchored to the ground by micropiles. A simplification are check dams *strengthened with cement*, where less than half of the cement is used compared to reinforced boulder check dams. The *boulder check dams* without any reinforcement are referred to as artificial step-pool sequences in this study. The field of use of such boulder check dams without reinforcement is restricted to channels with bed slopes

Table 3.4 Fields of use for boulder check dams (after Lenzi 2002)

	Boulder check dams (artificial step-pool sequences)	Check dams strengthened with cement	Check dams with reinforced concrete framework
Bed slope:	$S < 0.12$ to 0.14	$S < 0.18$ to 0.20	$S < 0.18$ to 0.20
Bed material:	Widely graded, many large boulders	Graded, prevalence of gravel/pebbles	Uniform, prevalence of sand, gravel, small pebbles
Morphology:	Step-pool	Short step-pool sequences	Not very structured channel
Interventions:	None	Few	Many
Sediment transport:	Bedload	Bedload, hyperconc. flow	Bedload, hyperconc. flow, debris flow
Degree of safety (RI):	20 to 30 years	30 to 50 years	> 50 years

$S \leq 0.14$. A widely graded distribution of the bed material with an abundance of large boulders is required. Furthermore, the channel itself has a step-pool morphology in its original state and the channel bed was not influenced by previous interventions. Sediment transport is dominated by bedload transport rather than hyper-concentrated or debris flow conditions. Uncemented boulder check dams are suitable for a degree of safety up to floods with RI = 20 to 30 years (Lenzi 2002).

In the following sections, the state-of-the-art for the design of artificial step-pool sequences is summarized and approaches to estimate the block size, block arrangement, step height and spacing, and step stability are reviewed. All measures are indicated in prototype scale as Part B on artificial step-pool systems mainly addresses practitioners. Furthermore, findings on failure mechanisms of such systems are presented.

3.4.1 Geometry

This section presents approaches to estimate the geometry of artificial drop structures (step height, scour depth, and step length) used as bed stabilization measures in steep streams. The review is not restricted to step-pool sequences but approaches for individual bed sills and check-dam sequences are presented for comparison. The definition sketch for each system is given in Figure 3.9 and the main parameters are summarized in the following as they are defined differently depending on the system.
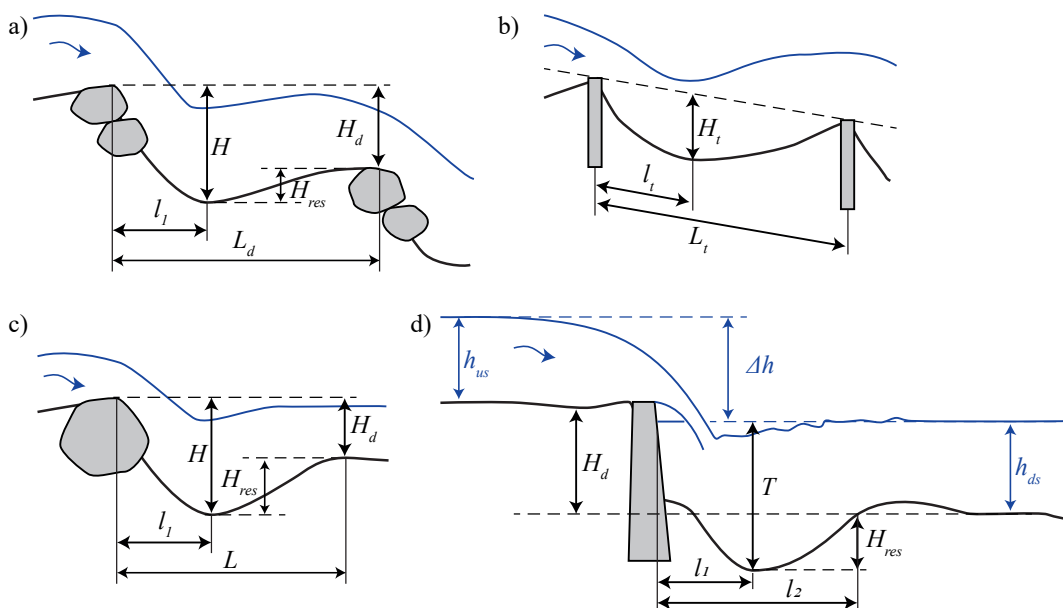
Figure 3.9 Schematic longitudinal profiles of a) a step-pool sequence, b) a check-dam sequence, c) an individual step-pool unit, and d) an individual drop structure

In a step-pool sequence (Figure 3.9a), the step spacing L_d is defined as the horizontal distance between two subsequent step crests and the step height H is the vertical distance between the step crest and the lowest point in the scour pool. For an individual step-pool unit (Figure 3.9c), the step length L is defined as the horizontal distance from the step crest to the end of the pool. In a step-pool sequence, the step length equals the step spacing if the scour expands to the downstream step ($L = L_d$). For low discharges or large step spacings, i.e., no geometric interference with the downstream step, the step length is smaller than the step spacing ($L < L_d$). The drop height H_d is the difference between two step crests and the residual depth (often referred to as scour depth) is defined as $H_{res} = H - H_d$. The distance l_1 is the spacing between step crest and the deepest point in the scour pool. Figure 3.9b shows the parameter definition of a check dam sequence according to Volkart (1972). The spacing L_t is the distance between two check dams parallel to the bed, l_t is the distance to the deepest point in the scour pool, and the scour depth H_t is the horizontal scour depth relative to the initial flat channel bed. Note that the difference between L_d and L_t (referred to as step wavelength Λ in natural step-pool systems, Figure 3.5) is smaller than 0.5% for bed slopes $S \leq 0.10$. For individual drop structures (Figure 3.9d), the scour water depth T is defined as the sum of the scour depth, i.e., residual depth H_{res}, and the downstream flow depth h_{ds}. Transferred to step-pool systems, the scour water depth T equals the step height $H \approx T$ in case of comparable flow depths in the upstream and downstream step-pool unit ($h_{us} \approx h_{ds}$), i.e., the difference in up- and downstream flow depth Δh is approximated with the drop height ($\Delta h \approx H_d$).

Step-pool systems

Thomas *et al.* (2000) proposed an approach to estimate step height based on field data of eight streams in Colorado with bed slopes ranging between 0.015 and 0.081. The bed material consisted of grains with diameters $d_{50} = 39$ to 72 mm and the step-forming blocks had diameters $D = 450$ to 630 mm. Drop height H_d was the independent parameter and step height H and step length L are obtained with Equations (3.12) and (3.13) using unit discharge of a 25-year flood q_{25}, bed slope S, and channel width W as input parameters.

$$H = W \left[-0.018 + 1.394 \frac{H_d}{W} + 5.514 \frac{S \, q_{25}}{\sqrt{g} \, W^{3/2}} \right] \qquad (3.12)$$

$$L = W \left[0.409 + 4.211 \frac{H_d}{W} + 87.341 \frac{S\, q_{25}}{\sqrt{g}\, W^{3/2}} \right] \tag{3.13}$$

These equations were applied to four individual step structures („vortex weirs") located in a stream with an order of magnitude lower bed slopes compared to the streams the equations were obtained from. The emerging step length L of the vortex weirs agreed well with Equation (3.13). However, step height H was larger than predicted with Equation (3.12) as finer material was present in vortex weir pools.

Check-dam sequences

Volkart (1972) conducted flume experiments for a check-dam sequence and developed Equation (3.14) for clear-water (CW) and Equation (3.15) for sediment feed (SF) conditions with sediment concentration $C_s = q_s / ((\rho_s - \rho)\, q) < 0.134\%$, where q_s = unit gravimetric sediment transport rate, ρ_s = sediment density, ρ = water density, and q = unit water discharge. The experiments were conducted for bed slopes $S = 0.006$ to 0.07 and the mean grain diameter in prototype scale was $d_m \approx 30$ to 90 mm ($\lambda = 25$). The distance from the crest to the deepest point in the scour pool was estimated with Equation (3.16). The parameters are defined in Figure 3.9b.

$$H_t = 1.25\, \frac{q^{1/2}\, S^{1/2}\, L_t^{2/3}}{d_{90}^{5/12}\, (s-1)\, g^{1/4}} \tag{3.14}$$

$$H_{t,s} = 1.25\, \frac{q^{1/2}\, S^{1/2}\, L_t^{2/3}}{d_{90}^{5/12}\, (s-1)\, g^{1/4}} \left[1 - 0.526 \frac{S\, L_t}{d_{90}} \left(\frac{q_s}{q\, (\rho_s - \rho)} \right)^{1/8} \right] \tag{3.15}$$

$$l_t = L_t \left(\frac{H}{L_t} \right)^{1+15\,S} (3.5 + 150\, S) \tag{3.16}$$

Whittaker (1987) investigated the scour dimensions of step-pool systems under CW and SF conditions using successive discrete weirs, i.e., check-dam sequences comparable to Volkart's (1972) setup. Note that the parameter definition for step-pool system (Figure 3.9a) is used in the following even though a check-dam structure was investigated. The experiments were conducted in two different flumes with channel widths $W = 0.13$ and 0.20 m (model scale) and bed slopes ranging from $S = 0.098$ to 0.248. The weirs were spaced $L_d = 0.25$ and 0.50 m apart (model scale) and three sediment mixtures with $d_{90} = 0.005$ to ~ 0.012 m (model scale) were used. The following equations were developed to predict the scour depth H_{res}, and the vertical depth of flow in the scour hole, herein approximated

by the step height H, for CW conditions:

$$H_{res} = 0.9121 \frac{(q - q_{cr})^{0.4526} \, H_d^{0.5877}}{d_{90}^{0.2666}} \tag{3.17}$$

$$H = 1.4115 \frac{(q - q_{cr})^{0.5034} \, H_d^{0.476}}{d_{90}^{0.2311}} \tag{3.18}$$

with q_{cr} = unit water discharge at incipient conditions for a given slope and grain size distribution. Whittaker (1987) used the vertical difference between the weir crest and the top of the scour instead of the drop height H_d. Moreover, Whittaker (1987) developed a relation to estimate the reduction in step height as a function of the volumetric sediment transport rate $q_{s,v}$, yielding:

$$\frac{H}{H_{max}} = \ln \left(\frac{0.8662 \, S^{0.1097} \, q^{0.2164}}{d_{90}^{0.0579} \, q_{s,v}^{0.1778}} \right) \tag{3.19}$$

with H_{max} = maximum step height for low sediment transport rates. Note that the definitions of step height in Equation (3.19) and (3.18) differ within the study of Whittaker (1987).

Marion *et al.* (2004) conducted flume experiments with a sequence of artificial sills focusing on the effect of sill spacing on scour depth resulting in Equation (3.20). Therein, $H_e = 1.5 \, (q^2/g)^{1/3}$ is the critical energy head, $a = (S - S_{eq})/L$ is the morphological jump height with S_{eq} = equilibrium slope being estimated with a bedload transport equation or the Shields parameter for CW conditions. Furthermore, $SI = 0.5(d_{84}/d_{50} + d_{50}/d_{16})$ is the sorting index equaling the geometrical standard deviation σ_g for log-normal distributions.

$$\frac{H}{H_e} = 2.68 \left(\frac{a}{H_e} \right)^{0.43} SI^{-0.19} \left(1 - e^{-0.14 \frac{L}{H_e}} \right) \tag{3.20}$$

The experiments were conducted in a channel with $W = 0.5$ m, $S = 0.045$ to 0.08 using bed material with $d_{50} = 8.9$ mm (model scale) and $SI = 1.5$. Furthermore, flume data from Lenzi *et al.* (2002) and field data of the Cordevole River in Italy were used to develop Equation (3.20) extending the application range to $S = 0.14$ and $SI \approx 6$. In general, Equation (3.20) can be applied to conditions with $0.19 < a/H_e < 1.9$ and contains both, data with geometrical interference (i.e., scour dimensions are reduced by the downstream

sill) and without interference. Marion *et al.* (2004) observed interference for $L/H_e \leq 15$ independent of the grain size distribution of the base material. Geometrical interference strongly depends on the flow conditions as a check-dam sequence may be non-interfering at low discharge and interfering at high discharges (Marion *et al.* 2004).

Marion *et al.* (2006) extended the analysis of Marion *et al.* (2004) and investigated the effect of sediment supply ($C_s < 0.12\%$) on the resulting scour depth. The scour depth decreased on average by 15% in channels with $S = 0.074$ and up to 40% in channels with $S = 0.042$ in SF experiments. No additional parameter was required to incorporate the effect of sediment supply in Equation (3.20). The parameter $a =$ morphological jump height, which was initially introduced by Gaudio *et al.* (2000), accounts for the effect of sediment supply. If the scour expands to the downstream bed sill, the morphological jump height equals the drop height $a = H_d$. Marion *et al.* (2006) observed that the equilibrium slope S_{eq} (i.e., slope in between two bed sills in case the scour does not expand to the downstream sill) increased in sediment supply experiments leading to a decrease of a and therewith also a decrease of the maximum scour depth H. As a consequence, the approach initially proposed by Marion *et al.* (2004) was recalibrated resulting in:

$$\frac{H}{H_e} = 3.0 \left(\frac{a}{H_e} \right)^{0.60} SI^{-0.19} \left(1 - e^{-0.25\frac{L}{H_e}} \right) \tag{3.21}$$

Individual drop structures

Kotoulas (1967) developed Equation (3.22) to estimate the scour depth of artificial drop structures, i.e. bed sills. It was developed for CW conditions and should only be applied when Equation (3.23) is satisfied. The parameters are defined in Figure 3.9d.

$$H \approx T = H_{res} + h_{us} = 0.78 \frac{\Delta h^{0.35} q^{0.7}}{d_{90}^{0.4}} \tag{3.22}$$

$$5 < \frac{q^{1/2} \Delta h^{1/4}}{d_{90}} < 25 \tag{3.23}$$

If the overflow jet is submerged by the downstream flow, an undulating water surface emerges and the jet impinges more horizontally on the river bed. Consequently, the scour water depth for the submerged case T' was found to be reduced to 84% of the free overflow scour water depth T, i.e., $T' \approx 0.84\ T$ (Kotoulas 1967). Furthermore, Kotoulas (1967) developed relations to estimate the distance between the crest and the maximum scour

depth l_1 as well as the total scour length l_2:

$$l_1 = 3.9 \frac{\Delta h^{0.27} q^{0.54}}{g^{0.27} d_{95}^{0.08}} \tag{3.24}$$

$$l_2 = 2.7 \frac{\Delta h^{0.45} q^{0.90}}{g^{0.45} d_{95}^{0.80}} \tag{3.25}$$

For the submerged case, where the scour pool is shallower and more expanded, the following relations were found: $l_1' = 1.13\,l_1$ and $l_2' = 1.6\,l_2$. Equations (3.22) to (3.25) were developed for CW conditions. However, Tschopp and Bisaz (1972) found that the scour water depth T was reduced by approximately 20 to 30% in experiments with sediment supply ($0.6\% < C_s < 3.6\%$).

Lenzi *et al.* (2003) analyzed scour hole geometries below 73 grade-control structures like check dams and bed sills with drop heights $H_d = 0.2$ to 5 m in channels with $S = 0.02$ to 0.16. They developed a relation for the step height normalized with the critical flow depth $h_c = (q^2/g)^{1/3}$, including results from flume experiments conducted by Lenzi *et al.* (2002):

$$\frac{H}{h_c} = 1.21 \frac{H_d}{h_c} + 0.96; \qquad R^2 = 0.95 \tag{3.26}$$

The hydraulic loading in terms of jet thickness expressed with h_c and the drop height H_d are the key parameters determining scour depth (i.e. step height). However, spurious correlation is present in Equation (3.26) as the step height $H = H_d + H_{res}$ includes drop height. Using the scour depth H_{res} instead still provides reasonable results but with a much larger scatter (Lenzi *et al.* 2002).

3.4.2   Effect of block size and block arrangement

Lenzi (2002) recommended to use at least two large blocks underneath the step-forming blocks. Arching the step towards the upstream can provide further structural stability owing to jamming effects. Lateral bank protection is required because bank failure can trigger the failure of the overall step-pool structure. The step height H is defined based on the size of the largest boulders (D_{90}, D_{100}) present in the stream (Lenzi 2001). An average ratio of $H/D_{90} = 2$ should be maintained within a range of $1 < H/D_{90} < 4$. The arrangement of the step-forming blocks was systematically varied by Kaspar (2017) and Lange (2019) conducting physical flume experiment with $S = 0.08$, $W = 6$ m, $H_d = 1.12$ m,

$L_d = 14$ m, and using step-forming blocks with mean block weight $M_B = 4.5$ t (Figure 3.10, $\lambda = 20$). A summary is provided in Maager *et al.* (2019). All experiments were conducted with clear-water (CW) conditions.

First, the step-forming blocks were placed subsequently in a row without superposition of blocks (1). The blocks started to move apart from each other forming a block carpet already for $q \leq 2$ m^2/s. Second, to avoid block carpet formation, the blocks in the downstream row were slightly inclined to avoid early movement of these blocks (2). A step-pool like structure developed as the scour deepened but the blocks in the downstream row slid into the pools at $q = 3$ m^2/s. Configurations (1) and (2) used two auxiliary blocks (orange blocks in Figure 3.10) placed in between the steps to reduce the scour pool depth and extent. However, the scour pools were not deep enough for the auxiliary blocks to unfold their purpose, yet. The third configuration comprised steps in which the blocks were superposed forming a two-layered step (3). A second row of auxiliary blocks was added (orange blocks, Figure 3.10) to reduce the scour extent. This configuration sustained hig-
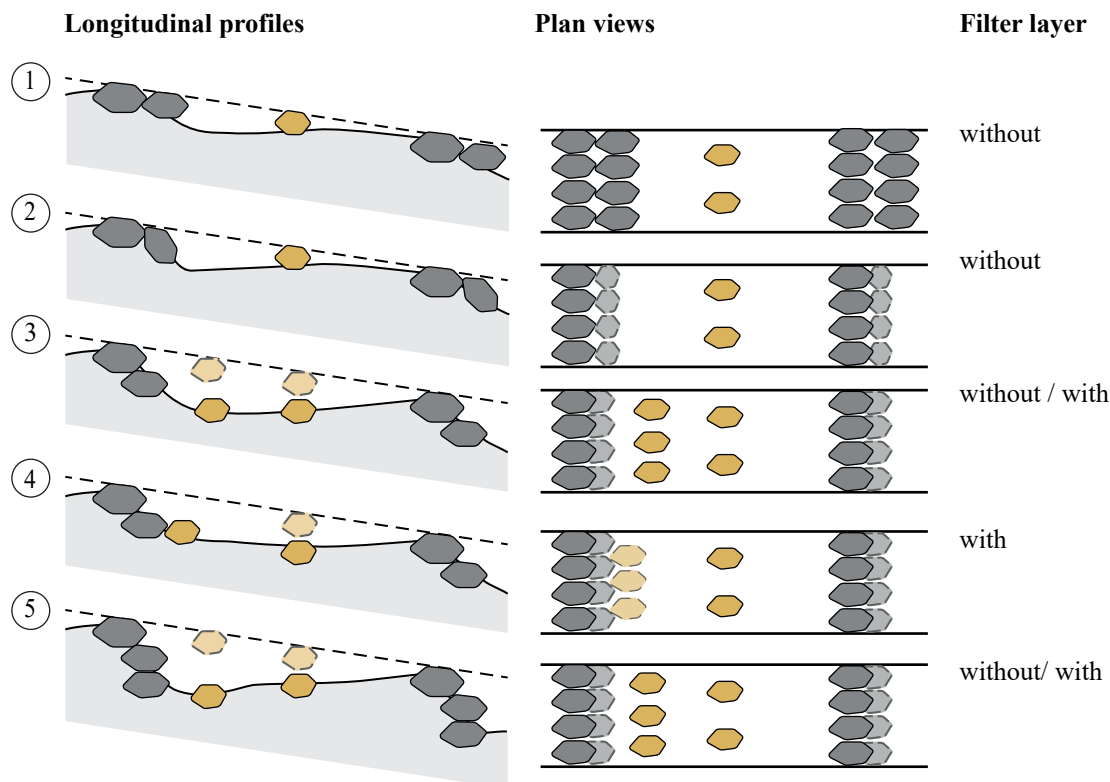
Figure 3.10 Variation of block arrangement in a channel with $S = 0.08$ and $W = 6$ m, drop height $H_d = 1.12$ m, step spacing $L_d = 14$ m, mean block weight $M_B = 4.5$ t (scale factor $\lambda = 20$); configurations 1 to 3 investigated by Kaspar (2017) and 4 to 5 by Lange (2019); an overview is provided in Maager *et al.* (2019)

her discharges up to $q = 6$ m^2/s. Internal erosion of the fine material within the steps led to undermining, flow through the steps, and exposure of the top row blocks to the flow. To avoid this process chain, the steps were placed on a filter layer (FL) avoiding internal erosion. This configuration (3, FL) sustained discharges $q > 6$ m^2/s.

The configuration was extended using a third layer of blocks incorporated into the step. In configuration (4), the auxiliary blocks were placed immediately downstream of the lower block row and were buried instead of being placed close to the initial bed surface. Configuration (4) sustained discharges up to $q = 6$ m^2/s and was similarly stable compared to configuration (3). Lastly, a third block layer was added underneath the step while maintaining two rows of auxiliary blocks placed in between the steps (5). Thereby, step height increased by approximately 20% in comparison with configuration (3). The system sustained $q = 7$ and 6 m^2/s with and without a FL, respectively.

This systematic investigation of block arrangement demonstrated that at least two super-positioned block rows are required to obtain the desired step-pool morphology with hydraulic jumps increasing energy dissipation. Bed stability increased using auxiliary blocks with the purpose of reducing the scour pool depth. A filter layer may further increase bed stability as internal erosion of fine material in the vicinity of the steps is reduced and the step-forming blocks are less exposed to the flow.

3.4.3 Step-pool stability

A common method to assess the stability of artificial step-pool sequences is to apply a force balance for the step-forming blocks. For example, Lenzi (2002) approximated the velocity at which the step-forming block starts sliding with $v_f \approx 3\sqrt{D_a}$ or $v_f \approx 4\sqrt{D_b}$ with $D_a = a$-axis of the grain directed in flow direction and $D_b = b$-axis of the grain perpendicular to the flow. This failure velocity v_f, estimated for the smallest step-forming blocks, is compared with the mean approach flow velocity of a step. The approach flow velocity upstream of a step is approximated by the critical flow velocity $v_{us} \approx v_c = \sqrt{g\,h_c}$ with $h_c = $ critical flow depth. For uncemented boulder check dams, a safety factor of at least 1.2 to 1.3 has to be considered (Lenzi 2002). However, the force balance has the shortcoming that it does not consider failure due to scouring. So far, no approaches exist to account for something along those lines.

3.4.4 Failure mechanisms

Zhang *et al.* (2018) investigated the failure mechanisms of a single artificial step-pool unit in flume experiments with $S = 0.032$ and $W = 4$ m (prototype scale, $\lambda = 8$). The step-pool unit was constructed following the recommendations of Thomas *et al.* (2000) placing a single layer of six boulders with a *b*-axis ranging from 0.61 m to 0.83 m. The largest keystone was placed in the center of the step. The cavities in between the blocks were filled up with fine material to obtain a jammed state of the artificial step. The experiments were conducted under stationary CW conditions. Zhang *et al.* (2018) observed 40 step failures and distinguished the three distinct mechanisms: i) keystone dislodgement, ii) integral failure, and iii) dislodgement of other step stones. *Keystone dislodgement*, i.e., the keystone alone moved first, accounted for 47.5% of all observed failures. The *integral failure* associated with the movement of at least three stones including the keystone accounted for 42.5% of all failures. Consequently, the keystone was involved in 90% of all failure occurrences. The remaining 10% were related to step failure associated with the *dislodgement of boulders other than the keystone*. The step failure modes rolling and sliding dislodgement were distinguished both accounting for approximately 50% of all step failures. In the former process, the step-forming block rotated into the downstream pool whereas the step was destabilized at its foundation and the whole step slid into the downstream pool in the latter. Step failures were observed at 2.2 m²/s $< q <$ 2.8 m²/s.

3.4.5 Case studies

Several case studies with artificial step-pool sequences from Switzerland, Italy, the USA, and China are presented. An overview regarding channel properties and design parameters is provided in Table 3.5. Note that the results from the physical model tests are presented herein for the Weisse Lütschine and Betelriedgraben case studies, which may slightly deviate from the final prototype design.

Steinbach (SZ, Switzerland)

The Steinbach Stream is located in central Switzerland and has a catchment area (CA) of 3.2 km² (Beffa 2016). The project reach has an average bed slope of $S = 0.12$ and a channel width $W = 8$ m. Figure 3.11 shows a longitudinal profile sketch of the sequence. Step-forming blocks with $M_B = 0.7$ to 3 t (equivalent spherical grain diameter $D_{eq} = 0.9$

Table 3.5 Case studies with S = bed slope, W = channel width, q_{100} = unit discharge for flood with RI = 100 years, H = step height, H_d = drop height, D = diameter of step-forming blocks, L_d = step spacing, step-pool sequence reinforced with concrete is marked in **bold**

	S	W	q_{100}	H	H_d	D	L_d
	[-]	[m]	[m²/s]	[m]	[m]	[m]	[m]
Steinbach [a]	0.12	8	4.0	-	-	0.9 - 1.4	-
Maira [b]	0.08	10-15	~23	3.5	-	1.6-2.4	14
Betelriedgraben[c]	0.08-0.15	5-7	3.3-4.6	-	0.6-1.8	1.2-1.8	7-22
Weisse Lütschine[d]	0.06	12	8.2	-	0.84	1.6-1.9	14
Maso di Spinelle[e]	0.10-0.14	23.5	3.6	1-3.5	-	1.65	10-25
Baxter Creek[f]	0.10	2	-	-	-	-	14
East Alamo Creek[f]	0.03	-	-	0.9-1.3	0.30	1.7	6.0-6.8
	0.05	-	-	1.1-1.5	0.50	1.7	5.6-6.4
Diaoga River[g]	0.096	-	-	1	-	0.2 - 1.0	5-12

[a]Beffa (2016), [b]Laboratorium 3D (2022), [c]VAW (2015), [d]HSR (2017), [e]Lenzi (2002), [f]Chin *et al.* (2009), [g]Yu *et al.* (2010)

to 1.4 m) were used. The pools were filled with two layers of auxiliary blocks with d = 0.3 to 0.6 m. The step-pool structure experienced a flood with peak discharge $q \approx 3$ m²/s corresponding to a RI ≈ 30 years. Massive bank erosion was observed due to the formation of alternate bars associated with the large aspect ratios leading to horizontal oscillation of the flow. The flow concentration, especially downstream of a bend, led to the destruction of steps. Even though the large step-forming blocks were mobilized, they still remained in the system and were not transported further downstream. The bank protection was initially designed using the blocks from the channel bed but was replaced with a more robust rip-rap design to avoid bank erosion in the future. The costs were estimated to amount to ~40% of the costs for a concrete check-dam sequence, even though more maintenance was required compared to a check-dam sequence.
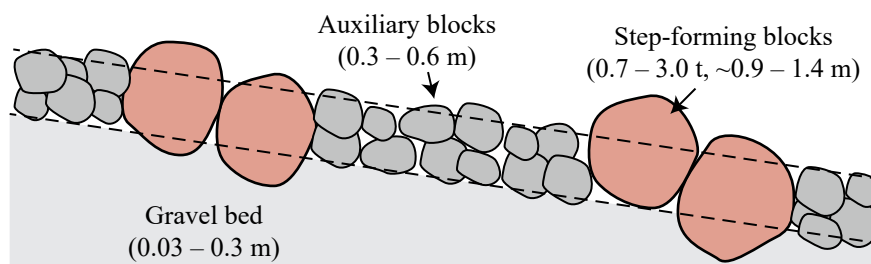
Figure 3.11 Longitudinal profile sketch of the step-pool sequence in the Steinbach Stream (adapted from Beffa 2016)

Maira (GR, Switzerland)

An ~200 m-long reach of the Maira Stream in Promotogno (GR) was stabilized using artificial step-pool sequences (Figure 3.12). The channel has a bed slope $S = 0.08$ and a channel width $W = 10$ to 15 m. The design discharge, corresponding to RI = 100 years, was extremely high with $q = 23$ m^2/s requiring an extraordinary stable system. The Laboratorium 3D in Biasca, Switzerland, conducted flume experiments to optimize the step-pool geometry (Laboratorium 3D 2022). A sequence of 14 steps was constructed with step spacing $L_d = 14$ m and step height $H = 3.5$ m. At least four layers of blocks were used in a step and large boulders were placed almost continuously on the entire bed resulting in a high placement density. The top layer of the steps consisted of the largest blocks with a block weight of 11 to 18 t ($D \approx 1.6$ to 2.4 m). The remaining step-forming blocks had a block weight of ~6 t and smaller blocks (2 to 3 t) were used as auxiliary blocks in between the steps. The block material was used from the neighbouring Bondasca valley, where a massive rock avalanche with a volume of ~3 Mio. m^3 had triggered several debris flow events in the Bondasca Stream (GEOPRAEVENT AG 2022) leading to short transport routes decreasing construction costs substantially.

Figure 3.12 Artificial step-pool sequence in Maira Stream (GR) in 2022; view against flow direction (Photo: C. Tognacca)

Betelriedgraben (BE, Switzerland)

The Betelried Stream is rerouted around the Blankenburg village as debris flow events pose a risk to the nearby settlement (VAW 2015). Therefore, physical experiments were conducted at VAW to design an artificial step-pool sequence as grade-control work for the newly constructed channel. The bed slope ranges between $S = 0.08$ in the lower and 0.15 in the upper part. Two layers of blocks were used for artificial step-pool units with maximum diameter of $D_{eq} = 1.8$ m ($M_B \approx 8$ t).

In the 8%-reach, a channel width of $W = 5$ m and step spacing of $L_d = 7$ and 22 m was recommended resulting in drop heights of $H_d = 0.6$ and 1.8 m, respectively, sustaining the design discharge $q = 4.6$ m^2/s with RI = 100 years. The configuration with $L_d = 22$ m resulted in well-defined hydraulic jumps whereas configuration with $L_d = 7$ m resulted in an undulating water surface being in phase with the channel bed, i.e., similarly to the flow conditions for antidune morphology. Even though both configurations sustained a discharge $q = 6.0$ m^2/s (overload scenario), an abrupt failure destabilizing the entire system has to be expected for configurations with a large step spacing. On the contrary, the step-pool sequences with the shorter step spacing, i.e., higher placement density, was expected to fail more gradually.

The step-pool configuration proposed for the 8%-sloped reach with $L_d = 7$ m was further tested in a 15%-sloped reach. The channel width had to be increased to $W = 7$ m in order to sustain the 100-year flood. However, the system failed during the overload scenario reducing the bed slope from 0.15 to 0.13.

Weisse Lütschine (BE, Switzerland)

A single check dam interrupting the longitudinal connectivity was replaced by a step-pool sequence in the Weisse Lütschine Stream in the canton of Bern, Switzerland. Physical flume experiments were conducted at Hochschule für Technik Rapperswil (HSR) in Switzerland to optimize the step-pool geometry and to test its stability (HSR 2017). The mean bed slope of the channel was $S = 0.06$ and the design discharge corresponding to a 100-year flood was $q_{100} = 8.2$ m^2/s. The stream bends to the left in the lower part of the test section and the increase in shear stress at the outside of the stream bend was carefully evaluated.

A total of 14 steps with step spacing $L_d = 14$ m and drop height $H_d = 0.84$ m proved to be the optimal geometry. The block arrangement is illustrated in Figure 3.13. The steps
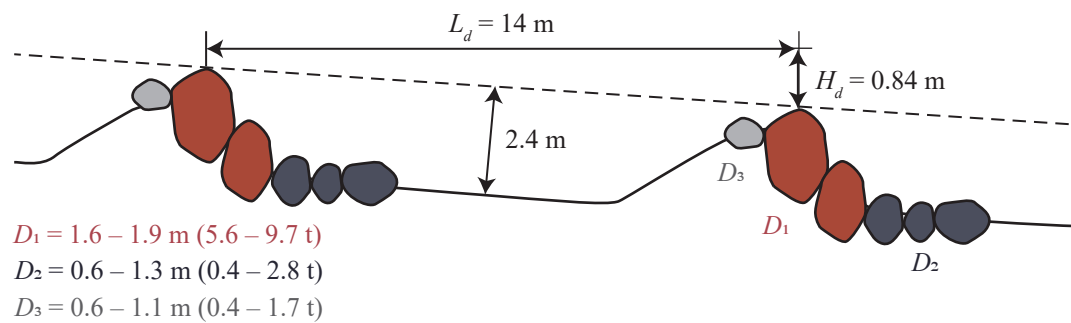
Figure 3.13 Recommended step-pool geometry for Weisse Lütschine Stream with D_1 = step-forming blocks, D_2 = blocks for scour protection, D_3 = blocks upstream of step (HSR 2017)

consisted of two rows of blocks with diameters D_1 = 1.6 to 1.9 m. Furthermore, a 2.5 to 3.0 m-long scour protection containing blocks with diameter D_2 = 0.6 to 1.3 m was placed in the scour pool. Upstream of the steps, a single row of blocks with diameter D_3 = 0.6 to 1.1 m was recommended. The step toes in the bend were reinforced with a 3.0 to 4.0 m-long block carpet consisting of blocks with diameter D_2. It was recommended to combine the concept of uncemented and cemented boulder check dams by strengthening every second step by reinforcing the step with concrete.

Maso di Spinelle (Northern Italy)

The example in the Maso the Spinelle River in Italy follows the design guidelines proposed by Lenzi (2002). Boulder check dams without reinforcement were constructed in a 500 m long reach (Lenzi 2002). A step height of H = 1.0 to 3.5 m was selected with H = 2.5 m being the most frequent and blocks with D_a = 1.6 to 1.7 m corresponding to the a-axis were used. A step spacing L_d = 10 to 25 m was selected while taking the natural terrain into account by placing the steps at suitable places. According to Lenzi and Comiti (2003), an initial steepness ratio $c = H/(S\,L)$ = 1.1 to 1.3 was implemented during the construction in 1997, i.e., the slope in between the boulder check dams was slightly reversed. The bed was surveyed four years later in 2001 (Lenzi and Comiti 2003). Behind long-spaced steps, a well-defined scour hole developed and sediment deposited downstream of the bed leading to a bed slope of $S \approx 0.04$ to 0.05. Erosive processes prevailed in more narrow-spaced steps, i.e., the scour depth increased but no depositional processes were observed. At some steps, the scour depths was not altered indicating that the implemented geometry was already similar to the equilibrium geometry with the experienced flow rates. Moreover, bar formation was observed particularly in between long-spaced steps (Lenzi

and Comiti 2003). Comparing the approach flow velocity ($v_{us} = 3.3$ m/s) with the minimal sliding velocity ($v_f = 3.8$ m/s) of the step-forming blocks leads to a safety factor of 1.2 (Lenzi 2002). During the construction works of the artificial step-pool reach, a flood with a peak unit discharge of $q = 1.8$ m^2/s occurred having a RI = 7 to 10 years. Two years later, a flood with peak discharge $q = 2.2$ m^2/s corresponding to RI = 20 to 25 years occurred and neither of them caused severe damage to the boulder check dams.

Baxter Creek (California, USA)

A 70-m long culverted reach of the Baxter Creek in California, USA, was daylighted in 1996 (Chin *et al.* 2009). The new channel featuring $S = 0.10$ and $W = 2$ m has a trapezoidal cross-section. Five steps were built out of the rocks from the excavation site with an initial step spacing $L_d = 14$ m. Rearrangement of the large blocks into steps with smaller spacing was observed in post-construction surveys (Chin *et al.* 2009). A total of 20 steps were observed in 2005, after the channel had experienced at least a 14-year storm event (rainfall intensity). The step-pool sequences rearranged into an average step spacing of $L_d = 2.9$ m and an average steepness factor of $c = 1.1$ agreeing well with the steepness factor proposed by Abrahams *et al.* (1995).

East Alamo Creek (California, USA)

The East Alamo Creek in California, USA, was restored in 2001, where a 180-m long channel section was realized as a step-pool sequence (Chin *et al.* 2009). The reach was divided into two sub-reaches with a bed slope of $S = 0.03$ and 0.05, respectively. As a design discharge, a 100-year flood was chosen. The step-forming blocks had a diameter of 1.7 m and the step heights and step lengths were chosen slightly different for the sub-reaches (Table 3.5).

Diaoga River (Southwest China)

An artificial step-pool system was built in the Diaoga River, located in the southwest of China (Yu *et al.* 2010). A total of 12 artificial steps were built in the heavily incised reach of 260 m length with an average bed slope of $S = 0.096$. The step-forming boulders had a diameter ranging from 0.2 to 1.0 m and higher resulting in $H = 1$ m. The steps are spaced between $L_d = 5$ and 12 m, resulting in a mean steepness factor $c = 1.5$.

4   Methodology

4.1   Overview

This chapter summarizes the experimental setup of the present study. Model similitude and scale effects are discussed in Section 4.2. Section 4.3 and 4.4 summarize the experimental setup of self-organizing step-pool systems with macrorough sidewalls (Part A) and artificial step-pool systems (Part B), respectively. Afterwards, Section 4.5 presents the instrumentation used in both Parts A and B. Section 4.6 describes the automatized step-pool detection algorithm and the accuracy and uncertainties are declared in Section 4.7.

4.2   Model similitude and scale effects

Physical hydraulic modeling requires scaling from the prototype scale to a model scale. Therefore, geometrical, kinematic, and dynamic similitude have to be satisfied between prototype and model scale (Heller 2011). However, exact model similitude is only feasible in a „miniature universe" where all physical parameters are scaled including geometry, fluid properties, gravitational acceleration, and atmospheric pressure. Differences between prototype and model scale may arise due to scale effects because not all relevant force ratios, e.g., inertial force, gravity force, or viscous force, can be kept constant between the prototype and the model (Heller 2011). The scale factor is defined as:

$$\lambda = \frac{L_P}{L_M} \qquad (4.1)$$

where L_P = the characteristic length in the prototype scale and L_M = the corresponding length in model scale. Herein, the experiments were scaled by a factor $\lambda = 20$ (Part A and B) which is in the range of scale factors applied in other experimental investigations of steep channels (Weichert 2006; Zimmermann 2009; Tamagni 2013). Froude similitude was chosen as the inertial and gravitational forces are decisive in open channel flows (Heller 2011). The resulting scale factors for all relevant quantities are detailed in Table 4.1. The Froude number F is defined as the square root of the ratio between inertial and gravitational force:

$$\mathsf{F} = \frac{V}{\sqrt{L\,g}} \qquad (4.2)$$

Table 4.1 Scale factors for Froude similitude with $\lambda = 20$

Quantity	Units	Scale factor		
Length	[m]	λ	=	20
Area	[m^2]	λ^2	=	400
Volume	[m^3]	λ^3	=	8'000
Time	[s]	$\lambda^{1/2}$	=	4.47
Velocity	[m/s]	$\lambda^{1/2}$	=	4.47
Discharge	[m^3/s]	$\lambda^{5/2}$	=	1'789
Mass	[kg]	λ^3	=	8'000
Sediment discharge	[kg/s]	$\lambda^{5/2}$	=	1'789

where V = a characteristic velocity, L = a characteristic length scale, and g = gravitational acceleration. However, applying Froude similitude, other force ratios such as the Reynolds number, i.e., the ratio between inertial and viscous force, $\mathsf{Re} = (LV)/\nu$, with ν = kinematic viscosity, are not scaled correctly. Thus, the viscous forces may not be correctly accounted for in Froude similitude. Scale effects regarding hydraulic properties emerging from not properly modeling the viscous forces are negligible for $\mathsf{Re} > 10^4$ in experiments with a rough bed (Tamagni 2013). This condition is satisfied for all experimental test runs throughout the present study.

Modeling bedload transport processes is challenging as the small grains used in the physical model are mobilized at lower discharges because the critical dimensionless shear stress θ_c depends on the particle Reynolds number $\mathsf{Re}_{*d} = (u_* d)/\nu$. Therein, the shear velocity is defined as $u_* = (\theta_c (s - 1) g d)^{1/2}$ where d = grain diameter, ν = kinematic viscosity, and $s = \rho_s/\rho = 2.65$ = relative sediment density with ρ_s = sediment density and ρ = water density. According to the Shields diagram, θ_c varies between 0.03 and 0.047 for $\mathsf{Re}_{*d} < 200$. In steep mountain streams, the particle Reynolds numbers of the grains are generally larger than 200 and assuming a constant value for θ_c is reasonable. However, smaller grains are used in the model sediment mixtures with $\mathsf{Re}_{*d} < 200$. Zarn (1992) proposes a conversion from the prototype GSD to the model GSD in three steps, which was applied to a case study in Switzerland by Simonett and Weitbrecht (2011). First, the GSD was converted using the geometric scale factor, i.e., $d_M = d_P/\lambda$. Second, the grain fraction $d = 0.22$ to 4 mm with $2 < \mathsf{Re}_{*d} < 200$ were coarsened to obtain the same shear velocities for prototype and model conditions, i.e., $u_{*,M} = u_{*,P}$, resulting in

$d_M = (1/\lambda)\, d_P\, (\theta_P/\theta_M)$, where θ_M needs to be determined iteratively using the Shields diagram. Third, the grains smaller than 0.22 mm were eliminated as other processes like apparent cohesion become relevant. This leads to a further coarsening of the sediment mixture.

4.3 Part A - Self-organizing step-pool systems

Physical flume experiments were conducted at VAW at ETH Zurich in a rectangular recirculating tilting flume approximately 13.5 m long, 0.6 m wide, and 0.6 m deep. A total of six sidewall roughness types were tested with a smooth, a fixed rough, and a mobile rough bed. Figure 4.1 shows the experimental setup for a channel with macrorough sidewalls. All measures of Part A are indicated in model scale.

A mesh flow straightener was installed at the flume inlet to ensure homogeneous in-flow conditions. The upper boundary consisted of an adjustable block ramp ~1 m long, followed by the 9.6 m long test reach, and a ~1.5 m long block carpet at the downstream end. The large blocks at the downstream end further stabilized the bed as no sidewall roughness elements were present. The bed would have been eroded as bed shear stress increased due to the smooth sidewalls without these large blocks. The bed slope was controlled with an adjustable weir at the downstream end of the flume. The sediment outflow was captured in a submerged filter basket, which was connected to three weighing cells. The automatized traversing system was equipped with a laser distance sensor (LDS) and an ultrasonic distance sensor (UDS). The experiments were conducted at initial bed slopes
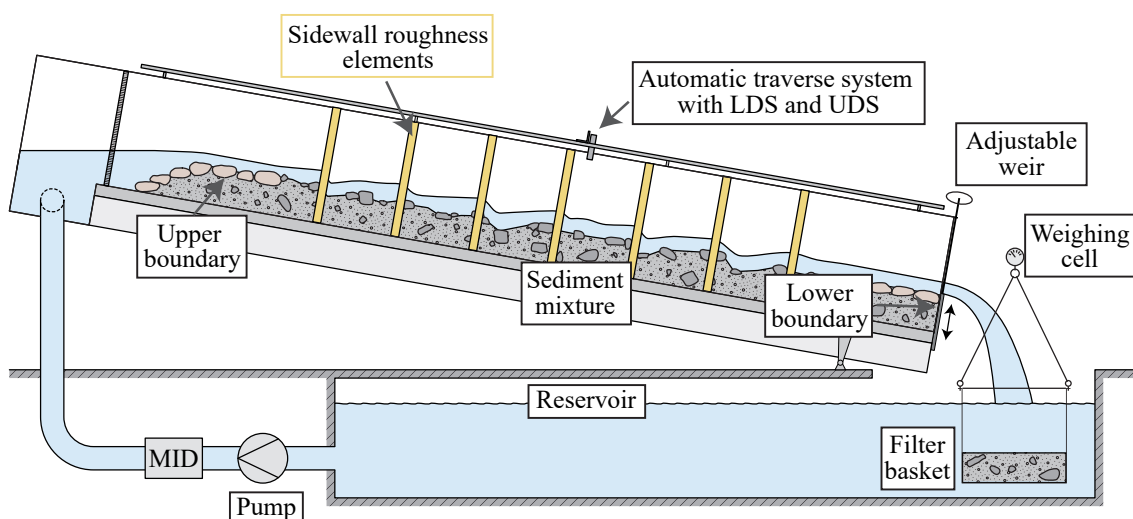

Figure 4.1 Illustration of the flume used for the self-organizing step-pool systems

$S = 0.04, 0.06,$ and 0.10 and channel widths $W = 0.3$ m and 0.6 m. Most of the experiments were conducted in the narrow channel. The flume sidewalls consisted of glass covered with a protective foil on one side and of wood on the other side. An equivalent sand roughness $k_w = 0.5$ mm was assumed according to literature for the smooth sidewall experiment without additional roughness elements, as the protective foil was rather scuffed.

4.3.1 Modeling macrorough sidewalls

A total of six sidewall roughness types were investigated in the present study. Pairs of rectangular form work panels with constant length $l = 5$ cm in flow direction and thickness $r = 5.4$ and 2.7 cm, protruding into the flow, were mounted to both flume sidewalls spaced $s = 25, 55,$ and 115 cm apart. The sidewall types are summarized in Table 4.2 and parameters $l, r,$ and s are defined according to Figure 4.2a,b. Sidewall roughness is expressed as the standard deviation of the mean bank position σ_w.

The sidewall types consisting of the thick ($r = 5.4$ cm) and thin ($r = 2.7$ cm) roughness elements are referred to as RR-Series and R-Series, respectively. The roughness types' designation further includes the element spacing s in centimeters. For example, sidewall roughness type RR55 consists of elements with thickness $r = 5.4$ cm spaced $s = 55$ cm apart. Furthermore, configuration RR55 was tested with alternate instead of parallel roughness element placing (RR55A). The roughness elements were symmetric along and across the flume in all experiments expect for this latter configuration RR55A. Smooth sidewall experiments (designation "0") served as a reference. Herein, the term smooth sidewalls exclusively refers to this sidewall type without roughness elements and not to the hydraulic roughness regime unless stated differently. Figure 4.2c shows a flume side view for sidewall roughness type R55 and Figure 4.2d the corresponding view into the flume against

Table 4.2 Overview of the sidewall roughness types

Type	r [cm]	s [cm]	r/s [-]	σ_w [cm]
RR25	5.4	25	0.22	2.0
RR55, RR55A[*]	5.4	55	0.10	1.5
RR115	5.4	115	0.05	1.1
R25	2.7	25	0.11	1.0
R55	2.7	55	0.05	0.7
R115	2.7	115	0.02	0.5

[*]Alternating elements on left and right side of the flume
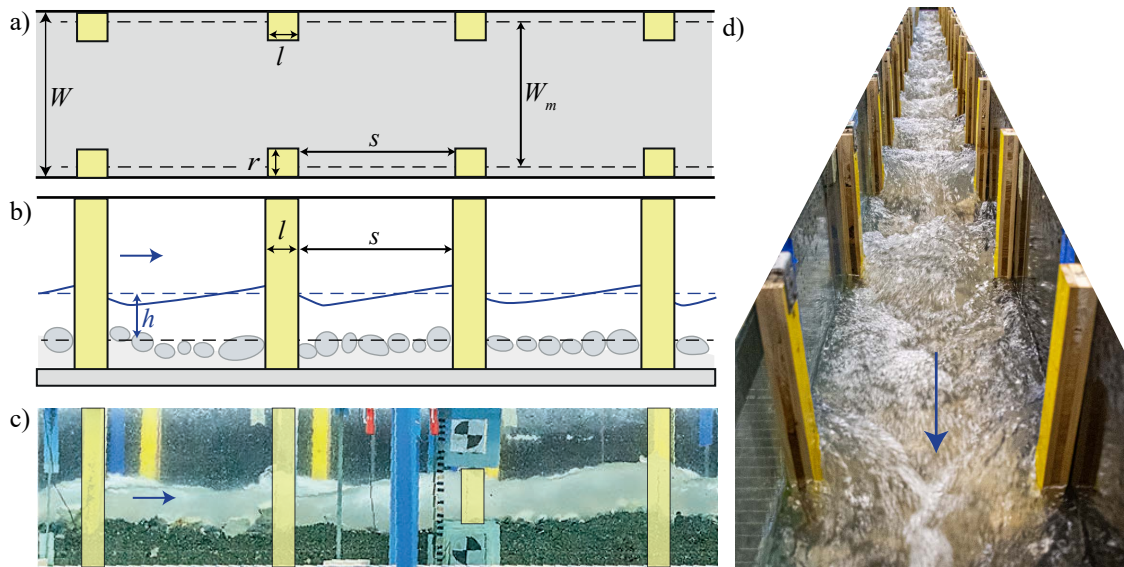
Figure 4.2 Definition of the investigated sidewall roughness types (parameter definition: Table 4.2), a) top view scheme, b) side view scheme, c) flume from the side (R55), d) view into the flume against flow direction (R55)

flow direction. The parameters r, s, and l were selected that the standard deviation of the mean bank position σ_w was comparable to the one obtained in the field study for Shatford Creek, Canada (Section 3.2.2, Zimmermann 2010). The maximum relative sidewall roughness $\sigma_w/W_m = 0.071$ in the flume was comparable to $\sigma_w/W_m = 0.08$ in the field. This sidewall roughness parameter σ_w is the standard deviation of the differences between the actual bank position and a mean bankline (mean banklines: dashed lines in Figure 4.2a). The differences between the actual bank position and the mean bank line were not normally distributed as an artificial type of bank or sidewall roughness was modelled herein. The terms banks and sidewalls are used synonymously throughout the study.

4.3.2 Bed and block material

The grain size distribution (GSD) of the sediment mixture used in the experiments with self-organizing step-pool systems is presented in Figure 4.3. Furthermore, the GSD used in the studies by Hohermuth and Weitbrecht (2018) and Zimmermann (2010) are included for comparison. The sediment mixture used herein was similar to the sediment mixture used in Hohermuth and Weitbrecht (2018). The sediment mixture was comprised of 70% base material with grain diameters $0.25 < d < 32$ mm and 30% coarse fractions $30 < D < 90$ mm (Figure 4.4). The 2-mm overlap between the base and coarse sediment resulted due to technical constraints. The characteristic grain diameters were
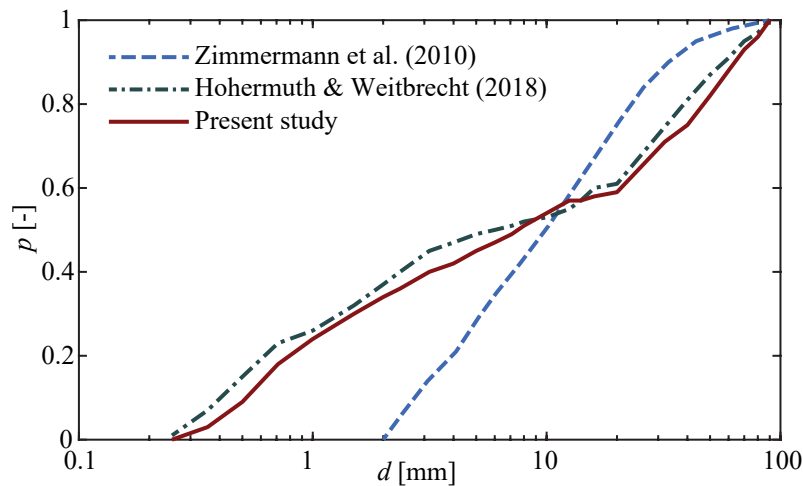
Figure 4.3 GSD of the sediment mixtures used in the present study and in the studies of Hohermuth and Weitbrecht (2018) and Zimmermann *et al.* (2010) serving as a reference

$d_{16} = 0.66$ mm, $d_{50} = 7.5$ mm, $d_{84} = 53.3$ mm, and $d_{90} = 64$ mm. The mean grain diameter was $d_m = 21.9$ mm and the sediment mixture was widely graded with a geometric standard deviation of $\sigma_g = \sqrt{d_{84}/d_{16}} = 8.7$.

Figure 4.5 shows the digital elevation model (DEM) and the corresponding orthophoto obtained with Structure from Motion (SfM) photogrammetry (Section 4.5.2) for the experiment with sidewall roughness type R55 (Table 4.2). The bed surface consisted mainly of grains of the coarse fraction ($30 < D < 90$ mm) as the finer base material was eroded after the first interval had been applied (i.e., $q > 0.01$ m²/s).
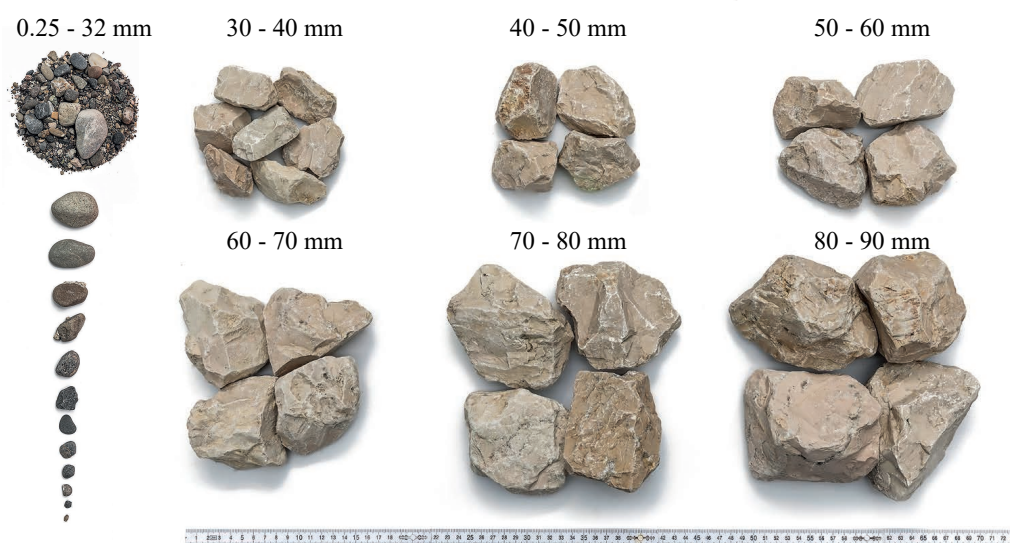
Figure 4.4 Material used for the self-organizing step-pool experiments (70% base material 0.25 - 32 mm, 30% coarse fractions 30 - 90 mm)
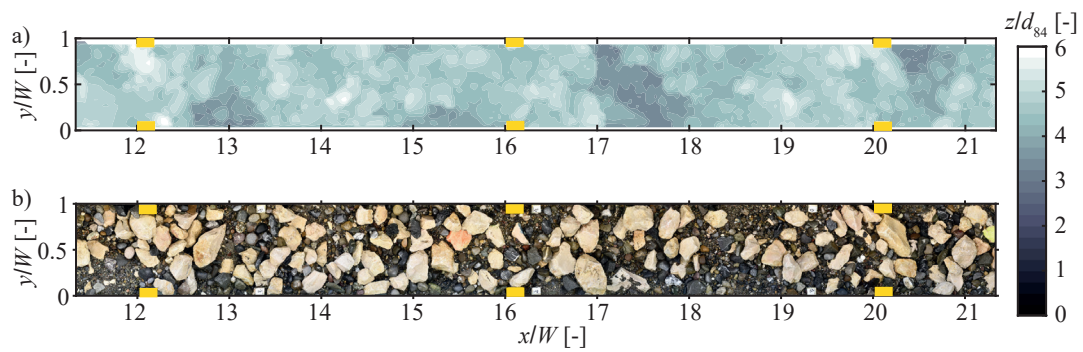
Figure 4.5 a) DEM with z/d_{84} = bed elevation normalized with the characteristic grain diameter d_{84} = 0.053 m, and b) the corresponding orthophoto for sidewall roughness type R115 (Maager *et al.* 2022a).

4.3.3 Test program and procedure

The test program of the self-organizing step-pool systems is presented in Table 4.3. Experiments were conducted for three different bed slopes S = 0.04, 0.06, and 0.10, for a channel width W = 0.3 m and 0.6 m, with six macrorough sidewall types RR25 to R115, and with smooth sidewalls („0") serving as a reference. Table 4.3 summarizes the roughness element density r/s, the relative sidewall roughness σ_w/W_m, and estimates for the jamming ratio W_m/d_{84} for each experiment.

Fixed smooth bed (FS) and fixed rough bed (FR) experiments were conducted to isolate the effect of macrorough sidewalls on flow resistance in conditions where bed roughness was constant. Afterwards, mobile rough bed (MR) experiments were conducted allowing the bed to adjust to the increase in discharge. The setup and procedure of the fixed smooth and rough beds (FS and FR) and the MR experiments are described in the following sections.

Fixed bed experiments (FS & FR)

The fixed *smooth* bed (FS) consisted of form work panels with an equivalent sand roughness of approximately k_b = 0.5 mm according to literature. The reach-averaged flow velocity v was measured for unit stream powers qS = 0.002 to 0.010 m²/s (see Section 4.5.1). The fixed *rough* bed (FR) consisted of a rough surface containing blocks of the coarse fraction (30 < D < 90 mm, Figure 4.4) held in place with a thin layer of cement. To obtain the rough bed surface, the base sediment mixture (0.25 < d < 32 mm) was initially placed into the flume. Afterwards, the boulders of the coarse fraction (30 < D < 90 mm)

Table 4.3 Test program for Part A. S = bed slope, W_m = mean channel width, sidewall roughness types according to Table 4.2, r/s = ratio of roughness element thickness to spacing, σ_z/W_m = relative sidewall roughness, W_m/d_{84} = jamming ratio

Bed type	Bed slope S	W_m	Sidewall type	r/s	σ_w/W_m	W_m/d_{84}
	[-]	[m]		[-]	[-]	[-]
Fixed bed experiments (FS: smooth bed and FR: rough bed)						
FS, FR	0.04, 0.06, 0.10	0.282	RR25	0.22	0.071	-
FS, FR	0.04, 0.06, 0.10	0.291	RR55	0.10	0.051	-
FS, FR	0.04, 0.06, 0.10	0.296	RR115	0.05	0.037	-
FS, FR	0.04, 0.06, 0.10	0.291	R25	0.11	0.035	-
FS, FR	0.04, 0.06, 0.10	0.296	R55	0.05	0.025	-
FS, FR	0.04, 0.06, 0.10	0.298	R115	0.02	0.018	-
FS, FR[*]	4, 6, 10	0.300	0	0	0	-
Mobile rough bed experiments (MR)						
MR	0.10	0.282	**RR25**	0.22	0.071	~5.6
MR	0.10	0.291	**RR55**	0.10	0.051	~5.6
MR	0.10	0.291	**RR55A**	0.10	0.051	~5.6
MR	0.10	0.296	**RR115**	0.05	0.037	~5.6
MR	0.10	0.296	**R55**	0.05	0.025	~5.6
MR	0.10	0.298	**R25**	0.02	0.018	~5.6
MR	0.10	0.300	**0**[*]	0	0	~ 5.5
MR	**0.06**	0.296	R55	0.05	0.025	~5.6
MR	**0.04**	0.296	R55	0.05	0.025	~5.6
MR	0.10	**0.591**	RR55	0.10	0.025	**~11.3**

[*]Experiment repeated

were randomly placed on top with a placement density of $\lambda_D \approx 0.15$. Therein, the same portion of the coarse fraction blocks were used as in the sediment mixture for the mobile bed experiments. Afterwards, a water discharge $q < 0.02$ m^2/s (i.e., $qS < 0.002$ m^2/s for $S = 0.10$) was applied being large enough to enable bed armoring but small enough to prevent the formation of steps and pools. Finally, the bed was fixed with a thin layer of cement to prevent the bed from adjusting to an increase in discharge. This fixed rough bed primarily exerted boundary resistance due to the lack of bed forms.

The RR-Series and the R-Series with a fixed rough bed were conducted separately (Figure 4.6a and 4.6b, respectively). In the RR-Series, a total of 32 roughness element pairs with $r = 5.4$ cm were placed $s = 25$ cm apart leading to the roughest sidewall type
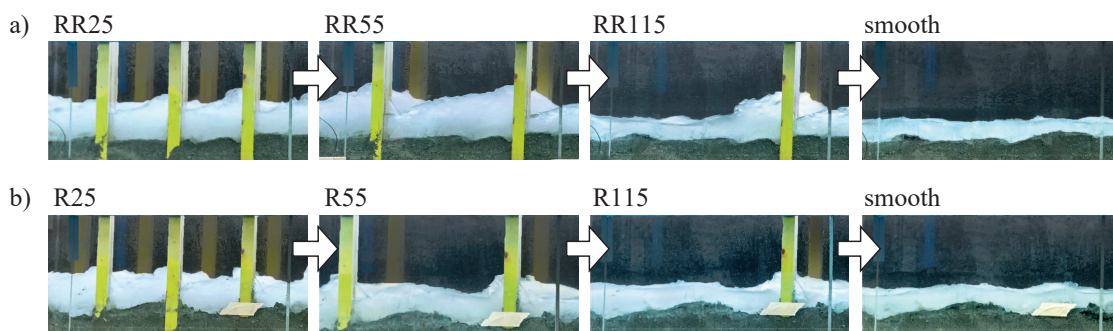
Figure 4.6 Flume side-view for fixed rough bed (FR) experiments with $S = 0.10$ and $q = 0.04$ m^2/s for a) RR-Series ($r = 5.4$ cm), b) R-Series ($r = 2.7$ cm)

RR25. The fixed rough bed was created as previously described and reach-averaged flow velocities (see Section 4.5.1) were measured for at least three different flow stages corresponding to unit stream powers $qS = 0.002$ to 0.010 m^2/s. Measurements were conducted at $S = 0.04$, 0.06, and 0.10 for each sidewall roughness type to investigate a wide range of hydraulic conditions (e.g., u_*, h/d). Afterwards, every second pair of roughness element was removed resulting in a spacing of $s = 55$ cm (RR55). The emerging holes were filled with the base sediment mixture and fixed with a layer of cement. Again, mean flow velocity measurements were conducted for all three bed slopes. This procedure was repeated leading to sidewall type RR115 and finally to smooth sidewalls as all roughness elements were removed. The same procedure was repeated for the R-Series with the thin roughness elements $r = 2.7$ cm starting with 32 pairs of elements spaced 25 cm apart (R25). This procedure allowed to maintain the same bed roughness for the entire RR- and R-Series, respectively. Thus, the experiment with a fixed rough bed and smooth sidewalls (0) was conducted twice to have a reference experiment with smooth sidewalls for both the RR- and R-Series.

Mobile rough bed (MR) experiments

A 25 cm thick layer of the well-mixed sediment mixture described in Section 4.3.2 was placed into the flume. The mixture was slightly compacted and the surface was flattened prior to starting the experiments. Afterwards, stationary clear-water (CW) experiments were conducted increasing the unit stream power by increments of $\Delta(qS) = 0.001$ m^2/s and letting the bed adjust until a stable condition was reached. A stable bed condition was attained when the mean bed elevation change Δz was smaller than 0.2 mm / 10 min indi-

cating that the mean bed elevation change over a 10-min time span was smaller than the smallest grain in the sediment mixture. The mean bed elevation changes were calculated from the cumulative sediment outflow captured in the filter basket. A mean bed elevation change smaller than 0.2 mm / 10 min corresponds to an average unit sediment transport rate of approximately $q_s \leq 6$ g/(sm) over a time span of ten minutes. Moreover, stable conditions related to low sediment transport rates were confirmed by visual observations. On average, stable conditions were reached after 2.1 h (±33%) with a minimum and maximum duration of 0.8 h and 4.1 h, respectively, for some extreme cases. The reach-averaged flow velocity (Section 4.5.1) was measured once stable conditions were reached at bed-forming discharge. Afterwards, the discharge was decreased step-wise and additional flow velocity measurements were conducted at smaller q. Finally, the discharge was decreased to zero, the bed was drained, and bed topography was measured (Section 4.5.2).

The majority of MR experiments were conducted in the narrow channel with $W = 0.3$ m and $S = 0.10$ (Table 4.3). In addition, sidewall type R55 was further tested for $S = 0.04$ and 0.06, and sidewall type RR55 in the wide channel width $W = 0.6$ m. The experiment with smooth sidewalls (0) was repeated with smaller unit stream power increments $\Delta(qS) = 0.0005$ m²/s to test the reproducibility.

4.3.4   Sidewall correction modifications for macrorough sidewalls

The present section elaborates on the modifications of a commonly used sidewall correction procedure for macrorough sidewalls. The generalized Einstein-Johnson (GEJ) sidewall correction procedure is described in Section 2.3.3. Figure 4.7 illustrates the calculation steps of the present study to obtain a sidewall correction valid for steep rough channels with macrorough sidewalls. Initially, the fixed bed experiments (FS and FR) were conducted with smooth sidewalls with an equivalent sand roughness $k_w = 0.5$ mm estimated from literature. Both the protective foil covering the glass-side of the flume and the wood on the other side were rather scuffed.

In step 1, the sidewall friction factor f_w was calculated using Equation (2.5) of Keulegan (1938) for the fixed smooth and rough beds (FS and FR). Afterwards, the bed friction factor f_b was calculated using Equation (2.28) being valid for rectangular channels. Therewith, the bed shear stress was estimated using the hydraulic bed radius R_b, thus, applying Equations (2.27) and (2.29). Subsequently, the bed friction factor f_b was then used to determine the hydraulic bed roughness parameters $k_{b,FS}$ for the smooth bed and $\sigma_{z,FR}$ for

Fixed Bed Experiments

<u>Step 1</u>: Smooth sidewalls, $k_w = 0.5$ mm (assumption based on literature)
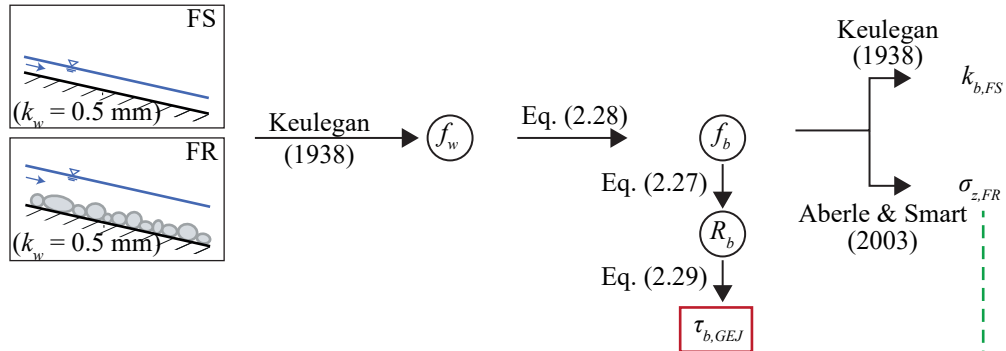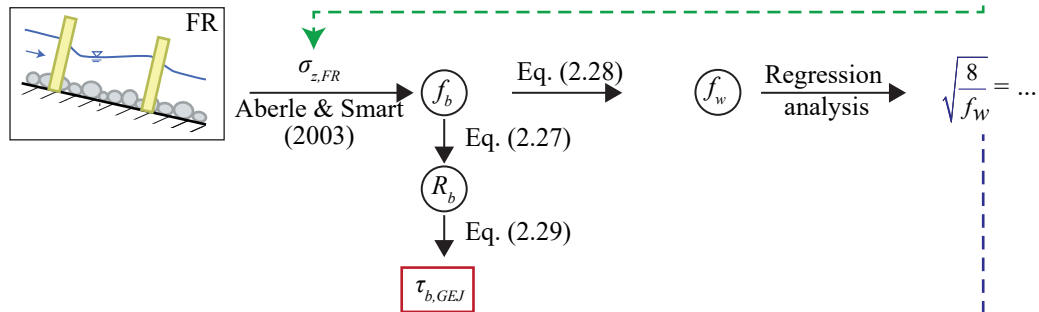
Mobile Bed Experiments

<u>Step 3</u>: Rough & smooth sidewalls
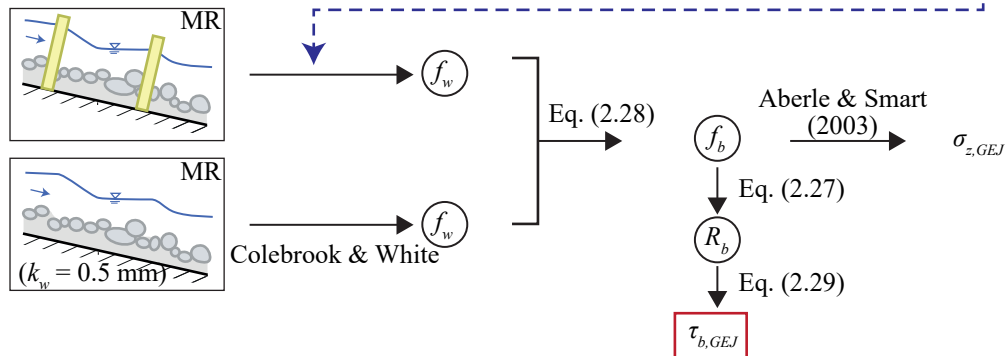
Keulegan, 1938 (Eq. 2.5)

$$\sqrt{\frac{8}{f}} = 5.74 \log\left(\frac{12.2R}{k}\right)$$

Hydraulic bed radius (Eq. 2.27)

$$R_b = \frac{f_b}{f}R$$

Colebrook & White (Eq. 2.25)

$$\frac{1}{\sqrt{f_w}} = -2\log\left(\frac{2.51f}{\text{Re}\, f_w^{3/2}} + \frac{1}{3.71f_w}\frac{fk_w}{4R}\right)$$

Aberle & Smart, 2003 (Eq. 2.9)

$$\sqrt{\frac{8}{f}} = 3.86\ln\left(\frac{h}{\sigma_z}\right) - 1.19$$

Bed shear stress (Eq. 2.29)

$$\tau_{b,GEJ} = \rho g R_b S$$

Bed and sidewall friction factor (Eq. 2.28)

$$f_b = f + \frac{2h}{W}(f - f_w)$$

Figure 4.7 Calculation steps of the GEJ sidewall correction procedure modified for macrorough sidewalls (adapted from Maager *et al.* 2022c)

the fixed rough bed. The former was in agreement with literature and the latter resulted in similar values of σ_z obtained from LDS-measurements (Section 4.5.2).

Step 2 of the fixed bed experiments includes test runs with a fixed rough bed (FR) and macrorough sidewalls. Contrary to step 1, the k_w-value cannot be determined from literature as the log-law is not applicable to macrorough sidewalls. However, as the fixed rough bed remained constant, the estimates for $\sigma_{z,FR}$ determined in step 1 were used to estimate the bed friction factor f_b and the sidewall friction factors were calculated using Equation (2.28). Afterwards, a regression analysis was conducted to directly obtain the flow resistance coefficient $\sqrt{8/f_w}$ using a set of dimensionless parameter combinations including sidewall parameters (r, s, σ_w), channel (bed) parameters (W, S, σ_z), and hydraulic parameters (h, R, F, Re). The resulting empirical relation was then used to apply the sidewall correction to steep rough channels with macrorough sidewalls.

In the final step 3, the results were transferred from the FR to the MR experiments. Therein, the previously obtained relation for $\sqrt{8/f_w}$ was applied to estimate the sidewall friction factor f_w. Again, the bed friction factor f_b, hydraulic bed radius R_b, and finally the bed shear stress $\tau_{b,GEJ}$ were obtained. Note that $k_w = 0.5$ mm was assumed for the reference experiments with smooth sidewalls. The obtained bed friction factors f_b were inserted into Equation (2.9) by Aberle and Smart (2003) resulting in estimates for bed roughness $\sigma_{z,GEJ}$. These estimates were finally compared to σ_z from LDS-measurements to validate the modified sidewall correction procedure.

4.3.5 Step location and narrowing sections

The jamming state hypothesis implies that steps are more likely to form in narrow channels (Zimmermann *et al.* 2010) but also in narrowing sections (Golly *et al.* 2019; Saletti and Hassan 2020). To test this hypothesis, the flume was divided into a narrow region (NAR) and a wide region (WID) consisting of multiple narrow and wide patches (Figure 4.8). The NAR regions were defined as the channel-spanning areas located from $\Delta x_{NAR} = 1.5\, d_{max} = 13.5$ cm upstream to the downstream end of the roughness elements. The remaining areas belonged to the WID regions. The steps detected were either assigned to be located in a WID or NAR region.

Similarly to Saletti and Hassan (2020), the share of the steps located in the NAR region with respect to the total number of steps n_{NAR}/n_{tot} was compared to the share of the NAR area on the total area A_{NAR}/A_{tot}. A random distribution of the steps would lead to similar
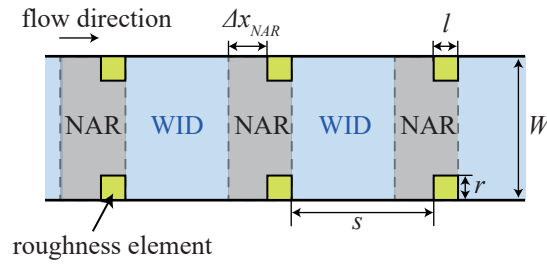
Figure 4.8 Definition scheme of WID = wide regions and NAR = narrow regions in the self-organizing MR experiments, Δx_{NAR} is the length of the NAR upstream of the roughness elements

ratios $n_{NAR}/n_{tot} \approx A_{NAR}/A_{tot}$. However, if steps were more likely to form in the NAR region, then $n_{NAR}/n_{tot} > A_{NAR}/A_{tot}$. The choice of the parameter Δx_{NAR} influenced the assignment of the steps to either NAR or WID and the error was estimated by varying the parameter by ±25%. The resulting upper and lower estimated for n_{NAR}/n_{tot} are presented later in the analysis. The area ratio A_{NAR}/A_{tot} was also affected by the choice of Δx_{NAR}.

4.4   Part B - Artificial step-pool systems

Part B investigated artificial step-pool sequences in which the step-forming blocks were manually placed into the base material. The same tilting flume was used as in Part A (Section 4.3) but the setup was adapted to the artificial step-pool sequences (Figure 4.9). All units are indicated in prototype scale unless stated differently as Part B aims at providing recommendations for practitioners. The following parameter range was investigated within the present study:

- Bed slope S = 0.04 ... 0.08
- Normalized step spacing L_d/W = 0.8 ... 3.1
- Normalized drop height H_d/D_{eq} = 0.3 ... 0.8
- Relative step-forming block size D_{eq}/d_{84} = 6.7 ... 10.6
- Froude number   F   = 0.53 ... 1.16
- Aspect ratio W/h = 1.7 ... 16.1
- Dimensionless bed shear stress θ_D = 0.017 ... 0.083
- Sediment feed rate $q_{s,in}$ = 0 ... 20% of transport capacity (TC)

Six to eight equally spaced steps were placed on top of a $z = 6.6$ m (i.e., $z/d_{84} \approx 33$, $z/D_{eq} \approx 4$) thick layer of base material (Section 4.4.1) to model the artificial step-pool systems. The step-pool configurations and the properties of the step-forming blocks are
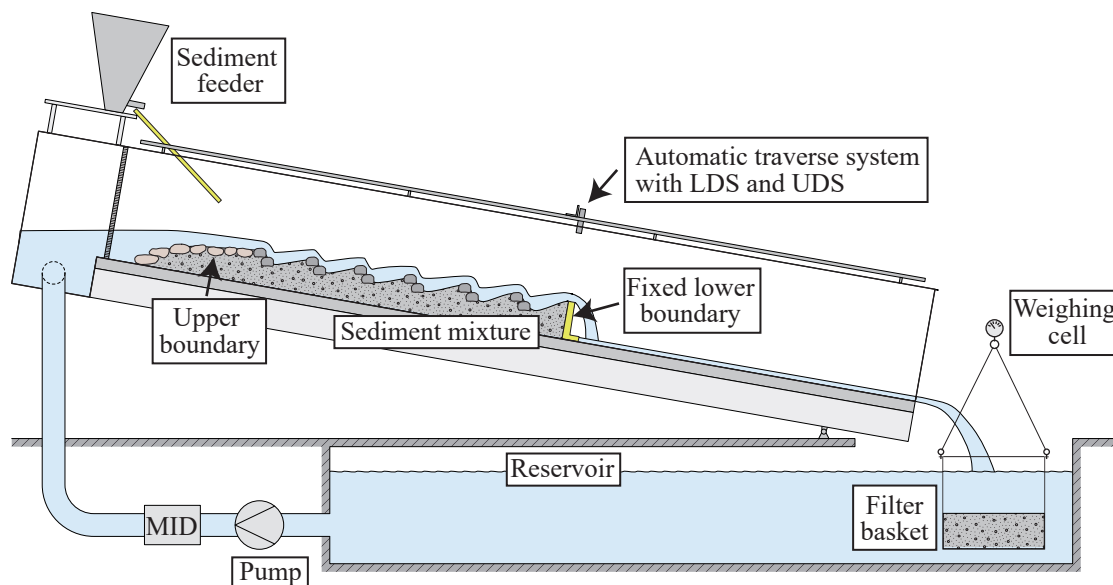
Figure 4.9 Illustration of the flume used for the artificial step-pool sequences

described in Section 4.4.2. The upper boundary consisted of an approximately 18 m (0.9 m in model scale) long mobile block ramp comprising blocks between 8.8 to 14.4 t (1.1 and 1.8 kg in model scale) with placement densities between $\lambda_{D_{eq}}$ = 0.41 to 0.46. The lower boundary consisted of an L-shaped gate with the crest fixed at z = 6.6 m (= initial bed elevation) with free overflow conditions. The procedure and information on sediment feed rates are provided in Section 4.4.3. A detailed test program is presented in Section 4.4.4 and the instrumentation is described in Section 4.5.

4.4.1 Base sediment mixtures

Two widely graded sediment mixtures served as base material for the model tests with grain size distributions (GSDs) presented in Table 4.4 and Figure 4.10. Both mixtures had the same mean diameter d_m but differed in their maximum grain diameter d_{max}. The Kleine Schliere Stream, which is a typical mountain stream in the Canton of Obwalden, Switzerland, served as a model for the mixture with the larger d_{max} = 64 cm (M64). The second mixture (M40) had a d_{max} = 40 cm approximately corresponding to d_{95} of M64.

Table 4.4 Characteristic grain diameters of the base mixtures M40 and M64 (prototype scale)

	d_{16} [cm]	d_{30} [cm]	d_{50} [cm]	d_{84} [cm]	d_{90} [cm]	d_m [cm]	σ_g [-]
M40	0.8	1.3	4.1	21.2	26.2	9.0	5.1
M64	0.7	1.2	3.5	17.8	24.8	9.0	5.0

Thus, the coarsest 5% of the grains were removed from M64 to obtain M40. Afterwards, grains with diameter $16 < d < 40$ cm were added to M40 to create the same d_m as in M64. The model sediment was converted from model to prototype scale following the recommendations of Zarn (1992) (Section 4.2). The characteristic grain size diameters and the geometric standard deviation $\sigma_g = \sqrt{d_{84}/d_{16}}$ are listed in Table 4.4 in prototype scale.
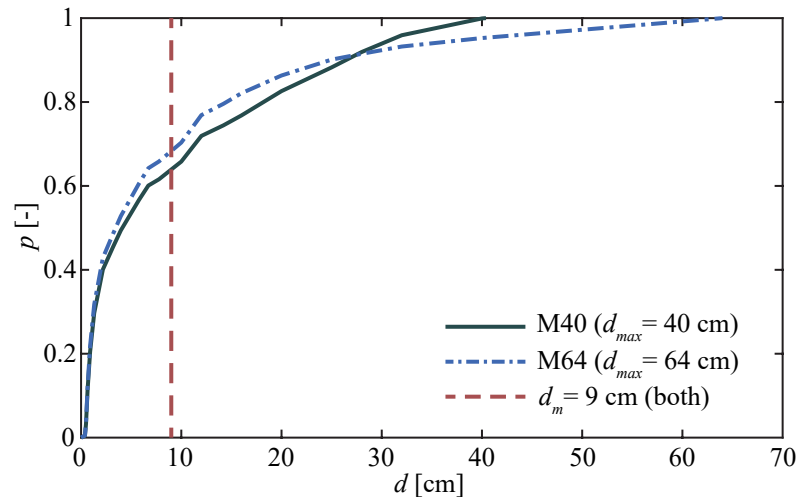
Figure 4.10 GSD of the base sediment mixtures M40 and M64 with d_{max} = 40 and 64 cm, respectively (prototype scale, characteristic grain diameters according to Table 4.4)

4.4.2   Step-pool configurations and block material

Step-pool configuration

Figure 4.11a and 4.11b show a schematic longitudinal profile and a plan view of the tested step-pool configurations, respectively. The base configuration (BASE) consisted of two *step-forming block* layers (Figure 4.11c, R1 and R2) following the recommendations of Lenzi (2002). In addition, previous studies demonstrated that placing large blocks in between steps, herein referred to as *auxiliary blocks* (A1 and A2), reduced the scour depth and therefore increased step stability (Kaspar 2017; Maager *et al.* 2019). More information is detailed in Section 3.4.2. The auxiliary blocks A1 and A2 were placed at approximately $L_{A1} = D_{eq}$ and $L_{A2} = L_d/2$ downstream of the step crest, respectively.

A pyramid configuration (PYR) was investigated in which a block row (P) was added immediately upstream of the base step (Figure 4.11d). This block row aims at providing additional stability to the R1 blocks by reducing the exposure to the flow and therewith preventing tilting in downstream direction. Moreover, tilting against flow direction is pre-
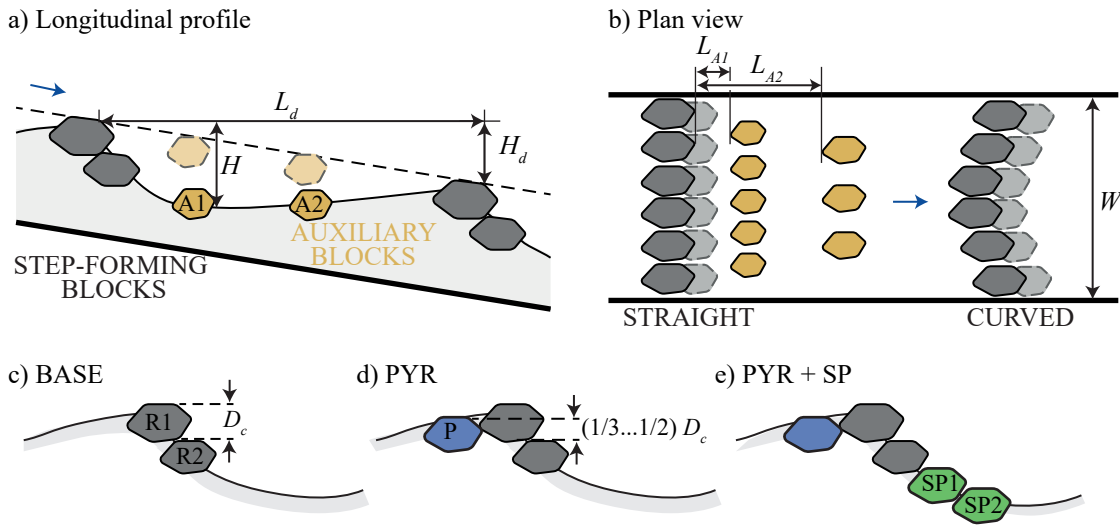
Figure 4.11 Schematic overview of step-pool block arrangement and configurations, a) longitudinal profile (dashed lines: initial condition), b) plan view, c) base configuration (BASE), d) pyramid (PYR) configuration, e) pyramid + scour protection (PYR+SP) configuration

vented as the R1 blocks are supported by the P blocks located underneath. Two additional block rows for scour protection (SP1 and SP2) were added downstream of the step toe in configuration PYR+SP (Figure 4.11e). Therewith, the step is more robust against scouring processes. The vast majority of the experiments were conducted using the base configuration and a straight step in plan view. However, the effect of a curved step in plan view (CUR) was tested in the wide channel with $W = 12$ m (Figure 4.11b).

Table 4.5 provides an overview of how many step-forming and auxiliary blocks were used depending on the channel width W. A more detailed test program is presented later in Section 4.4.4. Four and six blocks were used in each row in channels with $W = 6$ and 9 m, respectively. Only seven blocks were used for the BASE configuration in the widest channels with $W = 12$ m with the purpose of testing the effect of jamming, i.e., the interlocking of the step-forming blocks with the sidewalls. Eight blocks were used in the step configuration with the step curved towards the upstream direction (CUR) with the purpose of amplifying the jamming and therewith potentially increasing step stability.

Step-forming block material

The artificial step-pool sequences consisted of angular blocks ranging from 2.4 to 9.6 t (0.3 to 1.2 kg in model scale). The step-forming blocks were divided into categories B1 to B4 and colored accordingly to facilitate the differentiation during the experiments (Table 4.6 and Figure 4.12). The upper and lower limit of block weight M_{min} and M_{max}, the

Table 4.5 Parameters of block configurations with W = channel width, R1 = top row, R2 = bottom row, P = pyramid row, SP1 = first scour protection row, SP2 = second scour protection row, A1 = first auxiliary block row, A2: second auxiliary block row (see Figure 4.11)

| | W [m] | Step-forming blocks [#] | | | | | Auxiliary blocks [#] | | # of Exp. |
		R1	R2	P	SP1	SP2	A1	A2	
BASE	6	4	4	-	-	-	3	2	16
PYR	6	4	4	4	-	-	3	2	1
PYR+SP	6	4	4	4	4	4	3	2	1
BASE	9	6	6	-	-	-	5	3	2
PYR	9	6	6	6	-	-	5	3	2
BASE	12	7	7	-	-	-	6	4	6
CUR	12	8	8	-	-	-	6	4	1

mean block weight M_B, the a-, b-, and c-axes, and the number of blocks used in each category are indicated. The block weight and the corresponding a-, b-, and c-axis length were determined for each block and the average values are presented. The weight distribution of each category is presented in Appendix A.3.1. Furthermore, the equivalent spherical diameter D_{eq} is calculated as:

$$D_{eq} = \left(\frac{6\,M_B}{\rho_s\,\pi}\right)^{1/3} \tag{4.3}$$

with ρ_s = 2'650 kg/m³ = density of the step-forming blocks. The b-axis of the blocks was well approximated with D_{eq} calculated from the mean block weight M_B (Table 4.6). Three different combinations of B1 to B4 blocks were used for the artificial step-pool sequences resulting in steps with mean block weights:

Table 4.6 Properties of the step-forming block categories B1 to B4 with a block weight ranging from M_{min} to M_{max}, mean block weight M_B (±0.5 t), a-, b-, and c-axis (±0.2 m), and equivalent spherical diameter D_{eq} (Equation 4.3)

| | M_{min} ... M_{max} | M_B | a-axis | b-axis | c-axis | D_{eq} | # of blocks |
	[t]	[t]	[m]	[m]	[m]	[m]	[-]
B1	2.4 ... 4.8	3.8	1.9	1.5	1.1	1.4	164
B2	4.8 ... 6.4	5.4	2.2	1.6	1.3	1.6	133
B3	6.4 ... 8.0	7.2	2.4	1.7	1.3	1.7	58
B4	8.0 ... 9.6	8.8	2.4	1.8	1.5	1.9	43

Figure 4.12 Step-forming blocks (coloured) used for the artificial step-pool sequences and sediment mixture SM64 (model scale [cm])

- M_B = 4.6 t: R1 (top row) → B2 (5.4 t)   R2 (lower row) → B1 (3.8 t)

- M_B = 6.3 t: R1 (top row) → B3 (7.2 t)   R2 (lower row) → B2 (5.4 t)

- M_B = 8.0 t: R1 (top row) → B4 (8.8 t)   R2 (lower row) → B3 (7.2 t)

The top row blocks R1 comprised blocks of the larger block category and the lower row blocks R2 of the smaller block category. Thus, the top row blocks, which were more prone to tilting into the downstream pool, are capable of sustaining higher hydraulic stresses. Category B1 and B2 blocks were used for the auxiliary blocks A1 and A2, respectively. In general, all blocks used to build the artificial step-pool sequences were selected randomly from the block deposit of each category unless indicated otherwise. The placement density $\lambda_{D_{eq}}$ and the block weight density λ_{M_B} of the step-pool sequences are defined as:

$$\lambda_{D_{eq}} = \frac{1}{L_d\,W} \sum_{i=1}^{N} n_i\,\pi\left(\frac{D_{eq,i}}{2}\right)^2 \tag{4.4}$$

$$\lambda_{M_B} = \frac{1}{L_d\,W} \sum_{i=1}^{N} n_i\,M_{B,i} \tag{4.5}$$

with n_i = number of blocks, $D_{eq,i}$ = spherical block diameter, and $M_{B,i}$ = weight of blocks in rows i = R1, R1, A1, A2, P, SP1, and SP2.

4.4.3 Experimental procedure

At the beginning of the investigation, three discharge variation regimes (DVRs) were applied to the same step-pool sequence to investigate potential effects of steady and unsteady flow and of clear-water (CW) and sediment feed (SF) conditions mainly on the scour dimensions and bed stability. Based on the results of the DVR-Series (test runs DVR1 to DVR3 in Table 4.9) the discharge regime leading to the least stable step-pool system and to deeper scour depths was selected. The parameters defining the investigated hydraulic regimes and the sediment supply rates are summarized in the following.

The unit discharge negatively correlated with bed slope according to hydrological data of 18 steep streams (Figure 3.1). Consequently, the product of unit discharge and bed slope qS, referred to as unit stream power, was selected to be step-wise increased instead of choosing a fixed unit discharge increment. Increasing the unit stream power by increments of $\Delta(qS) = 0.10$ m²/s led to the unit discharges q presented in Table 4.7 for the investigated bed slopes $S = 0.04$, 0.06, and 0.08. The unit stream power is linked to a reference RI based on hydrological data (Table 3.2). However, these RI are a rough indication only as they deviate substantially due to the inherent heterogeneity of steep streams. Figure 4.13 provides an overview of the three investigated discharge regimes. Therein, the mean unit stream power qS (± standard deviation σ_{qS}) with RI of 100 years = 0.45 ±0.23 m²/s is indicated in gray (using data of Table 3.2).

Table 4.7 Overview of the unit stream power stages qS and the corresponding unit discharges q_S for bed slopes S, t_{tot} = total duration of the unsteady hydrograph, r_q = relative increase in discharge compared with previous interval defined by Equation (4.6)

Interval	qS [m²/s]	$q_{4\%}$ [m²/s]	$q_{6\%}$ [m²/s]	$q_{8\%}$ [m²/s]	r_q [-]	t_{tot} [h]	Remarks
1	0.1	2.50	1.67	1.25	-	-	
2	0.2	5.00	3.33	2.50	-	-	$<HQ_{\sim30}$ (steady)
3	0.3	7.50	5.00	3.75	1.00	2.4	$>HQ_{\sim30-50}$ (unsteady)
4	0.4	10.00	6.67	5.00	1.33	3.2	
5	0.5	12.50	8.33	6.25	1.25	4.0	$>HQ_{\sim100}$
6	0.6	15.00	10.00	7.50	1.20	4.8	
7	0.7	17.50	11.67	8.75	1.17	5.6	
8	0.8	20.00	13.33	10.00	1.13	6.4	
...	...	...	...	...	...	...	... until the system failed
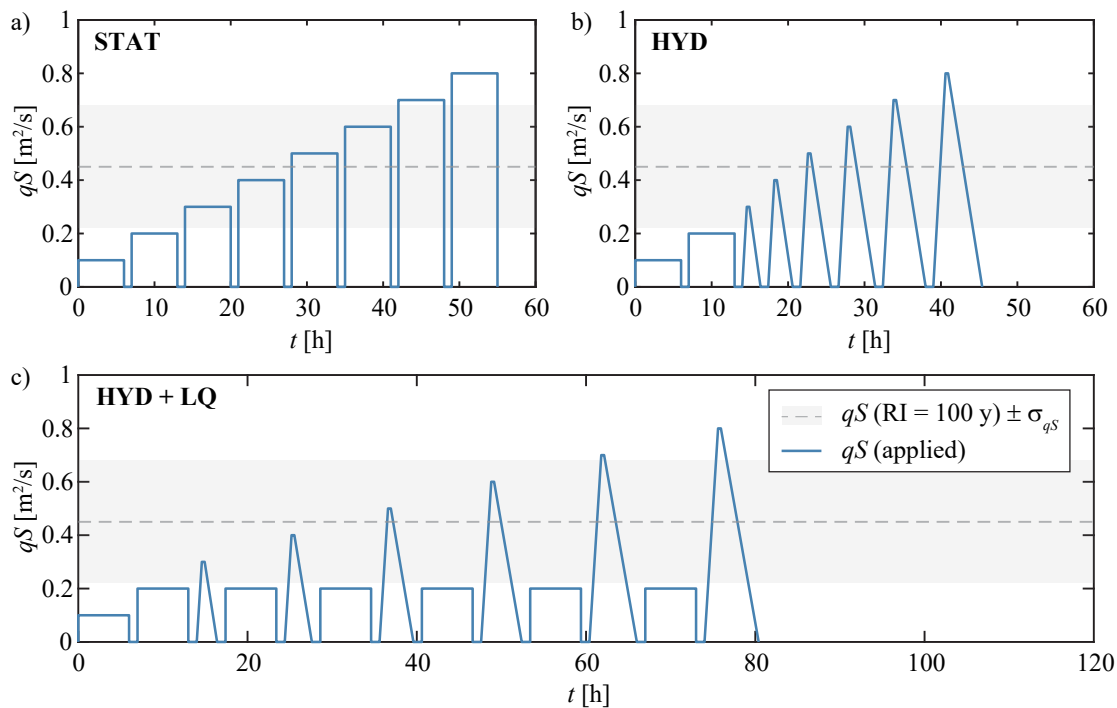
Figure 4.13 Investigated discharge regimes with qS = unit stream power, a) stationary discharge regime (STAT), b) discharge regime with hydrographs (HYD), and c) HYD regime with intermittent periods of low flow (HYD+LQ)

Stationary conditions (STAT)

In the stationary discharge regime (STAT) presented in Figure 4.13a, the water discharge was held constant for t_{stat} = 6 h (1.34 h in model scale) replicating the duration in other stationary flume studies (Zimmermann *et al.* 2010; Kaspar 2017; Hohermuth and Weitbrecht 2018; Zhang *et al.* 2018; Lange 2019; Maager *et al.* 2019). The duration was long enough for sediment outflow to decrease close to zero indicating stable bed conditions (Kaspar 2017; Lange 2019). After each interval, the bed was drained to obtain bed topography measurements (Section 4.5.2).

Hydrographs (HYD)

Triangular-shaped hydrographs (HYD, Figure 4.13b) were applied because stationary conditions hardly reflected the discharge regimes in natural mountain streams. The first two intervals were still conducted under steady flow conditions each lasting t_{stat} = 6 h. The high-frequency and low-intensity floods (RI < 30 years) were assumed to last longer than the low-frequency and high-intensity floods, thus, stationary conditions were considered to be reasonable. However, for flood events with RI > 30 to 50 years, hydrographs were

applied. The main parameters are the total duration of the unsteady hydrographs t_{tot}, the peak arrival time as a percentage of the total duration, and the peak duration t_{peak}.

Prior to defining these parameters, the shape of four hydrographs observed in the Erlenbach stream (Turowski *et al.* 2009, 2013) with RI = 30 to 50 years and two synthetic hydrographs used in laboratory experiments of the Kleine Schliere and Betelriedgraben streams with RI = 100 to 300 years were analyzed (VAW 2014, 2015) (see Appendix A.3.2). The four measured flood events in the Erlenbach stream (CA = 0.7 km^2) have a total duration of approximately 2 h and the peak arrived after 1/6 to 1/4 of the total hydrograph duration t_{tot}. The synthetic hydrographs of Betelriedgraben stream (CA = 12 km^2) was triangular-shaped with the peak arriving at 1/3 of the total duration of 3 to 4 h. Moreover, the synthetic hydrograph of the Kleine Schliere stream (CA = 21 km^2) was triangular-shaped with an inflexion point in the descending limb of the hydrograph, the total duration was approximately t_{tot} = 6 h, and the peak arrived after 1/4 of the total duration. In addition to these hydrographs presented in the Appendix, a total duration t_{tot} = 3 to 5 h was assumed for the short but high-intensity thunderstorm event (RI = 100 years) for the mountain streams Milibach and Alpbach merging in Meiringen, Switzerland (Simonett and Weitbrecht 2011).

Based on the shape of the above presented hydrographs of four mountain streams, the peak was defined to arrive after 1/4 of the total duration t_{tot} and to last for t_{peak} = 20 min (~4.5 min in model scale). Moreover, the total hydrograph duration proportionally increased with the relative increase of discharge, $t_{i,tot} = r_q \, t_{i-1,tot}$ where t_{i-1} is the hydrograph duration of the previous interval and r_q is defined as:

$$r_q = 1 + \frac{q_i - q_{i-1}}{q_{i-1}} \tag{4.6}$$

The duration of the first hydrograph in interval 3 was set to $t_{3,tot}$ = 2.4 h in order to have a total duration of approximately 4 h in interval 5 with unit stream power qS = 0.5 m^2/s corresponding to a flood with RI = 100 years (Table 4.7, marked in red).

Hydrographs with intermittent periods of low flows (HYD+LQ)

A third DVR was tested with small floods occurring between the major floods (Figure 4.13c). During these small floods, the overflow jet impinges more vertically on the bed in the vicinity of the step toe. This potentially leads to an increase in scour depth ,

a preferential removal of fine particles, and may trigger step destabilization. Thus, small stationary floods with unit stream power $qS = 0.2$ m^2/s (RI < 30) were tested with a duration of $t_{stat} = 6$ h in between the unsteady hydrographs. Typical hydrographs of mountain streams have an inflexion point in the receding limb after which the discharge decreases slowly over a longer time period (e.g., hydrographs of Erlenbach or Kleine Schliere Stream, Appendix A.3.2). Thus, these stationary periods of low discharge may also be interpreted as the slowly decreasing and longer lasting decreasing limbs of the hydrographs.

Sediment supply

Clear-water (CW) conditions are rare in steep mountain streams during high-intensity floods unless the reach is located downstream of a bedload retention structure. Thus, the unsteady hydrographs ($qS \geq 0.3$ m^2/s) were tested with sediment supplied as sediment hydrographs (Figure 4.14). The sediment peak arrived simultaneously with the hydrograph peak as this is suggested to occur during large floods in steep streams (e.g., Lenzi *et al.* 1999, 2004). Sediment supply started when a threshold water discharge q_{ini} (i.e., initial unit stream power $(qS)_{ini} = 0.2$ m^2/s) was exceeded and the minimum feed rate of the sediment feeder of $Q_{s,min} = 30$ g/s (model scale) was supplied. This minimum feed rate corresponds to $Q_{s,min} \approx 54$ kg/s or to $q_{s,in} \approx 9$ kg/(sm) in prototype scale for a 6 m wide channel.

Only a fraction of the calculated total transport capacity (TC) was supplied due to technical constraints in the laboratory. The filter basket downstream of the flume has a maximum capacity of ~1'100 kg (model scale) corresponding to a maximum sediment yield
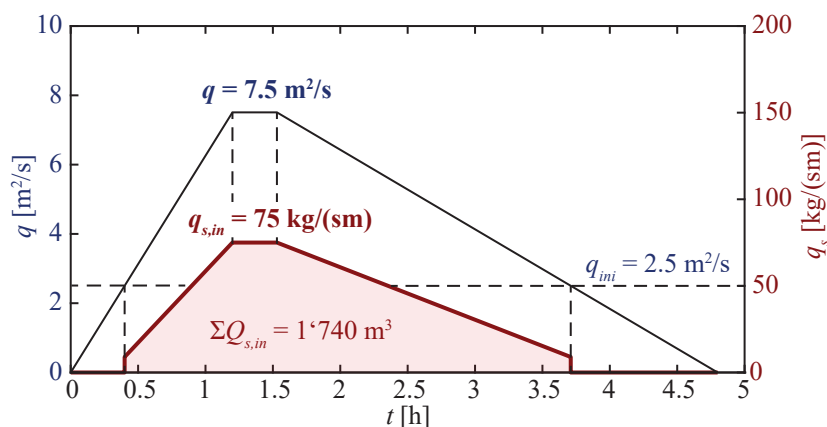

Figure 4.14 Hydrograph and corresponding sediment graph for peak unit water discharge q, peak sediment feed rate q_s, and the cumulative sediment inflow ΣQ_s for $S = 0.08$ and $W = 6$ m (see Table 4.7 for hydrograph duration and Table 4.8 for sediment supply rates)

of ~4'750 m^3 (prototype scale) assuming a bulk density $\rho_{s,bulk}$ = 1'850 kg/m^3 (Bezzola 2021). According to preliminary estimations, it is technically feasible to supply approximately 15 to 20% of the estimated TC in experiments with bed slopes $S \leq 0.08$ and channel width $W \leq 12$ m. The TC during peak flow was calculated using Equation (2.43) by Rickenmann (1990). Even though steep streams are generally supply-limited during ordinary floods (Section 3.2.3), very high sediment transport rates may be reached during exceptional floods with a high RI (Lenzi *et al.* 2004). However, the decrease in scour depth was most pronounced for sediment feed rates $\leq$ 25% TC in laboratory experiments on check dam sequences (Appendix A.3.3, VAW 2018). A further increase in sediment feed rate did not alter the scour depth remarkably as the sediment was most likely transported through the system. No sediment was supplied to the channel during the first two steady interval as scour depth is expected to be higher in CW compared to sediment supply experiments representing conservative conditions.

Table 4.8 Overview of the applied sediment feed rates; S = bed slope, W = channel width, q = unit discharge, $q_{s,in}$ = unit gravimetric sediment feed rate during peak, $\Sigma Q_{s,in}$ = sediment yield of the overall sediment graph, C_s = sediment concentration

	W = 6 m			W = 9 m			W = 12 m		
q	$q_{s,in}$	$\Sigma Q_{s,in}$	C_s	$q_{s,in}$	$\Sigma Q_{s,in}$	C_s	$q_{s,in}$	$\Sigma Q_{s,in}$	C_s
[m^2/s]	[kg/s/m]	[m^3]	[%]	[kg/s/m]	[m^3]	[%]	[kg/s/m]	[m^3]	[%]
Bed slope S = 0.06 (q_{ini} = 3.33 m^2/s)									
5.00	33	300	0.38	41	530	0.49	47	770	0.55
6.67	41	580	0.37	53	1'060	0.47	61	1'570	0.54
8.33	49	960	0.35	64	1'710	0.45	74	2'610	0.53
10.00	57	1'360	0.34	75	2'570	0.44	87	3'900	0.51
11.67	64	1'890	0.32	85	3'510	0.43	no test runs		
Bed slope S = 0.08 (q_{ini} = 2.50 m^2/s)									
3.75	42	370	0.67						
5.00	54	740	0.64						
6.25	65	1'210	0.61						
7.50	75	1'740	0.59						
8.75	85	2'430	0.57	no test runs			no test runs with SF		
10.00	94	3'140	0.56						
11.25	104	3'940	0.54						
12.50	113	4'270[a]	0.53						
13.75	113	4'540[b]	0.48						
15.00	113	4'570[c]	0.44						

[a,b,c] Sediment supply started at q_{ini} = 3.75 m^2/s, 4.25 m^2/s, and 5.63 m^2/s, respectively

Table 4.8 summarizes the peak sediment feed rates $q_{s,in}$, the corresponding sediment yields $\Sigma Q_{s,in}$, and the sediment concentration during peak flow C_s of experiments with bed slope $S = 0.06$ and channel widths $W = 6$, 9, and 12 m, and for $S = 0.08$ and $W = 6$ m. The parameters for the sediment graphs in experiment with $S = 0.08$ and unit discharge $q \geq 12.5$ m^2/s needed to be adjusted to avoid exceeding the maximum capacity of the filter basket. Therein, the sediment feed rate was not further increased and the sediment graph duration was slightly decreased by increasing q_{ini}.

4.4.4   Test program

Table 4.9 summarizes the test program for the artificial step-pool sequences. Initially, the effect of the discharge variation regime (experiments DVR1 to DVR4) and sediment feed (experiments SF0 to SF2) was investigated. To this end, a presumably stable step-pool geometry was selected to conduct the DVR-Series to avoid an early collapse and to ensure potential differences in step stability and scour dimensions becoming evident. Therefore, the largest blocks were selected with an average block weight $M_B = 8.0$ t being arranged in the BASE block configuration (Figure 4.11). The applied discharge regimes were previously described in Section 4.4.3. Experiment DVR4 was tested with the HYD+LQ regime while supplying sediment during the hydrograph intervals (HYD+LQ+SF). Exactly the same step-forming and auxiliary blocks were used to build the steps in the DVR-Series. Therewith, potential effects originating from differences in block size and placement in case of randomly selecting the blocks from the block deposit were minimized.

Test series SF0 to SF2 further investigated the effect of sediment feed rate for $S = 0.06$ and for smaller blocks with mean block weight $M_B = 4.6$ t. Contrary to the DVR4 experiment, the discharge regime HYD was tested without the intermediate periods of low flows (HYD+SF). Additionally to CW conditions (SF0: 0% of transport capacity supplied) and feed rates corresponding to 20% of the estimated TC (SF2), an experiment with a sediment feed rate of 10% TC (SF1) was investigated. Therefore, half of the peak sediment supply rate $q_{s,in}$ for 20% TC, indicated in Table 4.8, was supplied to the flow. Based on the results of the DVR-Series (Section 6.5), the discharge regime (HYD) was selected to further proceed with and the effect of sediment feed (HYD+SF) was tested for selected experiments using 20% transport capacity.

Subsequently, the effect of the channel parameters bed slope and channel width were investigated with experiment SW1 to SW7 for bed slope ranging between 0.04 and 0.08

Table 4.9 Test program of the artificial step-pool sequences (bold: parameter changed)

Exper. ID	Base mixture d_{84} [m]	Bed slope S [-]	Channel width W [m]	Block weight M_B [t]	Drop height H_d [m]	Sed. feed TC [%]	Block config.	Discharge regime
Discharge variation regime (DVR) and sediment feed (SF)								
DVR1	0.18	0.08	6	8.0	1.12	0	BASE	STAT
DVR2	0.18	0.08	6	8.0	1.12	0	BASE	**HYD**
DVR3	0.18	0.08	6	8.0	1.12	0	BASE	**HYD+LQ**
DVR4	0.18	0.08	6	8.0	1.12	**20**	BASE	**HYD+LQ+SF**
SF0[*]	0.18	**0.06**	6	**4.6**	**0.75**	0	BASE	HYD
SF1	0.18	0.06	6	4.6	0.75	**10**	BASE	HYD+SF
SF2	0.18	0.06	6	4.6	0.75	**20**	BASE	HYD+SF
Bed slope and channel width (SW)								
SW1	0.18	**0.04**	6	4.6	0.75	0	BASE	HYD
SW2	0.18	0.04	**12**	4.6	0.50	0	BASE	HYD
SW3	0.18	0.06	**9**	4.6	0.75	0	BASE	HYD
SW4	0.18	0.06	**12**	4.6	0.75	0	BASE	HYD
SW5	0.18	0.06	12	4.6	0.75	**20**	BASE	HYD+SF
SW6	0.18	**0.08**	6	4.6	0.75	0	BASE	HYD
SW7	0.18	0.08	**12**	4.6	0.75	0	BASE	HYD
Block weight (BW)								
BW1	0.18	0.08	6	**4.6**	1.12	0	BASE	HYD
BW2	0.18	0.08	6	4.6	1.12	**20**	BASE	HYD+SF
BW3	0.18	0.08	6	**6.3**	1.12	0	BASE	HYD
BW4	0.18	0.08	6	6.3	1.12	**20**	BASE	HYD+SF
BW5	0.18	0.08	**12**	**8**	1.12	0	BASE	HYD
BW6	0.18	**0.06**	12	8	**0.75**	0	BASE	HYD
Drop height (DH)								
DH1	0.18	0.06	6	4.6	**1.12**	0	BASE	HYD
DH2	0.18	0.06	6	4.6	1.12	**20**	BASE	HYD+SF
DH3	0.18	0.06	6	4.6	**0.40**	0	BASE	HYD
Block arrangement (BA)								
BA1	0.18	0.06	6	4.6	0.75	0	**PYR**	HYD
BA2	0.18	0.06	6	4.6	0.75	0	**PYR+SP**	HYD
BA3	0.18	0.08	12	8	1.12	0	**CUR**	HYD
Base sediment mixture (SM)								
SM1	**0.21**	0.06	9	4.6	0.75	0	BASE	HYD
SM2	0.21	0.06	9	4.6	0.75	0	**PYR**	HYD
SM3	0.21	0.06	9	4.6	0.75	**20**	PYR	HYD+SF

[*]also referred to as reference experiment REF

and channel widths ranging from 6 to 12 m. Experiment SF0, also referred to as reference experiment (REF), may be used for comparison in this SW-Series as it served as an overall reference experiment. Moreover, the effect of the step-pool parameters block weight (BW), drop height (DH) and block arrangement (BA) were tested in the corresponding BW-, DH-, and BA-Series. The mean block weight M_B varied between 4.6 and 8.0 t and selected experiments were tested with SF. The drop height H_d varied between 0.40 and 1.12 m resulting in step spacing L_d between 6.7 and 18.8 m depending on the bed slope. Regarding block arrangement, the step pool configurations PYR, PYR+SP, and CUR were investigated (Section 4.4.2) in addition to the BASE configuration. Last but not least, the effect of the base sediment mixture (SM) was investigated with experiment SM1 to SM3. Therein, the PYR configuration was additionally tested with sediment supply.

The results presented in Chapter 6 follow the parameter designations in terms of marker shape, color, and size presented in Figure 4.15. Experiments with CW conditions have white and experiments with SF filled marker faces. Experiments with bed slope $S = 0.04$, 0.06, and 0.10 are expressed as circles, diamonds, and squares, respectively. The BASE configuration was used unless the marker shape changed to a triangle facing upwards (PYR), a star shape (PYR+SP), or a triangle facing to the left (CUR). The block weight was represented by the marker size, which increased with increasing block weight. The drop height is represented by the color, i.e., green markers refer to small, blue markers to intermediate, and black markers to large drop heights. The channel width is represented by the color brightness, i.e., the brighter colors indicated wide channels and dark colors narrow channels. The majority of the experiments were conducted with base mixture M64 and only three experiments (SM1 to SM3) with M40, which are represented by a different color.

Artificial step-pool systems: Parameter designation			
Sediment supply	**Bed slope**	**Block configuration**	**Block weight**
◇ clear-water	○ $S = 0.04$	△ PYR	▫ $M_B = 4.6$ t
◆ 10% TC	◇ $S = 0.06$	★ PYR+SP	▫ $M_B = 6.4$ t
◆ 20% TC	▫ $S = 0.10$	◁ CUR	☐ $M_B = 8.0$ t
Drop height	**Channel width**	**Base mixture (special case)**	
◇ $H_d < 0.50$ m	◇ $W = 6$ m	◇ M40	
◇ $H_d = 0.75$ m	◇ $W = 9$ m		
◇ $H_d = 1.12$ m	◇ $W = 12$ m		

Figure 4.15 Parameter designation of the artificial step-pool systems investigated in Part B

4.4.5   Stability assessment

Figure 4.16 shows the relationship between unit discharge and the decrease in bed slope $\Delta S = S - S_{ini}$. The unit discharge at which the reach-averaged bed slope decreased by more than 1% (i.e., $\Delta S < -0.01$) was defined as the unit discharge $q_f(1\%)$ of system failure. In the example presented in Figure 4.16a, the mean bed slope decreased at a unit discharge $q_f(1\%) = 8.25$ m²/s. Consequently, the system sustained $q_{stab} = 7.50$ m²/s representing the precedent interval of $q_f(1\%)$.
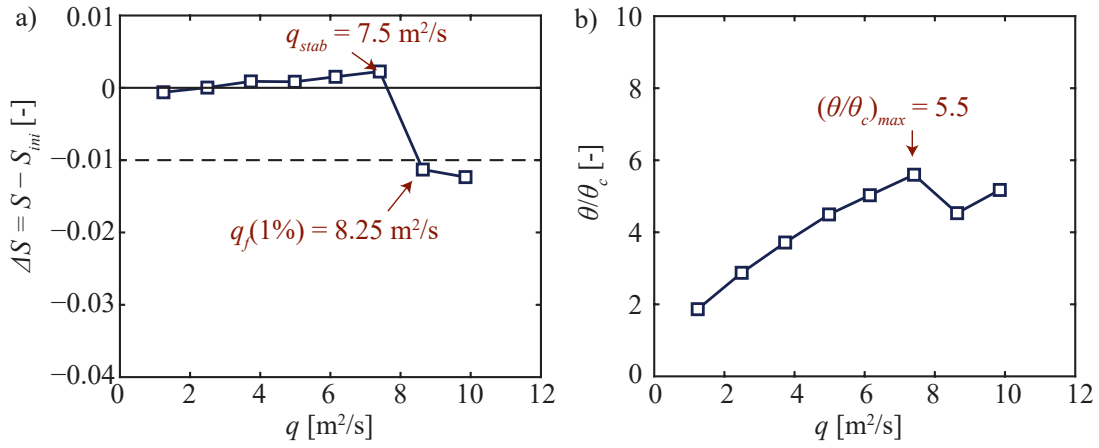

Figure 4.16 Stability assessment: a) decrease of bed slope $\Delta S = S - S_{ini}$ and b) Shields ratio θ/θ_c as a function of unit water discharge q for an exemplary experiment

Moreover, the Shields ratio θ/θ_c was used to compare the stability of the step-pool sequences (Figure 4.16b):

$$\frac{\theta}{\theta_c} = \frac{R_b\,S}{(s-1)\,d_{84}}\frac{1}{\theta_c} \tag{4.7}$$

with R_b = hydraulic bed radius determined following the sidewall correction procedure described in Section 2.3.3 assuming an equivalent sand roughness of $k_w = 0.5$ mm for the smooth flume sidewalls. The critical bed shear stress θ_c was determined using Equation (2.42) developed by Lamb *et al.* (2008). The maximum Shields ratio $(\theta/\theta_c)_{max}$ is defined as the maximum Shields ratio observed at $q \leq q_{stab}$. Eventually, the bed shear stress started to increase again when continuing with the experiments despite the decrease in bed slope by more than 1% (e.g., last interval in Figure 4.16b). Nevertheless, these Shields ratios were not considered in the analysis because they were observed in systems with much smaller bed slopes ($\Delta S < -0.01$) compared to the initial state. Furthermore,

the Shields ratio θ_D/θ_c was used to assess the step-forming block stability:

$$\frac{\theta_D}{\theta_c} = \frac{R_b\, S}{(s-1)\, D_{eq}} \frac{1}{\theta_c} \tag{4.8}$$

Therein, the equivalent spherical diameter D_{eq} was used for bed shear stress normalization instead of d_{84} of the base material.

4.4.6 Failure mechanism assessment

The experiments were documented with side view pictures taken every 5 to 10 seconds with a Nikon DX3 camera with a wide-angle lens with 14 mm focal length capturing ~3.5 m of the flume. Moreover, two to three GoPro 8 cameras were installed to observe the steps located outside of the side view camera perimeter. Therewith, time lapse videos were recorded with a frequency of 1 to 2 Hz. Furthermore, the orthomoasic photos obtained with Structure from Motion (SfM) photogrammetry (Section 4.5.2) were used to identify the failure mechanisms.

Figure 4.17 shows three frames extracted from the GoPro time lapse video showing a step from the side. The time difference between each frame was 0.5 s in model scale corresponding to approximately 2.2 s in prototype scale. It is evident that the upper row block tilted into the downstream pool. All footage was analyzed manually to systematically categorize the relevant step failure mechanisms (Section 6.4).

Figure 4.17 Monitoring of failure mechanisms showing frames extracted from a time lapse video recorded with a GoPro 8 through the glass sidewall of the flume ($\Delta t \approx 2.2$ s in between photos in prototype scale)

4.5   Instrumentation

The present section summarizes the instrumentation used in Part A and B. First, the measurement of hydraulic parameters like discharge, mean flow velocity, and flow depth are presented. Second, the measurement techniques to obtain bed topography data are described. These data were used to determine channel bed parameters such as bed slope

and bed roughness. Finally, the procedure to measure the cumulative sediment outflow is summarized. All quantities are indicated in model scale unless stated otherwise.

4.5.1 Hydraulic parameters

The instrumentation to measure water discharge Q, reach-averaged flow velocity v, and local flow depths h is described. A small and a large pump was used for water discharges of $Q < 20$ l/s and $Q = 20$ to 100 l/s, respectively. The discharge was measured with a magnetic-inductive flow meter (MID) at a frequency of 1 Hz and accuracy of $\pm 0.5\%$. A median filter with a moving window of 5 s was applied to the data.

The reach-averaged flow velocity was determined with the salt dilution method described in Waldon (2004). A saline solution was added to the flow and conductivity was measured at seven to eight cross-sections in the flume. Pairs of aluminium stripes were glued to both sides of the flume and the conductivity measurements were conducted with a frequency of 100 Hz. For one measurement, salt tracer was added three times requiring approximately three to five minutes for a single reach-averaged flow velocity estimate. More information on the salt dilution method is presented in the Appendix A.1.1.

In Part B experiments, an ultrasonic distance sensor (UDS) was used to measure the water surface elevation (WSE) at the end of each discharge increment with stationary conditions or during the peak discharge for the hydrographs. The flow depth h was obtained by subtracting the bed elevation measurements (see subsequent section) from the WSE measurements (Figure 4.18). The width-averaged flow depth estimates were only reasonable in experiments with steady conditions, where the bed did not alter after decreasing the discharge to zero. The local flow depths may be underestimated in unsteady experiments, as
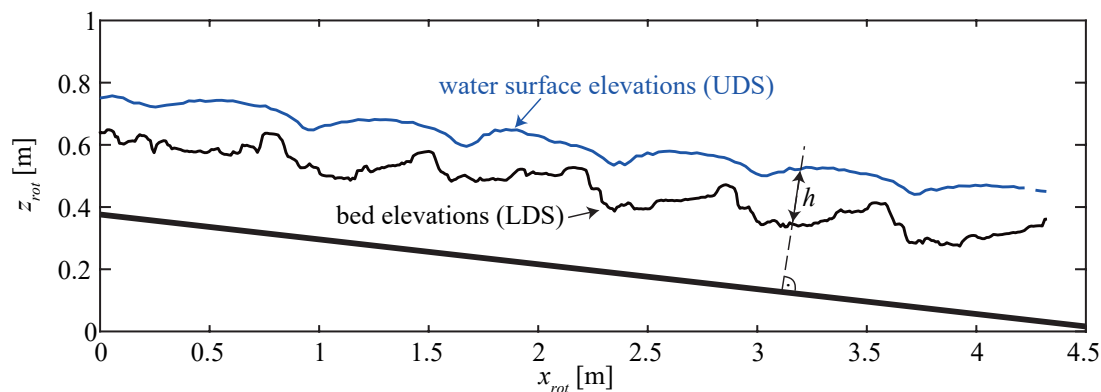

Figure 4.18 Longitudinal profile (covering ~80% of the test reach) of an experiment with artificial step-pool sequences (Part B) illustrating the bed and water surface elevations

the bed continued to adjust to the flow during the descending limb. Therefore, the reach-averaged flow velocities from the salt dilution method, measured during peak flow, were used for the analysis.

4.5.2 Bed topography and channel bed parameters

The instrumentation is presented for the bed topography measurements required to calculate the reach-averaged bed slope S and standard deviation of the bed elevations σ_z. The bed slope S was obtained from width-averaged longitudinal profiles by linear regression. For experiments with artificial step-pool sequences (Part B), the step crest-to-crest slope was calculated by conducting the regression analysis with points located in the vicinity of the initial step locations ($\Delta x \approx \pm D_{eq}$). Furthermore, the standard deviation of the bed elevations σ_z was determined following Aberle and Smart (2003).

Three methods were applied to obtain a DEM of the bed topography. Point measurements were conducted with a LDS mounted on the automatized traverse system of the flume. The LDS measurements were used for immediate evaluation of the bed slope at the end of each interval. However, the data acquisition time per measurement point was rather high resulting in a low spatial resolution. Therefore, SfM photogrammetry was applied to obtain a high resolution DEM requiring only short data acquisition times but time-consuming post-processing. The temporal development of the scour depths were monitored with a camera taking side-view pictures to capture the temporal evolution of the scour depths during the experiments. The three methods are detailed in the following sections.

Laser Distance Sensor (LDS)

Point measurements were conducted with a frequency of 100 Hz for 0.1 s using a Baumer LDS with ±1 mm accuracy, mounted on the automatized traverse system. Note that ~1 s was required for the traverse to move from one point to another resulting in long measurement periods to obtain a high resolution DEM. In Part A (9.6 m long test reach), a DEM was obtained with a resolution of 0.05 m in longitudinal (x)- and transversal (y)-direction. Five to nine longitudinal profiles were measured in the 0.3 and 0.6 m wide channels, respectively, resulting in ~970 to ~1'740 points. In Part B, four to seven longitudinal profiles were obtained depending on the channel width resulting in a resolution of 0.01 m in x-direction and ~0.08 m in y-direction. The resolution in y-direction was approximately equal to the b-axis of the step-forming blocks.

Structure from Motion (SfM)

A high resolution DEM was obtained using SfM photogrammetry. All photos were taken perpendicular to the channel bed with a camera Nikon D7500 mounted on the auto-matized traverse system. Ground control points (GCPs) were placed pairwise close to the bed on each side of the flume with a spacing ≤0.9 m. The x-, y-, and z-coordinates of each GCP were measured with the LDS enabling a transformation of the SfM data into the local LDS coordinate system. The camera overlap was ~85 and ~65% in x- and y-direction, re-spectively, following the recommendations of Morgan *et al.* (2017). The software Agisoft Metashape Professional was used and the highest alignment accuracy and a medium dense cloud quality was selected to generate the dense point clouds. In addition, orthomosaics of the overall test reach were generated with a resolution of 0.25 mm/pixel.

The generated dense clouds were exported and post-processed using Matlab. First, only points located within the region of interest were selected and outliers in particular located close to the channel walls were removed. Afterwards, a regular mesh grid with 0.001 m resolution in both x- and y- direction was generated applying a triangulation-based linear interpolation. A sensitivity analysis showed that applying a median filter with window length of 0.002 m (i.e, the median of each 4 mm^2 area was used) was ideal to eliminate spikes. This post-processed data was finally used to determine bed slope S, the standard deviation of the bed elevation σ_z, but also to determine the geometric relations such as step height H or step length L.

Side photos

A Nikon camera D3X was used to take side-view photos every five to ten seconds capturing approximately 3.5 m of the flume (Figure 4.19). After removing distortion effect with a lens correction filter using Adobe Photoshop, the longitudinal profiles of the WSE
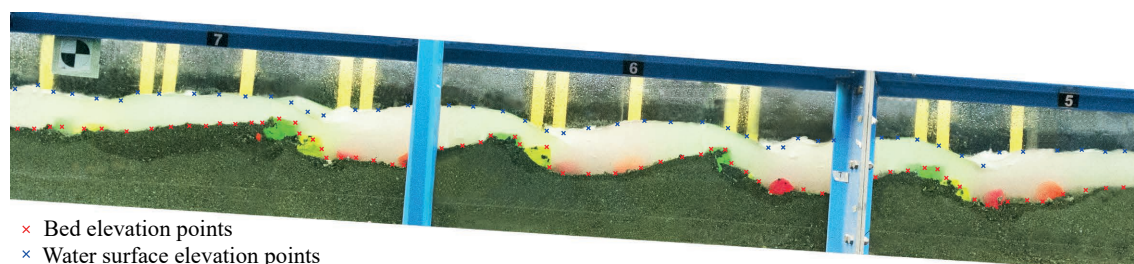

× Bed elevation points
× Water surface elevation points

Figure 4.19 Example of photo taken from the side with bed elevation estimates (red crosses) and WSE estimates (blue crosses)

and the bed elevation were manually digitized using Matlab. Three control points were glued to the channel walls (only one is visible in the top left corner in Figure 4.19) and were used to convert the coordinate system into the LDS coordinate system.

This method allowed to monitor the temporal evolution of both bed and water surface elevation throughout the experiment. However, certain limitations have to be considered. First, a significant amount of uncertainty emerged as manually selecting the data points is related to a certain degree of subjectivity. Second, the reference system depends on properly defining the three control points. To determine the uncertainty originating from the digitizing process itself, eleven randomly selected longitudinal profiles were digitized ten times each. The step-pool detection algorithm (Section 4.6) was applied and the step height H, i.e., the difference between the step crest and the deepest point in the scour, was estimated. As a result, ten step height estimates were obtained for four steps in each of the eleven photographs resulting in $n = 440$ step height estimates. The absolute error was calculated as $\Delta H = H - H_m$ with $H =$ step height estimate and $H_m =$ mean value of these ten step height estimates. The standard deviation of the absolute error was $\sigma_{\Delta H} = 5.8$ mm corresponding to the mean diameter of the base material ($\sigma_{\Delta H} \approx d_m$) and to 7 % of the the step-forming block size ($\sigma_{\Delta H} \approx 0.07 \, D_{eq}$). The mean relative error was $\Delta H / H_m = 4\%$ for the 440 estimates for H.

The photos from the side only provide information on the bed elevations and WSE close to the sidewalls. It may not be representative for the overall channel width. Figure 4.20 compares the bed elevations obtained from the photos and the width-averaged LDS measurements. Only steps III to VI were stable in the presented example whereas step I and II already failed. Despite the limitations and uncertainties described above, the profiles agree well enough for the purpose of quantifying the temporal evolution of scour depth during the experiments. All digitized profiles were manually checked and excluded from analysis in case they strongly deviated from the LDS longitudinal profiles.

4.5.3 Sediment outflow

The sediment outflow was continuously measured with 1 Hz frequency as the sediment was captured in a filter basket attached to three weighing cells at the downstream end of the flume. A buoyancy correction was required because the filter basket was fully submerged. The filter basket was located ~1 m below the flume end. The overflow jet impinged on the filter basket generating an unsteady force on the basket increasing the
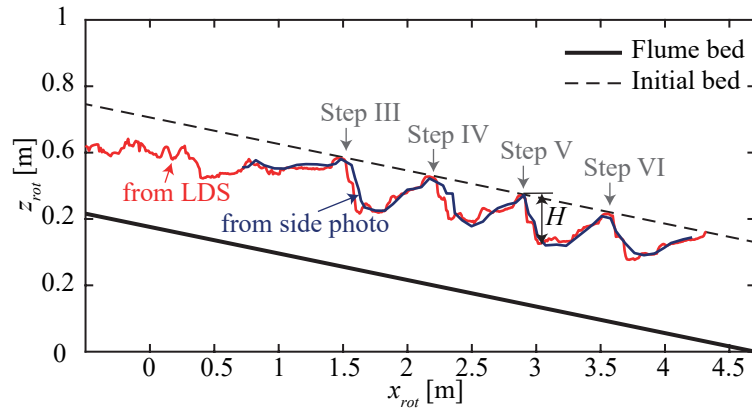
Figure 4.20 Comparison of bed elevations measured with LDS (red line) and obtained from digitizing photographs taken from the side (blue line). Data originate from experiment DVR2 (Table 4.9) at $q = 8.75$ m^2/s (prototype scale)

measured weight. This additional weight caused by the impinging jet correlated with the discharge and Appendix A.1.2 presents a procedure to correct for this effect. Finally, the cumulative sediment outflow was converted into a sediment outflow rate $q_{s,out}$.

4.5.4 Summary on instrumentation

Table 4.10 provides an overview of the methods used to determine hydraulic and channel bed parameters in Part A and B. The LDS data were only used in the analysis of the fixed bed experiments (SF and FR) of Part A. In Part B, the LDS data were compared with the SfM data (Section 4.7) but were not considered for the analysis. Moreover, LDS data provided an initial estimate for parameters S and σ_z after each discharge interval was terminated as they were immediately available contrary to the SfM estimates. The SfM data was used to estimate the bed parameters, i.e., σ_z and S, and the step-geometry parameters step height H and step length L in Part A and B. The reach-averaged flow velocity mea-

Table 4.10 Summary of instrumentation used in the present study

Method	Quantity	Part A	Part B
LDS	σ_z, S	Fixed bed (SF and FR)	SfM data comparison
SfM	σ_z, S, H, L	Mobile bed (MR)	Entire analysis
Salt dilution	v, h, f, θ etc.	Entire analysis	Entire analysis
UDS	v_{WSE}, h	Not measured	Comparison with salt dilution method
Side-view photos	$\Delta v / v_m$	Not evaluated	Streamwise velocity deviations

sured with the salt dilution method was used to calculate flow depth h, hydraulic radius R, Darcy-Weisbach friction factor f, bed shear stress θ etc throughout the study. The flow velocities originating from the UDS water surface elevation measurements were used for comparison with velocities obtained with salt dilution method in Part B (not presented). The streamwise flow velocity deviations $\Delta v/v_m$ were analyzed in Part B (Section 6.3.3) using the side-view photos.

4.6   Step-pool detection

The analysis of step-pool frequency and geometry of step-pool units strongly depends on the detection technique used (Zimmermann *et al.* 2008). Automatized step-pool detection algorithms emerged to avoid the subjectivity related to visual detection (Milzow *et al.* 2006; Zimmermann *et al.* 2008). Herein, the rule-based step-pool detection algorithm of Zimmermann *et al.* (2008) was slightly adapted. The algorithm scans the channel bed against flow direction and identifies steps, pools, and treads (sections neither belonging to a step nor a pool). Figure 4.21 illustrates the main steps of the algorithm with the required parameters. Therein, a step-pool unit was defined by a Top of Step (ToS), an End of Step (EoS), and an End of Pool (EoP). The algorithm was mainly required to detect step-pool units in the self-organizing step-pool systems (Part A). The width-averaged longitudinal profiles obtained with SfM photogrammetry with 1 mm resolution in x-direction were used in the step-pool detection analysis. First, the algorithm detected a local maximum EoP and identified the corresponding EoS which was the first point in upstream direction being equally high or higher. The algorithm proceeded to the second step if the horizontal distance between the EoP and EoS was larger than the minimum pool length $L_{p,min}$. Zimmermann *et al.* (2008) further included a minimum residual depth $H_{res,min}$ being the vertical distance between the EoP and the deepest point in the scour pool. Ho-
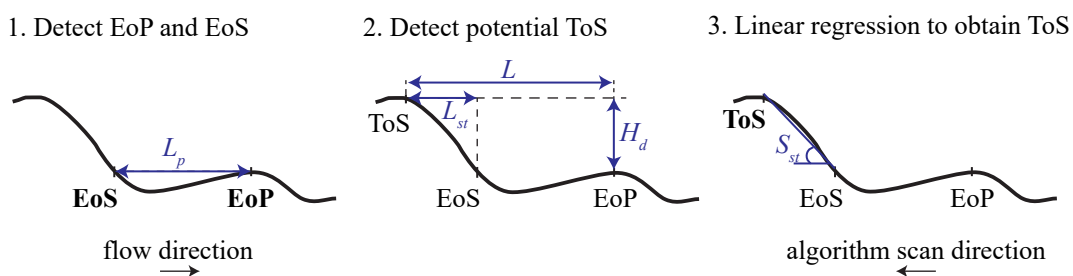

Figure 4.21 Calculation steps of the rule-based step-pool detection algorithm

wever, applying their criterion to the present data resulted in a minimum residual depth of approximately 0.001 m which was too small compared to the grain size $d_{84} = 0.053$ m of the sediment mixture for Part A. Consequently, this criterion was neglected.

Subsequently, the algorithm detected potential ToS, which were located upstream of the EoS while a minimum drop height $H_{d,min}$, a minimum step length L_{st}, and a maximum step length L must be complied with. Afterwards, a linear regression analysis was conducted with all points upstream of the EoS complying with the previously described parameters. To be classified as a potential ToS, the step slope originating from the linear regression needed to be larger than $S_{st,min} = S[°] + 10°$. Finally, among all points located upstream of the EoS, the data point with the highest coefficient of determination (R^2) was identified as ToS.

4.6.1 Calibration

The above presented parameters of the step-pool detection algorithm had to be calibrated. According to Montgomery and Buffington (1997), the step-pool morphology typically contains channel-spanning steps which formed due to the accumulation of large blocks and boulders. Thus, the algorithm was calibrated with the smooth sidewall experiments in which steps were visually determined at locations where a channel-spanning hydraulic jump formed in the downstream pool. The parameters summarized in Table 4.11 were selected in a way that the algorithm detects the same steps and pools as from visual observation in smooth sidewall experiments. The parameters were adjusted manually, but, a perfect agreement could not be achieved. The same parameter set was used to detect the step-pool units in all self-organizing step-pool experiments with macrorough sidewalls ensuring a consistent detection within the scope of the present study. Channel-spanning hydraulic jumps were less evident in rough sidewall experiments because the roughness elements highly disturbed the flow surface; in these conditions, the detection algorithm was the only consistent way of identifying steps and pools.

The maximum step-pool unit length, which is the horizontal distance between the ToS and the EoP, was selected to $L_{max} = 3\,W$. It is in agreement with field observations where relative step length was $1 < L/W < 4$ (Chin and Wohl 2005; Okazaki *et al.* 2006). The parameters minimum step length $L_{st,min}$, minimum pool length $L_{p,min}$, and minimum drop height $H_{d,min}$ were all scaled with d_{84} of the sediment mixture. The minimum step length and pool length equal at least one and three times d_{84}, respectively. Drop height

Table 4.11 Overview of the step-pool detection algorithm parameters (definition in Figure 4.21)

	Scaling factor	Range	Sensitivity	Description
L_{max}	$3\,W$	$0.9 - 1.8$ m	low	Max. step-pool unit length: horizontal distance between ToS and EoP
$L_{st,min}$	$1\,d_{84}$	0.053 m	low	Min. step length (ToS to EoS)
$L_{p,min}$	$3\,d_{84}$	0.159 m	high	Min. pool length (EoS to EoP)
$H_{d,min}$	$0.5\,d_{84}$	0.027 m	high	Min. drop height: vertical distance between ToS and EoS
$S_{st,min}$	$S[°] + 10°$	$12.3° - 15.7°$	medium	Min. step slope (linear regression of points upstream of EoS)

was specified to be higher than $0.5\,d_{84}$. The last criterion includes the minimum step slope $S_{st,min} = S\,[°] + 10°$ being identical to criterion in the algorithm described in Zimmermann *et al.* (2008).

4.6.2   Sensitivity analysis

A sensitivity analysis was conducted regarding the step-pool detection algorithm using the Part A experiments. The parameters $L_{p,min}$, $L_{st,min}$, L_{max}, $H_{d,min}$, and $S_{st,min}$ were varied from 0.3 to approximately 2 times their original values. Afterwards, the step-pool detection algorithm was applied to all experiments with smooth and rough sidewalls. Figure 4.22 shows the ratio between the number of steps in the reference case n_{ref}, i.e., the steps detected with the parameter set applied in this study (Table 4.11), and the number of steps obtained when the parameters were changed. The gray areas indicate a deviation of $\pm 50\%$ with regard to n_{ref}. For example, 25% more steps were detected on average by reducing the minimum pools length from $L_{p,min} = 3\,d_{84}$ to $2\,d_{84}$ (Figure 4.22a). On the contrary, 25% fewer steps were detected by increasing the minimum pool length to $L_{p,min} = 4.5\,d_{84}$.

Regarding minimum step length, the number of steps only changed considerably for $L_{st,min}/d_{84} \geq 2$ leading to a reduction of the step detected by ~25% (Figure 4.22b). However, setting the minimum step length to values higher than d_{84} is not reasonable as steps consisting of blocks with diameter d_{84} should not be excluded from the analysis. Selecting smaller minimum step heights did not alter the number considerably. Similarly, the maximum step length L_{max} was only sensitive in one direction (Figure 4.22c). A similar number of steps was detected for parameter ranges $2 < L_{max}/W < 6$. Fewer steps

were detected setting the maximum step-pool unit length to $L_{max}/W = 1$ only allowing step lengths smaller than one times the channel width. However, limiting this parameter to unity is not reasonable as field data demonstrated the step length to be in the range of $1 < L_{max}/W < 4$ (Chin and Wohl 2005; Okazaki *et al.* 2006). Thus, the parameters $L_{st,min}$ and L_{max} are both considered to be insensitive parameters if selected reasonably.

The minimum drop height $H_{d,min}$ presented in Figure 4.22d was a sensitive parameter. The parameter range $0.3 < H_{d,min}/d_{84} < 0.8$ resulted in a range of $\pm 30\%$ fewer or more steps detected by the algorithm. Reducing the minimum drop height certainly increased the number of detected steps and vice versa. Lastly, also changes in minimum step slope $S_{st,min}$ is a sensitive parameter. Overall, a minimum number of steps is obtained when the sensitive parameters $H_{d,min}$, $L_{p,min}$, and $S_{s,min}$ are increased by 20% and resulting in a maximum number of steps when they were decreased by 20%. This parameter set is presented in Figure 4.22f, indicating an uncertainty regarding the number of detected steps of approximately $\pm 36\%$ independent of the sidewall roughness.
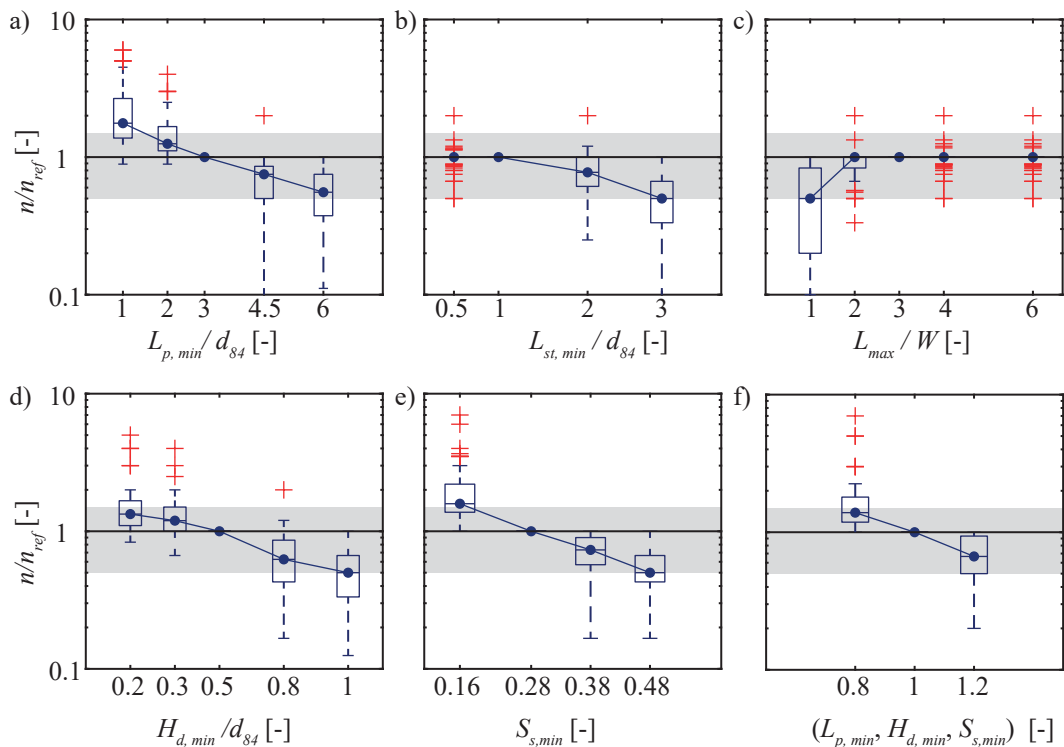

Figure 4.22 Sensitivity analysis of the step-pool detection algorithm parameters (shaded areas: $0.5 \leq n/n_{ref} \leq 1.5$) for a) minimum pool length $L_{p,min}$, b) minimum step length $L_{st,min}$, c) maximum step-pool unit length L_{max}, d) minimum drop height $H_{d,min}$, e) minimum step slope $S_{st,min}$, and f) variation of the sensitive parameter $L_{p,min}$, $H_{d,min}$, and $S_{st,min}$ by $\pm 20\%$ each

4.6.3   Step-pool detection in artificial step-pool systems

The algorithm was used to automatize the analysis to obtain the step geometry in Part B. It was more straight forward compared to the detection of step-pool units in Part A as the artificial step-pool units were more clearly defined. Nevertheless, the same parameters were selected as for the self-organizing step-pool sequences except for $L_{p,min}$, L_{max}, and $H_{d,min}$. The minimum pool length was set to at least 25% of the design step spacing ($L_{p,min} = 0.25\ L_d$), total step length should not exceed the design step spacing by more than 25% ($L_{max} = 1.25\ L_d$), and drop height was selected to be larger than 25% of the design step height ($H_{d,min} = 0.25\ H_d$). The parameter minimum R^2 was not required and the local maximum was selected as ToS. The location of the resulting ToS, EoS, and EoP were double-checked by manually inspecting the longitudinal profiles. The step length L detected by the algorithm may deviate from the design step spacing ($L \approx 0.25 ... 1.25\ L_d$), which is related to the definition of $L_{p,min}$ and L_{max}.

4.7   Accuracy and uncertainty

The experimental setup and the measurement devices are subject to systematic and random errors (Aigner *et al.* 2015). The systematic error emerging in the present study are listed and described below in model scale:

- Flume slope $\pm 0.1‰$
- Small pump ± 1 l/s
- Large pump ± 3 l/s
- Magnetic-inductive flow meter $\pm 0.5\%$
- Ultrasonic distance sensors $< \pm 1\%$
- Laser distance sensors ± 1 mm
- Positioning system ± 1 mm

Part A: Self-organizing step-pools sequences

The smooth sidewall experiment was repeated to test the reproducibility and to quantify the uncertainties attributed to the inherent heterogeneity of self-organizing step-pool systems (Section 5.2.2). Only eight intervals were used to determine the maximum relative errors (σ_i/i) of quantity i, which are summarized in the following:

- Mean flow velocity v: $\sigma_v/v \leq 7\%$

- Bed roughness σ_z: $\sigma_{\sigma_z}/\sigma_z \leq 18\%$

- Bed slope S: $\sigma_S/S \leq 8\%$

- Cumulative sediment outflow ΣQ_s $\sigma_{\Sigma Q_{s,out}}/\Sigma Q_{s,out} \leq 5\%$

In addition, the above presented sensitivity analysis of the step-pool detection algorithm parameters (Section 4.6.2) indicated that the uncertainty regarding the number of detected steps is estimated to be ±36%.

Part B: Artificial step-pool sequences

The relative error of the mean flow velocity was assessed by determining the reach-averaged value by repeating the measurement three times and by compiling measurements of six to seven sub-reaches. More information on the uncertainty of the mean flow velocity estimates is detailed in Appendix A.1.1. This error was not only related to the measurement procedure itself but also incorporated variability of flow velocity within the test reach. Regarding the channel bed parameters S and σ_z, the LDS measurements were compared to the SfM measurements to quantify the uncertainty related to the measurement techniques. Similarly, uncertainty related to geometric parameters like step height H and step length L were determined by comparing estimates originating from LDS and SfM topography data. The relative errors are summarized in the following:

- Mean flow velocity v: $\sigma_v/v \leq 20\%$ (on average 9%)

- Bed roughness σ_z: $\sigma_{\sigma_z}/\sigma_z \leq 0.5\%$

- Bed slope S: $\sigma_S/S \leq 5\%$

- Step height H: $\sigma_H/H \leq 9\%$

- Step length L: $\sigma_L/L \leq 13\%$

Both step height and lengths were on average 8% smaller using LDS data due to the smaller resolution particularly in lateral direction. Consequently, local minima or maxima in the topography may not be fully captured when using LDS data with low spatial resolution. Therefore, the high resolution topography data obtained with SfM were used for the analysis. The relative error originating from the mean flow velocity measurements is the main contributor to uncertainty compared to other errors related to the instrumentation.

5 Self-organizing step-pool systems

Parts of this chapter have been published in:

- *Maager* et al. *(2020): „Effect of bank roughness on step-pool systems in steep channels", proceedings of the 10th Conference on Fluvial Hydraulics (River Flow) 2020 in Delft, The Netherlands (online).*

- *Maager* et al. *(2022a): „Bed stability of step-pool channels with macrorough sidewalls.", Water Resources Research. [under review]*

- *Maager* et al. *(2022c): „Effect of macrorough sidewalls on flow resistance in steep rough channels", Water Resources Research, 58.*

5.1 Overview

This chapter presents the findings regarding the self-organizing step-pool systems in channels with macrorough sidewalls. Section 5.2 presents the results from the mobile bed experiments focusing on reproducibility and general observations of the natural step-pool sequences. Section 5.3 elaborates on the effect of macrorough sidewalls on flow resistance. An existing approach to estimate mean flow velocity was extended with a parameter accounting for sidewall roughness. A modified sidewall correction procedure based on the Einstein-Johnson approach is presented to improve bed shear stress estimation in steep channels with macrorough sidewalls. Finally, the results are combined and a bed stability assessment is presented in Section 5.4 concluding with implications regarding the competing hydraulic and granular effects contributing to the increase of bed stability. Herein, all quantities are presented in model scale.

5.2 Step-pool morphology in self-organizing step-pool systems

Section 5.2.1 presents the mobile bed experiments with smooth sidewalls. They were used to test the reproducibility (Section 5.2.2) and served as reference experiments to quantify the effects of macrorough sidewalls on the formation and stability of step-pool sequences. Section 5.2.3 presents the experiments with macrorough sidewalls focusing on the bed restructuring processes.

5.2.1 General observations of bed erosion and restructuring

The smooth sidewall experiments were conducted for a bed slope $S = 0.10$, a channel width $W = 0.3$ m, and an average jamming ratio $W/d_{84} \approx 5.5$. Figure 5.1 shows the

time series of the unit discharge q, cumulative sediment outflow ΣQ_s captured in the filter basket, and the unit sediment transport rate q_s, computed from ΣQ_s, for the smooth sidewall experiments „0" and „0 (rep)". The former was conducted with discharge increments $\Delta q = 0.01$ m²/s while the latter was repeated with smaller increments $\Delta q = 0.005$ m²/s to test reproducibility. The experiment „0" with larger discharge increments had a total duration of ~16 h, while „0 (rep)" lasted more than twice as long with a total duration of ~35 h. Both experiments were interrupted after $q = 0.08$ m²/s because bed erosion exposed the flume invert.

An increase in q_s measured at the downstream end of the flume was related to three mechanisms. First, the highest q_s was measured during the initial discharge increase (initial erosion, Figure 5.1) as flattening the bed prior to conducting the experiment led to a cover with fine sediment size fractions ($d \leq 20$ mm). These fine grains were eroded during the initial discharge increase while the larger blocks underneath were uncovered but remained in place. Second, the next discharge increase mobilized grain fractions, which were stable during the preceding interval, resulting in an increase in q_s at the beginning
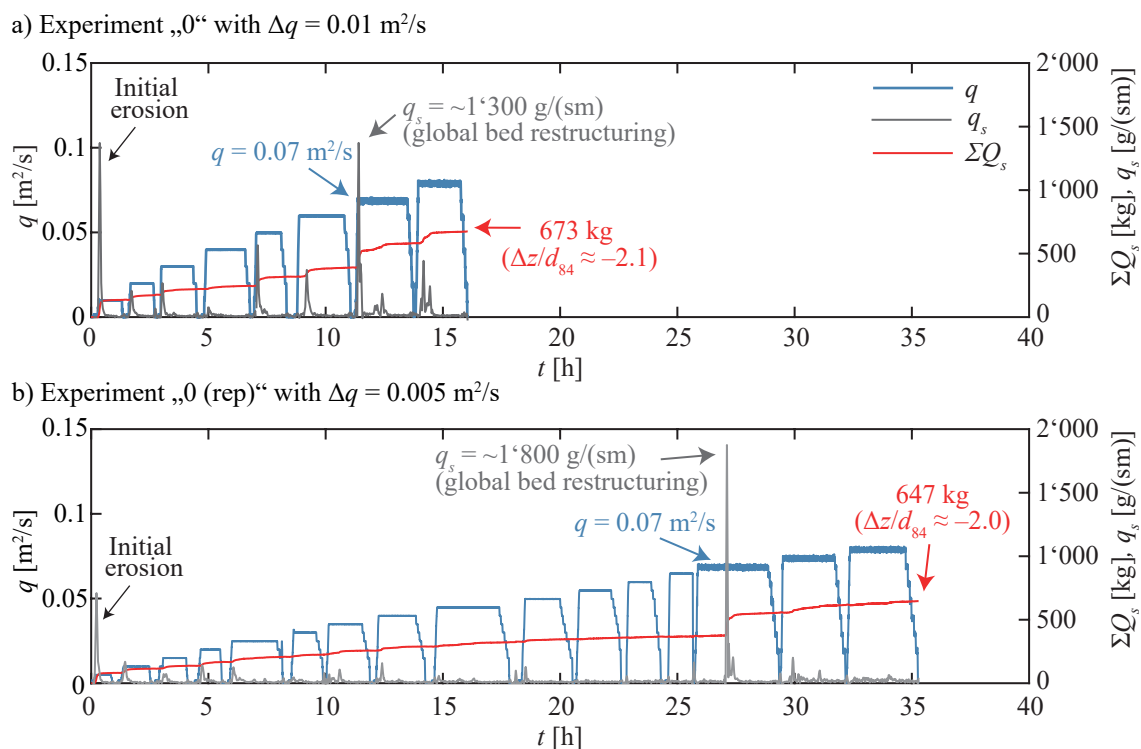

Figure 5.1 Times series of experiments with smooth sidewalls and discharge increment a) „0": $\Delta q = 0.01$ m²/s and b) „0 (rep)": $\Delta q = 0.005$ m²/s; $\Delta z/d_{84}$ = reach-averaged bed elevation changes after the entire experiment adapted from Maager *et al.* (2022a)

of each interval. Third, the sediment outflow rate q_s increased due to the destruction of step-pool units leading to a local or global restructuring of the bed.

High sediment outflow rates $q_s > 1'000$ g/(sm) were related to major bed elevation changes throughout large parts of the test section. However, bed elevation changes in the upstream part of the flume did not necessarily lead to a large increase in q_s because the sediment was sometimes deposited in the downstream flume sections, i.e.,the sediment was stored within the reach (Hayward 1980; Hassan and Zimmermann 2012). As a consequence, the sediment outflow rates did not correlate with the unit discharge q, which was also observed by Saletti *et al.* (2015).

Figure 5.2 shows side views of experiment „0" for an intermediate section ($6 < x/W <$ 20, end of test reach at $x/W = 32$) during major bed elevation changes for $q = 0.07$ m²/s. The maximum $q_s \approx 1'300$ g/(sm) measured at the beginning of the interval t_0 (Figure 5.1a) resulted from bed elevation changes in the downstream part of the flume ($x/W \geq 18$, not visible in Figure 5.2) leading to an erosion propagating upstream. Soon this triggered the collapse of steps located at $x/W \approx 12$ to 14 (Figure 5.2, $t_0 + 18$ min and $t_0 + 29$ min). These secondary bed restructuring waves propagating in upstream direction led to much smaller

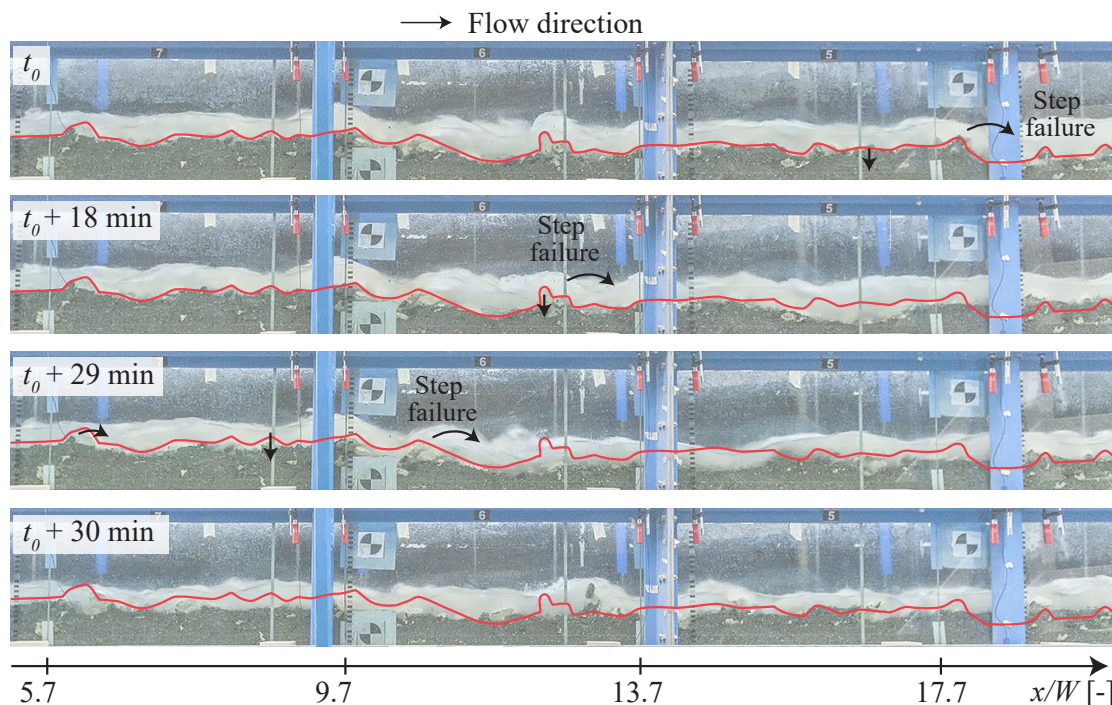**Figure 5.2** Global restructuring of the bed. Side view of the flume corresponding to an ~4 m long section (overall test section length $L_{tot} = 9.6$ m, i.e., $L_{tot}/W = 32$) for test run „0" with smooth sidewalls ($S = 0.10$, $W/d_{84} = 5.5$) at $q = 0.07$ m²/s and for different time steps (red line: bed elevation at t_0).

sediment outflow rates $q_s \approx 200$ g/(sm) compared to the initial erosion. The mobilized sediment deposited in the downstream part (e.g., at $x/W = 14$ to 18, Figure 5.2) and was not transported to the flume outlet. Similar progressive upstream erosion (PUE) patterns were observed by Comiti *et al.* (2009a) and Zimmermann (2009).

This PUE pattern either happened within a couple of minutes or over a longer time span of up to several ten minutes or hours. For example, the bed restructuring of the downstream part of the flume ($x/W = 18$ to 32, not visible in Figure 5.2) occurred within a few minutes and completely restructured ~3 to 4 m of the flume corresponding to 30 to 40% of the overall test section. However, the bed elevation changes in the middle and upper part of the flume ($x/W < 14$) occurred within a time span of approximately 20 to 30 minutes.

5.2.2   Reproducibility

The smooth sidewall experiment „0" with $\Delta q = 0.01$ m²/s was repeated with a smaller increment $\Delta q = 0.005$ m²/s referred to as „0 (rep)" to test reproducibility and effects related to the choice of Δq. Both experiments were interrupted after $q = 0.08$ m²/s because bed erosion reached the flume invert. The overall duration of experiment „0 (rep)" was more than twice as long as in experiment „0" due to the smaller Δq (Figure 5.1). However, the cumulative sediment outflow at the end of the experiments ($\Sigma Q_s = 673$ kg and 647 kg for „0" and „0 (rep)", respectively) was similar despite large differences in duration. These cumulative sediment outflow estimates correspond to an average bed elevation change of $\Delta z/d_{84} \approx 2.1$ and 2.0 for „0" and „0 (rep)", respectively. Furthermore, the highest sediment outflow rates q_s were observed for the same discharge $q = 0.07$ m²/s and the bed was fully restructured in both cases.
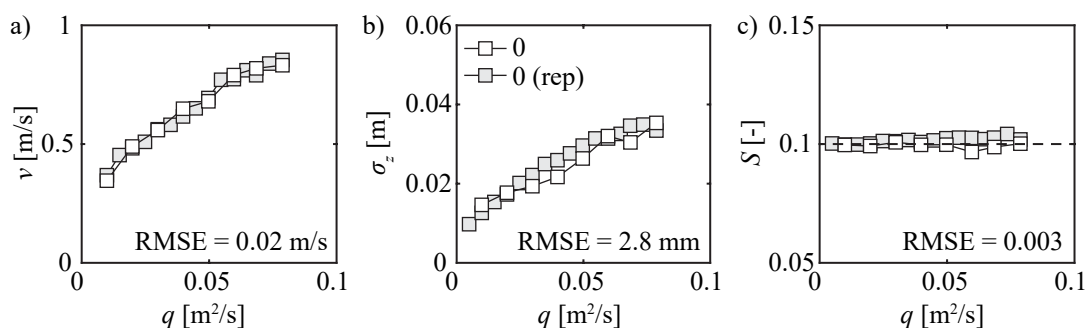

Figure 5.3 Reproducibility of hydraulic and bed parameters. a) Mean flow velocity v, b) bed roughness σ_z, and c) bed slope S as a function of unit discharge q for experiment „0" and „0 (rep)" with $S = 0.10$ and $W/d_{84} = 5.5$, RMSE = root mean square error

Figure 5.3 presents the mean flow velocity v, the standard deviation of the bed eleva-tions σ_z, and the bed slope S as a function of q for both experiments „0" and „0 (rep)". Therein, v and σ_z adjusted similarly to the increase in q while the bed slope was kept approximately at its initial value $S = 0.10$. The root mean square error (RMSE) of each parameter evaluated for experiment „0" and „0 (rep)" at the corresponding unit discharge was $\mathrm{RMSE}(v) = \pm0.02$ m/s, $\mathrm{RMSE}(\sigma_z) = \pm2.8$ mm, and $\mathrm{RMSE}(S) = \pm0.003$. Similarly, the differences in ΣQ_s were evaluated after each interval resulting in $\mathrm{RMSE}(\Sigma Q_s) = \pm16$ kg corresponding to a reach-averaged bed elevation change of $\Delta z/d_{84} \approx 0.05$. Consequently, the differences regarding v, σ_z, S, and ΣQ_s were small demonstrating good reproducibility and little influence of the discharge increment size.

Figure 5.4a shows the DEM of differences (DoD), expressed as Δz normalized with $d_{84} = 0.053$ m, before and after $q = 0.07$ m^2/s was applied. The bed was restructured throughout the entire test section in both experiments leading to bed elevation changes up to $|\Delta z/d_{84}| \approx 2$ to 3. In experiment „0" (Figure 5.4a), large parts of the bed were eroded in the downstream region ($x/W = 24$ to 32) and at the upstream end ($x/W = 0$ to 10), while sediment deposited mainly in the middle part ($10 < x/W < 24$). Similar results were obtained in experiment „0 (rep)" (Figure 5.4b). Therein, most of the channel bed erosion occurred in the middle to lower part ($15 < x/W < 28$). Some of the mobilized sediment deposited in the downstream region but the majority was transported out of the system leading to a higher maximum sediment outflow rate compared to „0". Overall, the results
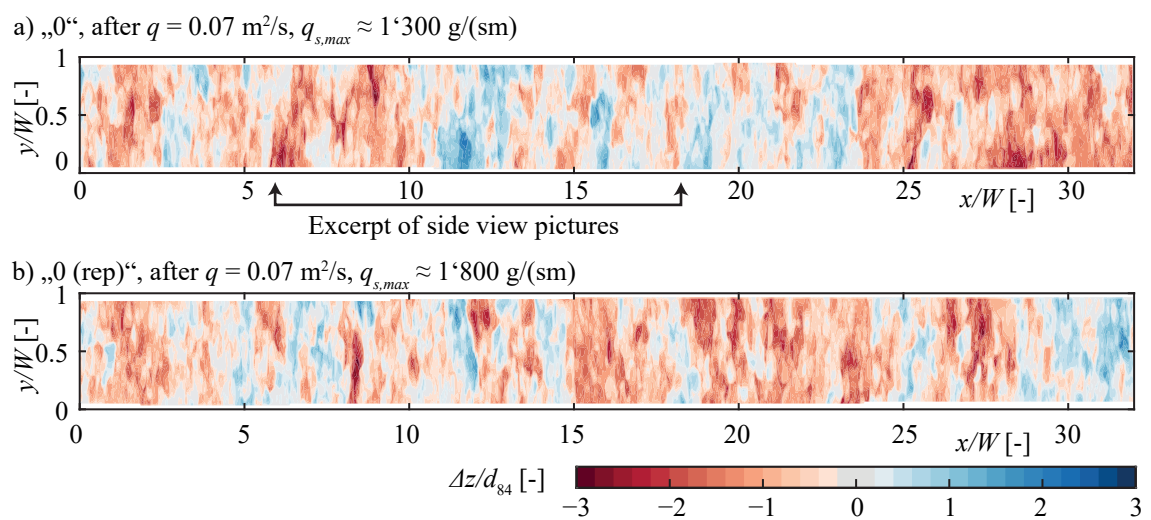
a) „0", after $q = 0.07$ m^2/s, $q_{s,max} \approx 1'300$ g/(sm)

Excerpt of side view pictures

b) „0 (rep)", after $q = 0.07$ m^2/s, $q_{s,max} \approx 1'800$ g/(sm)

$\Delta z/d_{84}$ [-]

Figure 5.4 Smooth sidewall experiments. Bed elevation changes Δz normalized with $d_{84} = 0.053$ m before and after $q = 0.07$ m^2/s was applied for a) „0"; the excerpt of the side view pictures presented in Figure 5.2 is indicated, and b) „0 (rep)"

from the smooth sidewall experiments allow an interpretation of differences observed later in macrorough sidewall experiments. The following aspects should be considered:

- The inherent randomness of the experiments regarding flow velocity, standard deviation of the bed elevation, and bed slope, and the cumulative sediment outflow are in the following ranges: v ±0.021 m/s, σ_z ±2.8 mm, S ±0.003, and $\Sigma Q_{s,out}$ ±16 kg (i.e., $\Delta z/d_{84} \approx$ ±0.05), indicating good reproducibility.

- The sediment outflow rate q_s measured at the flume outlet is not necessarily an adequate indicator for local bed elevation changes as the sediment mobilized in particular in the upstream region may deposit before reaching the flume outlet.

- The size of the discharge increment does not have a strong effect on hydraulic and bed parameters. Nevertheless, a natural flow regime (i.e., hydrographs with different shapes) may have an impact on bed stability and were tested in Part B (Section 6.5).

- The location of bed elevation changes after a step collapse exhibit a strong degree of randomness due to the initial location of large boulders and cannot be predicted.

In summary, the smooth sidewall experiment was well reproduced despite the smaller unit discharge increments more than doubling the experimental duration. Therefore, the macrorough sidewall experiments were continued with the larger unit discharge increments $\Delta q = 0.01$ m²/s (i.e., unit stream power increments $\Delta(qS) = 0.001$ m²/s).

5.2.3 General observations with macrorough sidewalls

The present section summarizes general observations of mobile rough bed (MR) experiments with macrorough sidewalls. The experiments were conducted using six macrorough sidewall types RR25, RR55, RR55A, RR115, R55, and R115 (Section 4.3.1) for bed slope $S = 0.10$ and a jamming ratio $W/d_{84} = 5.6$. Sidewall type R55 was additionally tested for bed slopes $S = 0.06$ and 0.04 and for sidewall type RR55, the channel width was varied from 0.3 to 0.6 m to obtain a larger jamming ratio $W/d_{84} = 11.3$. The test program is summarized in Table 4.3. The effect of macrorough sidewalls, bed slope, and jamming ratio are presented in the following.

Effect of macrorough sidewalls

Figure 5.5 shows the time series of unit discharge q, the unit sediment outflow rate q_s, and the cumulative sediment outflow ΣQ_s for experiments with macrorough si-
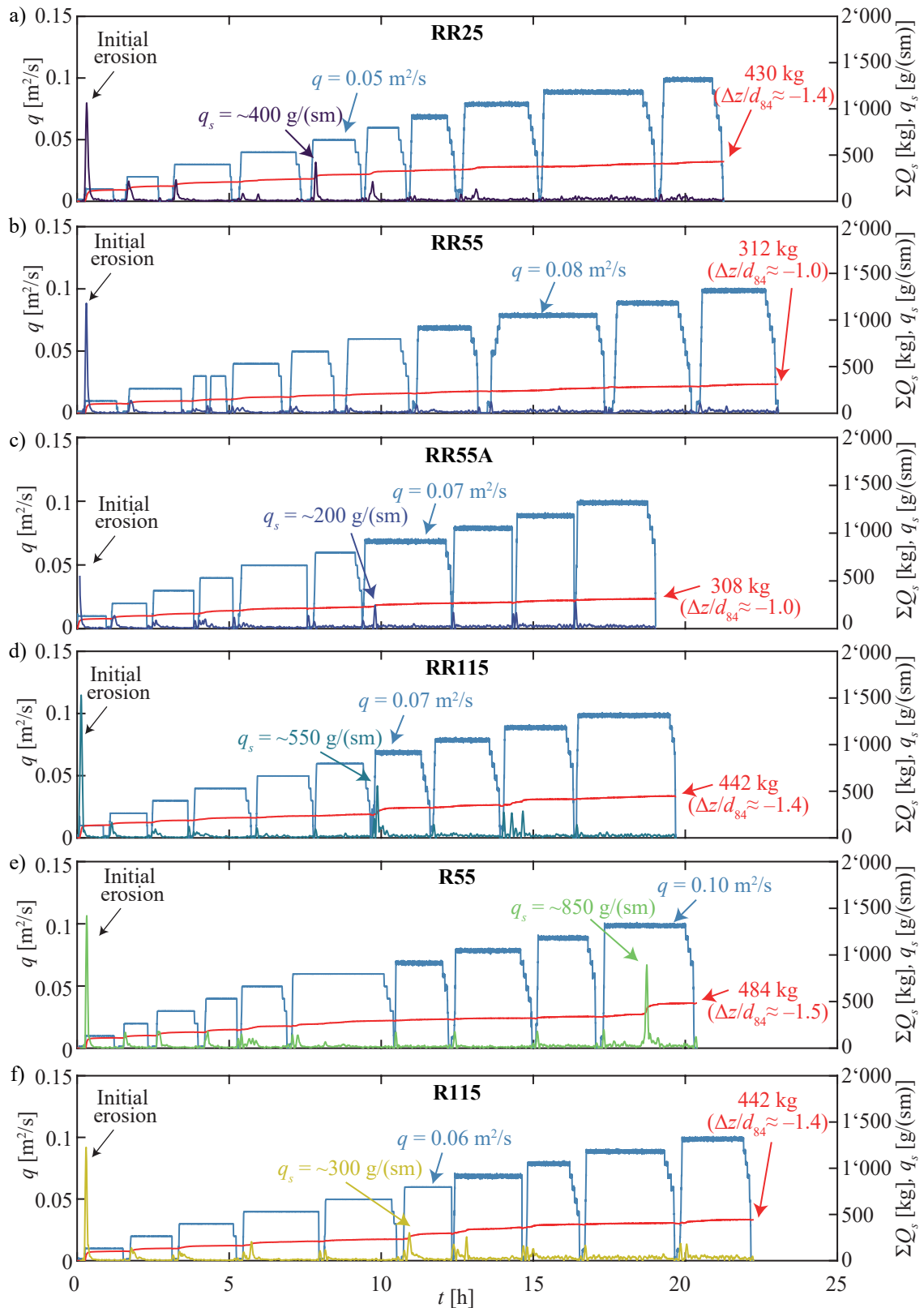
Figure 5.5 Time series of experiments with macrorough sidewalls. Unit discharge q, unit sediment outflow rate q_s, and cumulative sediment outflow ΣQ_s ($S = 0.10$, $W/d_{84} = 5.6$) for sidewall types a) RR25, b) RR55, c) RR55A, d) RR115, e) R55, and f) R115, $\Delta z/d_{84}$ = reach-averaged bed elevation changes

dewalls. Therein, $\Delta z / d_{84}$ is the reach-averaged vertical bed elevation change after the entire experiment, normalized with d_{84}. This parameter was calculated from ΣQ_s and $\Delta z / d_{84} = -1$ indicated that the bed was on average vertically degraded by a layer of thickness $d_{84} = 0.053$ m.

Similarly to the smooth sidewall experiments (Figure 5.1), the highest q_s were observed at the beginning of the experiment during the first interval (i.e., initial erosion). However, ΣQ_s and $\Delta z / d_{84}$ were generally lower in all experiments with macrorough sidewalls ($\Sigma Q_s < 484$ kg, i.e., $\Delta z / d_{84} > -1.5$) compared to the smooth sidewall experiments ($\Sigma Q_s \approx 650$ kg, i.e., $\Delta z / d_{84} > -2.0$) even though the latter was stopped earlier at $q = 0.08$ m^2/s. This indicates that the overall bed stability increased in experiments with macrorough sidewalls, which is further explained in Section 5.4. The maximum sediment outflow rates were lower in all macrorough tests compared to smooth sidewall experiments ($q_s < 850$ g/(sm) vs. $q_s = 1'300$ to $1'800$ g/(sm)). The bed elevation changes were more restricted to local parts of the test section and did not propagate through the entire test reach, particularly in the RR-Series experiments with the roughest sidewalls.

Effect of bed slope

Figure 5.6 presents the relation between unit discharge q and reach-averaged flow velocity v, bed roughness σ_z, and bed slope S for experiments R55 with bed slopes $S = 0.04$, 0.06, and 0.10. In all three experiments, v increased with increasing discharge and the differences between bed slopes were small. However, the increase in σ_z was more pronounced in steeper channels as the bed shear stress was higher suggesting that fewer steps emerged in channels with milder gradients (Section 5.4.2). The bed slope remained more
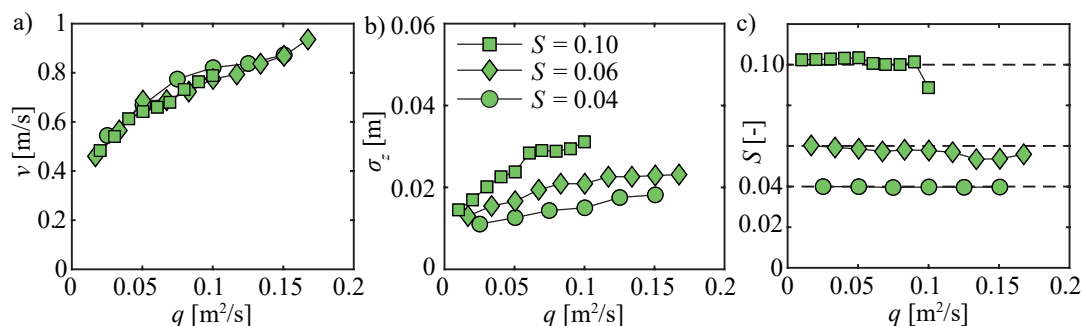

Figure 5.6 Effect of bed slope on hydraulic and bed parameters. Mobile bed experiments (MR) with sidewall type R55, $W/d_{84} = 5.6$, and $S = 0.04$, 0.06, and 0.10: a) mean flow velocity v, b) bed roughness σ_z, and c) bed slope S

or less constant for $S = 0.04$ and 0.06, while it decreased for $S = 0.10$ after $q = 0.10$ m^{2}s had been applied. The decrease in bed slope was related to erosion in the upstream and deposition in the downstream part of the flume (Figure A.12j).

Figure 5.7 shows the times series for q, q_s, and ΣQ_s of the R55 experiment conducted at bed slopes $S = 0.04$, 0.06, and 0.10. In the experiment with $S = 0.04$, the bed hardly changed for $q \leq 0.15$ m^2/s resulting in a total cumulative sediment outflow of $\Sigma Q_s < 160$ kg (i.e., $\Delta z/d_{84} \approx -0.5$) after the experiment was interrupted at $q = 0.15$ m^2/s (Figure 5.7a). In the corresponding experiment with bed slope $S = 0.10$ (Figure 5.7c), the overall bed elevation changes were more pronounced with $\Delta z/d_{84} \approx -1.5$, terminating the experiment after $q = 0.10$ m^2/s. Consequently, the experiment with $S = 0.04$ was more stable as almost no changes occurred. Much higher discharges were required to alter the bed significantly at milder slopes. According to Figure 5.7b (experiment with $S = 0.06$), the cumulative sediment outflow was $\Sigma Q_s = 348$ kg (i.e., $\Delta z/d_{84} \approx -1.1$, experiment interrupted after $q = 0.167$ m^2/s) being higher compared to the experiment with $S = 0.04$ but lower compared to the experiment with $S = 0.10$ (Figure 5.7c).
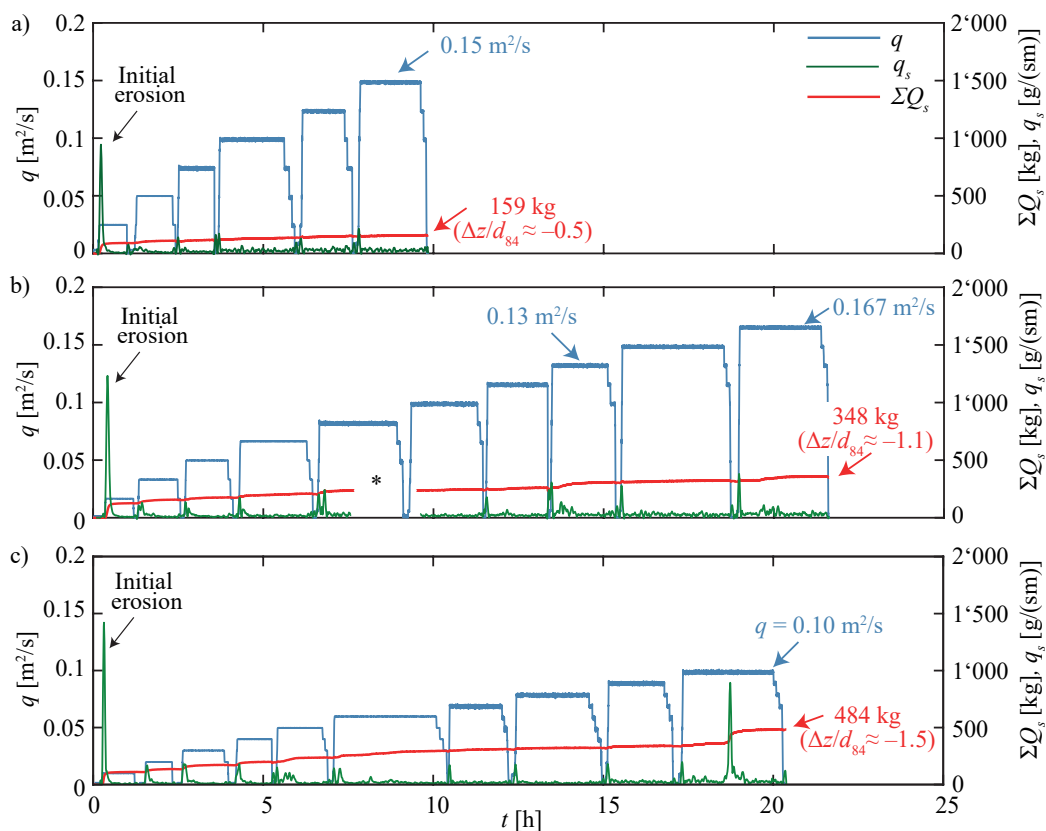

Figure 5.7 Effect of bed slope on the times series of experiments with sidewall type R55, $W/d_{84} = 5.6$; a) $S = 0.04$, b) $S = 0.06$ and c) $S = 0.10$; *data missing

Overall, the experiments conducted at different bed slopes demonstrated that much higher discharges were required to alter the bed in tests with moderate gradients (i.e., $S = 0.04$). Apparently, bed shear stress decreases with decreasing bed slope, i.e., the forces acting on the large grains were smaller.

Effect of jamming ratio

Experiment RR55 was additionally investigated in a wide channel ($W = 0.6$ m) for $S = 0.10$ increasing the jamming ratio W/d_{84} from 5.6 to 11.3. The cumulative sediment outflow at the end of the experiment, which was interrupted after $q = 0.08$ m²/s due to erosion to the flume invert, was $\Sigma Q_s = 1'157$ kg corresponding to $\Delta z/d_{84} \approx -1.8$ (Figure 5.8). The sediment yield in the wide channel was much higher compared to the corresponding experiment with RR55 in the narrow channel ($\Sigma Q_s = 312$ kg, i.e., $\Delta z/d_{84} \approx -1.0$ after $q = 0.10$ m²/s, Figure 5.5b). This indicates that bed stability decreases with increasing jamming ratio being consisted with the finding of Zimmermann *et al.* (2010).
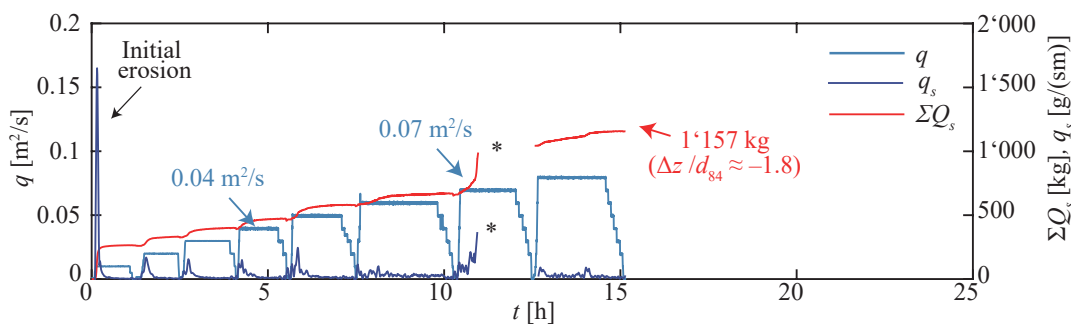

Figure 5.8 Times series of experiments with sidewall type RR55, $W/d_{84} = 11.3$, and $S = 0.10$; *data missing (corresponding experiment with $W/d_{84} = 5.6$ according to Figure 5.5b)

Summary of experiments with macrorough sidewalls

The most important effects of macrorough sidewalls on bed elevation changes, sediment outflow, and bed restructuring are:

- The maximum sediment outflow rate q_s, the cumulative sediment yield ΣQ_s, and the reach-averaged bed elevation changes $\Delta z/d_{84}$ decrease with increasing sidewall roughness.

- Much higher discharges are required to alter the bed in a channel with moderate bed slope ($S = 0.04$) indicating an increase in bed stability with decreasing bed slope.

- Sediment outflow rate q_s, cumulative sediment yield ΣQ_s, and the normalized bed elevation changes $\Delta z/d_{84}$ increase when jamming ratio W/d_{84} increases from 5.6 to 11.3 supporting the jammed state hypothesis by Zimmermann *et al.* (2010).

5.3   Effect of macrorough sidewalls on bed shear stress

Herein, the effect of macrorough sidewalls on flow resistance and bed shear stress in steep rough channels is investigated. Section 5.3.1 compares the total flow resistance observed in the experiments to approaches from literature. Section 5.3.2 classifies the macrorough sidewall flow into reattachment flow (RAF) and normal recirculating flow (NRF) to facilitate the subsequent analysis. A hydraulic geometry approach is extended with a parameter accounting for macrorough sidewalls enabling mean flow velocity estimation (Section 5.3.3). Finally, a commonly used sidewall correction procedure is modified to quantify the reduction in bed shear stress related to macrorough sidewalls (Section 5.3.4).

5.3.1   Total flow resistance

The overall flow resistance in steep channels with macrorough sidewalls is compared to approaches from literature. Figure 5.9a shows the friction coefficient $\sqrt{8/f}$ as a function of the relative submergence h/σ_z for the mobile rough bed (MR) experiments. The Darcy-Weisbach friction factor f was computed from the reach-averaged flow velocity measurements (Section 2.2). Flow resistance decreased, i.e., $\sqrt{8/f}$ increased, with increasing h/σ_z, particularly for smooth sidewall experiments (white squares), because the effect of the friction exerted by the rough bed diminished. Data from smooth sidewall experiments agreed well with the logarithmic approach proposed by Aberle and Smart (2003) (Equation (2.9)). However, the overall flow resistance was highly underestimated for rough sidewall experiments (Maager *et al.* 2020, 2022c). For the roughest sidewall types RR25, RR55, and RR55A in the narrow channel ($W = 0.3$ m), $\sqrt{8/f}$ even slightly decreased with increasing h/σ_z indicating that the majority of the friction exerted on the flow originated from the sidewalls and not the bed. Furthermore, flow resistance did not further decrease at $h/\sigma_z > 5$ in the experiments with moderately macrorough sidewalls (R55) and bed slopes $S = 0.04$ (green circles) and 0.06 (green diamonds). Thus, the effect of macrorough sidewalls was more pronounced in channels with milder gradients due to the higher aspect ratios h/W.
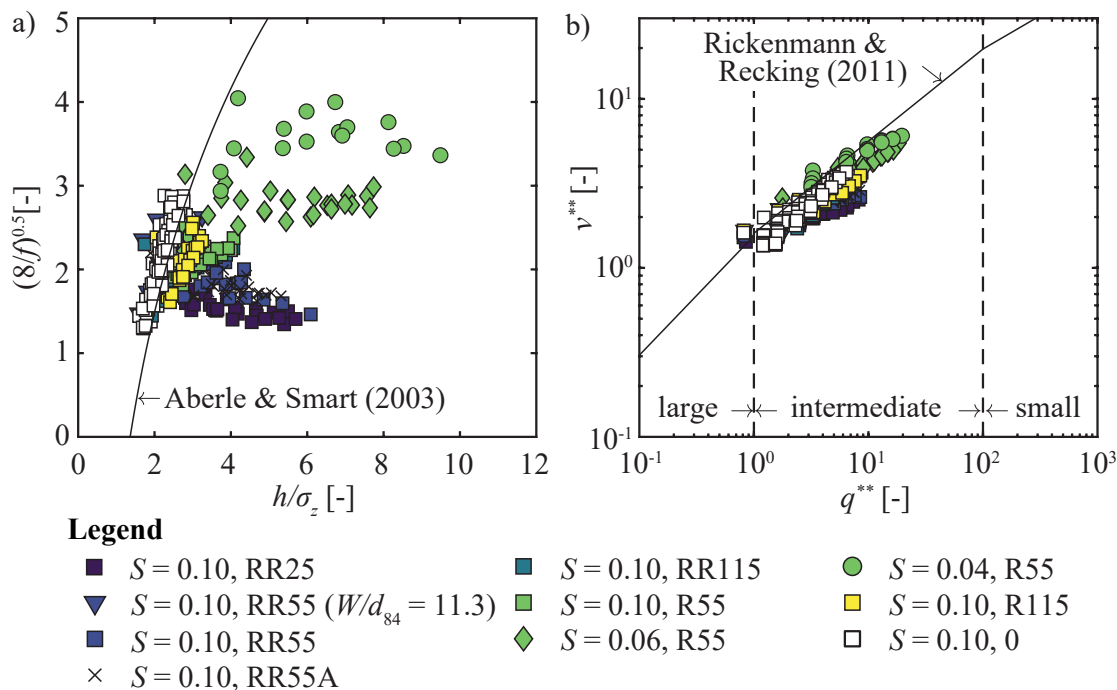
Figure 5.9 Effect of macrorough sidewalls on flow resistance. Mobile rough bed experiments (MR) for $W/d_{84} = 5.6$ unless stated differently: a) friction coefficient $\sqrt{8/f}$ as a function of the relative submergence h/σ_z compared to Equation (2.9) by Aberle and Smart (2003), b) comparison with dimensionless approach, i.e., Equations (2.14), (2.15) with $q^{**} \leq 1$: large, $1 < q^{**} < 100$: intermediate, and $q^{**} \geq 100$: small scale roughness (Rickenmann and Recking 2011)

Figure 5.9b compares data of the present study with the dimensionless approach by Rickenmann and Recking (2011) (Section 2.2.1). The majority of the data was assigned to intermediate scale roughness ($1 < q^{**} < 100$) and only few data at very low discharges were classified as large scale roughness ($q^{**} < 1$). In general, the data agree well with Equation (2.18) for intermediate scale roughness (Rickenmann and Recking 2011). However, the dimensionless flow velocity v^{**} tends to be overestimated for experiments with macrorough sidewalls. Consequently, an approach to account for the friction induced by macrorough sidewalls is developed in the following.

5.3.2 Classification of flow types

Meile *et al.* (2011) observed reattachment flow (RAF) and normal recirculating flow (NRF) regimes in flume experiments with macrorough sidewalls in smooth channels with small gradients (see Section 2.5). The flow reattached to the sidewalls in the RAF regime before reaching the downstream roughness elements leading to fully developed recirculating wakes. Flow resistance increased with increasing roughness density r/s as more energy dissipating wakes were present for higher r/s. In the NRF regime, the wakes were

limited by the downstream elements in case roughness density was further increased leading to a decrease in energy dissipation. This section demonstrates that these macrorough flow regimes are also applicable in steep rough channels.

Figure 5.10 shows the ratio v/v_0 as a function of the roughness density r/s, where v = reach-averaged flow velocity and v_0 = flow velocity corresponding to smooth sidewalls. The results from the fixed rough bed (FR) experiments (Figure 5.10a-b) and fixed smooth bed (FS) experiments (Figure 5.10c-d) are presented. As bed roughness was constant, the decrease in mean flow velocity was fully attributed to the friction exerted by the macrorough sidewalls. An increase in flow resistance is related with a decrease in flow velocity. Consequently, a minimum ratio v/v_0 is expected for roughness densities $r/s \approx 0.10$ to 0.15 following the concept of Meile *et al.* (2011). According to Figure 5.10a, v/v_0 reaches a minimum in between sidewall types RR55 and RR25 confirming the threshold value for r/s. Similarly, v/v_0 decreased for all investigated sidewall types in the R-series
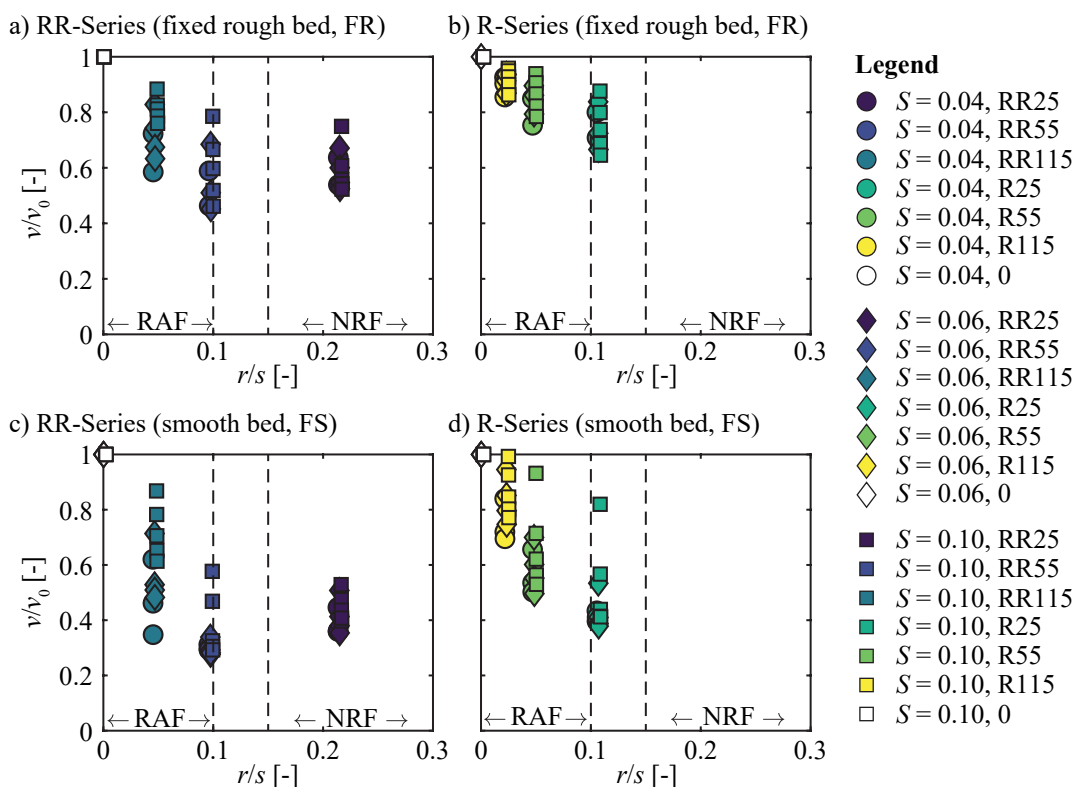

Figure 5.10 Classification of flow types. Ratio between the mean flow velocity v to the corresponding mean flow velocity with smooth sidewalls v_0 as a function of roughness density r/s for fixed rough bed (FR) experiments: a) RR-Series (r = 5.4 cm) and b) R-Series (r = 2.7 cm); and fixed smooth bed (FS) experiment: c) RR-Series, d) R-Series; RAF = reattachment flow type, NRF = normal recirculating flow type; $W/d_{84} = 5.6$ in all experiments

but no data points were obtained for $r/s > 0.15$. The same trend was observed in the experiments with a smooth bed, but, the decrease in v/v_0 was much more pronounced as the sidewalls were much rougher compared to the smooth bed. Based on these results, the sidewall types RR55, RR115, R55, and R115 were assigned to the RAF regime, RR25 was assigned to NRF and R25 was transitional. Consequently, the concept of RAF and NRF regimes for macrorough sidewalls is also valid in steep rough channels.

5.3.3 Mean flow velocity prediction

Steep mountain streams typically have macrorough banks but existing approaches to estimate mean flow velocity do not account for such sidewall roughness. Therefore, data from the mobile rough bed (MR) experiments were used to develop an equation for reach-averaged flow velocity. The hydraulic geometry approach (Equation (2.11)) was extended with the parameter b accounting for macrorough sidewalls:

$$v = c_1\, g^{\frac{1-m_1}{2}}\, S^{m_2}\, q^{m_1}\, k^{\frac{1-3\,m_1}{2}}\, (1 - c_2\, b) \tag{5.1}$$

where c_1, c_2, m_1, m_2 = coefficients, and $k = \sigma_z$ = bed roughness parameter. Ideally, the parameter b approaches zero for smooth sidewall conditions to enable an application to channels with both smooth and macrorough sidewalls. The most promising parameter combinations for b are the roughness density r/s, the relative sidewall roughness σ_w/W_m, and the product of relative sidewall roughness and relative submergence $(\sigma_w/W_m)\,(h/\sigma_z)$.

A regression analysis was conducted for the RAF flow types (RR55, RR115, R55, and R115) with $n_{RAF} = 309$ velocity estimates by bootstrapping $n = 1'000$ times resulting in the coefficients presented in Table 5.1. Therein, the coefficients' mean values are presented with the 95% confidence interval (CI) taken from the 1000 estimates being approximately normally distributed. The coefficient of determination R^2 and the root mean square error (RMSE) indicate the goodness of fit of each parameter set. Note that no regression analysis was conducted for the NRF flow regime due to the limited parameter range and the small sample size with $n_{NRF} = 29$.

The best result was obtained using $b = (\sigma_w/W_m)(h/\sigma_z)$ as sidewall roughness parameter (ID 3b) and using the same coefficients $m_1 = 0.60$ and $m_2 = 0.20$ as in Aberle and Smart (2003). The effect of the macrorough sidewalls was more pronounced for high relative submergence h/σ_z decreasing the RMSE. However, the resulting equation requi-

Table 5.1 Coefficients of Equation (5.1) obtained from a regression analysis; R^2 = coefficient of determination, RMSE = root mean square error; fixed coefficients in **bold**

ID	Parameter b	c_1	m_1	m_2	c_2	R^2	RMSE [m/s]
1	(r/s)	0.99 ± 0.11	0.44 ± 0.03	0.14 ± 0.05	1.5 ± 0.28	0.881	0.047
2a	(σ_w/W_m)	1.11 ± 0.13	0.48 ± 0.03	0.20 ± 0.06	3.75 ± 0.48	0.903	0.042
2b	(σ_w/W_m)	0.93 ± 0.02	**0.60**	**0.20**	4.94 ± 0.47	0.797	0.061
3a	$(\sigma_w/W_m)(h/\sigma_z)$	1.11 ± 0.05	0.49 ± 0.01	0.21 ± 0.03	1.08 ± 0.07	0.926	0.037
3b	$(\sigma_w/W_m)(h/\sigma_z)$	0.99 ± 0.01	**0.60**	**0.20**	1.37 ± 0.05	0.947	0.031
Reference		0.96	0.60	0.20	-	(Aberle and Smart 2003)	

res iterative solving and spurious correlation between flow velocity and flow depth might contribute to the increase in predictive power. Using the roughness density r/s (ID1) and relative sidewall roughness σ_w/W_m (ID2) instead, led to a similar result in terms of R^2 and RMSE. However, the predictive power decreased when keeping the coefficients m_1 and m_2 as proposed by Aberle and Smart (2003). Contrary to approaches 3a and 3b, the parameter b does not include flow depth to account for the wetted perimeter of the sidewalls. However, as the effect of rough sidewalls was more pronounced at high relative submergence, the coefficient m_1 adjusted instead, because of the correlation between h and q.

Herein, the approach 2a using $b = \sigma_w/W_m$ as a sidewall roughness parameter is presented in more detail because the standard deviation of the mean bank positions σ_w can be determined in the field for arbitrary bank shapes. Inserting the coefficients in Equation (5.1) leads to (Maager *et al.* 2022c):

$$v = 1.11\, g^{0.26}\, S^{0.20}\, q^{0.48}\, \sigma_z^{-0.22} \left(1 - 3.75\, \frac{\sigma_w}{W_m}\right) \tag{5.2}$$

Applying Equation (5.2) to channels with σ_z/W_m = 0.010, 0.025, and 0.050 reduces the mean flow velocity by 3.8, 9.4, and 18.8%, respectively. Equation (5.2) is restricted to the RAF regime and the following parameter ranges: $0.81 < q^{**} < 19.6$, relative submergence $1.7 < h/\sigma_z < 9.5$, $0.49 < h/d_{84} < 3.4$, aspect ratios $1.7 < W/h < 22.6$, relative sidewall roughness $\sigma_w/W_m < 0.052$, and Froude numbers $0.42 < F < 0.92$. It is worth pointing

out that the reach-averaged flow condition in mobile bed experiments, in which step-pool units formed, were subcritical to near-critical agreeing with the observation of others (e.g., Comiti *et al.* 2009a; Piton and Recking 2019).

Figure 5.11 shows the measured v_{meas} and calculated mean flow velocity v_{calc}. Equation (5.2) predicts v with a mean prediction error (PE) $\leq 8.1\%$ for all sidewalls types. However, the mean flow velocity in smooth sidewall experiments was over-predicted at low velocities by ~20% and under-predicted at high flow velocity by ~10%. This difference is related to the coefficient $m_1 = 0.48$ being lower compared to $m_1 = 0.60$ proposed by Aberle and Smart (2003). As previously discussed, this coefficient m_1 indirectly accounts for relative submergence for macrorough sidewalls. Thus, it is recommended to use Equation (2.13) by Aberle and Smart (2003) for smooth sidewall conditions despite the low mean PE = 7.3% of Equation (5.2).

Data extracted from Zimmermann (2009) and Comiti *et al.* (2009a), who conducted experiments in channels with rough sidewalls, were used for the validation of Equation (5.2). The former study comprises experiments with bed slope $S = 0.03$ to 0.11, mean channel widths $W_m = 0.245$ and 0.511 m, and relative sidewall roughness $\sigma_w/W_m \leq 0.09$, corresponding to measurement in Shatford Creek (Zimmermann *et al.* 2010). Estimates for v, σ_z, and S were digitized for test runs 4, 5, 6, 10, 11, 13, 14, 17, 18, 26, and 27 found
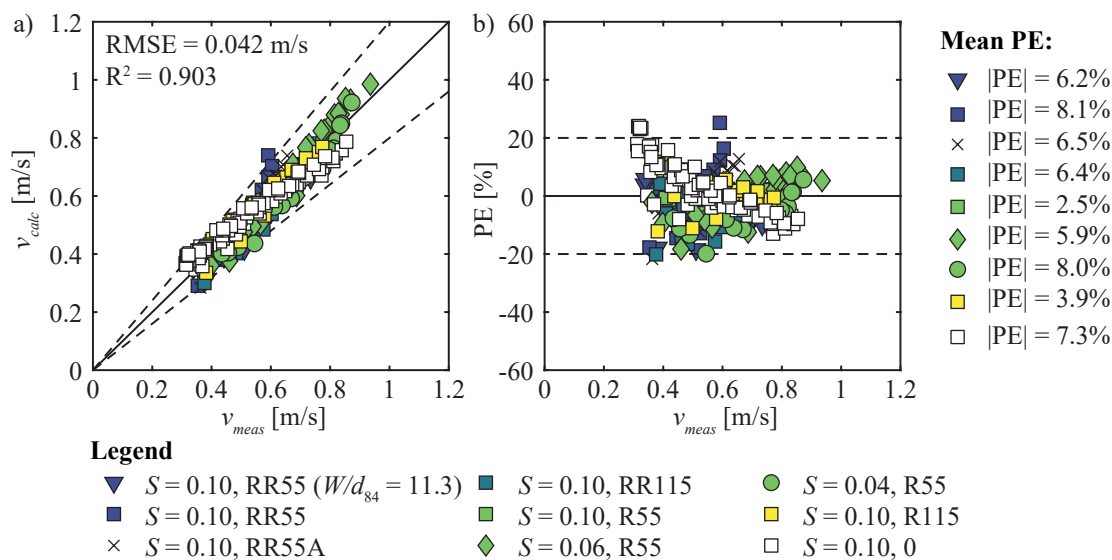

Figure 5.11 Mean-flow velocity estimation in steep channels with macrorough sidewalls ($W/d_{84} = 5.6$ unless stated differently): a) measured v_{meas} and calculated mean flow velocity v_{calc} with Equation (5.2) and b) corresponding prediction error (PE); solid line = perfect agreement, dashed lines: ±20% prediction error (PE) (modified after Maager *et al.* 2022c)

in the appendix of Zimmermann (2009). Comiti *et al.* (2009a) conducted experiments with large flat pebbles mounted to both sidewalls resulting in a standard deviation of the channel width of $\sigma_W \approx 0.040$ m. Assuming that the standard deviation of the bank deviations is equal to 0.5 σ_W results in $\sigma_w/W_m \approx 0.04$. This assumption implies that the banks are symmetric; σ_w/W_m may be slightly smaller in case the banks are not perfectly symmetric. The experiments were conducted for bed slopes $S = 0.08$ to 0.14 and a mean channel width $W = 0.46$ m.

According to Figure 5.12, the mean flow velocities were predicted with PE $\leq \pm 25\%$ when complying with the application range of Equation (5.2) demonstrating the applicability for more irregular types of sidewall roughness (natural banks, large boulders). The mean flow velocity may be under- and overestimated up to ±50% for data points outside of the application range. The mean flow velocity tends to be underestimated particularly in the narrow channel experiments by Zimmermann (2009) (white squares) likely associated with the slightly higher relative sidewall roughness compared to the present study.
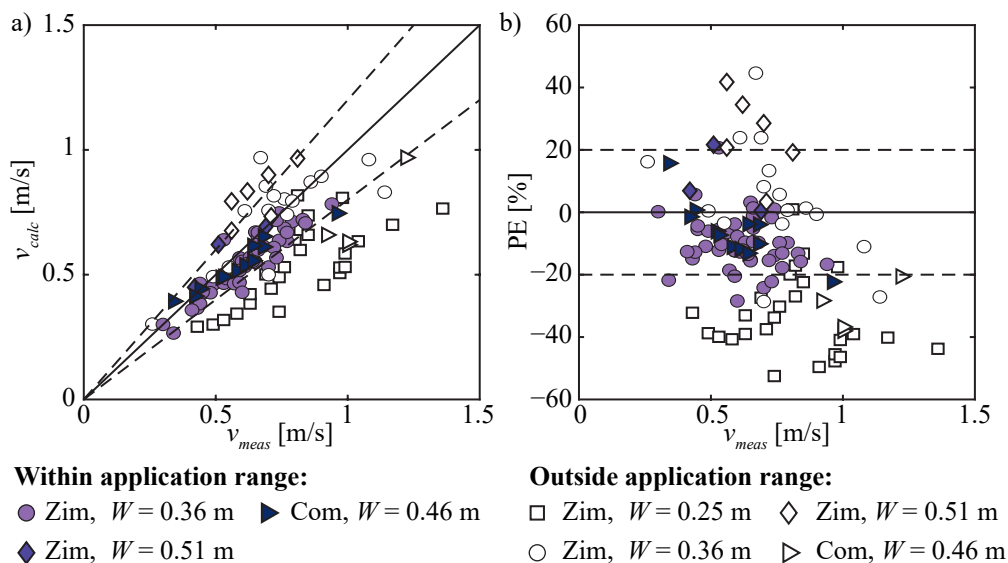

Figure 5.12 Validation of hydraulic geometry approach to estimate mean flow velocity. a) Measured v_{meas} and calculated mean flow velocity v_{calc} with Equation (5.2) for data of Zim = Zimmermann (2009), Com = Comiti *et al.* (2009a); b) corresponding prediction error (PE); solid line = perfect agreement, dashed lines: ±20% PE (modified after Maager *et al.* 2022c)

5.3.4   Bed shear stress estimation

Knowledge of the bed shear stress is important to assess bed stability. The present section addresses research question A1, which aims at quantifying the bed reduction in bed shear stress due to friction caused by different types of macrorough sidewalls (Sec-

tion 1.3). Therefore, the generalized Einstein-Johnson (GEJ) sidewall correction procedure was modified to account for resistance caused by macrorough sidewalls (Section 4.3.4). The modifications were divided into three main steps which are summarized in Figure 4.7. The effect of macrorough sidewalls was isolated by conducting flume experiments with constant bed roughness (fixed bed experiments). In Step 1, the hydraulic bed roughness was determined for the fixed bed experiments. In Step 2, an empirical equation was developed to estimate the sidewall friction coefficient f_w (i.e. $\sqrt{8/f_w}$) for macrorough sidewall flow as the bed friction coefficient f_b was known from step 1. The results were afterwards transferred to mobile bed experiments in which the bed could freely adjust to an increase in discharge. The empirical relation for sidewall friction ($\sqrt{8/f_w}$) enabled the determination of the resulting bed shear stress (Step 3).

Fixed bed experiments

Initially, the hydraulic bed roughness parameters $k_{b,FS}$ and $k_{b,FR} = \sigma_{z,FR}$ were determined for the experiments with smooth sidewalls with a fixed smooth bed (FS) and a fixed rough bed (FR) (Step 1 in Figure 4.7). An equivalent sand roughness for the smooth sidewalls had to be assumed (i.e., $k_w = 0.5$ mm). The GEJ sidewall correction procedure was then applied to obtain bed shear stress $\tau_{b,GEJ}$ (Section 4.3.4). The bed shear stress estimated with GEJ was compared to estimates of the FDM (i.e., $\tau_{b,h}$) representing the maximum bed shear stress and the HRM (i.e., $\tau_{b,R}$) representing a lower bound for bed shear stress (Section 2.3). According to Figure 5.13a, similar ratios $\tau_{b,R}/\tau_{b,h}$ and $\tau_{b,GEJ}/\tau_{b,h}$ resulted for the experiment with both smooth bed and sidewalls indicating that bed and sidewalls were comparably rough ($k_w = 0.5$ mm $\approx k_{b,FS}$). This was confirmed by using Equation (2.5) to determine the hydraulic bed roughness resulting in $k_{b,FS} = 0.44$ mm (± 0.09 mm). For this case, the sidewalls contributed approximately 5 to 30% to the shear stress depending on the aspect ratio h/W_m.

In case of a fixed *rough* bed (FR) and smooth sidewalls (Figure 5.13b), the sidewalls contributed to $\sim 10\%$ of the total friction for aspect ratios $h/W_m \approx 0.40$. This is reasonable as the rough bed exerted more friction compared to the smooth sidewalls (i.e. $k_w \ll k_{b,FR}$). Estimating the hydraulic roughness with Equation (2.9) of Aberle and Smart (2003) results in $k_{b,FR} = \sigma_{z,FR} = 12.3$ mm (± 1.6 mm) which compares well with $\sigma_{z,LDS} \approx 15$ mm from the LDS measurements. The slight underestimation may be due to the layer of cement covering the grains in the fixed bed slightly reducing surface roughness.
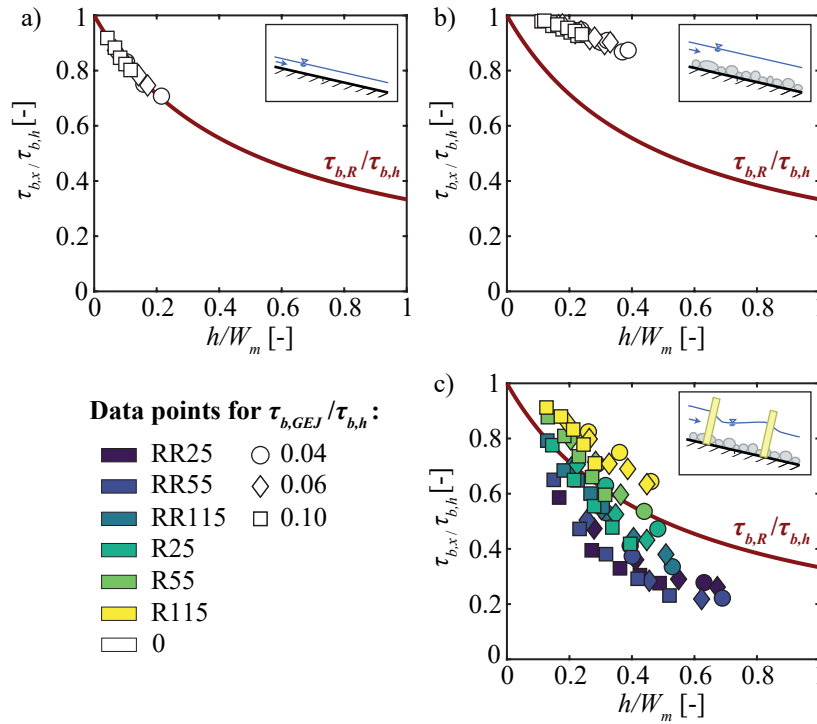
Figure 5.13 Bed shear stress estimation in steep channels with constant bed roughness. Bed shear stress $\tau_{b,R}$ (HRM) and $\tau_{b,GEJ}$ (GEJ) divided by maximum bed shear stress $\tau_{b,h}$ (FDM) for a) smooth sidewalls and a fixed smooth bed (FS), b) smooth sidewalls and a fixed rough bed (FR), c) macrorough sidewalls and a FR

The common sidewall correction procedure described in Guo (2015) cannot be applied to the sidewalls tested in the present study as k_w-values are not available from literature. The hydraulic bed roughness parameters previously obtained in Step 1 (i.e., $k_{b,FR} = \sigma_{z,FR}$) were used to estimate the bed friction factor f_b (Step 2, Figure 4.7). Afterwards, the sidewall friction factor was calculated using Equation (2.28). As a result, the sidewall friction amounted up to almost 80% of the total friction exerted on the flow in test runs with a fixed rough bed and macrorough sidewalls (RR25 and RR55, Figure 5.13c). The data points plot well below the HRM line indicating that the sidewalls were much rougher than the channel bed. For experiments with moderately rough sidewalls (e.g., R55 and R115), the HRM estimates still served as a lower boundary for bed shear stress. Consequently, bed and sidewalls were equally rough.

An empirical relation was developed to directly calculate the sidewall friction coefficient $\sqrt{8/f_{w,RAF}}$ for the RAF regimes (RR55, RR115, R55, and R115: $n_{RAF} = 44$):

$$\sqrt{\frac{8}{f_{w,RAF}}} = 0.24 \left(\frac{W_m}{\sigma_w}\right)^{0.64} \left(\frac{\sigma_w}{R}\right)^{-0.33} \tag{5.3}$$

with a coefficient of determination $R^2 = 0.925$ (Maager *et al.* 2022c). The friction factor $f_{w,RAF}$ increases with increasing relative roughness σ_w/W_m. Furthermore, a high relative submergence of the sidewall channels σ_w/R decreases flow resistance. The equation is restricted to the following parameter range: $0.81 < q^{**} < 20.1$, $1.7 < h/\sigma_z < 12.9$, $0.49 < h/d_{84} < 3.7$, $1.5 < W_m/h < 22.6$, $\sigma_w/W_m < 0.052$, and $0.37 < \mathsf{F} < 1.78$.

Mobile bed experiment (MR)

The results from the fixed bed experiments were transferred to mobile bed experiments (Step 3 in Figure 4.7), in which the bed could freely adjust to an increase in discharge, eventually forming step-pool sequences. The modified sidewall correction procedure was applied by first estimating the sidewall friction coefficient $\sqrt{8/f_w}$ with Equation (5.3), calculating the corresponding bed friction coefficient f_b with Equation (2.28), and finally computing the bed shear stress $\tau_{b,GEJ}$. Figure 5.14a shows the ratios $\tau_{b,R}/\tau_{b,h}$ and $\tau_{b,GEJ}/\tau_{b,h}$ for all investigated RAF sidewall types.

In contrast to the fixed bed experiments with macrorough sidewalls (Figure 5.13c), the estimates for $\tau_{b,GEJ}$ are equally large or larger than $\tau_{b,R}$ indicating that the channel sidewalls are similarly rough compared to the channel bed. Consequently, the HRM approximately serves as a lower boundary estimate for bed shear stress in mobile rough bed experiments with macrorough sidewalls. Note that also experiment RR25 belonging to the NRF type is presented applying Equation (5.3) as no reliable approach is available for the NRF regime due to the small sample size ($n_{NRF} = 9$ velocity estimates). The sidewall shear stress for RR25 tends to be overestimated because an increase in relative sidewall roughness σ_w/W_m did not lead to an increase in flow resistance in the NRF regime (Section 5.3.2). Consequently, the bed shear stress $\tau_{b,GEJ}$ was assumed to be underestimated in the RR25 experiments by applying this approach.

Overall, the macrorough sidewalls decreased bed shear stress by approximately 35 to 45% (Figure 5.14a) for sidewall types RR55 and RR55A (both $W = 0.3$ m) and aspect ratios $h/W_m \geq 0.3$. The decrease was less pronounced in the channels with sidewall types R115, R55, and RR55 ($W = 0.6$ m). Experiments R55 (green squares) and RR55 in the wide channel (blue triangles) had the same relative sidewall roughness $\sigma_w/W_m = 0.025$. The relative decrease in bed shear stress $\tau_{b,GEJ}/\tau_{b,h}$ was comparable indicating that Equation (5.3) provides consistent results for experiments with the same relative roughness but different channel widths.
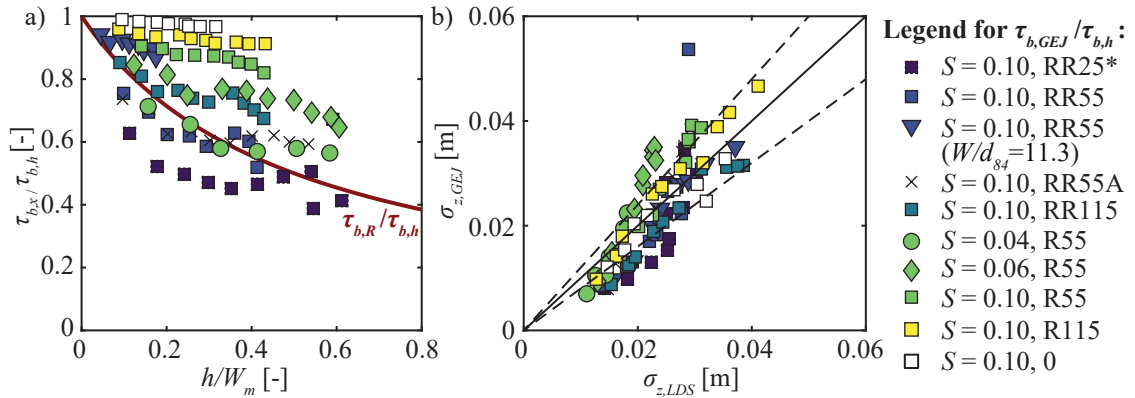
Figure 5.14 Bed shear stress estimation in steep channels with mobile rough beds. a) Bed shear stress $\tau_{b,R}$ (HRM) and $\tau_{b,GEJ}$ (GEJ) divided by maximum bed shear stress $\tau_{b,h}$ (FDM), b) comparison of the measured $\sigma_{z,LDS}$ and calculated from the GEJ sidewall correction procedure $\sigma_{z,GEJ}$ (dashed lines: ±20%), $W/d_{84} = 5.6$ unless stated otherwise, *NRF flow type: $\tau_{b,GEJ}$ tends to be underestimated

The relative decrease in bed shear stress $\tau_{b,GEJ}/\tau_{b,h}$ differed depending on the bed slope as macrorough sidewall friction was more pronounced the smaller the bed slope was. The flow depth was generally higher in channels with milder gradients. However, this effect is accounted for by presenting the $\tau_{b,GEJ}/\tau_{b,h}$ as a function of h/W_m. In addition to this effect, the bed was generally rougher in steep gradient channels (Figure 5.6b) thus exerting more friction to the flow. Consequently, the relative decrease in bed shear stress was less pronounced in steep channels compared to channels with moderate gradients.

To validate the application of the modified sidewall correction procedure, the bed roughness parameter $\sigma_{z,GEJ}$ was computed inserting f_b obtained from the GEJ procedure into Equation (2.9). The roughness parameter was then compared with the $\sigma_{z,LDS}$ obtained from the LDS measurements (Figure 5.14b). Similar bed roughness parameters are expected (i.e., $\sigma_{z,LDS} \approx \sigma_{z,GEF}$) if the sidewall friction factor $\sqrt{8/f_w}$ was well predicted with Equation (5.3). Indeed, a good agreement was obtained as most of the data lie within the ±20% boundaries expect for the experiments with milder gradients (green circles and diamonds) which are overestimated by up to ~30%. Thus, Equation (5.3) may underestimate sidewall friction in channels with milder gradients in particular for high aspect ratios $h/W_m \gtrsim 0.4$.

Bed roughness $\sigma_{z,GEJ}$ was underestimated in experiment RR25 (NRF) by applying Equation (5.3), as expected. Underestimating bed roughness indicates that sidewall friction was overestimated by applying the RAF approach to the NRF experiment. No independent data for different types of macrorough sidewalls were available for validation.

Nevertheless, Equation (5.3) was derived from fixed bed experiments and validated for mobile bed experiments being at least partly independent, i.e., validation data originated from different experimental test setups, albeit in the same flume and with the same instrumentation.

5.3.5 Implications on bed stability assessment

Knowledge of bed shear stress is crucial to assess bed stability. Research question A1 focused on the quantification of bed shear stress in steep channels with macrorough sidewalls (Section 1.3). It was hypothesized that the bed shear stress decreases significantly due to sidewall friction, thereby at least partly explaining the observed increase in bed stability. The following results support this hypothesis:

- Sidewall shear stress accounted for 70 to 80% of the total shear stress at high flow stages (i.e., $h/W_m > 0.4$, Figure 5.13c) for the roughest sidewall types RR25, RR55, and RR55A investigated in a channel with a fixed rough bed.

- The share of sidewall friction was less pronounced in mobile bed experiments, accounting for 35 to 45% in RR55 and RR55A for $h/W_m > 0.4$ (Figure 5.14a). It was related to the emerging step-pool units leading to an increase in bed roughness and therewith to an increase of friction induced by the channel bed.

- The relative reduction in bed shear stress in channels with macrorough sidewalls primarily depends on the relative sidewall roughness σ_w/W_m, the aspect ratio h/W_m, and to a lesser degree on the relative bed roughness σ_z/h.

For the first time, the modified sidewall correction approach developed herein enables the estimation of bed shear stress in steep rough streams with macrorough sidewalls. The approach was validated with different sidewall roughness types comprising natural bankline variations and large boulders (Figure 5.12). The estimation of bed shear stress in step-pool channels with macrorough sidewalls advances on long standing questions of how steps form and how much load they can withstand by allowing to untangle hydraulic and granular controls on step frequency, formation, and stability as detailed in the next section.

5.4 Effect of macrorough sidewalls on step occurrence and stability

The overall bed stability was assessed using bed elevation changes as a proxy for bed stability. The bed is considered stable when bed elevation changes were small (Section 4.3.3). Moreover, the step frequency was analyzed for the macrorough sidewall types investigated in the present study (Section 5.4.2). Section 5.4.3 compares the geometric relations of the step-pool units to relations from literature. As previous studies demonstrated, steps are assumed to form more frequently in narrowing regions (Zimmermann *et al.* 2010; Golly *et al.* 2019; Saletti and Hassan 2020). These steps in the narrowing regions may even be more stable due to the interlocking of the large step-forming grains and the rough sidewalls. Consequently, steps located in the narrowing sections were assumed to substantially influence the overall morphology and bed stability. Section 5.4.4 analyses step location and Section 5.4.5 elaborates on the stability of steps located in narrow and wide regions of the flume. These results are finally used to address research question A2 (Section 1.3) quantifying the contribution of hydraulic and granular controls to an increase in bed stability in step-pool streams with macrorough sidewalls (Section 5.5).

5.4.1 Overall bed stability

Zimmermann *et al.* (2010) found sediment transport rates q_s to be an indicator for bed stability (Section 3.3.4). Local bed adjustments were associated with small q_s (class 1 and 2 disturbances) and progressive upstream erosion (PUE) patterns entirely restructuring the channel bed with high q_s (class 3 disturbance). Herein, sediment outflow rates were highest in smooth sidewall experiment with $q_s = 1'200$ to $1'800$ g/(sm). On the contrary, experiments with macrorough sidewall were associated with generally lower sediment outflow rates $q_s \leq 850$ g/(sm) (Section 5.2.3). However, using q_s as an indicator for bed stability has certain limitations. Major bed elevation changes clearly lead to an increase in q_s but local changes may not appear as an increase in q_s, particularly when the test reach is long and the eroded sediment deposits in the lower reach (Section 5.2.2). Thus, the DEM of differences (DoD) are evaluated using the high resolution DEM obtained with SfM photogrammetry (Section 4.5.2).

Figure 5.15 shows the DoD (i.e., $\Delta z/d_{84}$) for all investigated sidewall types for the interval during which the maximum sediment output rates $q_{s,max}$ were measured at the flume outlet (Figure 5.5). The bed elevation changes occurred more locally (i.e., $\Delta x/W < 3 \dots 5$)

for rougher sidewall types (e.g., RR25, RR55, and RR55A, Figure 5.15a-c). The maximum bed elevation changes (defined by 1st and 99th percentile of $\Delta z/d_{84}$) ranged from $\Delta z/d_{84} = -1.5$ to 1.0 indicating that grains with diameter up to $1.5\ d_{84} \approx 0.08$ m, corresponding to the largest fraction used in the present study (Figure 4.4), were mobilized at least locally. However, the reach-scale changes expressed by the median $\Delta z/d_{84} = -0.03$ to -0.06 were in the range of the uncertainty quantified in Section 5.2.2 (i.e., $\Delta z/d_{84} \pm 0.05$). Thus, the reach-averaged bed elevation changes were small implying exceptionally sta-

a) RR25, after $q = 0.05$ m²/s, $q_{s,max} \approx 400$ g/(sm)

b) RR55, after $q = 0.08$ m²/s, $q_{s,max} < 100$ g/(sm)

c) RR55A, after $q = 0.07$ m²/s, $q_{s,max} \approx 200$ g/(sm)

d) RR115, after $q = 0.07$ m²/s, $q_{s,max} \approx 550$ g/(sm)

e) R55, after $q = 0.10$ m²/s, $q_{s,max} \approx 850$ g/(sm)

f) R115, after $q = 0.06$ m²/s, $q_{s,max} \approx 300$ g/(sm)
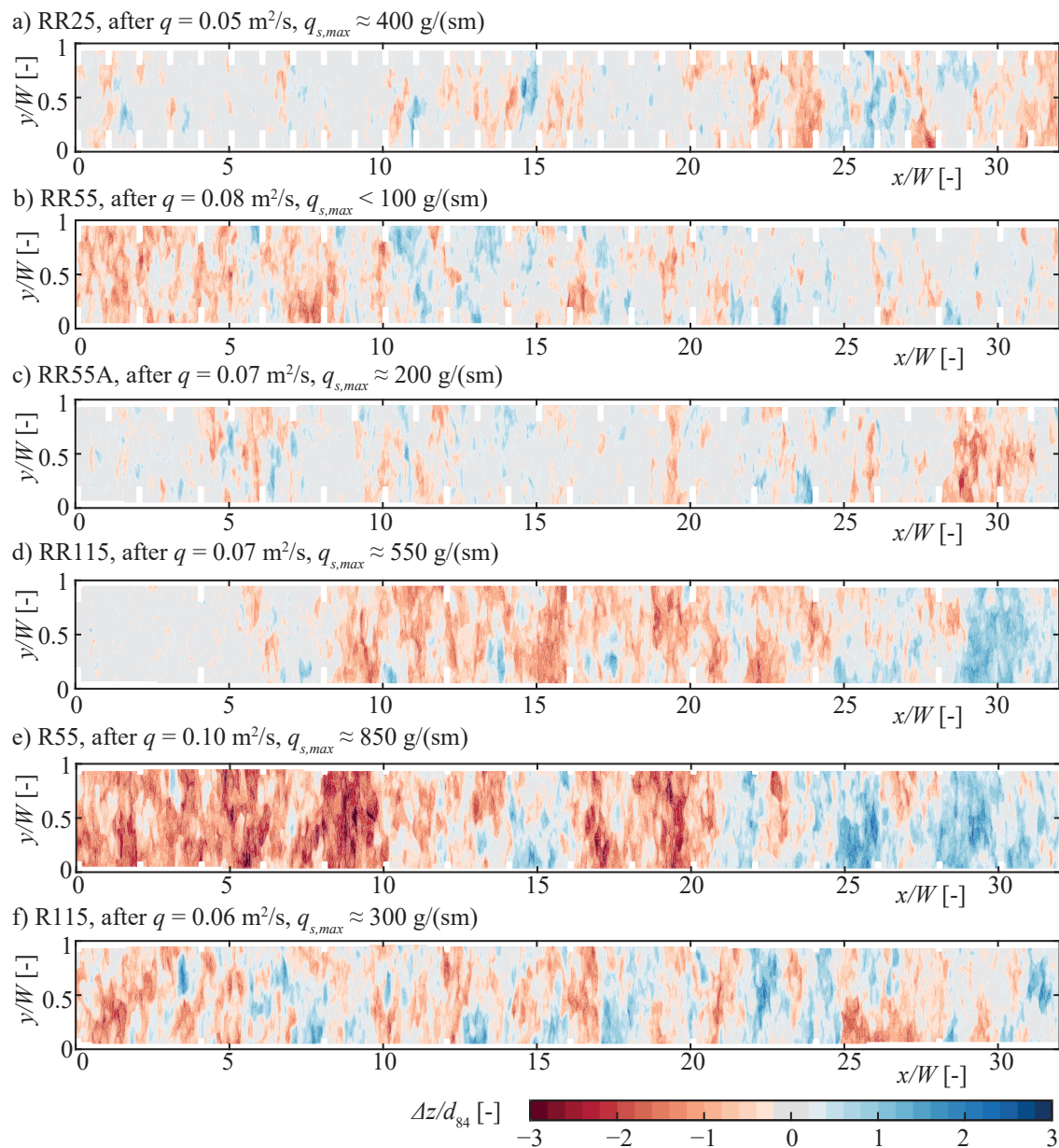
Figure 5.15 Bed elevation changes $\Delta z/d_{84}$ for rough sidewall experiments after maximum sediment outflow was observed ($q_{s,max}$) for a) RR25, b) RR55, c) RR55A, d) RR115, e) R55, and f) RR115; y-axis is exaggerated ~3.5 times; roughness elements are indicated by white rectangles

ble beds in experiments RR25, RR55, and RR55A. For instance, considering experiment RR25 (roughest sidewall type, Figure 5.15a), the bed erosion occurred mainly at the downstream end of the flume ($x/W \geq 20$ to 25) whereas bed elevation changes were less pronounced in the upstream part ($x/W \leq 20$). The PUE pattern (as observed for smooth sidewall experiments, Figure 5.2) was interrupted as some large boulders jammed immediately upstream in the narrowing section of the roughness elements at $x/W = 20$.

In the moderately rough experiments RR115, R55, and R115 the bed elevation changes expanded over large sections (i.e., $\Delta x/W > 5...10$) or even over the entire test reach (Figure 5.15d-e). The maximum bed elevation changes (defined by 1st and 99th percentile of $\Delta z/d_{84}$) ranged from $\Delta z/d_{84} = -2.5$ to 1.6 indicating that steps consisting of multiple blocks were mobilized as $2.5\ d_{84} = 0.13$ m $> d_{max}$. The median value was as small as $\Delta z/d_{84} = -0.50$ indicating bed degradation. Consequently, the bed in experiments with moderately sidewall roughness (RR115, R55, and R115) were less stable compared to RR25, RR55, and RR55A. Appendix A.2.1 shows the bed elevation changes of all mobile bed experiments for each interval.

So far, the bed elevation changes $\Delta z/d_{84}$ were analyzed for a single interval without differentiating erosion and deposition patterns. Figure 5.16 shows $\Delta z_{ero}/d_{84}$ = reach-averaged (cumulative) erosion and $\Delta z_{dep}/d_{84}$ = reach-averaged (cumulative) deposition evaluated after each interval. The reach-averaged (cumulative) bed elevation changes are defined as $\Delta z/d_{84} = (\Delta z_{ero} + \Delta z_{dep})/d_{84}$. The quantities are plotted as a function of unit stream power qS and dimensionless bed shear stress θ_b using d_{84} as a characteristic grain diameter (Equation (2.30)). The latter accounts for the sidewall roughness as the bed shear stress decreased in experiments with macrorough sidewalls (Section 5.3.4). According to Figure 5.16a, $\Delta z_{ero}/d_{84}$ was lowest for the smooth sidewall experiment in the narrow channel ($W/d_{84} = 5.5$) and the experiment with sidewall type RR55 in the wide channel ($W/d_{84} = 11.3$). Erosion volumes generally decreased as sidewall roughness increased. A similar trend was observed for the volumes deposited, even though the differences were less pronounced (Figure 5.16b). Consequently, the differences in cumulative bed elevation changes $\Delta z/d_{84}$ were smaller compared to the volumes eroded but the trend was still the same. These results support the finding that the smooth sidewall experiments were the least stable experiments together with the experiment in the wide channel with sidewall type RR55 (i.e., a small relative sidewall roughness).
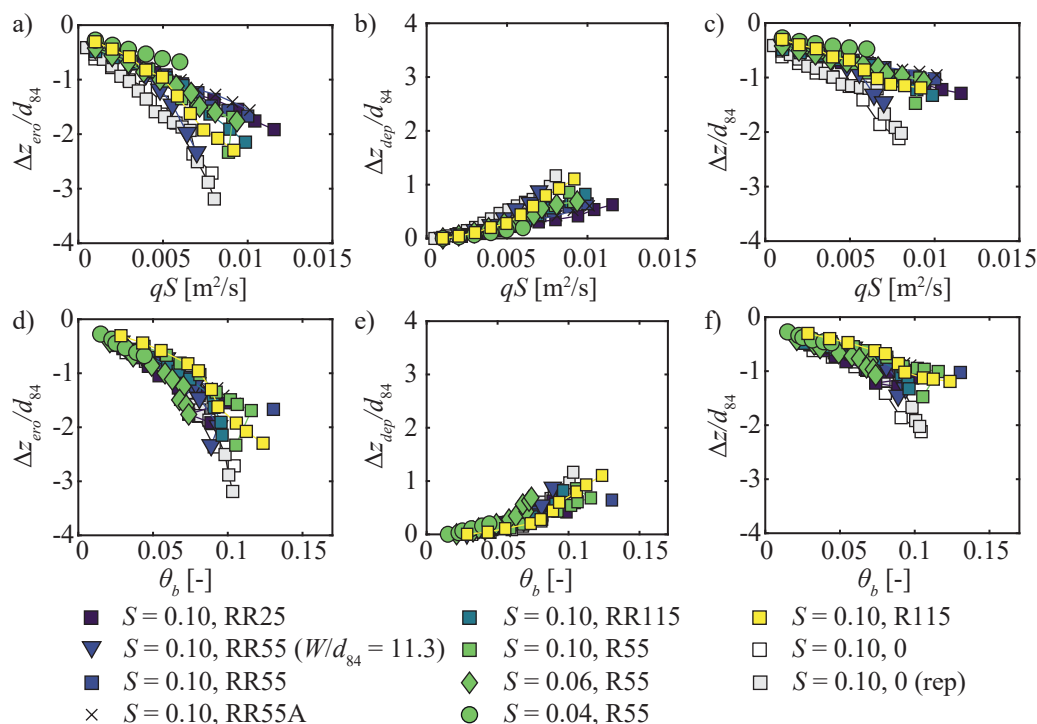
Figure 5.16 Cumulative bed elevation changes in experiments with macrorough sidewalls. $\Delta z_{ero}/d_{84}$, $\Delta z_{dep}/d_{84}$ = cumulative bed elevations changes due to erosion and deposition; $\Delta z/d_{84}$ = $(\Delta z_{ero} + \Delta z_{dep})/d_{84}$ = bed elevation changes as a function of a)-c) unit stream power qS and d)-f) dimensionless bed shear stress θ_b. All tests for W/d_{84} = 5.6 unless indicated otherwise.

Relating erosion and deposition patterns and the resulting bed degradation to θ_b results in less pronounced differences for $\theta_b \lesssim 0.08$ (Figure 5.16d-f). This implies that at least some of the increase in bed stability is attributed to hydraulic effects as the friction exerted by the macrorough sidewalls reduced bed shear stress therefore inhibiting grain mobilization (i.e., erosion, deposition, and overall degradation). However, at high $\theta_b \gtrsim 0.08$, the volumes corresponding to $\Delta z_{ero}/d_{84}$ and $\Delta z/d_{84}$ were smaller for the roughest sidewall types RR25 and RR55 indicating that granular effects like sidewall-grain interlocking of large blocks forming stable steps may become important at these conditions and further increase bed stability.

Furthermore, the erosion and deposition patterns allow conclusions on the degree of restructuring, i.e., particle activity. Particle activity is high when large parts of the flume are affected by either erosion, deposition, or both. The highest particle activity was clearly observed in the smooth sidewall experiments and it decreased with increasing sidewall roughness. The lowest particle activity was observed in experiment with sidewall type RR25, RR55, and RR55A and for experiments in the channels with milder gradients S = 0.06 and 0.04 and sidewall type R55.

To conclude, the overall bed stability increased in experiments with macrorough si-dewalls confirming the results of Zimmermann *et al.* (2010). However, contrary to the conclusion of Zimmermann *et al.* (2010), the approach to estimate bed shear stress (Section 5.3.4) allowed to identify that this increase was at least partly attributed to hydraulic effects. This is demonstrated by the data collapse of the erosion and deposition patterns when bed shear stress was used as an indicator instead of unit stream power. However, the hydraulic effects could not fully explain the increase of bed stability when bed shear stress was high, in particular for the roughest sidewall types RR25 and RR55. Granular effects related to grain-grain and grain-sidewall interlocking may further contribute to the increase of bed stability for the roughest tested sidewalls and conditions were large boulders are frequently mobilized. Therefore, the frequency and stability of the detected step-pool units are analyzed in the following to get further insights on these granular effects.

5.4.2 Step frequency

Figure 5.17 shows step frequency n as a function of the unit stream power qS and the dimensionless bed shear stress θ_b, respectively. Step frequency n is the number of steps observed in the channel reach divided by the total reach length L_{tot} = 9.6 m. The Pearson's correlation coefficient p_{pear} is a measure for linear correlation of two variables with p_{pear} = ±1 indicating perfect correlation (positive or negative) and p_{pear} = 0 indicating
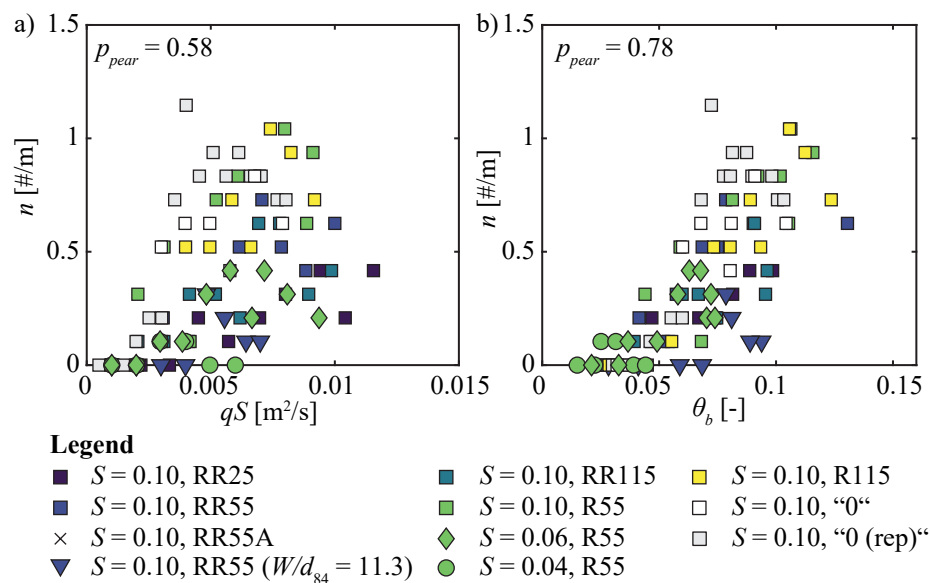

Figure 5.17 Step frequency n of all steps detected in the mobile bed experiments as a function of a) unit stream power qS and b) dimensionless bed shear stress θ_b; p_{pear} = Pearson's correlation coefficient, all tests for W/d_{84} = 5.6 unless indicated otherwise

zero correlation. The coefficient p_{pear} increases from 0.58 to 0.78 using θ_b instead of qS. Consequently, bed shear stress was a better predictor for step frequency as the effect of macrorough sidewalls is accounted for. Sidewall roughness was an important indirect control on step frequency, as fewer steps emerged related to the decrease in bed shear stress.

Figure 5.18 presents step frequency n for each sidewall type as a function of θ_b. The maximum step frequency observed was a function of the sidewall type, bed slope, and jamming ratio. The following paragraphs elaborate on the effect of macrorough sidewalls, bed slope, and jamming ratio. Moreover, the maximum step frequency is related to the critical Shields ratio θ_b/θ_c.

Effect of macrorough sidewalls

The maximum step frequency was observed in the smooth sidewall experiments with n_{max} = 0.8 to 1.1 steps per unit length (i.e., 8 to 11 steps in the 9.6 m long test reach, Figure 5.18f), followed by the moderately rough sidewall types R55 and R115 with n_{max} = 1 step per unit length (Figure 5.18d-e). Fewer steps emerged in the experiments of the RR-Series with the roughest sidewalls. The maximum step frequency observed in the RR-
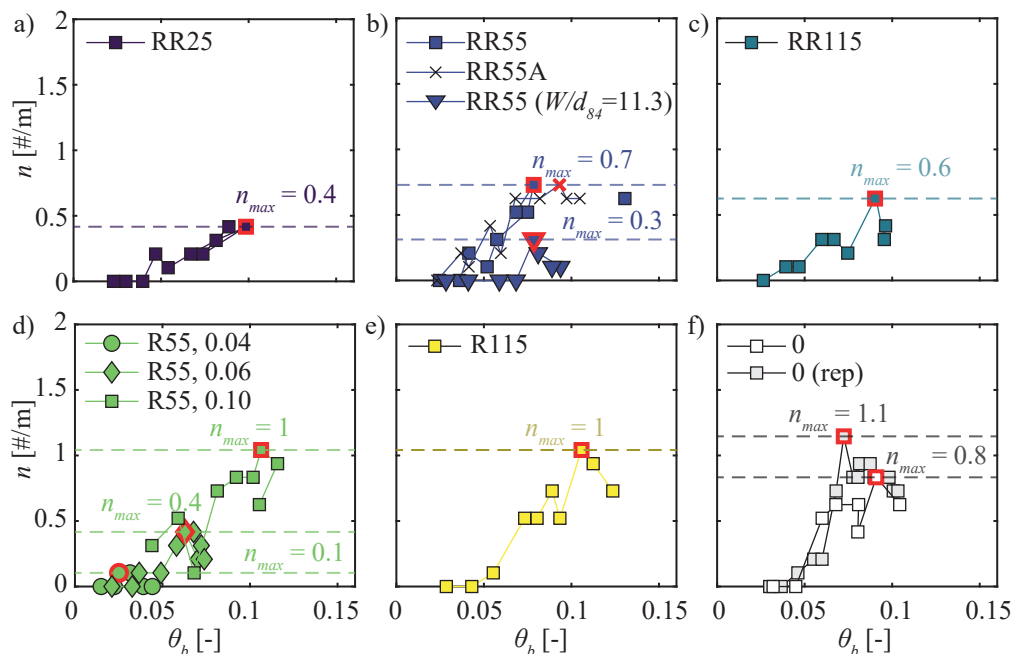
Figure 5.18 Step frequency n as a function of bed shear stress θ_b in the narrow channel (W/d_{84} = 5.6) and for bed slope S = 0.10 unless stated differently; a) RR25, b) RR55 and RR55A, c) RR115, d) R55, e) R115, f) smooth sidewalls; red markers: maximum number of steps n_{max}

Series was n_{max} = 0.7 and 0.6 steps per unit length for sidewall types RR55 and RR115, respectively (Figure 5.18b-c). The fewest steps were detected in the experiment with the roughest sidewall (RR25) with n_{max} = 0.4 step per unit length (Figure 5.18a).

A priori, more steps were expected to form in rough sidewall experiments because the narrowing sections of the roughness elements were assumed to trigger step formation. However, the opposite applied as step frequency was lowest in experiment RR25, i.e., with the roughest sidewalls. Particle activity was lowest in the RR-Series (Figure 5.16), i.e., the cumulative volumes eroded and deposited were small presumably due to the comparably small bed shear stress. Step-pool formation requires large enough θ_b resulting in the mobilization of the large boulders to trigger step-formation in the narrowing section. Consequently, step formation was inhibited as these large boulders remained immobile. This effect may be reinforced as stable steps located in the narrowing sections further limit particle activity (and thus step formation) by interrupting the progressive upstream erosion (PUE) pattern (Section 5.2.2). This effect is detailed in the subsequent Section 5.4.5.

Effect of bed slope and jamming ratio

Moreover, step frequency decreased with decreasing bed slope resulting in n_{max} = 0.4 and 0.1 for S = 0.06 and 0.04, respectively (Figure 5.18d). Bed shear stress in channels with moderate gradients may not be sufficiently high to mobilize the step-forming blocks, i.e., for step formation. These latter findings are in agreement with field observations, where isolated steps were observed in streams with bed slopes higher than ~0.04 and continuous step-pool sequences in streams with bed slopes exceeding ~0.07 (e.g., Whittaker and Jäggi 1982; Montgomery and Buffington 1997; Chin 1999; Church and Zimmermann 2007; Comiti and Mao 2012). Furthermore, fewer steps were detected in the wide channel (W/d_{84} = 11.3) with n_{max} = 0.3 steps per unit length (Figure 5.18b). This supports the jammed state hypothesis by Zimmermann (2010) stating that step formation is more likely in channels with W/d_{84} < 6.

Maximum step frequency

The bed was partly or fully restructured due to a progressive upstream erosion (PUE) pattern in most experiments except for RR25, RR55, and RR55A (Section 5.2.2). During these bed restructuring events, steps were destroyed and new steps formed. However, step frequency decreased after such an event resulting in a maximum step frequency observed

at a certain θ_b. In experiments with bed slope $S = 0.10$, the maximum step frequency n_{max} was observed at $\theta_b = 0.089 \pm 0.013$. This corresponds to the critical Shields parameter $\theta_c = 0.084$ calculated with Equation (2.42) by Lamb *et al.* (2008). The maximum step frequency was observed at $\theta_b = 0.063$ to 0.070 for the experiment with $S = 0.06$ which is also in the range of $\theta_c = 0.074$ predicted by Lamb *et al.* (2008). Consequently, the self-organizing step-pool systems evolve towards a state of maximum step frequency which is attained at Shields ratios $\theta_b/\theta_c \approx 1$.

Summary on step frequency

The main findings regarding step frequency in step-pool systems with macrorough sidewalls are summarized in the following:

- Bed shear stress θ_b accounting for macrorough sidewall friction is a better predictor for step frequency compared to unit stream power (Figure 5.17).

- Step formation requires the mobilization of the step-forming blocks. The decrease in bed shear stress related to macrorough sidewalls inhibits the mobilization of these large blocks. Consequently, step frequency decreases with increasing sidewall roughness (Figure 5.18).

- Step frequency decreases with decreasing bed slope confirming field observations. Bed shear stress may not be sufficiently high to mobilize the step-forming blocks, i.e., to trigger step formation.

- Step frequency decreases with increasing jamming ratio supporting the jammed state hypothesis.

- The self-organizing step-pool systems evolve towards a state of maximum step frequency which was attained at $\theta_b/\theta_c \approx 1$.

These finding contribute to a better understanding of step formation processes in steep rough channels with macrorough sidewalls.

5.4.3   Step geometry

This section presents the geometry of the steps detected with the automatized rule-based step-pool detection algorithm (Section 4.6) and compares them to literature. Figure 5.19 shows the normalized mean step height H_m/d_{84} with H = vertical distance between

step crest and the deepest point in the scour hole (Figure 4.21). Furthermore, the normalized mean step length L_m/W_m is presented with L_m = horizontal distance between the ToS and EoP determined by the algorithm (Figure 4.21). In addition to step height and step length, the steepness ratio $H_m/(L_m S)$ is shown in Figure 5.19.

The parameters H_m/d_{84}, L_m/W_m, and $H_m/(L_m S)$ are presented separately for the smooth sidewall experiments, the macrorough sidewall experiments, and the experiment with different bed slopes. In the smooth sidewall experiments, the relative step height increased from $H_m/d_{84} = 1$ to ~2 as bed shear stress θ increased. Similarly, Chin (1999) and Ashida et al. (1984) found the drop height H_d to be in the range of the mean grain diameter of the armour layer (Equations (3.3) and (3.4)). The average normalized step length ranged from $L_m/W_m \approx 1$ to 2 but smaller and larger ratios in the range of $L/W_m = 0.5$
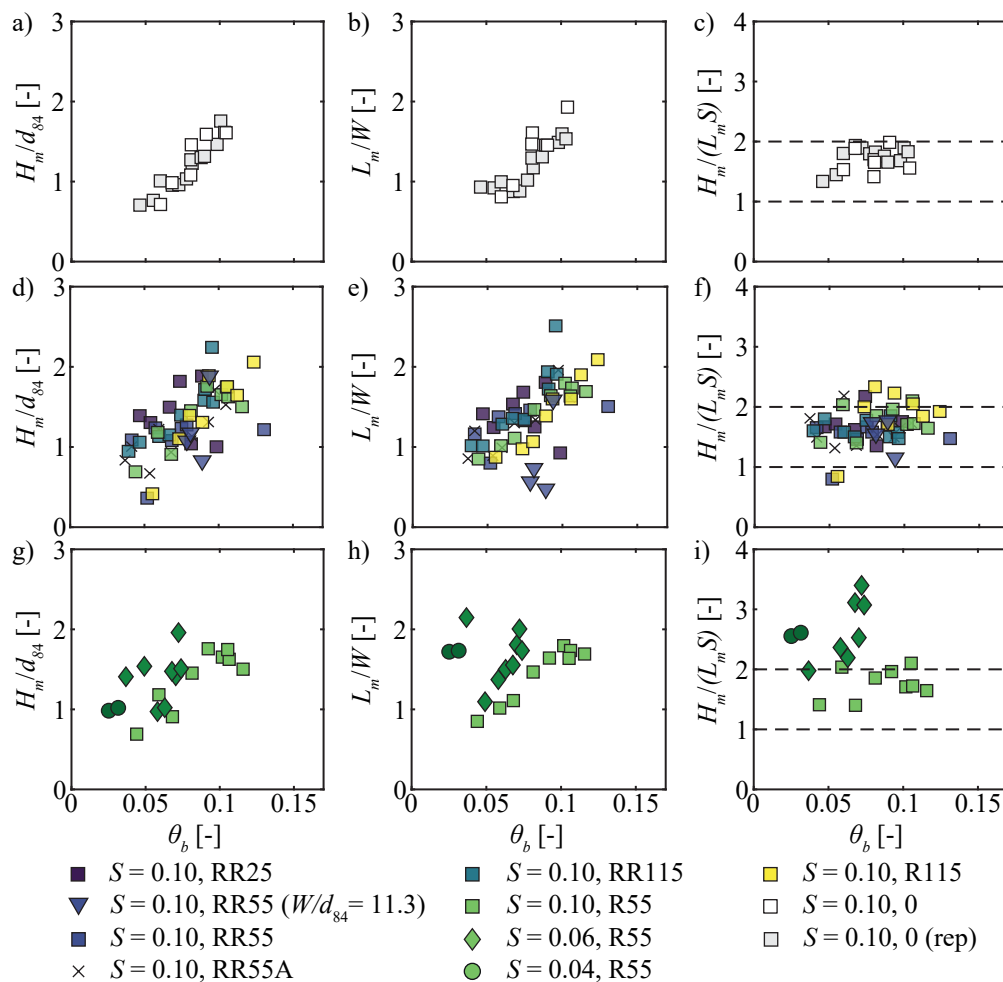
Figure 5.19 Normalized step height H_m/d_{84}, step length-to-width ratio L_m/W_m, and corresponding steepness ratio $H_m/(L_m S)$ as a function of Shields ratio θ/θ_c for a)-c) smooth sidewalls, d)-f) macrorough sidewalls, and g)-h) sidewall type R55 with S = 0.04, 0.06, and 0.10; W/d_{84} = 5.6 unless stated otherwise, dashed lines: steepness ratio according to Abrahams et al. (1995)

to 2.5 were obtained for individual steps. Note that the detection algorithm only allowed ratios $L/W < 3$. However, the L_m/W_m ratios of the detected step-pool units were in line with the findings by Chin *et al.* (2009) and Okazaki *et al.* (2006), who both evaluated field studies and found $L/W = 1$ to 4 and $L/W = 1$ to 2, respectively. Finally the obtained steepness ratios $H_m/(L_m S)$ ranged from approximately 1.25 to 2 which agrees well with the findings by Abrahams *et al.* (1995) who hypothesized that the bed evolves towards a state of maximum flow resistance which is the case for steepness ratios between 1 and 2.

A similar trend was observed in the rough sidewall experiments (Figure 5.19d-f). The geometric relations of experiments with bed slope ranging from $S = 0.04$ to 0.10 (Figure 5.19g-i) agree well with literature. However, the steepness ratios $H_m/(L_m S)$ were slightly higher for $S = 0.06$ and 0.04 than for $S = 0.10$. This result is in agreement with other studies, which found the steepness ratio to increase in channels with bed slopes below 0.05 to 0.07 (Wohl *et al.* 1997; Chartrand and Whiting 2000; Zimmermann and Church 2001; Comiti *et al.* 2005). To conclude, the geometry of the step-pool units, detected with the automatized step-pool detection algorithm, are in line with literature and macrorough sidewalls had no significant effect on step-pool geometry.

5.4.4   Step location

Prior to assessing step stability, the step locations in the NAR = narrow and WID = wide regions of the flumes are assessed (Section 4.3.5). Previous studies demonstrated that steps more likely formed in narrow or narrowing regions as the constrictions caused by the roughness elements triggered step formation (Zimmermann *et al.* 2010; Golly *et al.* 2019; Saletti and Hassan 2020). Following Saletti and Hassan (2020), the share of steps detected in the NAR region n_{NAR}/n is compared to the share of the area assigned to the narrowing region A_{NAR}/A with $A =$ total flume area. Steps are more frequent in the NAR region if $n_{NAR}/n > A_{NAR}/A$ and, vice versa, more frequent in WID regions if $n_{NAR}/n < A_{NAR}/A$. Note that only tests with $n \geq 3$ steps were considered in the analysis.

Figure 5.20 plots n_{NAR}/n and A_{NAR}/A for the sidewall types in which at least three steps have been identified. The RR-Series consisted of roughness elements with thickness $r = 5.4$ cm leading to local constrictions of $(2 r)/W = 36\%$, i.e., local jamming ratios of $(W - 2 r)/d_{84} = 3.6$. The R-Series have roughness elements with $r = 2.7$ cm constricting the flume by 18%, i.e., $(W - 2 r)/d_{84} = 4.6$. The dashed lines in Figure 5.20 represent A_{NAR}/A and the markers indicate the share of steps n_{NAR} located in the NAR region.
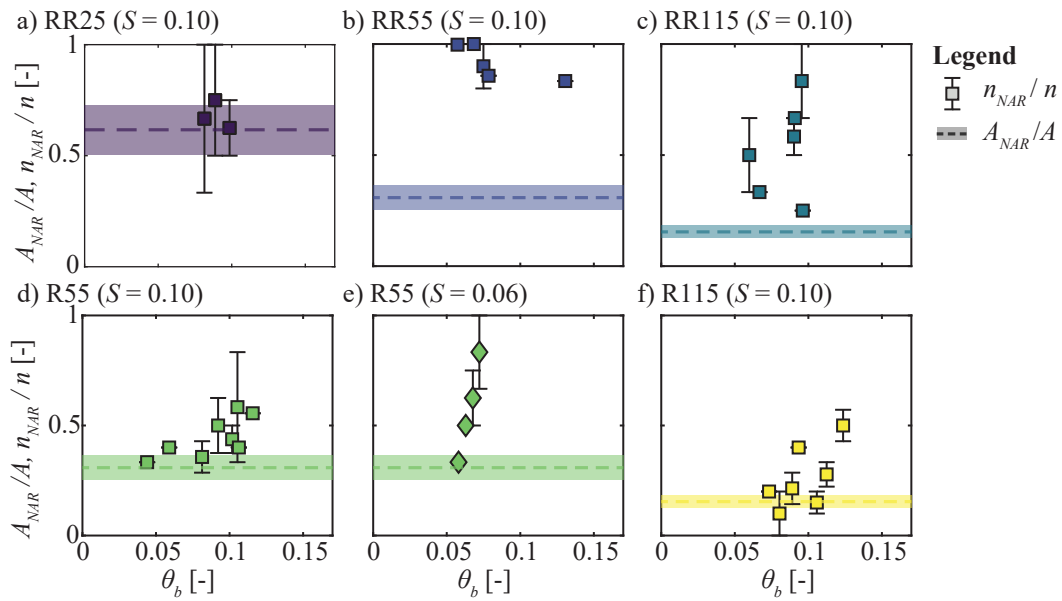
Figure 5.20 Share of steps in the NAR = narrowing region n_{NAR}/n as a function of θ_b compared to the share of the narrowing area A_{NAR}/A for sidewall types a) RR25, b) RR55, c) RR115, d) R55, e) R55 ($S = 0.06$), and f) R115; $S = 0.10$ unless stated differently

The shaded areas and the error bars originate from a sensitivity analysis of the parameters defining the NAR regions (Section 4.3.5). Steps were more likely to form in the NAR regions if the markers plot above the lines and the steps are randomly distributed in case of $n_{NAR}/n \approx A_{NAR}/A$.

According to Figure 5.20a, the steps were randomly distributed in the roughest sidewall experiment RR25. However, more than 80% of the steps were located in the NAR region in experiment RR55 even though only ~30% of the total area corresponded to the NAR region. The same applied to experiment RR115. Hence, steps more likely formed in the NAR region for the RR-Series experiments with an element spacing $s > 55$ cm, i.e. $s/W_m \gtrsim 2$. The steps were more randomly distributed in the R-Series as $n_{NAR}/n \approx A_{NAR}/A$ for sidewall types R55 and R115 during intervals with small bed shear stress ($\theta_b < 0.08$). However, the steps were more likely to form in the NAR regions when bed shear stress increased. The steps in the NAR region were either more stable and persistent while the steps in the WID section collapsed or the mobilized large grains preferentially formed new steps in the NAR region. These results support the jammed state hypothesis by (Zimmermann *et al.* 2010). Moreover, steps being located in the NAR regions are hypothesized to be more stable compared to steps located in the WID regions which is investigated in the subsequent section.

5.4.5 Step stability

Step stability was assess by comparing bed shear stress increments $\Delta\theta_b$ sustained by the steps. Detecting a step at the same locations during two subsequent intervals does not necessarily imply that this step persisted as a new step might have formed at the same location. Thus, the persistence of a step over subsequent intervals was visually confirmed using the 3D model and orthomosaic photos generated by Structure from Motion (SfM).

The probability distribution is presented for the increase in bed shear stress $\Delta\theta_b$ (Figure 5.21). The dashed lines show the maximum increase in bed shear stress $\Delta\theta_b = 0.025$ sustained by the reference experiment with smooth sidewalls. According to Figure 5.21, only few steps in the RR55 and RR115 experiment sustained much higher bed shear stress of $\Delta\theta_b \leq 0.055$ which were all located in the NAR region. Furthermore, experiment RR25 contained a single step being similarly stable but located in the WID region. However, the roughness elements were only spaced 0.25 m apart and the jamming effects of the grains with b-axis up to 0.09 m may still interact with the downstream elements even though they were assigned to the WID region. Overall, these results indicate that the increase in
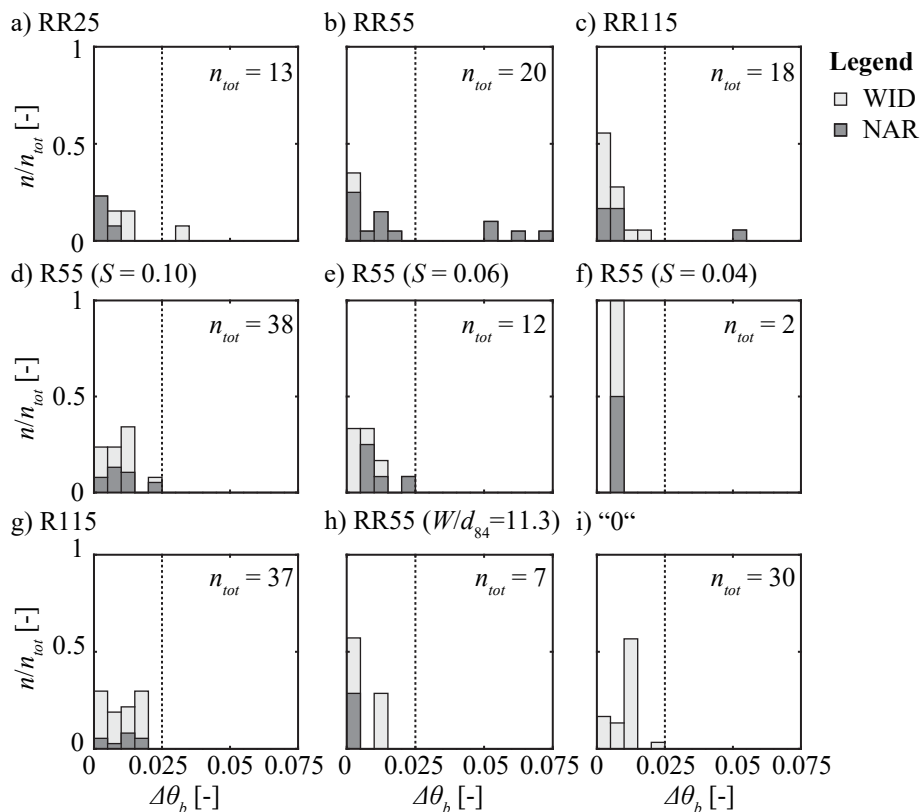
Figure 5.21 Probability distribution of bed shear stress increments $\Delta\theta_b$ sustained by each step, n_{tot} = total number of steps formed, $S = 0.10$ and $W/d_{84} = 5.6$ unless stated differently

bed stability in the R-Series was fully explained by the decrease in bed shear stress due to sidewall friction, i.e., hydraulic controls. However, interlocking of the step-forming grains with the roughness elements likely increased step stability in the RR-Series experiments, i.e., granular controls led to the formation of a few extremely stable steps that potentially increased the stability of the whole test reach. The role of hydraulic and granular effects contributing to bed stability in steep streams with macrorough sidewalls is elaborated in the following section.

5.5 Hydraulic versus granular controls in step-pool reaches

Herein, results regarding the effect of macrorough sidewalls on flow resistance, bed stability, particle activity, and step stability are summarized with a focus on the role of hydraulic and granular effects contributing to an increase in bed stability. Bed stability increased in channels with rough sidewalls as sediment outflow rates, cumulative sediment yield, and the bed elevation changes generally decreased with increasing sidewall roughness. Furthermore, the progressive upstream erosion (PUE) pattern completely restructuring the entire channel bed was only observed in the smooth sidewall experiment and the experiment with moderate sidewall roughness (R-Series).

Zimmermann (2010) attributed this increase in bed stability to granular effects, i.e., the interlocking of the step-forming grains with the rough sidewalls. However, no sidewall correction procedure was applied for steep rough channels with macrorough sidewalls and the effect of sidewall friction reducing bed shear stress was not accounted for. The present study provided a modified sidewall correction procedure to estimate bed shear stress in steep rough channels with macrorough sidewalls. This novel approach enabled untangling hydraulic and granular effects in their contribution to the increase in bed stability. The effect of *hydraulic controls* is supported by the fact that:

- The share of sidewall friction accounted for 5 and 40% of the overall shear stress in mobile bed experiments with macrorough sidewalls (Figure 5.14).

- Bed shear stress θ_b estimated with the novel sidewall correction procedure was a better predictor for step frequency than unit stream power which does not account for sidewall friction (Figure 5.17).

- Fewer steps emerged in the RR-Series experiments related to the reduction in bed shear stress (Figure 5.18).

- The self-organizing step-pool systems evolved towards a state of maximum step frequency, which was attained at $\theta_b/\theta_c \approx 1$ (Figure 5.18).

- Steps in the R-Series experiments did not sustain higher bed shear stress increments $\Delta\theta_b$ compared to smooth sidewall experiments indicating that the increase in bed stability was fully related to hydraulic effects (Section 5.4.5).

The following findings support the assumption that the increase in bed stability is related to *granular controls*:

- The steps in the RR-Series experiments preferentially formed in the narrow regions (Figure 5.18) and some of these steps were able to sustain significantly higher bed shear stress increments (Figure 5.21).

- The steps in the R-Series experiments were randomly distributed at when bed shear stress was low but step frequency increased in the narrow region at high bed shear stress (Figure 5.20).

- Step frequency decreased with increasing jamming ratio W/d_{84} from 5.6 to 11.3 (Section 5.4.2) supporting the jammed state hypothesis.

Overall, hydraulic effects fully explained the increase in bed stability in the experiments with moderately rough sidewalls (R-Series, $\sigma_w/W_m \leq 0.035$). However, granular effects played a major role in the RR-Series experiments ($\sigma_w/W_m > 0.035$), i.e., the roughest sidewall configurations, where jamming created a small number of very stable steps that had an effect on the entire test reach. The present study demonstrates for the first time that macrorough sidewalls are an important indirect control for step formation and stability highly affects the step-pool morphology in steep mountain streams. The sidewall correction procedure allowed to identify bed shear stress as the key driver for step frequency, dominating the overall number and stability of steps. Contrary to the initial expectations, step frequency negatively correlates with sidewall roughness, i.e., step frequency decreased with increasing sidewall roughness. Step formation requires mobilization of the large step-forming blocks. One the one hand, macrorough sidewalls reduce the bed shear stress inhibiting the entrainment of these large step-forming blocks. On the other hand, the local constrictions of the macroroughness elements ($(2\,r)/W = 36\%$ leading to local jamming ratios $(W - 2r)/d_{84} = 3.6$) triggered the formation of extraordinary stable steps

located in the narrowing sections. These stable steps interrupted the PUE pattern contributing to an increase in bed stability. These extraordinary stable steps were not observed for local constrictions in the R-Series of 18%, i.e., local jamming ratios $(W - 2r)/d_{84}$ = 4.6, i.e., the PUE was observed in these experiments. Nevertheless, the experiments highlighted that the global jamming ratio was an important parameter apart from the local jamming ratio or local channel constrictions inducing step formation. Comparing experiment RR55 in the wide channel (W/d_{84} = 11.3) and experiment R55 in the narrow channel (W/d_{84} = 5.6) with the same relative sidewall roughness σ_w/W = 0.025 shows that fewer steps emerge in globally wider channels, i.e., supporting the jammed state hypothesis by Zimmermann (2010).

These results advance the understanding of step formation and stability in that they demonstrate that i) hydraulic effects explain a large part of the observed increase in bed stability for rough sidewalls and ii) granular effects become important for strong local constrictions and may lead to the formation of a few extraordinarily stable steps, rather than increasing the stability of many steps by a little.

6 Artificial step-pool systems

Parts of this chapter have been published in:

- *Maager* et al. *(2022b): „Effect of discharge variations and sediment supply on the scour development and stability of artificial step-pool sequences", proceedings of the 39th IAHR World Congress in Granada, Spain.*

6.1 Overview

This chapter summarizes the main findings of the experiments with artificial step-pool sequences. Section 6.2 presents general observations and Section 6.3 focuses on hydraulics of step-pool channels. Section 6.4 classifies the observed failure mechanisms, elaborates on the frequency of occurrence of each failure type, and describes gradual and abrupt system failures. Three discharge regimes were tested (Section 6.5) to quantify the effect of hydrograph shape and duration on stability and geometry of artificial step-pool units. Section 6.6 summarizes the main findings regarding bed stability focusing on the effect of sediment supply, bed slope, channel width, base material, step-forming block size, drop height, block configuration, and placement density. Subsequently, Section 6.7 discusses bed adjustment mechanisms at different spatial scales. Finally, Section 6.8 compares the geometric relations of artificial step-pool systems to existing relations and proposes a novel equation to estimate mean step height in artificial step-pool systems. All measures are indicated in prototype scale ($\lambda = 20$) unless stated differently as this part addresses practitioners primarily.

6.2 General observations

Experiments SF0 and SF2 (Table 4.9) are used to describe general observations during experiments with artificial step-pool sequences. The SF0 experiment was conducted under clear-water (CW) conditions and experiment SF2 with sediment feed (SF), i.e., 0 and 20% of the transport capacity (TC) was supplied, respectively. They were both conducted with bed slope $S = 0.06$, channel width $W = 6$ m, and using sediment mixture M64 with $d_{84} = 0.18$ m. The BASE step-pool configuration (Figure 4.11) was tested with mean block weight $M_B = 4.6$ t, drop height $H_d = 0.75$ m, resulting in a step spacing of $L_d = 12.4$ m. Figure 6.1 shows the temporal evolution of the unit discharge q, the unit sediment feed rate $q_{s,in}$, and sediment outflow rate $q_{s,out}$. The highest $q_{s,out}$ was observed at the beginning of the first interval (i.e., initial erosion). The base material was immediately eroded

exposing the step-forming boulders as the artificial step-pool units were initially covered with the base material to flatten the bed.

In the CW experiment SF0 (Figure 6.1a), bed erosion related to the increase in scour depth mainly occurred during the ascending limb of the hydrographs shortly before and after peak flow was reached. Partial or complete failure of one or several steps resulted in an increase in sediment transport. However, the eroded material was not necessarily transported to the flume outlet as it was partially deposited in the subsequent pools. Consequently, minor bed elevation changes did not appear as an increase in $q_{s,out}$. Step failures leading to a considerable decrease in bed slope clearly appeared as an increase in $q_{s,out}$, e.g., at $q = 6.67$ m^2/s in the SF0 experiment.

During the sediment supply experiment SF2 (Figure 6.1b), the sediment inflow rate $q_{s,in}$ was in the same range as $q_{s,out}$ indicating that most of the sediment supplied was transported through the entire test reach. A small lag between $q_{s,in}$ and $q_{s,out}$ was observed during the first two sediment supply intervals, implying sediment deposition in the
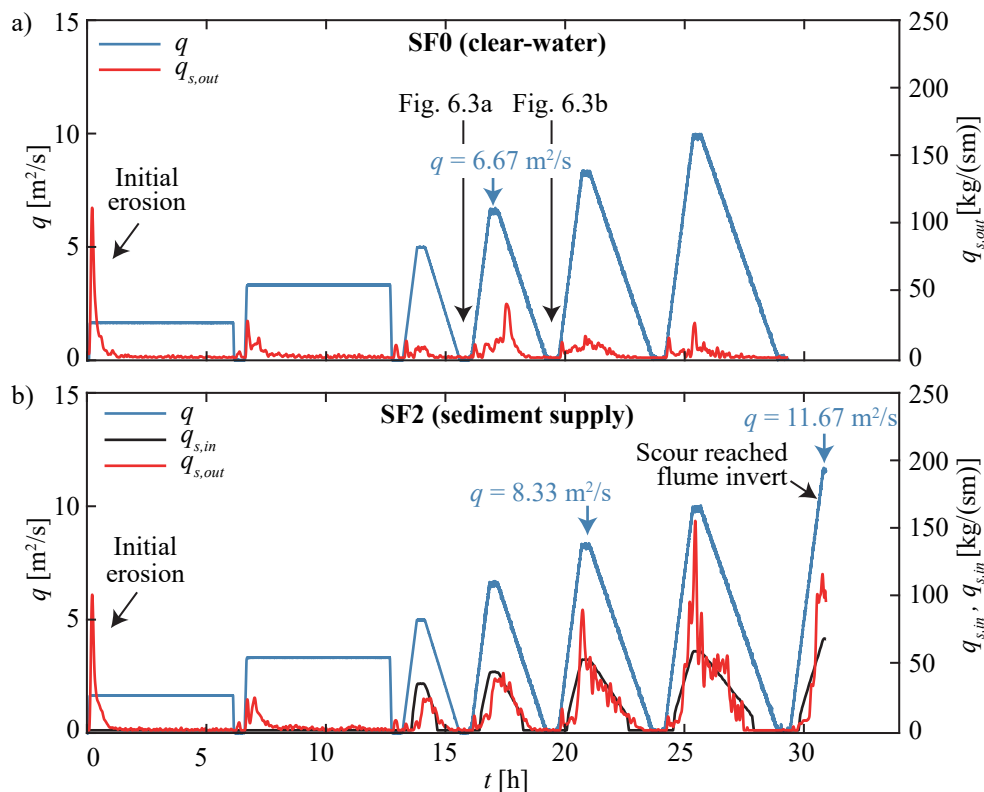
Figure 6.1 Time series of unit discharge q, unit sediment inflow rate $q_{s,in}$, and unit sediment outflow rate $q_{s,out}$ for experiment a) SF0: clear-water (CW) conditions and b) SF2 with ~20% sediment feed (SF)

test reach during the ascending limb. Similar to the CW experiment, local bed elevation changes did not increase the sediment outflow rate substantially. Sediment outflow rates $q_{s,out} > q_{,in}$ indicated that either one or several steps were partly or fully destroyed. Experiment SF2 was terminated during the peak flow $q = 11.67$ m^2/s as the scour depth reached the flume invert.

Figure 6.2 shows the decrease of the reach-averaged bed slope $\Delta S = S - S_{ini}$ and the Shields ratio θ/θ_c, defined by Equation (4.7), as a function of q. Experiment SF2 was terminated during the interval with $q = 11.67$ m^2/s and the red markers qualitatively show the expected decrease in ΔS and θ/θ_c. The bed slope S remained close to the initial bed slope S_{ini} up to $q_{stab} = 5.0$ and $q = 10.0$ m^2/s for experiments SF0 and SF2, respectively. Afterwards, the collapse of several steps led to a decrease $\Delta S = S - S_{ini} < -0.01$ at $q_f(1\%) = 6.67$ and 11.67 m^2/s, respectively. This discharge is referred to as critical discharge in terms of system failure (Section 4.4.5). The Shields ratio θ/θ_c increased with increasing discharge and reached a maximum value $(\theta/\theta_c)_{max}$ at q_{stab} (i.e., $(\theta/\theta_c)_{max} \approx 4$ to 6 for experiments SF0 and SF2, respectively). Note that d_{84} of the base material was used to calculate θ. Consequently, the bed material of experiments SF0 and SF2 sustained approximately 4 to 6 times higher bed shear stresses owing to the artificial step-pool units, consisting of blocks with diameter $D_{eq}/d_{84} \approx 7$ to 8.

Figure 6.3 shows orthophotos of the bed for experiment SF0 after discharge $q = 5.00$ and 6.67 m^2/s had been applied. One of the middle blocks in step VI tilted in flow direction but remained in the step during the interval with $q = 5.00$ m^2/s (Figure 6.3a). During the subsequent interval $q = 6.67$ m^2/s, two out of four blocks in the top row tilted into the
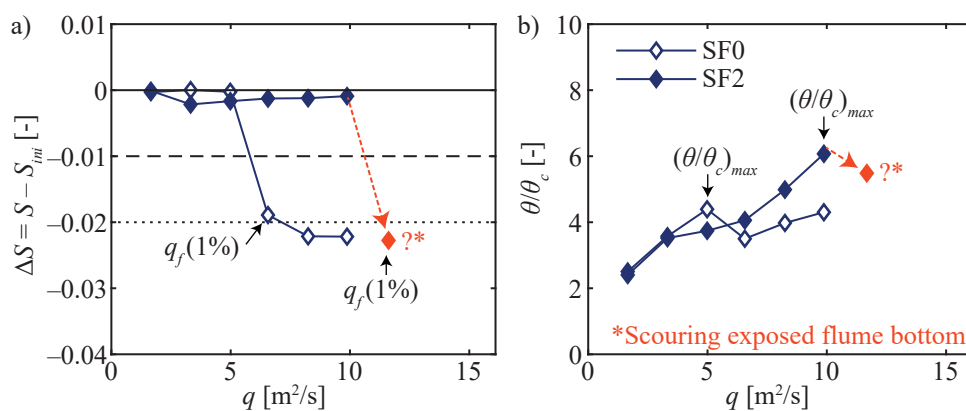

Figure 6.2 Bed adjustment to increasing discharge and increase in shear stress: a) decrease in bed slope $\Delta S = S - S_{ini}$ as a function of q; b) Shields ratio θ/θ_c as a function of q; SF0 = clear-water and SF2 = ~20% sediment supply
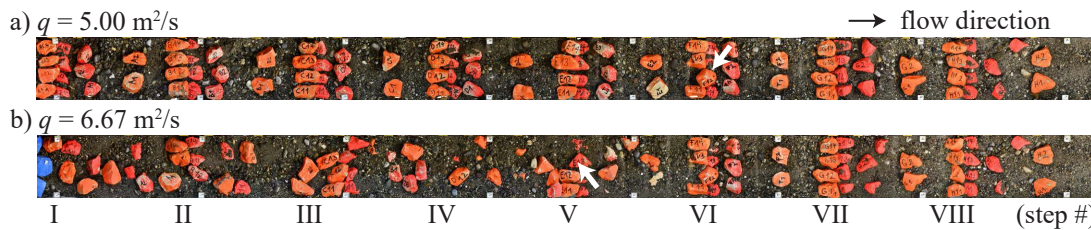
Figure 6.3 Destruction of the regular step-pool sequence during experiment SF0 (clear-water). Orthophotos of bed after a) $q = 5.00$ m^2/s and b) $q = 6.67$ m^2/s. Numbers indicate step locations, arrows the initial failures

downstream pool shortly after the peak discharge was reached. As a consequence, the upstream pool of step V further expanded and the scour depth increased leading to the destruction of step IV. This erosion pattern propagated upstream destroying steps III to I and is referred to as progressive upstream erosion (PUE). This erosion pattern was also observed in self-organizing step-pool systems (Figure 5.2). The PUE is described in more detail later in Section 6.4.2. The result was a block carpet with little resemblance with the initial, well-organized step-pool system (Figure 6.3b). These changes led to a decrease in bed roughness σ_z and bed slope ($\Delta S \approx -0.019$). The severe bed restructuring led to significant spikes in the sediment outflow rate $q_{s,out} \approx 40$ kg/(sm) at the flume outlet (Figure 6.1a). In experiment SF2 with SF, a similar failure process occurred as the PUE destroyed all upstream steps after the initial failure of step VII.

Experiments SF0 and SF2 served as examples to describe general observations in artificial step-pool systems. The system remained stable up to q_{stab} at which the maximum Shields ratio $(\theta/\theta_c)_{max}$ was reached. The reach-averaged bed slope decreased substantially (i.e., $\Delta S < -0.01$) after the subsequent interval with discharge $q_f(1\%)$ was applied. These parameters are used in Section 6.6 to describe bed stability in channels with artificial step-pool sequences. The decrease in bed slope, i.e., the resulting bed slope after systems failure ΔS, depended on the time of failure during the hydrograph. The decrease ΔS was more pronounced if step failure occurred during the ascending limb or during peak flow, whereas the decrease was less pronounced if the initial step failure occurred during the descending limb of the hydrograph. The failure modes of SF0 and SF2 were both abrupt, but other experiments showed a more gradual failure (see Section 6.4.5).

6.3 Hydraulic conditions

This section elaborates on the hydraulic conditions in artificial step-pool systems. Existing relations to estimate flow resistance are compared to the data of the present study. The parameter defining the hydraulic roughness of these systems is particularly of interest. Predicting mean flow velocity in these systems allows to determine the flow regime (sub- or supercritical) and the bed shear stresses, which is key for bed stability assessment. Two novel empirical relations are presented to estimate the reach-averaged flow velocity using the equivalent diameter D_{eq} of the step-forming blocks or the mean step height H as roughness parameters. Subsequently, the streamwise deviations from the reach-averaged flow velocity are analyzed allowing more precise flow velocity estimates at the step crests – a crucial input to assess the stability of the step-forming blocks.

6.3.1 Flow resistance

Figure 6.4a compares data of artificial step-pool systems with existing approaches to estimate the bed friction coefficient $\sqrt{8/f_b}$ using the Keulegan (1938) relation, the approach of Thompson and Campbell (1979), and the variable power equation (VPE) by Ferguson (2007) (Equations (2.5), (2.7), and (2.8), respectively). The Darcy-Weisbach bed friction factor f_b was determined applying the GEJ sidewall correction procedure (Section 2.3.3) assuming an equivalent sand roughness $k_w = 0.5$ mm for the smooth sidewalls. Using d_{84} of the base material leads to a pronounced underestimation of flow resistance, independent of the approach (not presented here). Therefore, the equivalent spherical diameter of the step-forming blocks D_{eq} was used instead. The results show that the friction factor was predicted considerably well with Keulegan (1938) being approximately an upper limit and the VPE approach constituting a lower limit for $\sqrt{8/f_b}$. The former was developed for channels with high relative submergence and tends to underestimate flow resistance in channels with small relative submergence, which also applies to artificial step-pool channels. Moreover, these results indicate that the step-forming blocks are decisive to estimate flow resistance in artificial step-pool channels and the size of the base material is of minor importance.

Figure 6.4b compares the logarithmic and linear approaches proposed by Aberle and Smart (2003) to estimate the friction factor $\sqrt{8/f_b}$ using Equations (2.9) and (2.10), respectively. Both approaches agree well with data from artificial step-pool systems confirming
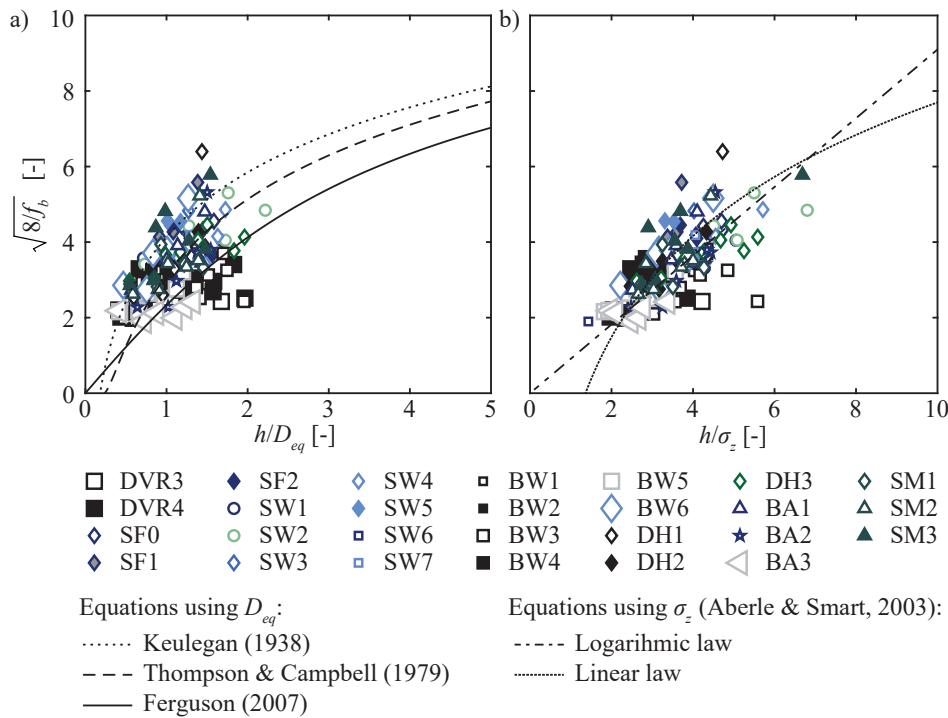
Figure 6.4 Comparison of bed friction factor $\sqrt{8/f_b}$ with approaches using a) the equivalent boulder diameter D_{eq} as a roughness parameter (Equations (2.5), (2.7), and (2.8) by Keulegan 1938; Thompson and Campbell 1979; Ferguson 2007, respectively) and b) the standard deviation of the bed elevations σ_z (Equations (2.9) and (2.10) by Aberle and Smart 2003); marker legend according to Figure 4.15

the results by Chen *et al.* (2020), who found σ_z to better estimate flow resistance in steep rough channels. Using σ_z directly incorporates the structure of the bed and does not require the choice of a characteristic grain diameter d_i. Nitsche *et al.* (2012), for example, determined σ_z in seven streams in Switzerland by measuring longitudinal profiles with a total station. Determining σ_z in the field became less challenging as photogrammetric methods (e.g., SfM), enabling the acquisition of high resolution DEMs, significantly improved. Nevertheless, it remains difficult to accurately survey the parts permanently filled with water, e.g. the pools, as these techniques do not allow to measure through the water surface, particularly if the surface is uneven, when air is entrained, or if turbidity is high.

6.3.2   Mean flow velocity

This section presents novel approaches to estimate mean flow velocity in artificial step-pool systems using the hydraulic geometry approach (Section 2.2.2):

$$v_m = c\, g^{\frac{1-m_1}{2}}\, S^{m_2}\, q^{m_1}\, k^{\frac{1-3\,m_1}{2}}   \tag{6.1}$$

Table 6.1 Parameters c, m_1, and m_2 fitted to the hydraulic geometry relation (Equation 6.1), R^2 = coefficient of determination, RMSE = root mean square error

ID	k [m]	c [-]	m_1 [-]	m_2 [-]	R^2 [-]	RMSE [m/s]
1	σ_z	1.08	0.58	0.23	0.912	0.27
2	D_{eq}	0.93	0.45	0.02	0.877	0.32
3	D_{eq}	0.86	0.44	-	0.877	0.31
4	H	1.39	0.49	0.17	0.847	0.31
Equation (2.13)[*]	σ_z	0.96	0.60	0.20	-	0.27

[*] Aberle and Smart (2003)

with c, m_1, m_2 = coefficients. The bed roughness parameter k was substituted by the standard deviation of the bed elevations σ_z, the equivalent grain diameter of the step-forming blocks D_{eq}, and the mean step height H (Figure 4.11). Table 6.1 summarizes the obtained coefficients c, m_1, and m_2 and the resulting goodness of fit indicated by the coefficient of determination R^2 and the root mean square error (RMSE). Using $k = \sigma_z$ (ID1) has the highest accuracy when estimating mean flow velocity. However, Equation (2.13) by Aberle and Smart (2003) shows a comparable RMSE and is recommended to estimate mean-flow velocity in artificial step-pool channels.

From the practitioner's perspective, σ_z is still challenging and time consuming to determine in the field in most cases. Therefore, D_{eq} was used as a proxy for bed roughness (ID2) which is a priori known being a design parameter. Mean flow velocity was predicted with $R^2 = 0.877$ and RMSE = 0.32 m/s. However, exponent m_2 of bed slope S did not significantly improve the result. Excluding bed slope and its exponent m_2 from the analysis (ID3) led to:

$$v_m = 0.86\, g^{0.28}\, q^{0.44}\, D_{eq}^{-0.16} \tag{6.2}$$

Using the mean step height – also a design parameter – as a bed roughness parameter (ID4) led to $R^2 = 0.847$ and RMSE = 0.31 m/s, yielding:

$$v_m = 1.39\, g^{0.26}\, S^{0.17}\, q^{0.49}\, H^{-0.24} \tag{6.3}$$

The measured and calculated mean flow velocities are presented in Figure 6.5. The prediction error (PE) was below 20% for most of the data using all three approaches and no systematic deviation could be observed. The mean absolute PE amounted to 5.9, 7.0,
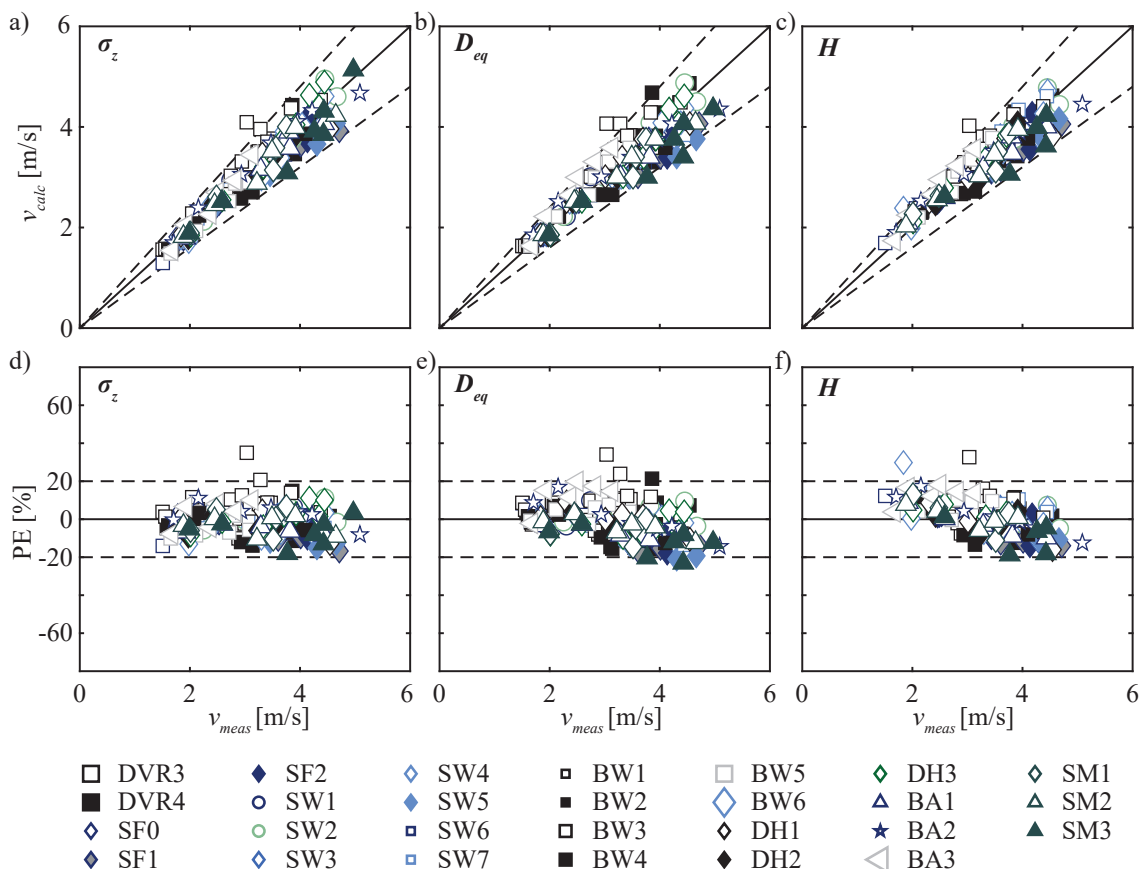
Figure 6.5 Comparison of measured and calculated mean flow velocity v_{meas} and v_{calc} with a) Equation (2.13), b) Equation (6.2), c) Equation (6.3), and d) to f) the corresponding prediction errors (PEs); marker legend according to Figure 4.15

and 7.3% using σ_z, D_{eq}, and H as bed roughness parameters, respectively. Consequently, the existing approach by Aberle and Smart (2003) using σ_z as bed roughness parameter, which was initially developed for self-organizing step-pool channels, is also applicable to artificial step-pool systems. Moreover, Equations (6.2) and (6.3) enable to estimate reach-averaged flow velocities in artificial step-pool systems.

6.3.3 Streamwise flow velocity variations

The streamwise velocity variations are of importance to assess the stability of the step-forming blocks, e.g., by applying a force balance. These velocity variations were analyzed using bed elevation and water surface elevation (WSE) longitudinal profiles digitized from side-view pictures taken during peak discharge assuming 2D flow (Section 4.5.2). Figure 6.6a shows bed and water surface elevations of experiment DVR4 for $q = 13.75$ m^2/s. The bed elevation and WSE profiles were used to calculate flow depth h which, in turn, was used to estimate the local depth-averaged flow velocity $v = q/h$.
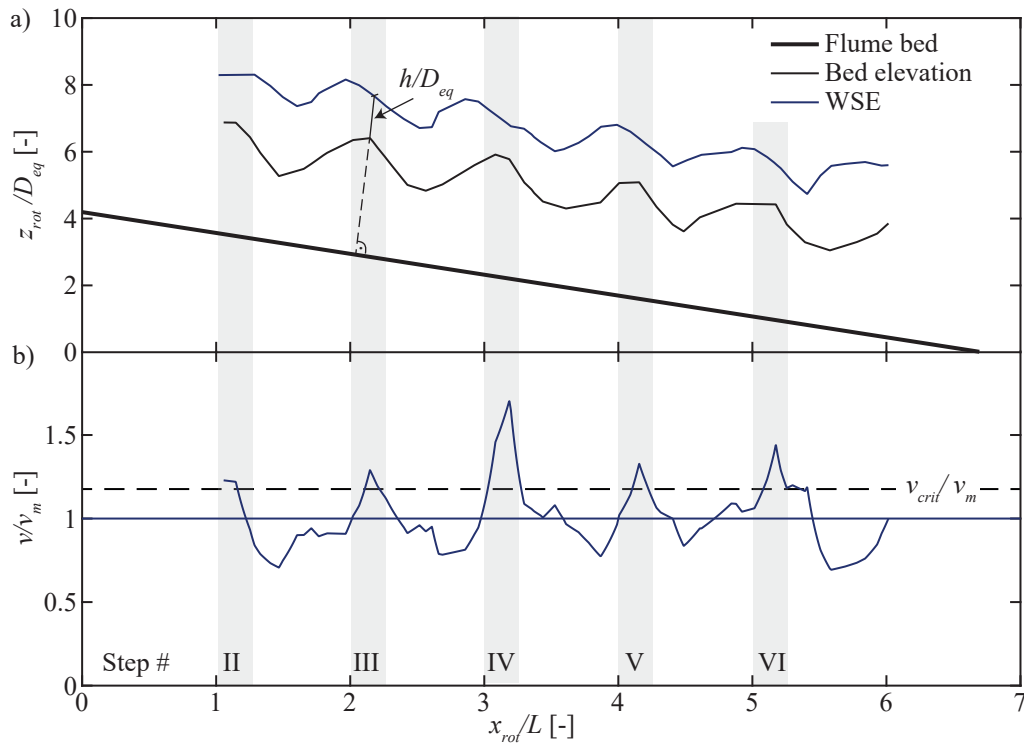
Figure 6.6 a) Longitudinal profile of bed elevations z_{rot}/D_{eq} and water surface elevation (WSE) for experiment DVR4 during peak flow $q = 13.75$ m^2/s, b) corresponding local velocity variations v/v_m with v_m reach-averaged flow velocity, and v_{crit} = critical flow velocity; step locations are indicated with gray boxes; h/D_{eq} = normalized flow depth

Figure 6.6b shows the longitudinal profile of the local flow velocity normalized with the reach-averaged mean flow velocity v/v_m. The solid blue line indicates the mean flow velocity (i.e., $v/v_m = 1$) and the dashed black line the critical flow velocity v_{crit}/v_m. Streamwise flow velocity deviated substantially from the mean particularly in the vicinity of the steps, i.e., the typical flow regime of step-pool channels oscillating between sub- and supercritical flow was observed (Church and Zimmermann 2007). Nevertheless, the reach-averaged flow velocity was smaller than the critical velocity (i.e., $v_m < v_{crit}$) indicating subcritical flow conditions (F $<$ 1) on the reach scale. The reach-averaged flow velocity obtained from the salt tracer measurements (Section 4.5.1) compares well with the mean flow velocity from the images (i.e., $v_{salt}/v_m = 0.93$ for DVR4 and $q = 13.75$ m^2/s). The deviation is in the range of measurement uncertainty ($\sigma_v/v \approx 9\%$, Section 4.7).

Figure 6.7a shows the probability p of the velocity deviations v/v_m for the DVR4 experiment at $q = 13.75$ m^2/s (i.e., corresponding to Figure 6.6). The 95%-percentile (PER) of v/v_m was used as a proxy for the high velocities in the vicinity of the steps. For experiment DVR4 and $q = 13.75$ m^2/s, PER(95%) = 1.41 leading to $(v - v_m)/v_m = \Delta v/v_m =$
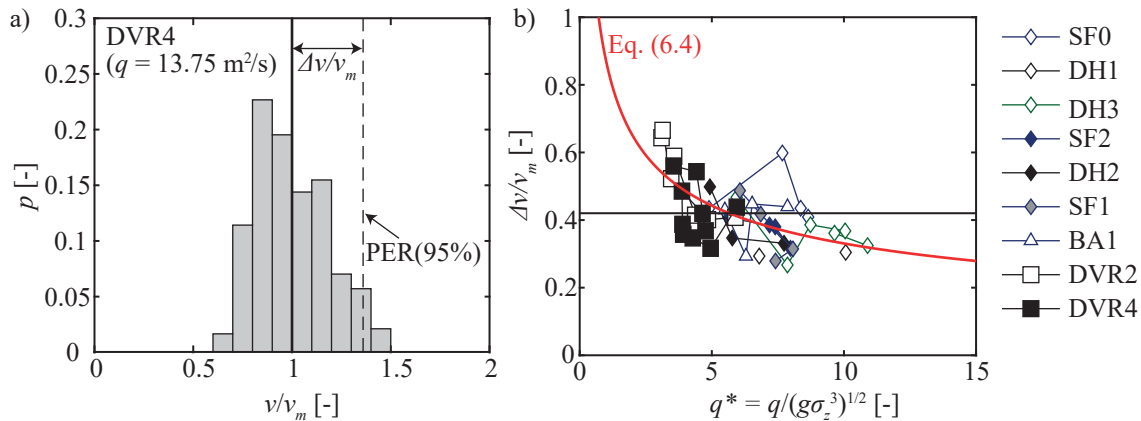
Figure 6.7 Streamwise flow velocity variations. a) Histogram of the relative velocity variations v/v_m during peak flow ($q = 13.75$ m²/s) of experiment DVR4. b) Relation between dimensionless discharge q^* and the velocity deviations $\Delta v/v_m$, analyzed for the indicated experiments (marker legend according to Figure 4.15) in comparison with Equation (6.4)

PER(95%) − 1 = 0.41. The 95%-percentile estimates are compiled in Figure 6.6b for all intervals of nine experiments and are plotted as a function of the dimensionless discharge $q^* = q/\sqrt{g\,\sigma_z^3}$.

The average relative streamwise velocity deviation was estimated to $\Delta v/v_m = 0.42$. However, $\Delta v/v_m$ was much more pronounced at low discharges, i.e., flow regimes referred to as impinging jet regime for submerged jet conditions or nappe flow for free jet conditions (Church and Zimmermann 2007). These deviations stem from the difference between the subcritical flow velocities in the pools and the supercritical flow velocities occurring at the step crest. The unit discharge q^*, normalized with σ_z, was used as this effect was even more pronounced in the presence of large step heights (i.e., large σ_z). The streamwise velocity deviations are assumed to decrease to zero for large submergence, skimming flow conditions, or if the typical step-pool bed forms are washed out. However, this may rarely ever happen in practice as a step-pool channel (without reinforced steps) may not sustain skimming flow conditions.

Knowledge of the streamwise velocity deviations, and especially the velocity in the vicinity of the step-forming boulders, is of interest when assessing step stability (e.g., Section 6.4.6). A reference velocity is required in a force balance analysis to estimate the drag and lift forces acting on a boulder. A regression analysis was conducted to estimate the streamwise relative velocity deviations as a function of the dimensionless unit discharge q^*, leading to:

$$\frac{\Delta v}{v_m} = 0.87\,q_*^{-0.42} \qquad (R^2 = 0.354) \tag{6.4}$$

The estimates of $\Delta v / v_m$ represent depth-averaged flow velocities but velocities also deviate in vertical and transversal direction as well as in time. Wilcox and Wohl (2007) conducted three-dimensional velocity measurements with time-averaged components in all three directions in the field obtaining velocity profiles at characteristic morphological locations (e.g., step crest, pools, treads) in a stream with $S = 0.10$. The streamwise velocity component contributed to the majority of the overall velocity while the transversal and vertical components accounted on average for 20% and 15% to the overall vector magnitude, respectively. Moreover, turbulence intensity expressed as the root mean square (RMS) of the time series in streamwise (RMS_x), transversal (RMS_y), and vertical (RMS_z) direction, were in the range of the overall vector magnitude. Thus, flow velocity in step-pool channels is highly variable in space and time.

Regarding the design of artificial step-pool sequences, it is recommended to use the reach-averaged flow velocity v_m to characterize the flow regime, to calculate the reach-averaged flow depth, and to predict bedload transport. The flow velocity deviations are useful to predict local streamwise velocity when applying a force balance to assess step stability (e.g., Section 6.4.6).

6.4   Failure mechanisms

Understanding the relevant failure mechanisms is crucial for the design of artificial step-pool sequences. On the one hand, the step-pool geometry can be adapted to avoid the most frequent failure mechanisms, i.e., increasing the structure's stability. On the other hand, it allows to assess the system's behavior in case of an overload scenario. Ideally, the step-pool geometry ensures the structure's stability for the selected design discharge and allows a gradual failure in case of an overload scenario. Research question B1 (Section 1.3) aims at identifying the relevant failure mechanisms leading to the destruction of artificial step-pool sequences. It was hypothesized that failure mechanisms were comparable to those in self-organizing step-pool systems. The present section reports the observed failure mechanisms, describes the typical progressive upstream erosion (PUE) pattern, and elaborates on the frequency of occurrence of each failure mechanisms. Furthermore, the effect of sediment transport as well as gradual and abrupt failure modes of artificial step-pool systems are discussed.
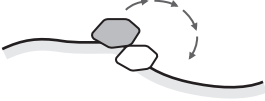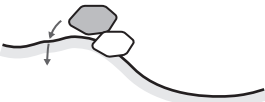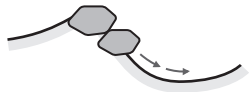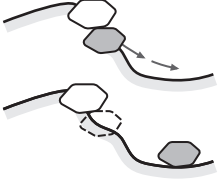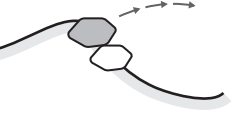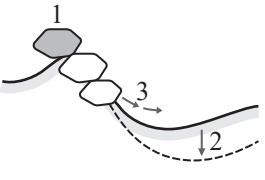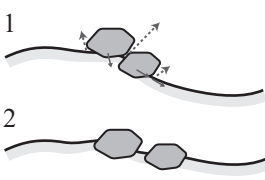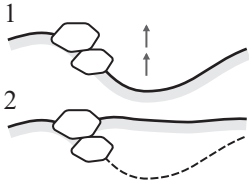
6.4.1   Classification of failure mechanisms

Table 6.2 summarizes all failure mechanisms observed during the experiments with artificial step-pool sequences. Therein, the five main processes *tilting*, *scouring*, *entrainment*, *internal erosion*, and *pool filling* were distinguished. The first group includes *tilting processes* in which one or several blocks of the upper row tilted either in or against flow direction. The upper row gets exposed to the flow when the upstream scour pool reaches the downstream step or base material is washed out from the step interspaces. Tilting in flow direction may lead to the complete destruction of the step whereas the step may persist when one or several blocks tilt against flow direction. The second class comprises *scouring processes* in which the step toe was destabilized as the scour depth increased. Four outcomes were observed:

- Total destruction: the entire step slid into the downstream pool and the blocks were buried potentially triggering a progressive upstream erosion (PUE) pattern (Section 6.4.2).

- Step displacement: the step slightly shifted in downstream direction, lowering the step crest in vertical direction. The step persisted and was not fully destroyed.

- A block carpet formed in case the lower block row moved away from the upstream row but the step-forming blocks were not fully buried.

- Jamming: The step toe was destabilized and blocks in the lower row slid into the downstream pool while the interlocking of the blocks in the upper row and the sidewalls prevented a total destruction. However, this fragile state was not sustained over a long period of time leading, in the end, to a total step destruction, triggering PUE.

The third class comprises processes related to the *direct entrainment* of large step-forming blocks. Compared to the tilting mechanisms, the step-forming blocks were less exposed to the flow. Due to the smaller block exposure, the drag and lift forces were smaller and higher near-bed flow velocities were required to mobilize the blocks. Contrary to the tilting process, the entrained blocks did not necessarily deposit in the downstream pool but they were transported over one or several steps. The speed at which this process occurred made it hard to detect from the video footage, thus, the block exposure served

Table 6.2 Overview of observed failure mechanisms (*us* = upstream, *ds* = downstream); gray blocks were initially affected

Process	Scheme	Description
Tilting ...in flow direction*		Block(s) of the upper row tilted in flow direction into the *ds* pool. Blocks in upper row were exposed to the flow as *us* scour reached the *ds* step.
...against flow direction		Block(s) of the upper row tilted against flow direction when the block(s) were exposed to the flow and base material was mobilized immediately *us* of the step.
Scouring A: destruction* B: displacement C: block carpet		Destabilization of the step toe as scour depth increased leading to A: complete destruction of the entire step, B: displacement of the entire step, or C: movement of the lower block row away from the upper block row resulting in a block carpet.
+ jamming		Block(s) in lower row were destabilized at the step toe and glided into the *ds* pool. However, the upper block row remained at their initial place due to jamming effects.
Entrainment Direct* (≠ tilting)		Direct entrainment of block(s) of the upper row. Contrary to tilting, the upper block row was not exposed to the flow but covered with base material.
Block stacking*		An entrained block deposits at the crest of the next *ds* step (1). Scour depth increases due to the increase in step height (2). The step toe is destabilized leading to the destruction of the entire step (3).
Internal erosion Subsidence		Washing out of base material leading to flow through the step. The step settled together as a whole, decreasing the step crest elevation.
Block carpet (gradual process)		The block rows slowly move apart from each other as base material is washed out of the steps. The process occurs gradually forming a block carpet.
Pool filling		Sediment deposits in the pools and the step-forming blocks are buried. Energy dissipation decreases due to the reduced bed roughness potentially destabilizing the whole system.

*Failure mechanism resulted in progressive upstream erosion (PUE, Section 6.4.2)

as an indicator. The block stacking mechanism was assigned to entrainment as either a step-forming or auxiliary block from the upstream reach was entrained and deposited at the step crest leading to an increase in step height. As a consequence, scour depth further increased leading to a destabilization of the step toe. Both mechanisms triggered an upstream migrating erosion pattern (i.e., PUE).

The fourth class is associated with *internal erosion*, i.e., the erosion of base material from the pore space in-between step-forming blocks. As a consequence, water flowed through the step washing out even more sediment. In some cases, the step subsided as a whole, lowering the step crest. It may lead to an increase of the upstream scour pool depths as the drop height of the upstream step slightly increases. Internal erosion patterns led to the formation of a block carpet as the step-forming blocks moved slowly apart. This process occurred gradually contrary to the block carpet formation related to scouring, which occurred rather abruptly.

Finally, *pool filling* with sediment was considered a failure mechanism as the reduction in bed roughness led to an increase in flow velocity potentially destabilizing steps downstream. Step failure due to collision with other step-forming blocks, as reported by Crowe (2002) for natural step-pool systems, was not observed herein because only the base material was supplied. Moreover, the step-forming blocks were rarely transported over long distances after step failure as they often came to rest in the subsequent pool.

6.4.2 Progressive upstream erosion (PUE)

Prior to assessing the frequency of occurrence of the failure mechanisms, the progressive upstream erosion (PUE) pattern is illustrated using experiment BW2 (Table 4.9). Figure 6.8 shows a sequence of side-view photos for the BW2 experiment conducted with $S = 0.08$, $W = 6$ m, $M_B = 4.6$ t, $H_d = 1.12$ m, and $L_d = 14$ m during the interval with $q = 8.75$ m^2/s and SF conditions. Approximately 90 seconds lie in between the photos in prototype scale. Step VI collapsed due to entrainment of the top row block during peak flow (not shown). The scour depth of the upstream step V increased leading to the destruction of step V (due to scouring) during the descending limb of the hydrograph. The scour depth of the upstream step IV increased, again, leading to a collapse of step IV. This erosion pattern propagated upstream until the upper boundary of the flume was reached. The reach-averaged bed slope decreased from $S_{ini} = 0.08$ by $\Delta S \approx -0.02$ to $S_{new} \approx 0.06$ within approximately six minutes (prototype).
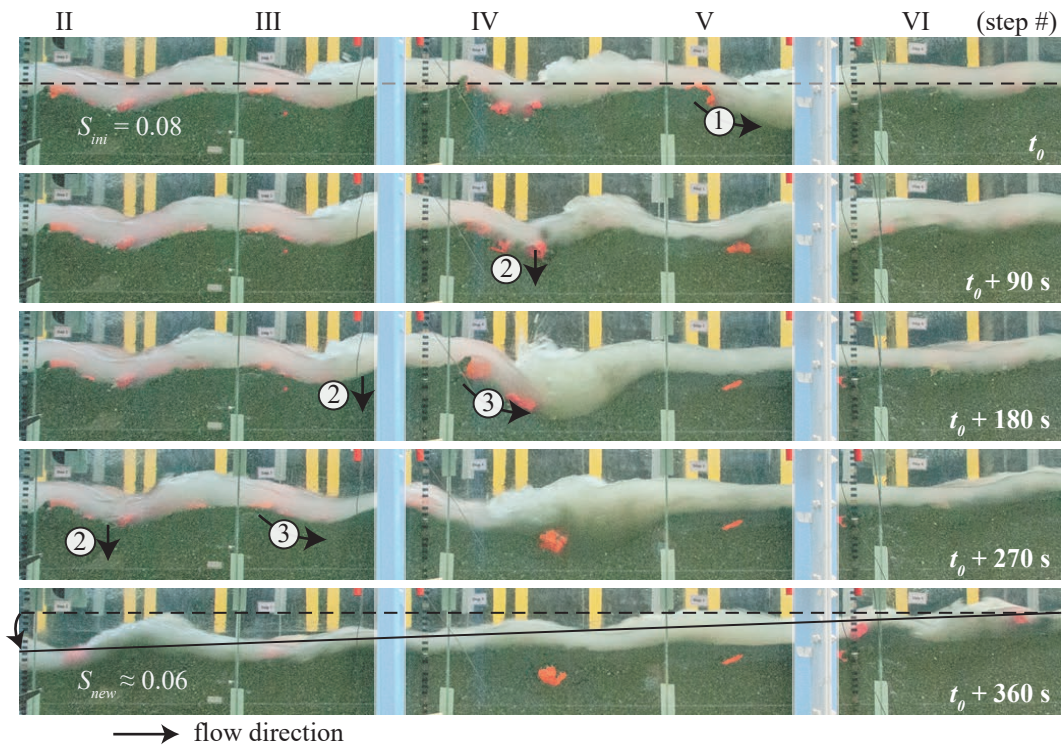
Figure 6.8 Side-view photos of experiment BW2 ($S = 0.08$, $W = 6$ m, $M_B = 4.6$ t, $H_d = 1.12$ m, $L_d = 14$ m, SF) for $q = 8.75$ m^2/s illustrating the PUE pattern, ①: Step failure due to scouring, ②: scour depth increase, ③: subsequent step failure (dashed line: initial bed slope $S = 0.08$, solid line: bed slope S_{new} resulting after PUE)

This mechanism was similar to the PUE pattern observed in self-organizing step-pool channels (e.g., Figure 5.2). However, in artificial step-pool systems, the erosion pattern propagated upstream within a very short time period (usually < 10 min, prototype) whereas the PUE occurred over a longer time period in self-organizing streams (occasionally >120 min, prototype). The decrease in bed slope ΔS was more pronounced in artificial step-pool systems. Fewer blocks were available because large blocks were only placed on the bed surface in Part B, whereas large blocks were also present in the substrate in Part A. Thus, fewer large blocks were available to re-stabilize the bed after a step failure compared to the self-organizing systems, limiting the self-stabilizing behavior of artificial step-pool sequences.

6.4.3 Frequency of occurrence

The present section identifies the frequency of occurrence of each failure mechanism. The mechanisms potentially triggering a PUE and being the most frequent at the same time are the most relevant regarding system failure. Figure 6.9 shows the frequency of occur-
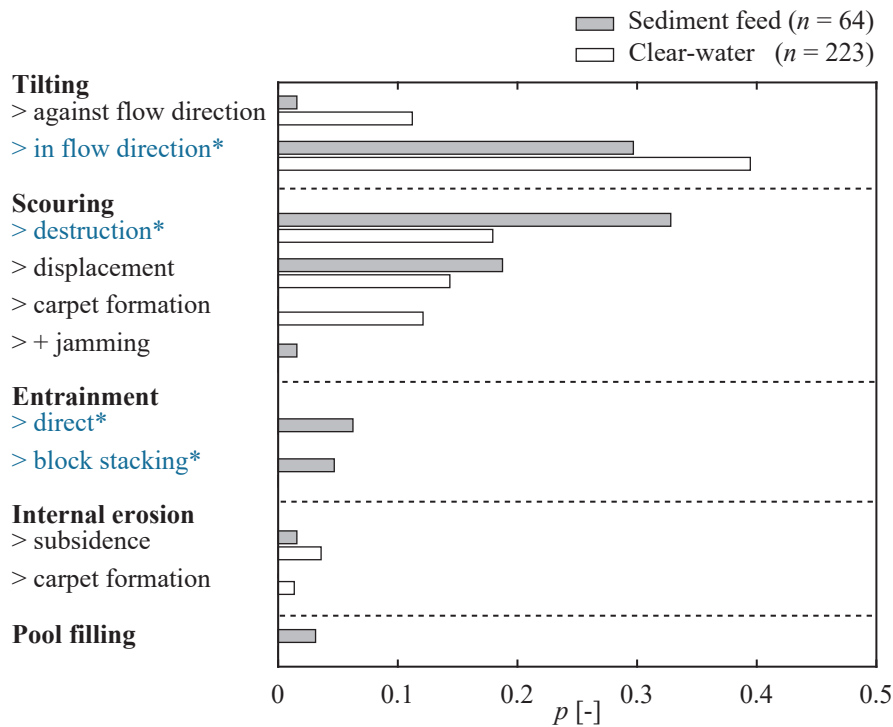
Figure 6.9 Frequency of occurrence p for all failure mechanisms; n = number of failure mechanisms (CW: 21 experiments with 146 discharge intervals; SF: 8 experiments with 58 discharge intervals); *Failure mechanisms resulting in PUE (Section 6.4.2)

rence p of all failure mechanisms identified during the experiments. Therein, 21 experiments with clear-water (CW) conditions (146 discharge intervals) and 8 experiments with sediment feed (SF) (58 discharge intervals) were analyzed separately. A total of n = 223 and 64 failures were observed in the CW and SF experiments, respectively.

Tilting in flow direction was the most frequent failure mechanism accounting for approximately 30 to 40% of all step failures in SF and CW experiments, respectively. Scouring leading to a complete destruction of the step was the second most frequent failure mechanism accounting for ~20 up to 35% for CW and SF experiment, respectively. The remaining mechanisms account for less than 20% of the step failures each. Figure 6.9 further shows that direct block entrainment and pool filling were observed during SF experiments only. The entrained blocks were less exposed to the flow in SF experiments, i.e., the step-forming blocks were covered or surrounded by fine sediment. Moreover, sediment supply generally decreased scour depth, thereby increasing flow velocity due to the decrease in bed roughness. Thus, higher bed shear stresses occurred and the step-forming (and the auxiliary) blocks were more easily entrained.

Figure 6.10 groups each process for CW and SF conditions. In CW experiments, the tilting mechanism was responsible for 51% of the cases, the scouring mechanism for 44%, and internal erosion for 5% of all step failures. In the SF experiments, 53% of the step failures were related to scouring, 31% to tilting, 11% to entrainment, 3% to pool filling, and 2% to internal erosion. Considering all failure mechanisms independently of sediment supply conditions, 46% and 45% of all failures were related to tilting and scouring processes, respectively. Internal erosion accounted for 5%, direct entrainment for 3% and pool filling for 1% of all observed step failures.

Zhang *et al.* (2018) investigated failure mechanisms for a single artificial step-pool unit (Section 3.4.4). They found that 50% of the step failures were associated with rolling (i.e., tilting) in which the step-forming grains rotated around a contact point with the grains underneath. The other 50% of the step failures were related to sliding dislodgement (i.e., scouring) where the step foundation was destabilized leading to a failure of the entire step. These results are consistent with the findings of the present study investigating failure mechanisms of continuous artificial step-pool sequences for the first time.

Within the scope of research question B1 (Section 1.3), it was hypothesized that failure mechanisms of artificial step-pool sequences are comparable to those in self-organizing step-pool systems. Crowe (2002) investigated step destruction in self-organizing step-pool systems and found 77% of all mechanisms were related to scouring. These scouring processes were divided into keystone tumbling and aggregate slumping accounting for 39 and 38% of all step failures, respectively (Section 3.3.5). Thus, artificial step-pool systems are
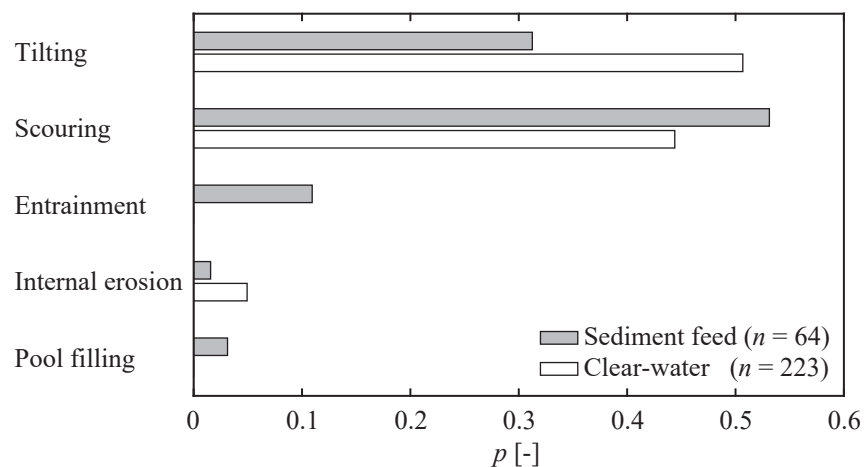

Figure 6.10 Frequency of occurrence p for all failure mechanisms aggregated into groups; n = number of failure mechanisms (clear-water: 21 experiments with 146 discharge intervals, sediment feed: 8 experiments with 58 discharge intervals)

more prone to tilting compared to self-organizing step-pool systems. Note that Crowe (2002) conducted sediment supply experiments and scouring was also more frequent in sediment supply experiments for artificial systems. Furthermore, the susceptibility to tilting of artificial step-pool systems may be related to the exposure of the upper row block as discussed in more detail in the following Section 6.4.4.

6.4.4   Effect of sediment supply

Tilting was more frequent in clear-water (CW) compared to sediment feed (SF) experiments (Figure 6.10). Figure 6.11 shows side-view photos of step number IV and V in experiments DVR2 and DVR4 ($S = 0.08$, $W = 6$ m, $H_d = 1.12$ m, $M_B = 8.0$ t) at $q = 10.00$ m^2/s with CW and SF conditions, respectively. The top row blocks of the step in Figure 6.11a were much more exposed to the flow due to internal erosion. As a consequence, water flowed through the step, further eroding the base material located immediately upstream of the step. The exposure of the step-forming blocks in CW experiments increased the likelihood of tilting either in or against flow direction. On the contrary, the steps in Figure 6.11b with SF were covered with fine sediments reducing block exposure and the likelihood of tilting.
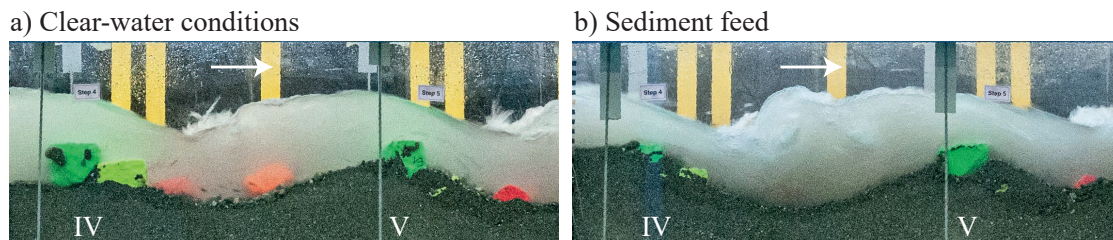

Figure 6.11 Side-view photos of steps IV and V at $q = 10$ m^2/s for a) clear-water conditions (DVR2) with upper row blocks (green) highly exposed to the flow and b) sediment supply conditions (DVR2) where the blocks were covered with fine sediments (adapted from Maager *et al.* 2022b)

Scouring was expected to be more frequent in CW experiments as deeper scours are expected but the opposite was observed (Figure 6.10). There are two explanations for this discrepancy. First, the steps in CW experiments failed at a smaller discharge due to tilting before the critical scour depth was reached. Second, the steps in SF experiments generally sustained higher discharges leading to larger (absolute) scour depths but at a higher discharge (Section 6.6.1).

6.4.5   Gradual vs. abrupt system failure

Research question B2 addresses the self-stabilizing character of artificial step-pool se-
quences (Section 1.3). It was hypothesized that these systems do have a self-stabilizing
character, i.e., that failure occurs gradually and the larger blocks rearrange leading to sta-
ble bed conditions. Herein, both gradual and abrupt failure modes were observed and the
differences are elaborated in the following. Figure 6.12 shows the decrease in bed slope
$\Delta S = S - S_{ini}$ and the Shields ratio θ/θ_c as a function of q for an experiment failing gra-
dually (DH1) and abruptly (DH2). These experiments were both conducted in a channel
with $S = 0.06$, $W = 6$ m, $H_d = 1.12$ m leading to $L_d = 18.7$ m, and step-forming blocks with
$M_B = 4.6$ t (Table 4.9). According to Figure 6.12a, the bed slope decreased step-wise in
experiment DH1 and the step-pool sequence was considered to fail gradually. On the con-
trary, the bed slope remained constant in experiment DH2 (Figure 6.12a) and decreased
instantaneously by $\Delta S = -0.014$ during peak flow with $q = 8.33$ m²/s, i.e., the step-pool
sequence failed abruptly. Despite the distinct difference in failure modes, the increase of
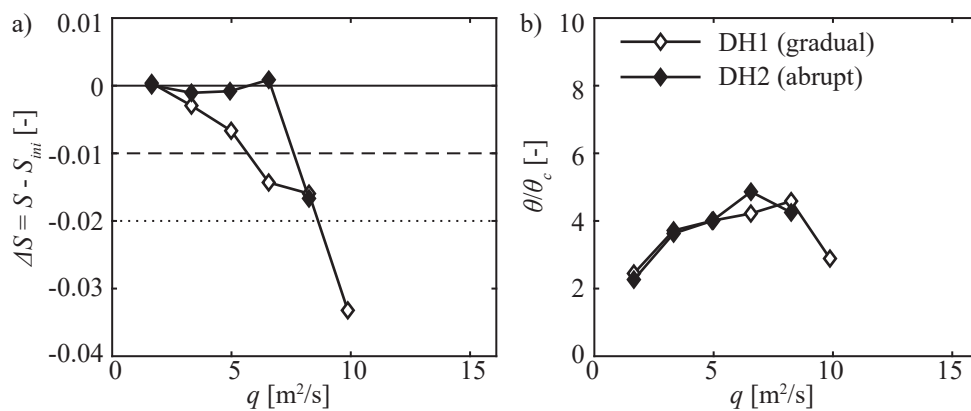the Shields ratio was comparable in both experiments (Figure 6.12b).

Figure 6.12 Evolution of slope and shear stress during gradual and abrupt failure. Experiment with
$S = 0.06$, $W = 6$ m, $H_d = 1.12$ m, $L = 18.7$ m, $M_B = 4.6$ t; DH1 = CW, DH2 = SF; a) bed slope
reduction $\Delta S = S - S_{ini}$ and b) Shields-parameter θ/θ_c as a function of unit discharge q

Figure 6.13 shows orthophotos of the flume, obtained with SfM (Section 4.5.2), illus-
trating the gradual failure of experiment DH1. The step-forming blocks started to move
already at small q but remained near their initial locations. For example, blocks in steps II,
III, and V already tilted against flow direction at $q = 3.33$ m²/s. The steps remained stable
and maintained their bed stabilizing function as the energy dissipating hydraulic jumps
persisted. Typical failure mechanisms related to block movement without leading to a to-

Gradual system failure:

A: Tilting - against flow direction   **C**: Scouring - destruction   **E:** Scouring - block carpet
B: Tilting - in flow direction   **D**: Scouring - displacement

$q = 1.67$ m²/s ($\Delta S = 0.03\%$)   → flow direction

$q = 3.33$ m²/s ($\Delta S = -0.29\%$)

$q = 5.00$ m²/s ($\Delta S = -0.67\%$)

$q_f = (1\%) = 6.67$ m²/s ($\Delta S = -1.43\%$)

$q = 8.33$ m²/s ($\Delta S = -1.59\%$)

$q = 10.00$ m²/s ($\Delta S = -3.32\%$)

I   II   III   IV   V   VI   VII   VIII   (step #)
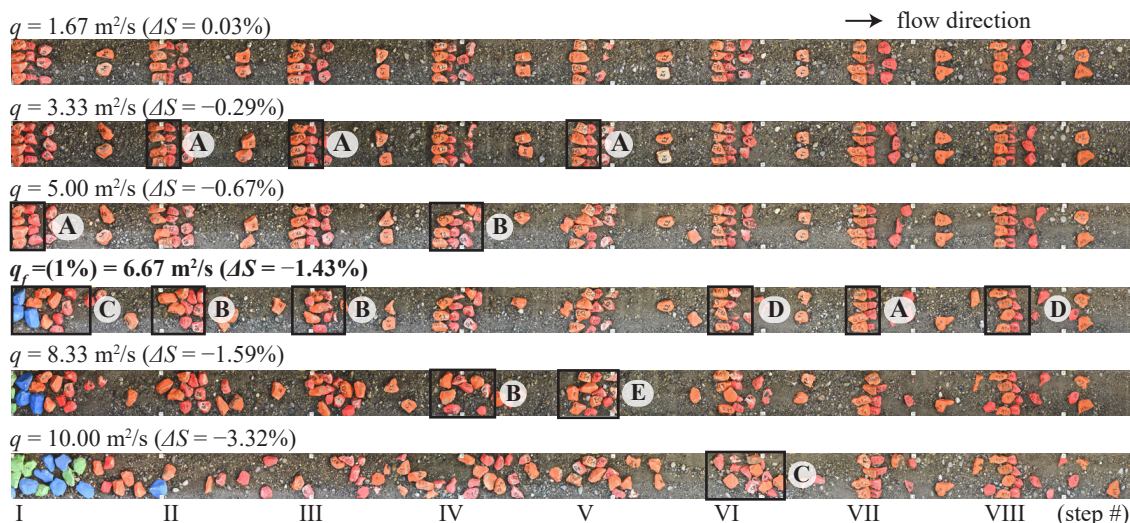
Figure 6.13 Orthophotos of experiment DH1 ($S = 0.06$, $W = 6$ m, $H_d = 1.12$ m, $L_d = 18.7$ m, and CW) illustrating the gradual system failure mode; photos were obtained after the intervals with unit discharge $q = 1.67$ to 10.0 m²/s; $\Delta S = S - S_{ini} = $ bed slope reduction; A-E: observed failure mechanisms (Table 6.2)

tal destruction of the step were: tilting against flow direction, tilting of single blocks in flow direction, or scouring leading to a displacement of at least parts or even the entire step.

In experiment DH1, these gradual failure mechanisms were observed at $q = 3.33$ and 5.00 m²/s for individual steps decreasing the overall bed slope step-wise by approximately $\Delta S = -0.3\%$ in between discharge intervals. This decrease in bed slope resulted from the movement of the step-forming blocks leading to a lowering of the average step-crest height. During the interval $q = 6.67$ m²/s, all steps experienced some changes and the bed slope decreased in total by $\Delta S = -1.43\%$. As a consequence, this discharge was considered as critical discharge in terms of failure $q_f(1\%)$. At this discharge, step II followed by step I were fully destroyed due to tilting in flow direction and scouring, respectively. Further increasing q led to the complete destruction of steps III to VI severely decreasing the bed slope by $\Delta S = -3.32\%$ at $q = 10$ m²/s.

Figure 6.14 shows orthophotos of experiment DH2 with an abrupt failure mode. Therein, the step-forming blocks remained at their initial positions while the bed slope was maintained at $S = 0.06 \pm 0.001$. Step V failed at $q = 8.33$ m²/ due to tilting in flow direction. This step failure triggered PUE destroying the upstream steps IV to I within a short time
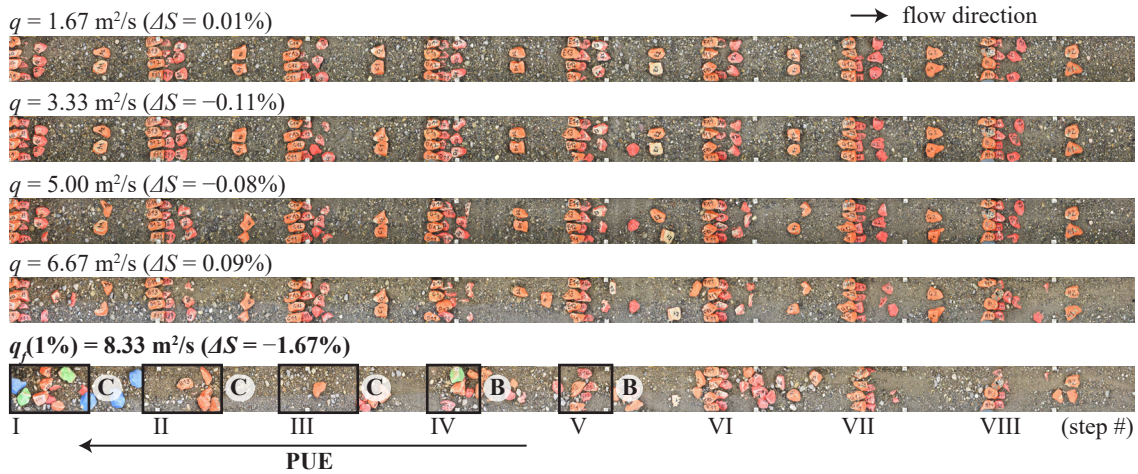
Abrupt system failure:

B: Tilting - in flow direction   **C**: Scouring - destruction

$q = 1.67$ m²/s ($\Delta S = 0.01\%$)   → flow direction

$q = 3.33$ m²/s ($\Delta S = -0.11\%$)

$q = 5.00$ m²/s ($\Delta S = -0.08\%$)

$q = 6.67$ m²/s ($\Delta S = 0.09\%$)

$q_f(1\%) = 8.33$ m²/s ($\Delta S = -1.67\%$)

I   II   III   IV   V   VI   VII   VIII   (step #)

← PUE

Figure 6.14 Orthophotos of experiment DH2 ($S = 0.06$, $W = 6$ m, $H_d = 1.12$ m, $L_d = 18.7$ m, and SF) illustrating the abrupt system failure mode ; photos were obtained after the intervals with unit discharge q; $\Delta S = S - S_{ini}$ = bed slope reduction; B,C: observed failure mechanisms (Table 6.2), PUE according to Section 6.4.2

period (10 to 15 minutes). The bed slope decreased by approximately $\Delta S = -1.67\%$ and $q_f(1\%) = 8.33$ m²/s was considered to be critical in terms of system failure.

To conclude on the system failure modes, a gradual failure was related to small adjustments of the step-forming blocks occurring already at small discharges. The system adapted to an increase in discharge by decreasing the reach-averaged bed slope at small discharges. On the contrary, experiments experiencing abrupt failure initially adapted to the increase in discharge by increasing bed roughness, i.e., increasing scour pool depth. The adaptation through a decrease in bed slope occurred later after a certain threshold for q was exceeded leading to a much more pronounced bed slope reduction. Experiments DH1 and DH2 represent examples with clearly distinguishable failure modes. Nevertheless, gradations in between gradual and abrupt failure modes were observed, where a clear assignment to either mode was more difficult.

An important difference between the gradual and abrupt failure modes was the system failure duration and the associated increase in bedload transport rate. The abrupt failure occurred within a single hydrograph leading to severe bed incision increasing sediment transport considerably (i.e., $q_{s,out} = 142$ kg/(sm) while feeding $q_{s,in} = 52$ kg/(ms)). Contrarily, the decrease in bed slope observed in a step-pool sequence failing gradually occurred over several discharge intervals. Consequently, the maximum bedload transport rate was

smaller with $q_{s,out} = 52$ kg/(sm) for $q \leq 6.67$ m^2/s (without sediment feed). However, the outcome in terms of total bed slope reduction was similar (Figure 6.12b).

Regarding research question B2; the self-stabilizing character of artificial step-pool systems was hardly achieved because $\sim$70% of the experiments with artificial step-pool sequences were prone to an abrupt system failure while only 30% failed gradually. First, the system failure was associated with a substantial decrease in bed slope and second, the bed hardly resembled the initial, highly organized step-pool system as the blocks were buried or scattered into a block carpet (Figure 6.14). An abrupt failure mode has to be expected when the step-pool sequences are stable, i.e., the steps remain in place while the scour pool depth increases. A stable system with larger scour pool depths is more susceptible to experience a PUE in which scouring processes are the key drivers. The parameters controlling bed stability of artificial step-pool systems are further discussed in Section 6.6.

6.4.6 Tilting - Single grain force balance

Tilting of the step-forming blocks in flow direction led to a step failure in approximately 30 to 40% of the cases in CW and SF experiments, respectively (Section 6.4.3). Predicting the stability of the step-forming blocks by applying a force balance may be a promising approach (e.g., Lenzi 2002). A single grain force balance, which is detailed in Section 2.4.1, was used to predict the reference velocity v_{ref} at which the step-forming blocks tilt into the downstream pool. This velocity was then compared with the observed velocity at which the steps tilted into the downstream pool. However, assumptions are required regarding drag and lift coefficients C_D and C_L, block exposure, and the tilting angle ϕ. These parameters were selected following literature (Section 2.4.1) and were systematically varied as follows: $C_D = 0.4$ to 0.7, $C_L = 0.7$ to 1.0, exposure from 0 to 1, $\phi = 20$ to $50°$ and bed slope $S = 0.04$ to 0.08, where the latter corresponds to the range investigated in the present study.

Figure 6.15 indicates the range of the predicted reference velocities v_{ref} as a function of the block weight M_B resulting from $n \approx 13'800$ parameter combinations (box plots), where the lift coefficient was the most sensitive parameter. Moreover, the solid black line shows the simplified relation by Lenzi (2002) to predict v_{ref} as a function of the equivalent diameter D_{eq}, i.e., approximately the b-axis of the step forming blocks. This simplified relation agrees well with the force balance analysis of the present study.
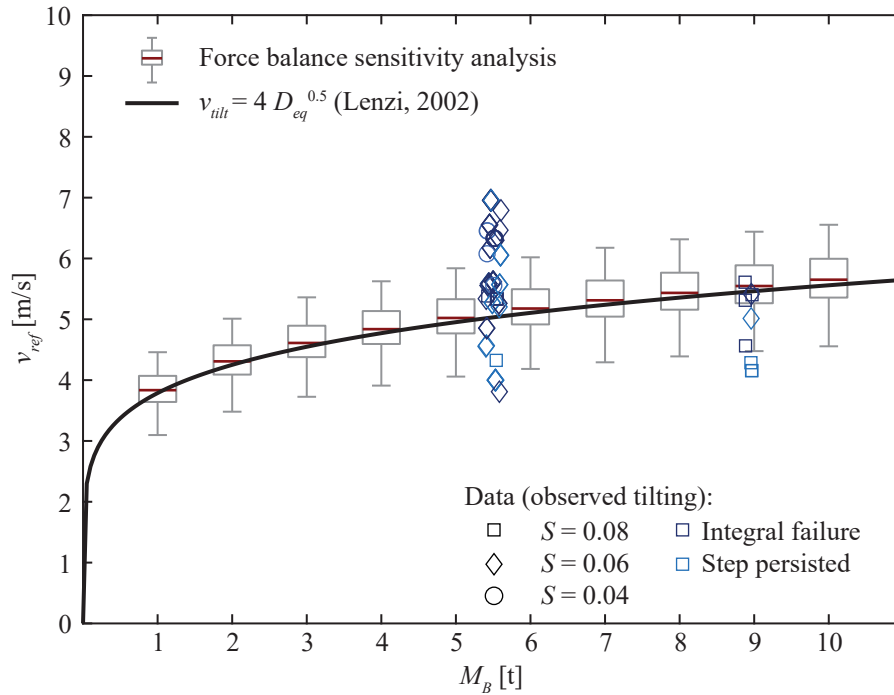
Figure 6.15 Reference velocity v_{ref} at which the step-forming blocks with block weight M_B tilt into the downstream pool, box plots: single grain force balance, solid line: simplified approach by Lenzi (2002), markers: experimental data

In addition, Figure 6.15 shows flow velocity estimates (markers) at which tilting was observed during the experiments. Therein, the mean block weight of the upper block row was used for the analysis. The dark blue markers indicate the occurrence of an integral step failure and the light blue markers indicate that one or more blocks tilted into the downstream but the step persisted. The 95%-CI streamwise velocity variations (Section 6.3.3) were considered to estimate the reference velocity v_{ref} at the step crest. The reach-averaged flow velocity was multiplied by $(1 + \Delta v/v_m)$ to account for higher flow velocities at the step crest using Equation (6.4).

The flow velocity at which the step-forming blocks tilted were in the range of the predicted flow velocity applying a single grain force balance but the scatter was substantial. A large amount of this scatter is attributed to the observed flow velocity, i.e., the velocity at which the tilting occurred. The majority of the failures related to tilting occurred at higher reference velocities as predicted for blocks with $M_B = 5.6$ t. However, some of the steps tilted at smaller lower flow velocities than predicted particularly when large blocks ($M_B = 9.0$ t) were used. It indicates that the near-bed reference velocities vary in vertical or transversal direction (Wilcox and Wohl 2007). Moreover, flow velocity fluctuations attributed to the highly turbulent flow, which are not considered in the present

analysis, further increase the reference velocity, potentially triggering tilting. Wilcox and Wohl (2007) found the turbulence intensity to be in the range of the overall vector magnitude but the fluctuation may be much shorter compared to the time required to destabilize the blocks.

To conclude, the single grain force balance may be used to roughly assess the boulder stability. However, precise predictions are not possible due to the uncertainties attributed to the input parameter, particularly to the lift coefficient C_L, but also due to highly heterogeneous flow conditions in step-pool channels varying both in space and time. Consequently, a single grain force balance may not be a practical approach to assess bed stability of artificial step-pool systems.

6.4.7   Summary on failure mechanisms

Herein, failure mechanisms of artificial step-pool sequences have been systematically analyzed for the first time. The majority of the step failures were related either to tilting of the upper row blocks (46%) or to scouring due to an undermining of the steps (45%) (Section 6.4.3). These mechanisms may also trigger a progressive upstream erosion (PUE) destroying all steps located upstream of the initial step failure (Section 6.4.2). Moreover, tilting was more frequent in CW compared to SF experiments (Figure 6.10). The step-forming blocks were much more exposed to the flow in CW compared to SF experiments due to internal erosion of fine material increasing the likelihood of tilting (Figure 6.11). A single grain force balance was applied to predict step stability, i.e., to determine flow velocity at which the step-forming boulder tilt into the downstream pool (Section 6.4.6). However, precise predictions are difficult owing to the uncertainties attributed to the input parameters (e.g., lift coefficient C_L).

6.5   Effect of the hydrograph shape

This section elaborates on the effect of three discharge variation regimes (DVR, i.e., hydrograph shapes) on bed stability, failure mechanisms, and step-pool geometry to address research question B3 (Section 1.3). A stationary regime (STAT), hydrographs (HYD), and hydrographs with intermediate periods of low flow conditions (HYD+LQ) were investigated for the exact same artificial step-pool sequences (experiments DVR1 to DVR3, Table 4.9). The investigated DVRs are detailed in Section 4.4.3. It was hypothesized that stationary conditions lead to a collapse at smaller discharges compared to hydrographs at-

tributed to the longer duration of peak discharge. The descending limb of the hydrograph was assumed to lead to larger scour depths close to the step toe as the free falling jet impinges more vertically on the channel bed triggering step failure. The DVR leading to the least stable system, representing conservative conditions, was selected to proceed with.

6.5.1 Effect on bed stability and failure mechanisms

Figure 6.16 shows the decrease in bed slope ΔS and the Shields ratio θ/θ_c as a function of unit discharge q for experiments DVR1 to DVR3. During the first six intervals (i.e., for $q \leq 7.50$ m^2/s) the bed slope remained stable at $S \approx 0.08$. Afterwards, the bed slope decreased by more than $\Delta S = -0.01$ at $q = 8.75$ to 10.00 m^2/s in experiments DVR1-2 and DVR3, respectively. Thus, all three discharge regimes were similarly stable and sustained discharges $q_{stab} = 7.50 \pm 1.25$ m^2/s. Furthermore, θ/θ_c increased with q and reached its maximum shortly before the steps collapsed (i.e., interval q_{stab}). Overall, Shield ratios of $(\theta/\theta_c)_{max} \approx 6$ were obtained, independent of the hydrograph shape.
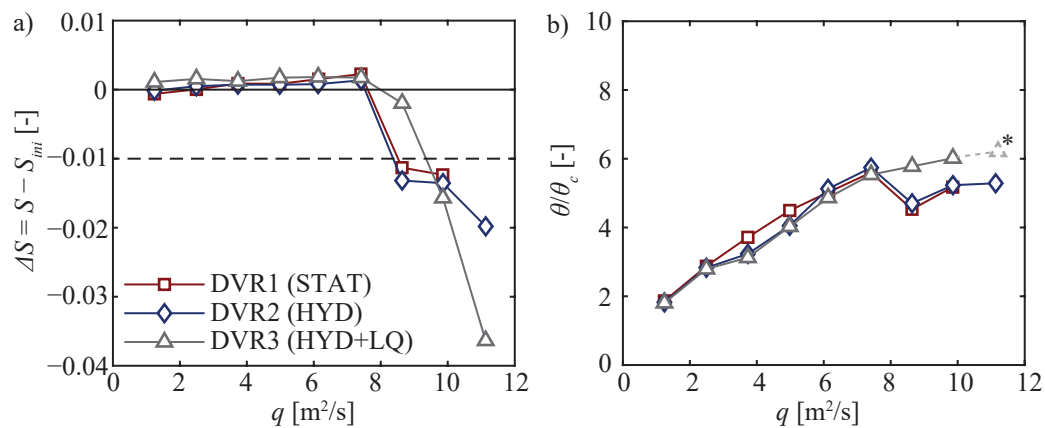

Figure 6.16 Effect of discharge variation regime on a) bed slope reduction $\Delta S = S - S_{ini}$, and b) Shields ratio θ/θ_c as a function of unit discharge q for experiments DVR1 to DVR3; [*]data missing

At a unit discharge $q = 8.75$ or 10.00 m^2/s, the first and second step were destroyed due to tilting of the upper row blocks either in or against flow direction. However, steps IV to VI remained stable up to $q = 11.25$ and 12.50 m^2/s at which the last step VI collapsed due to tilting. As a consequence, all steps were immediately destroyed due to PUE (Section 6.4.2). The failure mechanisms were independent of the hydrograph shape as the same steps collapsed in a similar way at approximately the same unit discharge.

6.5.2   Step-pool geometry

Figure 6.17a shows the mean (i.e., reach-averaged) step height H, i.e., the distance between the step crest and deepest point in the scour pool, normalized with drop height $H_d = 1.12$ m (Figure 3.9). The mean step height increased with discharge and the differences between the three experiments were smaller than $\pm 10\%$ (Figure 6.17b). The unsteady discharge regimes HYD and HYD+LQ resulted in slightly larger step heights, i.e., deeper scour pools, compared to the stationary discharge regime STAT. Keeping this in mind, the subsequent sections further elaborate on the temporal evolution of the scour depth during the experiments and on differences in bed elevations during DVR3 before and after the intermediate periods of low discharge between flood events.
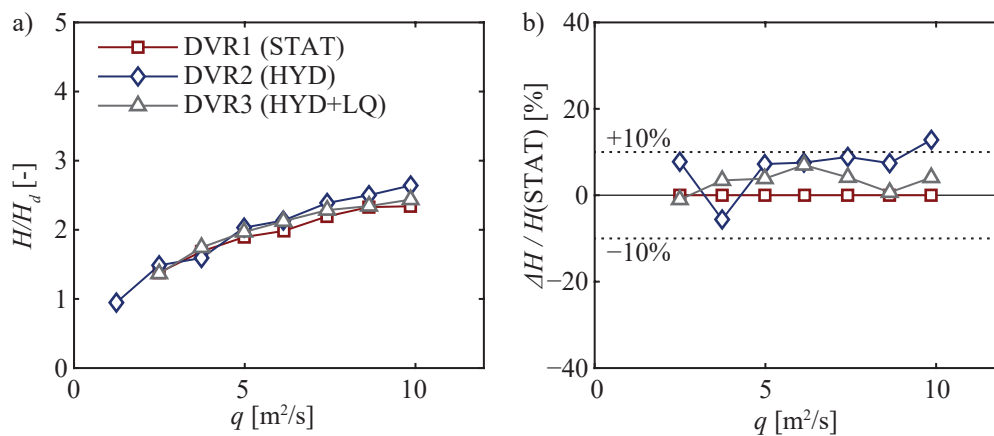

Figure 6.17 Effect of discharge variation regime on scour depth: a) ratio of mean scour depth H and drop height $H_d = 1.12$ m; b) relative scour depth in comparison with scour depth of the STAT experiment $\Delta H = H(X) - H(STAT)$

Temporal evolution of scour depth

The temporal evolution of the scour depth was obtained from side-view pictures capturing steps II to VI (Section 4.5.2). Figure 6.18 shows the ratio between the step height H at the time indicated on the abscissa to the step height H_{end} at the end of each interval for each experiment. The ratio $H/H_{end} = 1$ implies that H equals the step height at the end of the corresponding interval. Side-view pictures prior to the experiment (Start) and after 0.05, 0.10, 0.15, and 0.20 of the total interval duration $t_{stat} = 6$ h were analyzed for the STAT experiment. Similarly, side-view pictures were analyzed prior to the experiment (Start), at the beginning of the peak (P1), at the end of the peak (P2), and after 1/3 and 2/3 of the descending limb (DL) of the hydrograph (1/3 DL and 2/3 DL, respectively) for ex-
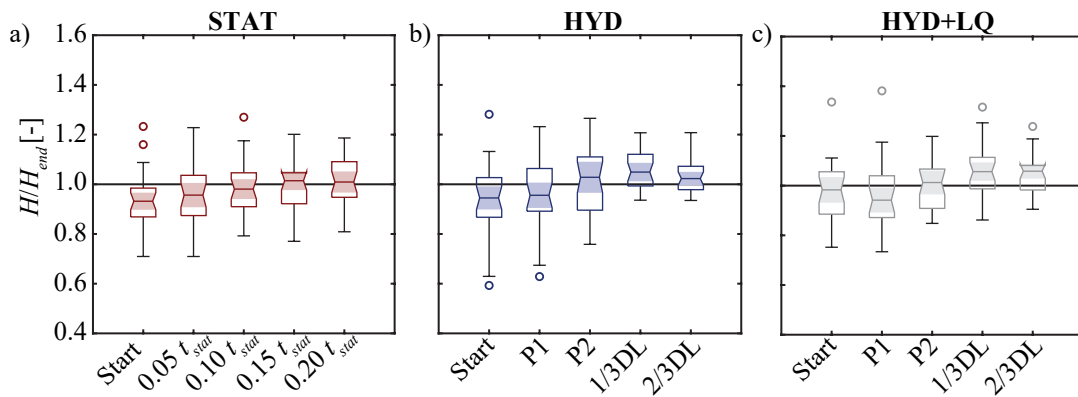
Figure 6.18 Temporal evolution of scour depth for different discharge variation regimes. Ratio between step height H and the step height at the end of the interval H_{end} for a) DVR1 (STAT) with t_{stat} = total duration of stationary intervals, b) DVR2 (HYD), c) DVR3 for hydrographs and intermediate periods of low flow (HYD+LQ); DVRs are defined in Section 4.4.3

periment HYD and HYD+LQ. Step height increased on average by 6.8 ±3.4% throughout a discharge interval in the STAT experiment (Figure 6.18a) and by 5.5 ±4.6% in the HYD experiment (Figure 6.18b). In the STAT experiment, the final step height was reached already after ~1/8 of the total experimental duration t_{stat} corresponding to 45 minutes in prototype scale. Thus, most changes occurred during this initial phase and the bed mostly remained stable during the remaining time.

Little changes occurred during the ascending limb of the hydrograph until the peak discharge was reached (Start to P1) in the unsteady experiment HYD. The preceding unit discharge, which was approximately 20% lower, was exceeded shortly before the peak discharge was reached and the bed started to adjust. At the end of the peak discharge (P2), i.e., ~20 minutes after P1, the bed adjusted significantly reaching on average higher scour depths compared to the final scour depth. During the first third of the descending limb (1/3 DL) with $q > 2/3\,q_{peak}$, H further increased reaching maximum values 4.9 ±3.7% higher than H_{end}. During the remaining 2/3 of the DL (i.e., $q < 2/3q_{peak}$), H decreased towards H_{end} as sediment most likely deposited in the pools at low discharges. Similar results were observed in the HYD+LQ experiments with intermediate periods of low flows (Figure 6.18c).

Overall, the bed adjusted in the STAT experiment at the beginning of the experiment (i.e., $t \le 1/8\,t_{stat} \approx 45$ minutes) and the system remained stable afterwards. The maximum step height was not substantially higher than H_{end} during any time of the interval. Considering the unsteady hydrographs (HYD and HYD+LQ), the bed mainly adjusted during

the 20-minutes long peak and approximately 15 minutes before and after, i.e., when the preceding peak discharge was exceeded. Step height was ~4.9 ±3.7% higher compared to the final step height at the end of the interval.

Effect of intermediate periods of low flow

This section focuses on bed elevation changes during the stationary intermediate periods of low flow between the hydrographs in HYD+LQ. Prior to the experiments, step height H was expected to further increase as the jet impinges more vertically on the bed during low flow conditions. Figure 6.19 shows the DEM of differences (DoD) normalized with $d_m = 9.0$ cm of the base material before and after the stationary intervals with $q = 2.50$ m^2/s. According to the DoD of the first three intervals (Figure 6.19a-c), the bed elevation changes Δz after the stationary intervals were smaller than $\pm d_m$ for >80% of the total area. However, after larger peak discharges $q \geq 7.50$ m^2/s (Figure 6.19d-f), sediment
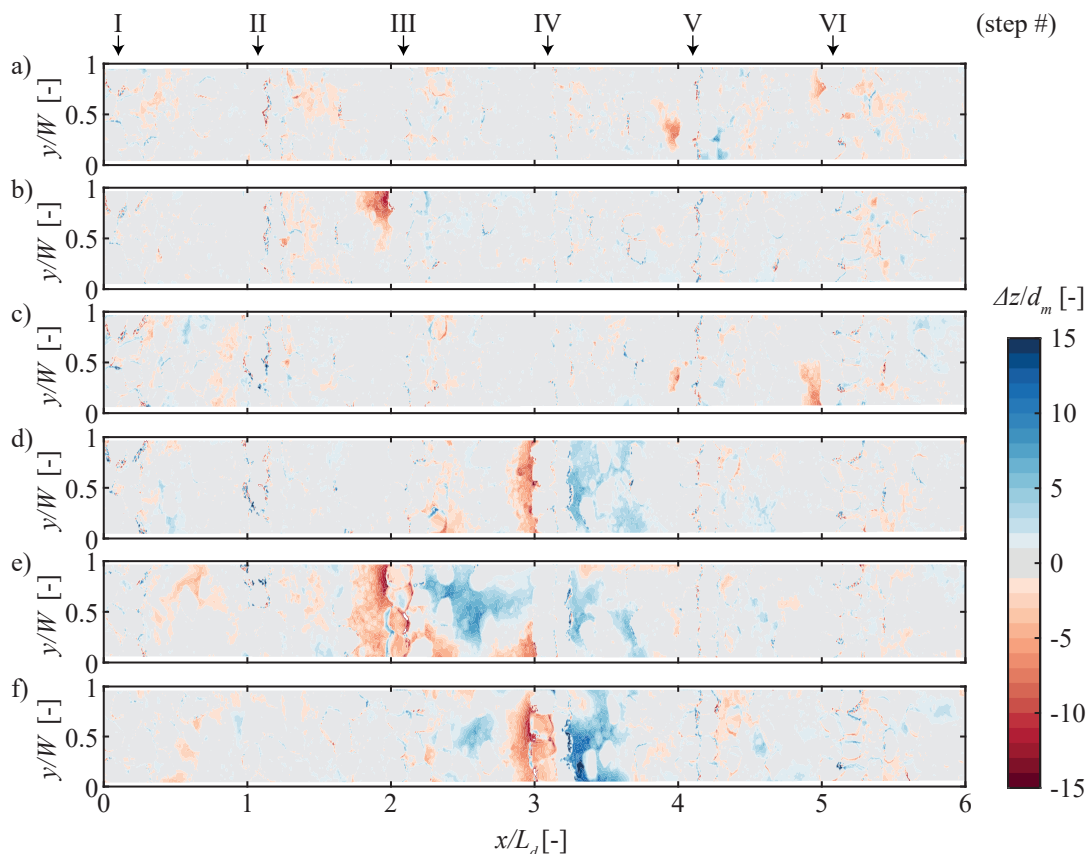

Figure 6.19 Bed elevation changes during low flow periods between hydrographs. Normalized DoD $\Delta z / d_m$ in experiment HYD+LQ before and after the stationary periods ($d_m \approx 9$ cm) for a) $q = 3.25$ m^2/s, b) $q = 5.00$ m^2/s, c) $q = 6.25$ m^2/s, d) $q = 7.5$ m^2/s, e) $q = 8.75$ m^2/s, and f) $q = 10.00$ m^2/s ; steps located at positions $x/L_d = 0, 1, 2, 3, 4, 5$

was eroded during low flow immediately upstream of one of the six steps. Furthermore, sediment was washed out of the pore spaces in between the step-forming blocks leading to flow through the entire step. The majority of the eroded sediment was deposited in the downstream pool. Overall, the intermediate periods of stationary low flow only led to local changes near a few steps and did not significantly alter the bed topography as the bed already adjusted to lower flow conditions during the DL.

6.5.3   Summary on hydrograph shape

Overall, similar results were obtained with the stationary regime (STAT), the unsteady regime (HYD), and the unsteady regime with intermediate periods of low flow (HYD+LQ) regimes:

- The bed remained stable up to q_{stab} = 7.50 ±1.25 m^2/s and maximum Shields ratios $\theta/\theta_c \approx 6$ were obtained irrespective of the discharge regime (Figure 6.16).

- A progressive upstream erosion (PUE) pattern was observed in all three discharge regimes.

- The step height was slightly larger in the unsteady experiments but the differences compared to the STAT experiment were generally smaller than 10% (Figure 6.17).

- The bed elevation changes occurred within the initial 45 minutes during the STAT experiment and shortly before and after peak discharge (20 minutes peak discharge plus 15 minutes before and after) of the HYD and HYD+LQ experiments, i.e., as soon as the preceding peak discharge was exceeded (Figure 6.18).

- In the HYD and HYD+LQ regime, the maximum step height was 4.9 ±3.7% higher during peak flow compared to the final step height, whereas the final step height was already reached after 1/8 of the total duration in the STAT experiment (Figure 6.18).

- Changes in bed elevation were generally smaller than ±d_m in the HYD+LQ experiment after the intermediate periods of low flow (Figure 6.19).

Referring to research questions B3 (Section 1.3), the hydrograph shape did not significantly alter bed stability and failure mechanisms. Neither did a longer peak flow duration nor a longer low flow duration substantially decrease step stability or alter the failure mechanisms of the artificial step-pool sequence. However, the step height tended to be slightly

larger in the unsteady regimes, even though the differences were small. Larger step heights represent more conservative conditions, even though it did not affect step stability in the present cases. Based on these results, the discharge regime HYD was selected for all subsequent experiments.

6.6 Bed stability

The present section summarizes the findings regarding bed stability of artificial step-pool systems. First, an overview of all experiments is provided followed by separate discussions on the effects of sediment supply, base material, bed slope, channel width, step-forming block size, block arrangement, drop height, and block placement density. Herein, research questions B4 and B5 (Section 1.3) focusing on the effect of sediment supply and other parameters on bed stability of artificial step-pool sequences are addressed.

Table 6.3 provides an overview of the critical unit discharge q_f(x%) at which the bed slope decreased by more than x%. Herein, the unit discharge q_f(1%) was selected to compare the experiments subsequently, thus, also $q_f(\geq 1.5\%)$ are referred to q_f(1%) in case bed slope decreased directly by more than 1.5%. Overall, the investigated artificial step-pool systems failed at unit discharges ranging from q_f(1%) = 2.50 to 15.00 m^2/s. According to the the data collected from eight steep streams in Switzerland and Italy, the unit discharge with recurrence interval (RI) of 100 years q_{100} lies between ~6.0 to 8.0 m^2/s for bed slopes $0.04 \leq S \leq 0.08$ investigated in this study (Table 3.2 and Figure 3.1). Consequently, the investigated systems sustained discharge smaller than a reference q_{100} but in some cases also much higher compared to q_{100}. However, these estimates for q_{100} only serve as an indicator and vary considerably depending on the catchment.

Table 6.3 summarizes whether a gradual or an abrupt system failure mode was observed during the experiments (Section 6.4.5). Overall, 20 out of 29 experiments showed an abrupt and the remaining 9 experiments a gradual failure. An abrupt system failure occurred in all sediment feed (SF) experiments and only experiments with clear-water (CW) conditions failed gradually. Thus, sediment supply has a major effect on the stability and failure mode of step-pool sequences, which is elaborated in the following section.

Table 6.3 Overview of stability and failure mode of artificial step-pool sequences. All experiments were conducted with the HYD regime and BASE step-pool configuration unless stated differently; $q_f(1\%)$ in bold; parameter definition according to Table 4.9

ID	d_{84} [m]	S [-]	W [m]	M_B [t]	H_d [m]	L [m]	TC [%]	$q_f(x\%)$ [m²/s] 0.5%	1.0%	1.5%	2.0%	Failure
Discharge variation regime (DVR) and sediment feed (SF)												
DVR1[α]	0.18	0.08	6	8.0	1.12	14.0	0	→	**8.75**	11.25		abrupt
DVR2	0.18	0.08	6	8.0	1.12	14.0	0	→	**8.75**	11.25		abrupt
DVR3[β]	0.18	0.08	6	8.0	1.12	14.0	0	→	→	**10.00**	11.25	abrupt
DVR4[β]	0.18	0.08	6	8.0	1.12	14.0	20	→	**13.75**	→	15.00	abrupt
SF0	0.18	0.06	6	4.6	0.75	12.5	0	→	→	**6.67**		abrupt
SF1	0.18	0.06	6	4.6	0.75	12.5	10	→	→	→	**10.00**	abrupt
SF2	0.18	0.06	6	4.6	0.75	12.5	20	→	→	→	**11.67**	abrupt
Bed slope and channel width (SW)												
SW1	0.18	0.04	6	4.6	0.75	18.8	0	12.50	→	**15.00**		gradual
SW2	0.18	0.04	12	4.6	0.50	12.5	0	12.50	→	**15.00**		gradual
SW3	0.18	0.06	9	4.6	0.75	12.5	0	→	→	**8.33**		abrupt
SW4	0.18	0.06	12	4.6	0.75	12.5	0	8.33	→	**10.00**	11.67	gradual
SW5	0.18	0.06	12	4.6	0.75	12.5	20	→	→	→	**10.00**	abrupt
SW6	0.18	0.08	6	4.6	0.75	9.4	0	→	**6.25**	7.50		~abrupt
SW7	0.18	0.08	12	4.6	0.75	9.4	0	5.00	→	**6.25**		gradual
Block weight (BW)												
BW1	0.18	0.08	6	4.6	1.12	14.0	0	→	**2.50**	5.00	7.50	~gradual
BW2	0.18	0.08	6	4.6	1.12	14.0	20	→	→	→	**8.75**	abrupt
BW3	0.18	0.08	6	6.3	1.12	14.0	0	6.25	→	**7.50**	8.75	~gradual
BW4	0.18	0.08	6	6.3	1.12	14.0	20	10.00	→	→	**11.25**	abrupt
BW5	0.18	0.08	12	8.0	1.12	14.0	0	5.00	→	**6.25**	7.50	~gradual
BW6	0.18	0.06	12	8.0	0.75	12.5	0	6.67	→	→	**10.00**	abrupt
Drop height (DH)												
DH1	0.18	0.06	6	4.6	1.12	18.7	0	5.00	**6.67**	8.33	10.00	gradual
DH2	0.18	0.06	6	4.6	1.12	18.7	20	→	→	**8.33**		abrupt
DH3	0.18	0.06	6	4.6	0.40	6.7	0	→	**8.33**	13.33		gradual
Block arrangement (BA)												
BA1[a]	0.18	0.06	6	4.6	0.75	12.5	0	→	→	**10.00**		abrupt
BA2[b]	0.18	0.06	6	4.6	0.75	12.5	0	→	**11.67**			~abrupt
BA3[c]	0.18	0.08	12	8.0	1.12	14.0	0	6.25	→	→	**8.75**	abrupt
Base sediment mixture (SM)												
SM1	0.21	0.06	9	4.6	0.75	12.5	0	→	→	→	**10.00**	abrupt
SM2[a]	0.21	0.06	9	4.6	0.75	12.5	0	→	→	**10.00**		abrupt
SM3[a]	0.21	0.06	9	4.6	0.75	12.5	20	→	→	→	**11.67**	abrupt

Discharge regimes [α]STAT, [β]HYD+LQ; step-pool geometry [a]PYR, [b]PYR+SP, [c]CUR

6.6.1   Effect of sediment supply

Research question B4 focuses on the effect of sediment supply on bed stability (Section 1.3). CW conditions were assumed to represent critical conditions regarding step stability as scour depths were hypothesized to be larger compared to SF conditions. First, the effect of sediment supply rates is investigated. Second, differences in reach-averaged flow velocities and the implications on the auxiliary blocks, located in between the step-forming blocks, are analyzed.

Sediment supply rate

The SF-series investigated the effect of different sediment supply rates expressed as percentage of the transport capacity (TC) while all other parameters were kept constant (Table 6.3). The experiments SF0, SF1, and SF2 were conducted under CW conditions, supplying ~10% TC, and ~20% TC of the base sediment mixture, respectively. The corresponding peak sediment supply rates q_s are summarized in Table 4.8. Figure 6.20 shows the decrease of bed slope ΔS, the Shields ratio θ/θ_c, and the reach-averaged flow velocity v as a function of unit discharge q. Experiment SF0 (CW) was the least stable experiment with $q_f(1\%) = 6.67$ m^2/s. The sediment feed experiments SF1 and SF2 sustained higher discharges failing at $q_f(1\%) = 10.00$ and 11.67 m^2/s, respectively. Furthermore, higher Shields ratios θ/θ_c were attained in SF experiments mainly because the bed slope was kept close to its initial value ($S \approx S_{ini}$) at higher discharges. Note that v was similar in both experiments with sediment feed (SF1 and SF2) as long as $S \approx S_{ini}$ (i.e., $q \leq 8.33$ m^2/s). This indicates that bed roughness, i.e., scour depth, was also similar in experiments SF1
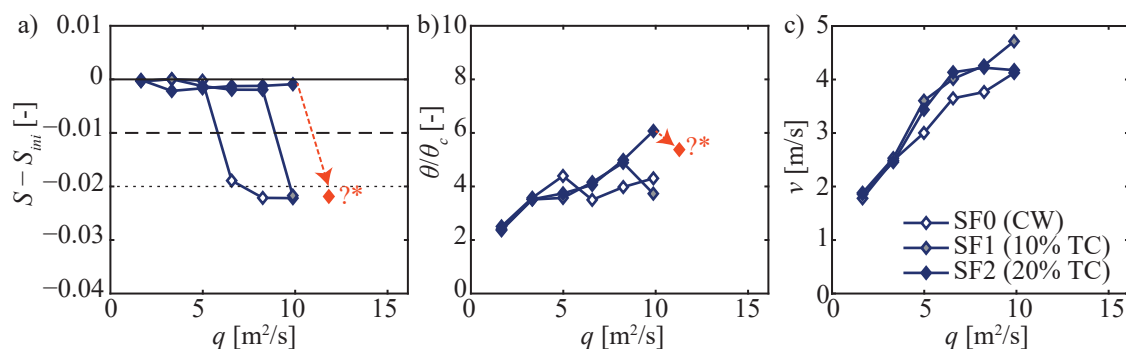
Figure 6.20 Effect of sediment feed on a) bed slope reduction $\Delta S = S - S_{ini}$, b) Shields ratio θ/θ_c, and c) reach-averaged flow velocity v for experiments SF0, SF1, and SF2 ($S = 0.06$, $W = 6$ m, $H_d = 0.75$ m, $M_B = 4.6$ t), CW = clear-water conditions, TC = transport capacity; *Experiment stopped because scour depth reached flume invert

and SF2. Consequently, it was assumed that similar results are obtained for higher sediment supply rates, i.e., >20% TC, compared to the SF1 and SF2 experiments.

Overall, the increase in bed stability in SF experiments may be related to differences in scouring mechanisms, block exposure, and jamming effects:

- Scour depth decreased by approximately 10% in SF compared to CW experiments (see also Section 6.8.4) confirming results of previous studies (e.g. Volkart 1972; Marion *et al.* 2006; VAW 2018). The step toe was destabilized at a lower discharge in CW experiments leading to a step failure associated with scouring (Table 6.2).

- Tilting processes were more likely to occur in CW experiments due to the higher exposure of the step-forming blocks (Figure 6.11). Erosion of the base material from the pore spaces in between the step-forming blocks occurred during sediment-starved conditions leading to flow through the step. Consequently, more base material was washed out upstream of the step increasing the exposure of the top row blocks.

- Jamming effects further increased step stability in sediment supply experiments as the pores between the step-forming blocks were filled with base material. The largest grains of the base material had diameters ranging from $d_{100} = 0.40$ and 0.64 m with $d_{84} \approx 0.20$ m. Thus, the large grains of the base material potentially interlocked with the step-forming blocks creating force chains within the step but also between the step and the sidewalls, diverting some of the forces acting on the boulder to the sidewalls.
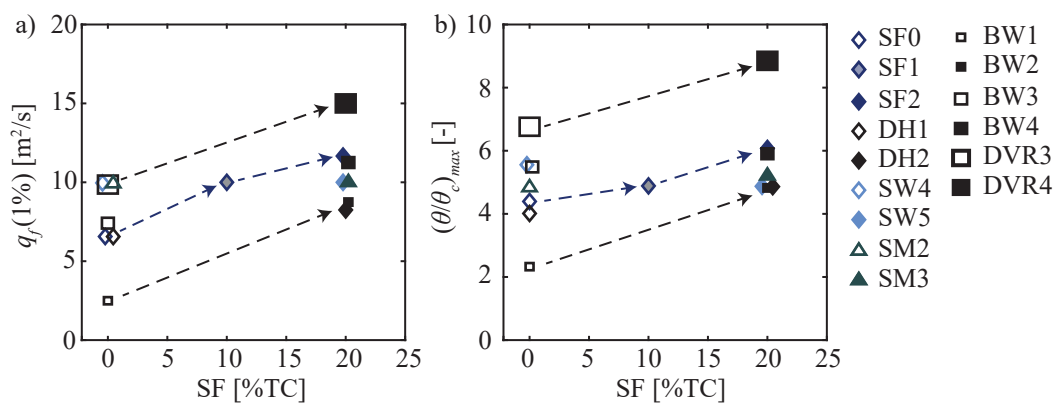
Figure 6.21 Effect of sediment feed rate expressed as percentage of the calculated transport capacity (% TC) on a) discharge of system failure $q_f(1\%)$ and b) maximum Shield ratio $(\theta/\theta_c)_{max}$; parameters of the experiments are indicated in Table 6.3

Six additional pairs of experiments were conducted with both CW and SF conditions (i.e., DVR3 and DVR4, SW4 and SW5, BW1 and BW2, BW3 and BW4, DH1 and DH2 and SM2 and SM2, see Table 6.3) confirming the above presented results. Figure 6.21 plots $q_f(1\%)$ and $(\theta/\theta_c)_{max}$ as a function of the sediment supply rate expressed as percentage of TC. The dashed lines indicate the trajectories for selected experiments showing that $q_f(1\%)$ and $(\theta/\theta_c)_{max}$ both increased with increasing sediment feed.

Reach-averaged flow velocity

Figure 6.22 shows the results of experiments DVR3 (CW) and DVR4 (20% TC) in more detail. Both tests were conducted with $S = 0.08$ and step-forming blocks with $M_B = 8.0\,\text{t}$. Experiment DVR3 (CW) failed earlier at $q_f(1\%) = 10.00\,\text{m}^2/\text{s}$ compared to the SF experiment DVR4 failing at $13.75\,\text{m}^2/\text{s}$. Flow velocity was generally higher in experiment DVR4 with SF compared to the CW experiment DVR3, particularly for discharges ranging from $q = 3.75$ to $8.75\,\text{m}^2/\text{s}$ (shaded areas in Figure 6.22). However, v decreased starting from $q \geq 7.50\,\text{m}^2/\text{s}$ in the DVR4 experiment as the auxiliary blocks, reducing the scour extent, were mobilized leading to an increase in scour depth.
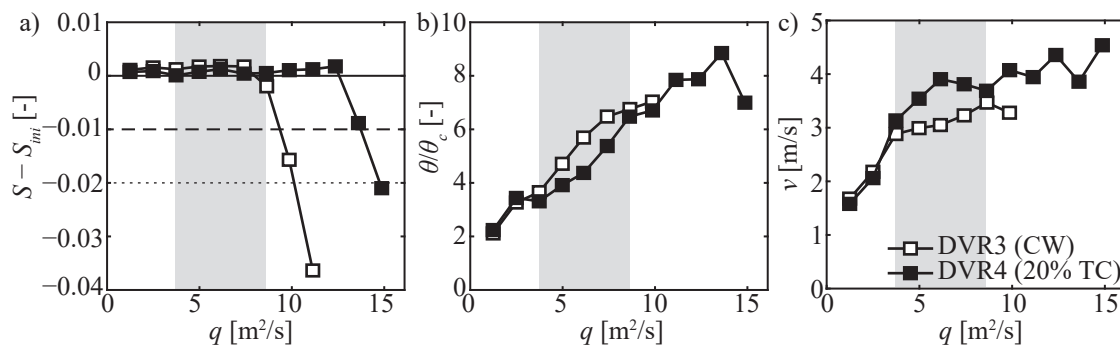
Figure 6.22 Comparison of CW(DVR3) and SF(DVR4) conditions showing a) bed slope reduction $\Delta S = S - S_{ini}$, b) Shields ratio θ/θ_c, and c) reach-averaged flow velocity v for experiments DVR3 and DVR4 conducted at $S = 0.08$, $W = 6\,\text{m}$, $H_d = 0.75\,\text{m}$, $M_B = 8.0\,\text{t}$

The mobilization of auxiliary blocks is illustrated in Figure 6.23 showing orthophotos of the DVR4 (20% TC) experiment. Therein, the auxiliary blocks were transported one or several steps downstream and occasionally left the test reach during intervals with discharge $q \geq 7.50\,\text{m}^2/\text{s}$. A similar process was observed for self-organizing step-pool systems by Hohermuth and Weitbrecht (2018) who found the near-bed velocity to increase in sediment supply experiments potentially destabilizing large step-forming boulders. The white circles in Figure 6.23b indicate pools in which one or several auxiliary blocks were trans-
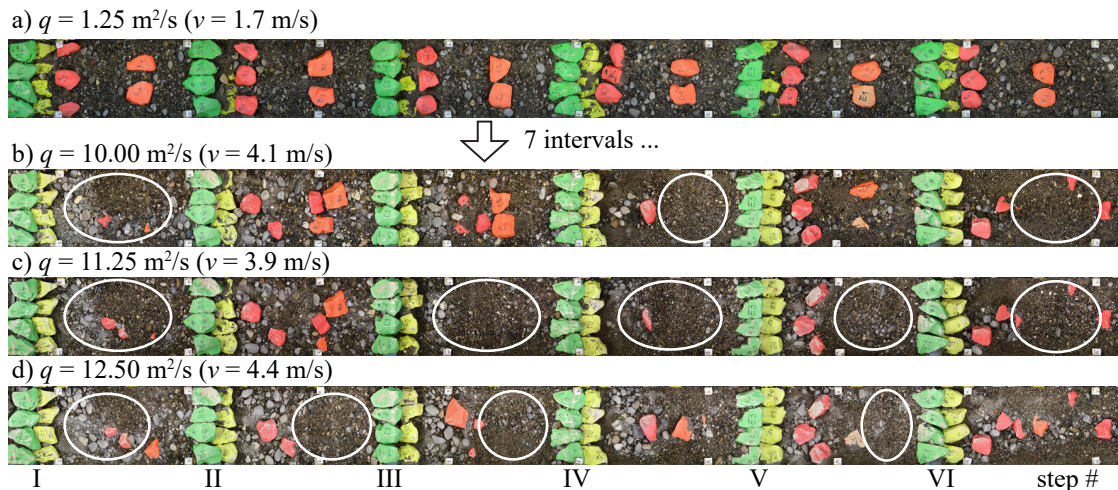
a) $q = 1.25$ m²/s ($v = 1.7$ m/s)

7 intervals ...

b) $q = 10.00$ m²/s ($v = 4.1$ m/s)

c) $q = 11.25$ m²/s ($v = 3.9$ m/s)

d) $q = 12.50$ m²/s ($v = 4.4$ m/s)

| I | II | III | IV | V | VI | step # |

Figure 6.23 Mobilization of auxiliary blocks in sediment supply experiments. Orthophotos of experiment DVR4 with 20% TC for a) first interval $q = 1.25$ m²/s, b) $q = 10.00$ m²/s, c) $q = 11.25$ m²/s, d) $q = 12.50$ m²/s; white circles indicate that auxiliary blocks were transported downstream

ported further downstream. Scour pool depth increased due to the absence of the auxiliary block resulting in an increase in bed roughness, while in turn led to the observed decrease in flow velocity. The auxiliary blocks mobilized upstream were deposited either in one of the downstream pools or left the test reach. These results demonstrate that larger auxiliary blocks are required in SF experiments to ensure that they remain in the pools fulfilling their purpose of reducing the scour extent.

Summary on the effect of sediment supply

The results confirmed the hypothesis associated with research question B4 (Section 1.3) that CW conditions represent the critical condition regarding step stability. The main reasons for the increase in step stability with increasing sediment feed was related to the exposure of the step-forming blocks in CW experiments (Figure 6.11) making tilting more likely, the decrease in scour pool depths in SF experiments (Section 6.8) decreasing the risk of step failure due to scouring, and more pronounced jamming effects in SF experiments increasing structural stability. From a practitioner's perspective, CW experiments provide a conservative estimate for the stability of artificial step-pool systems. However, the planners have to consider that the auxiliary blocks located in the pools, having the purpose of reducing the scour extent, were mobilized in SF experiments due to the increase of near-bed velocities (Figure 6.23). In natural streams, which hardy experience sediment-starved conditions during large floods, an abrupt failure is likely to occur because all sediment supply experiments failed abruptly (Table 6.3).

6.6.2   Effect of base sediment mixture

Two base mixtures were investigated herein. The majority of the experiments (90%) were conducted with base sediment mixture M64 and the remaining 10% with M40. Base sediment mixtures M64 and M40 had maximum grain diameters d_{max} = 0.64 and 0.40 m, respectively. To obtain M40, the coarsest 5% of the grains were removed from M64. Afterwards, grains with $16 < d < 40$ cm were added to M40 to obtain the same $d_m = 0.09$ m as in M64. Base sediment mixtures M64 and M40 have a characteristic grain diameter $d_{84} = 0.18$ and 0.21 m, respectively; the composition is detailed in Section 4.4.1. The base sediment mixture was assumed to have little effect on the stability of artificial step-pool sequences as the large step-forming blocks are dominant, (e.g., regarding flow resistance, Section 6.3.1, or bed stability, Section 6.6.5). Nevertheless, differences in base material may lead to different scour pool depths triggering step failure at a smaller discharge.

Figure 6.24 shows the bed slope reduction ΔS, Shields ratios θ/θ_c, and reach-averaged flow velocity v as a function of q for experiment SW3 and SM1 with base sediment mixtures M64 and M40, respectively (Table 6.3). These experiments were both conducted with $S = 0.06$, $W = 9$ m, $H_d = 0.75$ m, $M_B = 4.6$ t while only varying the base sediment mixture. The step-pool sequences failed at $q_f(1\%) = 8.33$ and 10.00 m²/s in experiment SW3 (M64) and SM1 (SM40), respectively, and similar maximum Shields ratios $(\theta/\theta_c)_{max} \approx 5$ were obtained. Mean flow velocities v were also comparable in both experiments. Consequently, the experiments were similarly stable as this small difference may be attributed to the inherent heterogeneity of the experiments.

Moreover, experiments BA1 (M64) and SM2 (M40) were compared, which only differed in terms of base material and channel widths (Figure 6.25). They were conducted
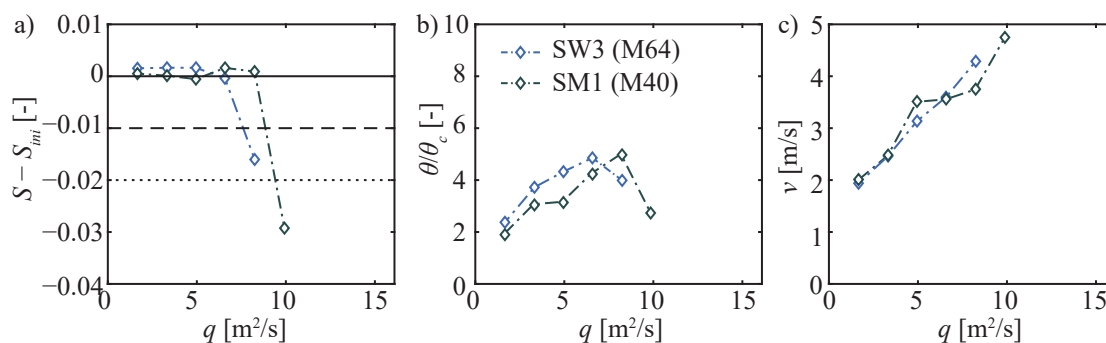

Figure 6.24 Effect of base sediment mixture M64 (SW3) and M40 (SM1) on a) bed slope reduction $\Delta S = S - S_{ini}$, b) Shields ratio θ/θ_c, and c) mean flow velocity v; parameters according to Table 6.3

with $S = 0.06$, $H_d = 0.75$ m, and $M_B = 4.6$ t using the PYR step-pool configuration (Figure 3.9). Experiment BA1 was conducted with $W = 6$ m and SM2 with $W = 9$ m. The system failure occurred at $q_f(1\%) = 10.00$ m^2/s leading to similar Shields ratios for both experiments confirming that the base sediment mixture did not affect step stability.
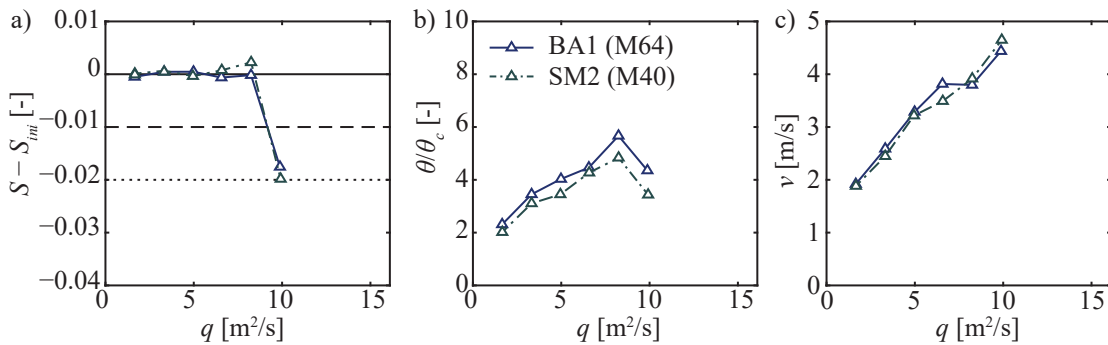

Figure 6.25 Effect of base sediment mixture M64 (BA1) and M40 (SM2) on a) bed slope reduction $\Delta S = S - S_{ini}$, b) Shields ratio θ/θ_c, and c) mean flow velocity v; parameters according to Table 6.3

Overall, the base mixture did not alter bed stability of artificial step-pool systems. The size of the large step-forming blocks dominated over the composition of the base material. However, both base sediment mixtures were primarily varied with regard to their maximum grain diameter d_{max} but had a similar geometrical standard deviation σ_g, the same mean diameter d_m, and only slightly different d_{84}. Using a sediment mixture with more pronounced differences in d_{84} may have an effect on the structural stability.

The ratio between the equivalent spherical grain diameter of the step forming blocks and the characteristic diameter of the base material D_{eq}/d_{84} is important to predict failure modes of bimodal sediment mixtures (Section 2.4.5). Herein, d_{84} was used to characterize the base material as grain sorting occurred at small discharges leading to the formation of an armour layer in the pools. According to Raudkivi and Ettema (1982), direct erosion of the blocks is expected for $D/d_{84} < 6$ as the large grains are highly exposed to the flow and block subsidence at $D/d_{84} > 17$ as the fine grains underneath are eroded prior to the mobilization of the large blocks. The ratio D_{eq}/d_{84} was in the range of 6.7 to 10.6 for all experiments conducted herein complying with the criteria of Raudkivi and Ettema (1982). These criteria are particularly important for the auxiliary blocks, which are loosely packed and directly placed on the base material. It is important to consider these ratios D_{eq}/d_{84} in the design of artificial step-pool systems.

6.6.3   Effect of bed slope

The present section addresses the effect of bed slope on the stability of artificial step-pool systems. Figure 6.26 shows $q_f(1\%)$ and $(\theta/\theta_c)_{max}$ as a function of bed slope S. Therein, experiments SW1 to SW7, SF0, and SF2 are presented which were conducted for bed slopes ranging from 0.04 to 0.08. Experiment SW1 and SW2 ($S = 0.04$) failed at $q_f(1\%) = 15$ m^2/s, while the system failure of experiments SW6 and SW7 ($S = 0.08$) was observed earlier at $q_f(1\%) = 6.25$ m^2/s. The remaining step-pool sequences with $S = 0.06$ failed at $q_f(1\%)$ ranging from 6.67 to 11.67 m^2/s. Note that more experiments were conducted at $S = 0.06$ and SF experiments were included, which were more stable compared to CW experiments (Section 6.6.1). Nevertheless, the artificial step-pool sequences failed at higher q_f for smaller bed slopes.

The maximum Shields ratio $(\theta/\theta_c)_{max}$ was almost independent of S. First, and in contrast to the unit discharge, bed shear stress inherently accounts for the increase in shear with increasing slope. Second, θ_c was calculated with Equation (2.42) proposed by Lamb *et al.* (2008) accounting for higher θ_c in steep channels, i.e., channels with low relative submergence. The Shields ratio accounts for the effect of bed slope as experiments with similar boundary conditions reached similar θ/θ_c. Within the tested range, S did not significantly alter the flow regime (i.e., generally subcritical flow $\mathsf{F} < 1$), scouring processes, or failure mechanisms.
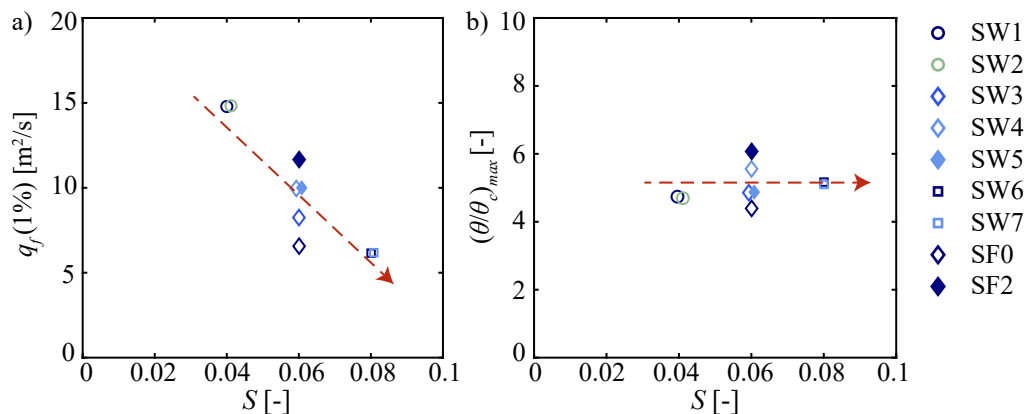
Figure 6.26 Effect of bed slope on bed stability: a) discharge of system failure $q_f(1\%)$ and b) maximum Shield ratio $(\theta/\theta_c)_{max}$ as a function of the bed slope S for the SW-series and experiment SF0 and SF2; marker color refers to different channel widths, empty markers to CW conditions, and filled markers to SF conditions (parameters are defined in Table 6.3)

6.6.4   Effect of channel width

Bed morphology

Bed morphology is assessed prior to the effect of channel width on the stability of artificial step-pool systems. The emergence of bed forms such as alternate bars can have a drastic impact on channel stability. The stress on the channel banks and bed locally increases due to the oscillating flow in horizontal direction in case of alternate bar formation. Bank erosion potentially leads to step failure, particularly when the step-forming blocks and the banks interlock with each other. Herein, all experiments were conducted in a rectangular channel with fixed smooth sidewalls and bank stability assessment was not part of the present study. Consequently, the formation of such bed forms needs to be considered carefully when planning artificial step-pool sequences.

Weichert (2006) observed macro-scale structures such as diagonal bars or even braided channel beds. His experiments were conducted with bed slopes $0.05 \leq S \leq 0.13$ and for jamming ratios $3.3 < W/d_{84}$ 13.3. The diagonal bars were observed in wide and steep channels leading to small flow depths (i.e. W/h is large). Figure 6.27 shows the regime theory derived by da Silva (1991) and extended by Zarn (1997). The transition from one bed form to another occurs gradually and not as abrupt as suggested by the diagram. Therein, the bed forms observed by Weichert (2006) agreed well with the criteria using d_m of
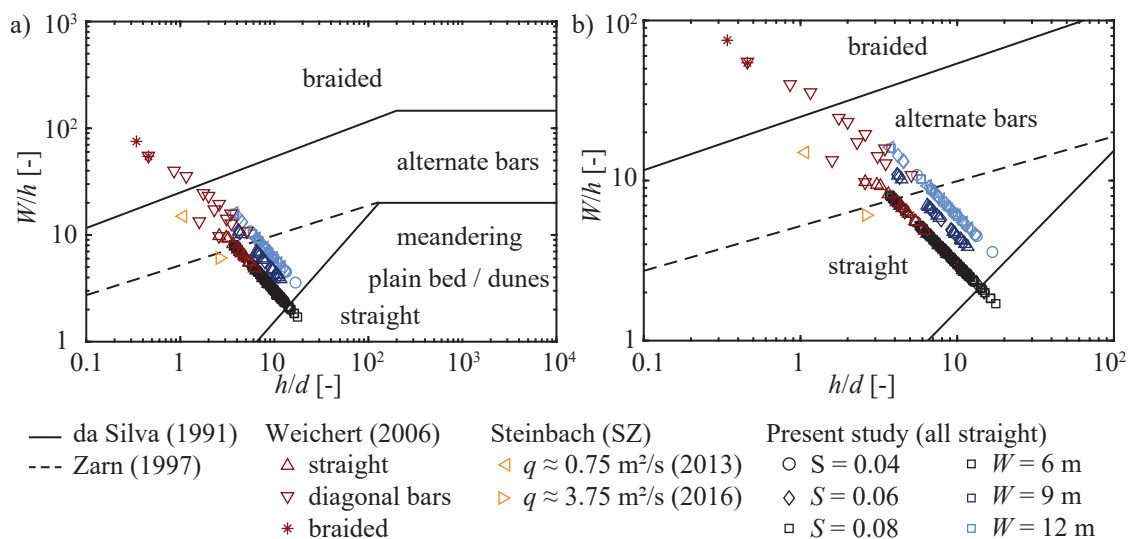
Figure 6.27 Regime theory adapted from Weichert (2006), with criteria by da Silva (1991) and Zarn (1997), showing field data of the Steinbach stream (Beffa 2016) and data of the present study (marker shape indicates slope and color indicates width)

the fully mixed sediment. Moreover, two data points from field observations of the Steinbach case study (Section 3.4.5), containing artificial step-pool sequences, are presented. These points correspond to the 2013 and 2016 floods with $q \approx 0.75$ and 3.75 m^2/s, respectively (Beffa 2016). The flood in 2013 destabilized the system as the banks eroded due to the formation of alternate bars leading to horizontal oscillation of the flow. Consequently, the observations from Steinbach correspond well with the regime theory by da Silva (1991) and Zarn (1997).

In the present study no alternate bars developed at any time, confirmed by visual observation. Comparing the artificial step-pool data with the regime theory in Figure 6.27 shows that some of the data fall within the alternate bar region even though no such bed forms were observed. They correspond to experiments in the wide channel ($W = 12$ m) and during intervals with small discharges, i.e., small flow depths and large aspect ratios W/h. Note that d_{84} of the base material was used as the bed coarsened already in intervals with smaller discharge armouring the bed. The flow was straightened at least at the step crest defined by the step-forming blocks. The formation of alternate bars may be inhibited if step spacing is smaller than the wave length of alternate bars. Small discharges were not capable of moving the step-forming boulders, thus, this flow straightening was maintained and the formation of alternate bars suppressed. Nevertheless, it is recommended to avoid a regime in which alternate bar formation is expected according to the criteria by da Silva (1991) and Zarn (1997) particularly for discharges capable of moving the step-forming blocks.

Jamming ratio and structural stability

Width controls the jamming ratio W/D, which is an important parameter for bed stability in self-organizing step-pool systems (Section 3.3.4), and bed stability was found to increase for small jamming ratios $W/D < 6$ (Zimmermann *et al.* 2010). Herein, the jamming ratio equals $W/D_{eq} \approx 4$, 6, and 8 for experiments conducted at $W = 6$, 9, and 12 m, i.e., in most of the experiment 4, 6, and 8 step-forming blocks were used in each row (Section 6.6.6). Consequently, the steps in the narrow channels were expected to sustain higher bed shear stresses compared to wide channels.

The unit discharge $q_f(1\%)$ and the Shields ratio $(\theta/\theta_c)_{max}$ are presented as a function of channel width W in Figure 6.28. Therein, the same experiments are compared as in the former section assessing the effect of bed slope (Section 6.6.3). Channel width W
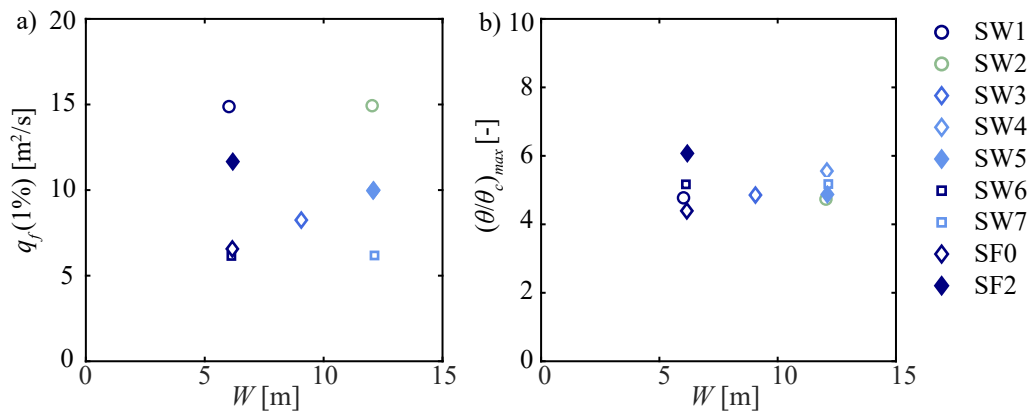
Figure 6.28 Effect of channel width on bed stability: a) discharge of system failure $q_f(1\%)$ and b) maximum Shield ratio $(\theta/\theta_c)_{max}$ as a function of channel width W for the SW-series and experiment SF0 and SF2; marker shape refers to bed slope, empty markers to CW conditions, and filled markers to SF conditions (parameters are defined in Table 6.3)

and $q_f(1\%)$ did not correlate well and the scatter was mainly attributed to variations in bed slope. Moreover, $(\theta/\theta_c)_{max}$ was almost constant for experiments with channel widths ranging from $W = 6$ to 12 m indicating that the stability of the artificial step-pool system was independent of channel width. Consequently, the jamming ratio is less relevant in artificial step-pool sequences compared to self-stabilizing step-pool systems. Step formation in the self-organizing system induced by jamming requires mobilization and transport of the large blocks. They preferentially deposit in narrow or narrowing regions due to block-sidewall interlocking. However, in artificial step-pool system, the steps are built and interlocking of the step-forming blocks is externally imposed on the system by placing the blocks tightly next to each other. Consequently, the jamming ratio $W/D_{eq} < 6$ is of lesser importance in artificial compared to self-organizing systems. The effect of block placement within the steps leading to jamming is further discussed in Section 6.6.6.

6.6.5   Effect of step-forming block size

The step-forming block size was assumed to be an important parameter for the stability of artificial step-pool sequences. Figure 6.29 relates bed slope reduction ΔS, Shields ratio θ/θ_c, and mean flow velocity v to the unit discharge q for experiments BW1, BW3, and DVR2 with a mean block weight of $M_B = 4.6$, 6.3, and 8.0 t, respectively (Section 4.4.2). These experiments were conducted with $S = 0.08$, $W = 6$ m, and $H_d = 1.12$ m and clear-water (CW) conditions. Both $q_f(1\%)$ and $(\theta/\theta_c)_{max}$ increased with increasing M_B indicating that block weight is an important parameter regarding step stability. The system failure occurred at $q_f(1\%) = 2.50$ m^2/s in experiment BW1 ($M_B = 4.6$ t) because the step-forming
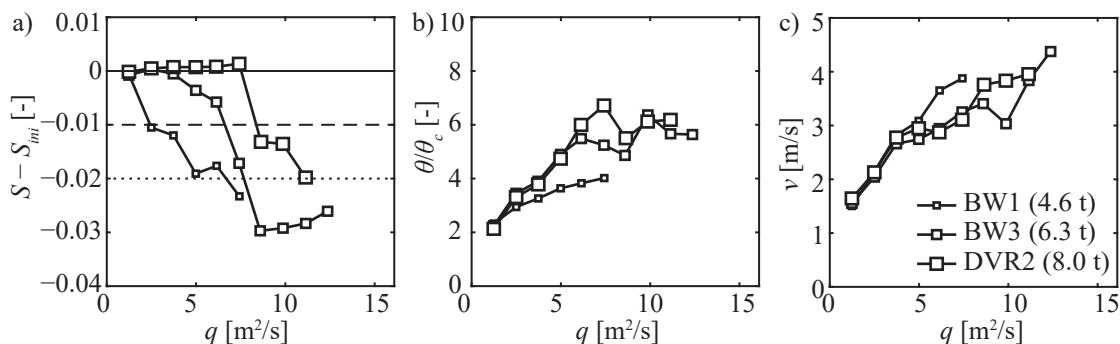
Figure 6.29 Effect of the step-forming block weight on bed stability: a) bed slope reduction $\Delta S = S - S_{ini}$, b) Shields ratio θ/θ_c, and c) reach-averaged flow velocity v as a function of q for experiments BW1, BW3, and DVR2; marker size reflects block weight; parameters according to Table 6.3

blocks were already mobilized at this discharge. On the contrary, all steps in experiment DVR2 ($M_B = 8.0$ t) remained at their initial positions up to $q = 8.25$ m²/s.

Figure 6.30 compares $q_f(1\%)$ and $(\theta/\theta_c)_{max}$ of the entire BW-series including the previously discussed experiments DVR2 to DVR4 and SF0 (parameters see Table 6.3). The system failure occurred between $q_f(1\%) = 2.5$ and 8.75 m²/s for step-pool sequences with $M_B = 4.6$ t and between $q = 6.25$ and 15.0 m²/s for $M_B = 8.0$ t. The steps consisting of the largest blocks sustained discharges approximately twice as high. The scatter was related to the variation of other parameters like sediment supply (Section 6.6.1), bed slope (Section 6.6.3), or step spacing (Section 6.6.7). Furthermore, experiments with large step-forming blocks sustained higher maximum Shields ratios $(\theta/\theta_c)_{max}$ ranging from approximately 2.3 to 4.8 and from 5.4 to 8.8 for $M_B = 4.6$ and 8.0 t, respectively. The scatter was large in experiments with $M_B = 8.0$ t between experiments DVR2, DVR3, and
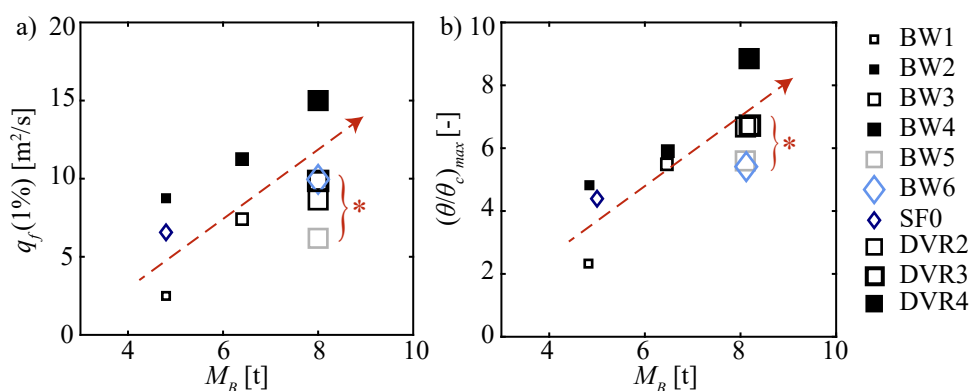

Figure 6.30 Effect of step-forming block weight M_B on a) critical discharge in terms of failure $q_f(1\%)$ and b) maximum Shields ratio θ/θ_c; *scatter between DVR2, DVR3 and BW5 attributed to jamming effects (see Section 6.6.6)

BW5 with similar boundary conditions ($S = 0.08$, $H_d = 1.12$ m, $M_B = 8.0$ t). This scatter is related to the jamming effects which are detailed in Section 6.6.6.

Overall, block weight M_B was the most important parameter controlling the stability of artificial step-pool sequences. The upper row block in the step is more exposed to the flow and therefore more susceptible for entrainment or tilting. Consequently, it is recommended to use the largest blocks in the upper row of the step.

6.6.6 Effect of block arrangement

The plan view shape of the step was changed from straight to a curved arrangement (CUR, Figure 4.11b). Experiment BA3 (CUR) was tested in the wide channel ($W = 12$ m) with steps consisting of eight blocks curved against flow direction to promote interlocking of the step-forming blocks increasing structural stability. The results were compared to experiment BW5 using 7 instead of 8 blocks preventing jamming effects. According to Figure 6.31a, system failure of BA3 (CUR) occurred at higher discharges $q_f(1\%) = 8.75$ m^2/s compared to the corresponding BW5 experiment failing at $q_f(1\%) = 6.25$ m^2/s. The curved step configuration BA3 (CUR) was equally stable as experiment DVR2 in the narrow channel ($W = 6$ m) using 4 blocks tightly placed side-by-side. Consequently, jamming of the step-forming blocks increased step stability but arching the steps did not further increase stability compared to jammed linear steps. Contrary to self-organizing step-pool systems, jamming effects are not restricted to channels with small jamming ratios $W/D \leq 6$ but depends on the (tight) placement of the step-forming blocks.

Moreover, block arrangement was adapted to prevent early step failures related to tilting or scouring as step failures attributed to these mechanisms accounted for approxim-
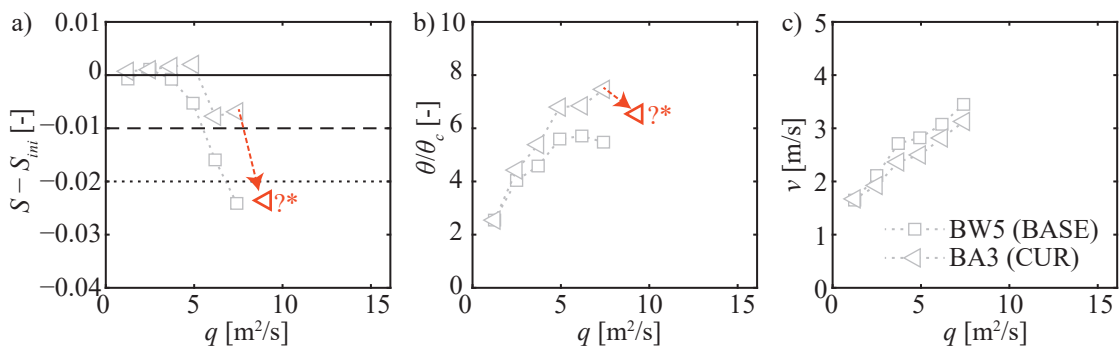

Figure 6.31 Effect of a curved step configuration on: a) bed slope reduction $\Delta S = S - S_{ini}$, b) Shields ratio θ/θ_c, and c) mean flow velocity v for experiments BW5 (CUR) and BA3 (BASE); parameters according to Table 6.3

ately 90% of observed step failures (Figure 6.10). Therefore, an additional block row was added upstream of the step (PYR, Figure 4.11d). On the one hand, the upper block row was less exposed reducing the risk of tilting in flow direction. On the other hand, the blocks forming the upper row were supported by the blocks underneath, thus, tilting against flow direction was also less likely to occur. The PYR configuration was additionally reinforced by adding two more block rows at the step toe of the BASE configuration (PYR+SP, Figure 4.11e), acting as scour protection. Experiment SF0 with the corresponding BASE configuration was used as a reference.

According to Figure 6.32a, step stability increased in both experiments BA1 (PYR) and BA2 (PYR+SP) with $q_f(1\%) = 10.00$ and 11.67 m^2/s compared to the reference experiments SF0 (BASE) with $q_f(1\%) = 6.67$ m^2/s. Moreover, higher maximum Shields ratios were obtained in the PYR and PYR+SP experiments (Figure 6.32b). Mean flow velocity v increased similarly in all three experiments indicating similar bed roughness, i.e., scour pool depths.
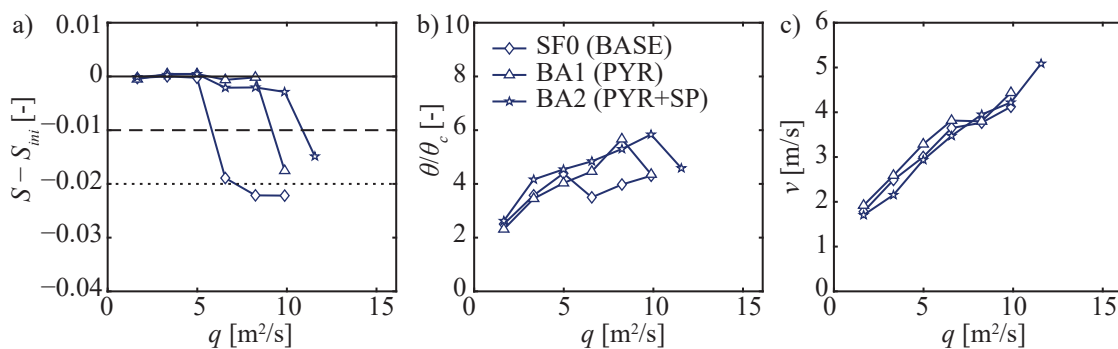

Figure 6.32 Effect of a PYR and PYR+SP configurations on: a) bed slope reduction $\Delta S = S - S_{ini}$, b) Shields ratio θ/θ_c, and c) mean flow velocity v for experiments SF0, BA1, and BA2; parameters according to Table 6.3

Overall, interlocking of the step-forming blocks (i.e., jamming effects) increased step stability. These jamming effects are attained either by a tight placement of the blocks in narrow channels or by a curved shape of the step. Moreover, step stability was further increased by using the PYR and PYR+SP configurations inhibiting step failure due to tilting or scouring at small discharges. However, these configurations are related to higher costs as more blocks are required. The block density λ_{M_B} (Equation (4.5)) increased from $\lambda_{M_B} = 0.8$ t/m^2 for the BASE configuration to 1.1 and 1.6 t/m^2 using the PYR and PYR+SP configuration, respectively. The effect of block density is further discussed in Section 6.6.8.

6.6.7   Effect of drop height and step spacing

Drop height H_d (and consequently step spacing $L_d = H_d/S$) was varied herein. Large drop heights, i.e. step spacings, lead to an increase of scour pool depths potentially destabilizing the step. Furthermore, the block placement density decreases with increasing H_d, i.e., fewer blocks are available to stabilize the bed. Figure 6.33 shows experiments DH1, SF0, and DH3 in which drop height was varied between $H_d = 1.12$, 0.75, and 0.40 m resulting in initial step spacings $L_d = 18.7$, 12.5 and 6.7 m, respectively. Note that DH3 had the smallest step spacing possible, still allowing for the placement of auxiliary blocks in between the steps. All experiments were conducted with CW conditions, $W = 6$ m, $S = 0.06$, and using blocks with $M_B = 4.6$ t. According to Marion *et al.* (2004), the scour properties are affected by the downstream step, i.e., geometrical interference is relevant, if the ratio between step spacing and critical energy head $L_d/H_e < 15$. In experiments DH1, SF0, and DH3, geometrical interference was relevant for all conditions excepts for the first interval ($q = 1.67$ m^2/s) in DH1 with the largest step spacing $L_d = 18.7$ m resulting in $L_d/H_e = 19$.

According to Figure 6.33, all experiments were similarly stable as DH1 ($H_d = 1.12$ m) and SF0 ($H_d = 0.75$ m) failed at $q_f(1\%) = 6.67$ m^2/s and DH3 ($H_d = 0.40$ m) failed at $q_f(1\%) = 8.33$ m^2/s. Moreover, similar maximum Shields ratios $(\theta/\theta_c)_{max} \approx 4$ were obtained in all experiments for $q < q_f(1\%)$, i.e., during stable conditions. However, experiment DH1 ($H_d = 1.12$ m) failed more gradually, whereas an abrupt failure was observed in experiment SF0 ($H_d = 0.75$ m) (definition of abrupt and gradual failure see Section 6.4.5). In experiment DH1 with $H_d = 1.12$ m showing a gradual failure, the blocks were mobili-
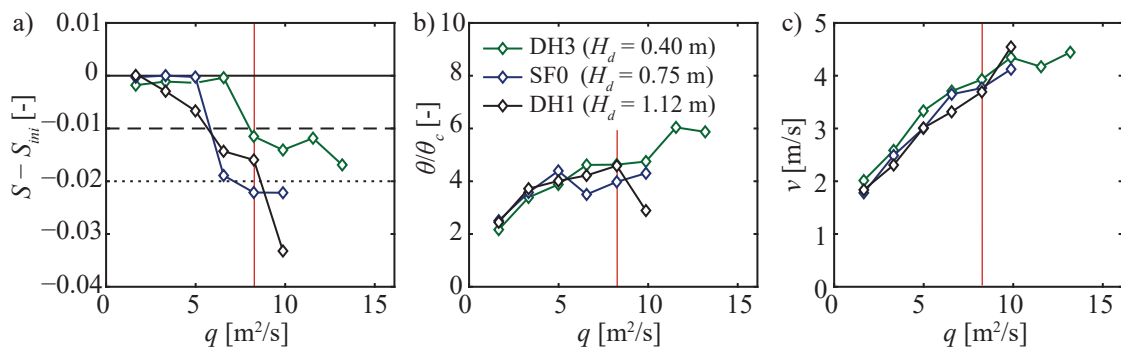

Figure 6.33 Effect of drop height on: a) bed slope reduction $\Delta S = S - S_{ini}$, b) Shields ratio θ/θ_c, and c) mean flow velocity v for experiments DH1 to DH3 and SF0; parameter according to Table 6.3; vertical red lines: $q \geq q_f(1\%)$ for all experiments

zed at smaller discharges compared to the other experiments. As fewer steps were present per unit area, less energy was dissipated, potentially leading to this early mobilization of the step-forming boulders, i.e., the bed slope had to decrease to attain similar velocities as in the experiments with more steps (Figure 6.33c). In experiment DH3 ($H_d = 0.40$ m) with the highest block placement density $\lambda_{D_{eq}}$, the bed slope was reduced instantaneously by more than 1% but the failure mechanisms was still considered gradual as the bed re-stabilized at a higher bed slope compared to the other experiments. Nevertheless, the system was less organized compared to the initial state and rather resembled a block carpet than a well-organized step-pool sequence.

To conclude, drop height and step spacing did not substantially influence bed stability but different failure modes were observed. For large drop heights (i.e., large step spacing), the step-forming blocks were mobilized at small q inducing failure of single steps. Consequently, the typical step-pool flow regime did not emerge because the steps disintegrated into a block carpet with a rather small block placement density (e.g., see Figure 6.13). For small drop heights, the typical step-pool flow regime did not evolve either. Step height was substantially limited by the downstream step leading to a less pronounced increase in bed roughness. Thus, mean flow velocity increased leading to the mobilization of the step-forming blocks. The resulting block carpet was more stable (i.e., bed slope reduction was less pronounced, Figure 6.33b) compared to experiments with larger drop heights. Regarding the design of artificial step-pool sequences, an optimal drop height (i.e., step spacing) is required to obtain the typical undulating flow regime with the emergence of hydraulic jumps. Recommendations are provided in Chapter 7.

6.6.8   Effect of block placement density

The block placement density $\lambda_{D_{eq}}$ (Equation (4.4)) and the block weight density λ_{M_B} (Equation (4.5)) are presented in Figure 6.34 for all experiments. A weak trend between θ/θ_c and $\lambda_{D_{eq}}$ or λ_{M_B} was detected indicating that stability increases with the placement density. Both $\lambda_{D_{eq}}$ and λ_{M_B} were calculated including the auxiliary blocks placed in the pools. Thus, the effect of the step-forming block weight, which is decisive for step stability, diminishes. Even though placement and block density alone did not predict $(\theta/\theta_c)_{max}$ very well, the diagram provides an overview of the investigated block placement densities and the related bed shear stresses sustained by the artificial step-pool systems.

Experiment BW1 with the smallest block weight $M_B = 4.6$ t sustained substantial-
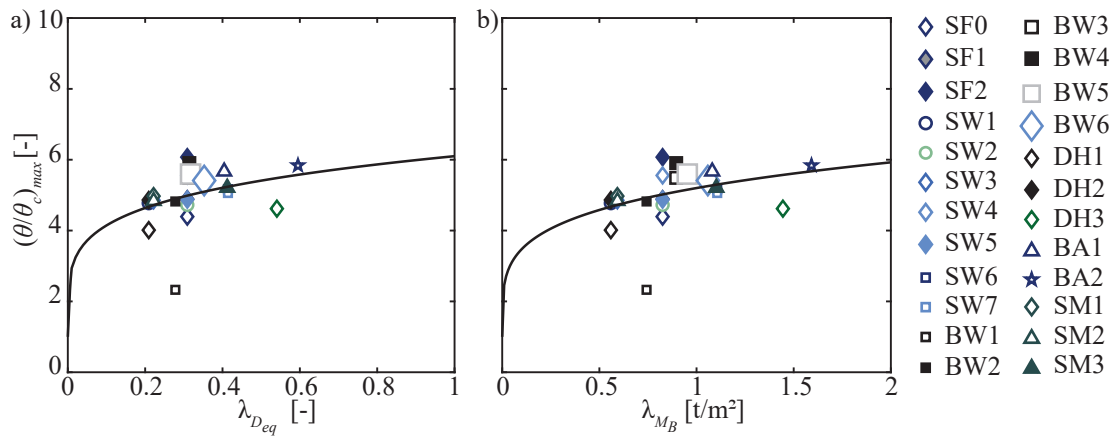
Figure 6.34 Effect of block placement density on bed stability. Maximum Shields ratio $(\theta/\theta_c)_{max}$ as a function of a) placement density $\lambda_{D_{eq}}$ and b) block weight density λ_{M_B} (experiments with strong jamming effects (DVR1 to DVR4, BA3) are not shown here, parameters according to Table 6.3

ly lower $(\theta/\theta_c)_{max}$ compared to the other experiments. Note that this experiment failed gradually and θ/θ_c increased continuously despite the gradual decrease of bed slope (Figure 6.29). The same applied to experiment DH3 with the smallest drop height $H_d = 0.40$ m.

Artificial step-pool sequences with continuous scour bed protection consisting of large boulders and placement densities $\lambda_{D_{eq}} \geq 0.6$ are assumed to sustain much higher discharges. For example, the artificial step-pool sequence in the Maira case study (Section 3.4.5) with a continous bed protection using auxiliary blocks with $M_B = 2$ to 3 t ($\lambda_{D_{eq}} > 1$) sustained a design discharge $q \approx 23$ m²/s (beffa tognacca GmbH 2020). However, the present study is limited to artificial step-pool systems with $\lambda_{D_{eq}} \leq 0.6$.

6.6.9   Synthesis on bed stability

The previous sections discussed the effect of channel parameters and parameters regarding the geometry of artificial step-pool sequences. The main results are:

- Steps were more stable in *sediment supply* experiments compared to clear-water experiments because scour depth was generally smaller, the step-forming blocks were less exposed to the flow, and jamming of step-forming blocks and grains of the largest fraction of base material potentially contributed to step stability (Section 6.6.1). However, the increase of near-bed velocity in SF experiments due to smaller scour depths led to the entrainment of the auxiliary blocks located in between the steps (Figure 6.23). Moreover, all SF experiments showed an abrupt failure (Table 6.3), in which bed slope decreased substantially in a short time period (Section 6.4.5).

- The *base material* in the range investigated herein did not alter step stability as the size of the step-forming boulders and auxiliary blocks predominated over the composition of the base material (Section 6.6.2).

- Steps in channels width milder *bed slopes* sustained higher unit discharges q (Section 6.6.3). However the maximum Shields ratio $(\theta/\theta_c)_{max}$ was independent of bed slope. Moreover, Equation (2.42) by Lamb *et al.* (2008) accounting for the increase of θ_c in steep streams attributed to the low relative submergence is also applicable to artificial step-pool systems.

- The *channel width* does not have a major impact on step stability as long as no alternate bars appear (Section 6.6.4). The regime theory of da Silva (1991) and Zarn (1997) may be used to predict the bed forms. However, alternate bar formation was less likely in artificial step-pool sequences as the highly organized steps inhibit lateral flow diversion.

- *Block weight* had the largest effect on step stability (Section 6.6.5) because smaller blocks are more easily entrained. Therefore, it is recommended to use larger blocks in the upper row of the step.

- *Jamming* of the step-forming blocks increased step stability. It was attained either by tightly placing the steps next to each other in narrow channels or by arching the step (CUR) in wide channels (Section 6.6.6). Jamming effects were not limited to small jamming ratios $W/D < 6$ in artificial step-pool systems as in self-stabilizing systems as the interlocking of the step-forming blocks can be imposed onto the system.

- *Drop height (or step spacing)* did not alter bed stability when using the same step-forming blocks (Section 6.6.7) but the failure modes differed substantially. The typical flow regime of step-pool sequences with emerging hydraulic jumps only appeared for an optimal drop height or step spacing as both small and large drop heights lead to systems with less energy dissipation.

- Step stability increased using *block configuration* PYR and PYR+SP preventing an early step failure due to tilting (PYR) and scouring (PYR+SP) (Section 6.6.6).

- *Placement density* correlated with step stability (Section 6.6.8) but it could not predict step stability alone because other parameters (e.g., block weight, block configuration) were decisive for step stability.

For the first time, an extensive parameter study was conducted to investigate bed stability of artificial step-pool sequences providing valuable insights regarding research questions B5 (Section 1.3). It aimed at quantifying the maximum discharge and bed shear stresses sustained by artificial step-pool systems depending on different channel and step-pool geometry parameters. All the above presented results contribute to a better understanding of the relevant processes of artificial step-pool sequences.

Block weight M_B was found to be the key parameter controlling the stability of the step-forming blocks. With regard to the design aid for practitioners (Chapter 7), an approach is required to relate the diameter of the step-forming blocks D_{eq} to the maximum bed shear stress observed in the step-pool systems. Therefore, a Shields-based approach is used to estimate the critical bed shear stress regarding the stability of artificial step-pool systems. The bed shear stress $\theta_{D_{eq}}$ was normalized with D_{eq} using Equation (4.8).

All experiments are compiled in Figure 6.35 relating block weight M_B to the maximum Shields ratio $(\theta_D/\theta_c)_{max}$ for stable conditions (i.e., $q \leq q_{stab}$). The weighted average $\pm$ the weighted standard deviation defines:

$$\left(\frac{\theta_D}{\theta_c}\right)_{max} = \frac{h\,S}{(s-1)\,D_{eq}}\frac{1}{\theta_c} = 0.69 \pm 0.13 \tag{6.5}$$

The weighted average and standard deviation were used to avoid a bias as more experiments were conducted for $M_B = 4.6$ t. According to the concept of Shields, a ratio $\theta_D/\theta_c = 1$ is expected as a stability threshold. However, the blocks in artificial step-pool sequences typically have a higher exposure than grains on a bed with more uniformly sized sediment. The parameter b describes the associated decrease in critical bed shear stress as:

$$\theta_D = b\,\theta_c \tag{6.6}$$

with $b = 0.69 \pm 0.13$ and θ_c = critical bed shear stress calculated with Equation (2.42) by Lamb *et al.* (2008). With regard to the design aid, Equation (6.6) is recommended to determine the step-forming block size D. Note that the minimum and maximum values of parameter b define the upper and lower threshold including all data (gray area in between
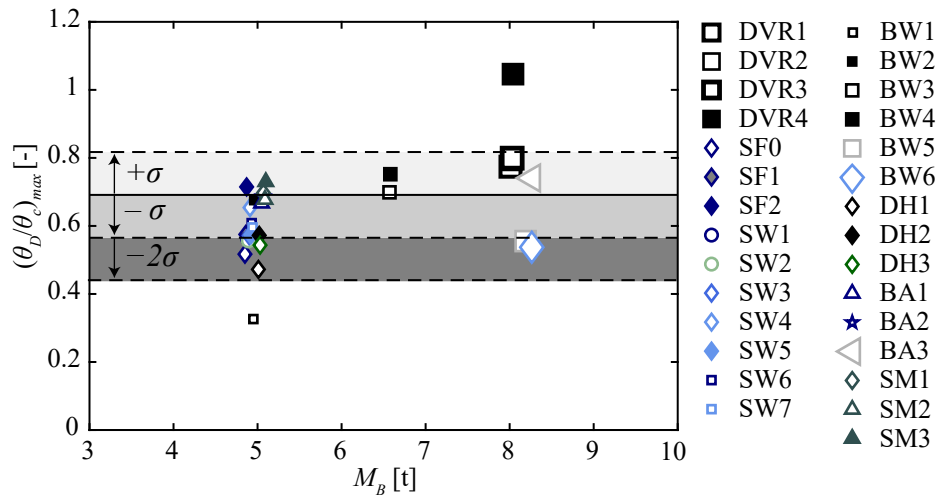
Figure 6.35 Maximum Shields ratio $(\theta_D/\theta_c)_{max}$ as a function of the mean block weight M_B for all artificial step-pool experiments; solid line and gray area are defined by Equation (6.5)

dashed lines in Figure 6.35) except for experiments SF0, BW1, BW6, DH1, and DH3. All of them were conducted under CW conditions and three of them showed a gradual failure mechanism. If a high degree of safety is required, the parameter b may be reduced by two times the standard deviation yielding $b = 0.43$.

6.7   Bed adjustments at different spatial scales

Self-stabilization mechanisms at different spatial scales presented by Weichert *et al.* (2008) (Section 3.3.4) are transferred from self-organizing to artificial step-pool systems in the following. The bed adjustment mechanisms of artificial step-pool systems are illustrated using two experiments showing a gradual and an abrupt failure before compiling the results of all experiments.

6.7.1   Identification of bed adjustment mechanisms

Figure 6.36 presents the dimensionless parameter $q^* = q/(g\,\sigma_z^3)^{1/2}$ as a function of bed slope S for experiment DH1 and DH2, which failed gradually and abruptly, respectively. The solid line represents the threshold between stable and unstable conditions described with Equation (3.11), which was obtained from self-organizing step-pool systems (Aberle 2000). In self-organizing systems, data points plot around this threshold, indicating that a certain bed roughness σ_z was expected for a given q and S. Increasing q shifts the bed towards an unstable condition which is related to a movement in positive y-direction (Figure 6.36). According to Weichert *et al.* (2009), the bed adjusts at different

scales by either increasing bed roughness σ_z, reducing bed slope S, or both, to reach a stable state (Figure 3.8). The increase in bed roughness occurs either through grain sorting (*micro*-scale), or geometry optimization (*meso*- and *macro*-scale), see also Section 3.4.3.

According to Figure 6.36, data points of artificial step-pool sequences plot below the threshold value for self-organizing systems. Artificial step-pool systems have a highly organized (i.e., optimized) geometry externally imposed onto the system. In self-organizing systems, high discharges are required to attain such an optimized step-pool geometry. In experiments showing an abrupt system failure (DH2), the bed slope remained constant during multiple discharge intervals. The increase in q was compensated by an increase in σ_z as the scour depth increased while the bed slope remained constant (trajectory A in Figure 6.36a). The system mainly adjusted in the *meso*-scale as the step-pool geometry was optimized. In artificial step-pool systems, the *micro*-scale adjustments, i.e. bed armoring, are negligible as bed roughness is dominated by the step-pool bed forms. Overall, the net trajectory for process A points in positive q^*-direction.

The systems could not further optimize their geometry at certain threshold discharge because the steps collapsed either due to tilting of the large step-forming blocks or due to step toe destabilization related to scouring (Section 6.4.3). Consequently, the bed adjusted at the *reach*-scale leading to a reduction of the reach-averaged bed slope S. The destruction of steps was related with a (temporary) decrease in σ_z (i.e., bed roughness decreased) leading to an even more pronounced reduction of S (trajectory B in Figure 6.36). In experiment DH2, the overall bed slope was significantly reduced by $\Delta S = -1.67\%$ as five out
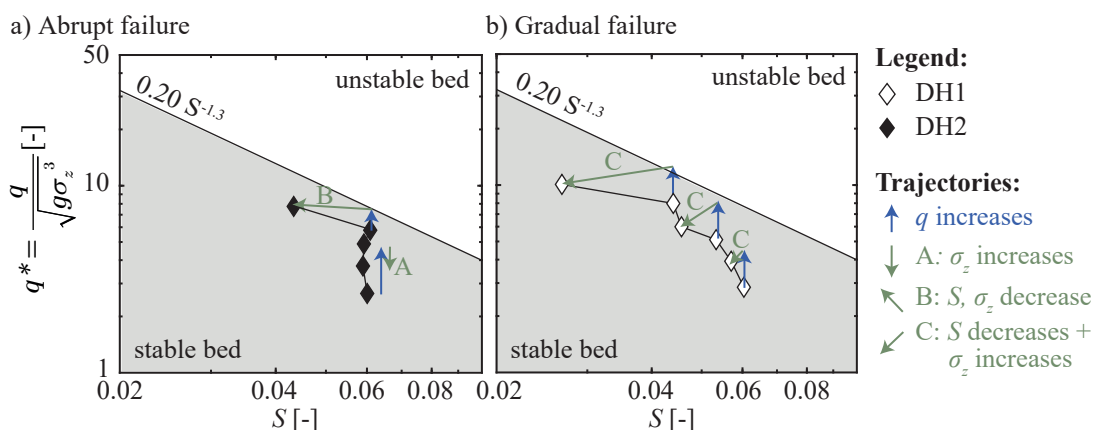

Figure 6.36 Stability diagram adapted from Weichert *et al.* (2009) for a) DH2 without sediment supply, gradual failure, b) DH1 with ~20% sediment supply, abrupt failure; solid line: Equation (3.11) according to Aberle (2000)

of eight steps collapsed in the upstream part due to a progressive upstream erosion (PUE) (Figure 6.14).

Bed slope continuously decreased in experiments with a gradual failure (DH1). The step-forming blocks started to move at $q \geq 3.33$ m^2/s (Figure 6.13). Therein, bed slope was step-wise decreased by $\Delta S \approx -0.003$ per interval. However, the scour depth increased for steps that still remained in place and the bed adjusted by increasing the overall bed roughness σ_z. The increase in q was compensated by optimizing the bed geometry, i.e., increasing σ_z, and reducing S simultaneously (trajectory C in Figure 6.36b).

To conclude, the bed adjustments in artificial step-pool systems were comparable to those in self-organizing systems with *meso-* and *reach*-scale adjustments being most important. These bed adjustments occurred consecutively in artificial step-pool systems failing abruptly, while they occurred simultaneously in artificial step-pool systems failing gradually. However, a gradual system failure was only attained in clear-water (CW) experiments and all sediment feed (SF) experiments showed an abrupt failure.

6.7.2 Bed adjustment in artificial step-pool systems

Figure 6.37 compiles all data of the experiments with artificial step-pool sequences. These data plot below or near the threshold value proposed by Aberle (2000) indicating that the bed adjustment mechanisms of self-organizing step-pool systems are generally applicable to artificial step-pool systems. Green diamonds refer to intervals with discharge in which the bed slope was not reduced by more than 1%, yet ($q < q_f(1\%)$ or $q \leq q_{stab}$) and the blue circles to conditions at which the system failed, i.e., $\Delta S < -0.01$ and $q \geq q_f(1\%)$. The bold green diamonds refer to discharge intervals q_{stab} representing the stable state prior to system failure. Most stable conditions (q_{stab}, bold green diamonds) were located close the the stability threshold for self-organizing systems (solid black line). Data plots generally below this threshold as the system may not be able to evolve to a state of maximum bed roughness σ_z, i.e., maximum step height and scour depth, as the large step-forming boulders were destabilized due to tilting or scouring processes prior to reaching this state. Nevertheless, this stability diagram clearly relates the bed slope S and the unit discharge q to a certain bed roughness σ_z.
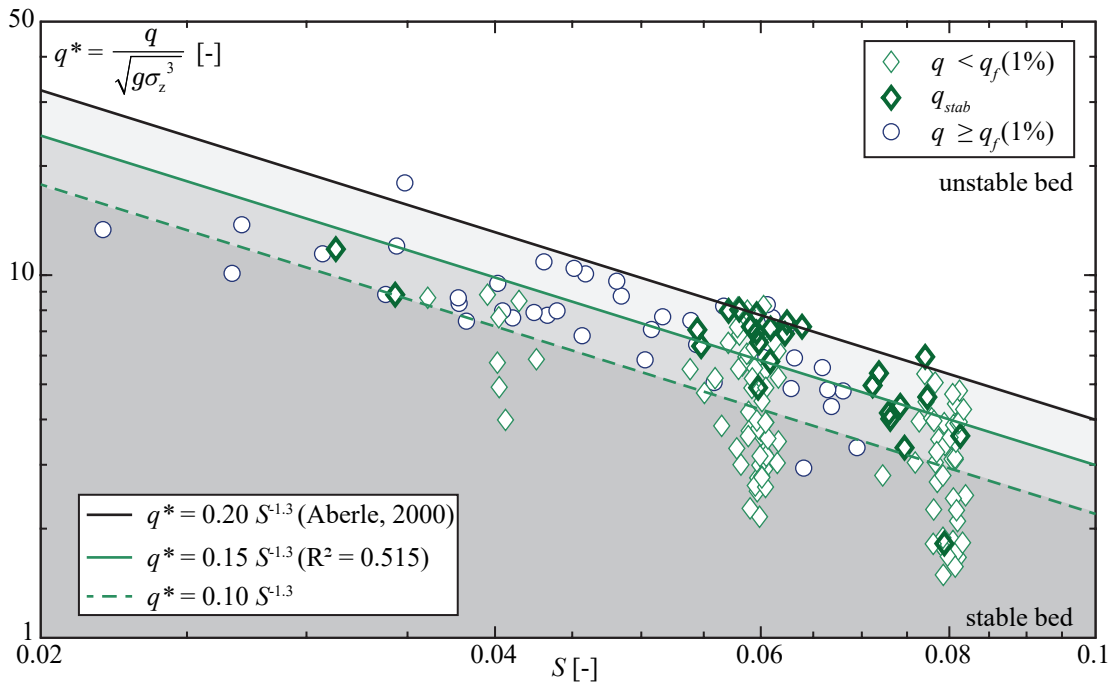
Figure 6.37 Stability diagram adapted from Weichert *et al.* (2009) for all experimental data; solid black line: Equation (3.11) by Aberle (2000); solid green line: Equation (6.7), and dashed green line: Equation (6.8)

Bed roughness can be predicted for a given S and q using the stability diagram. Vice versa, the unit discharge q_{stab} can be predicted for given S and σ_z. Therefore, a regression analysis was conducted for $q^* = m\,S^c$ by adjusting the coefficient m while maintaining the exponent $c = -1.3$ as proposed by Aberle (2000), leading to ($R^2 = 0.515$):

$$q_{stab} = 0.15\,S^{-1.3}\,\sqrt{g\,\sigma_z^3} \qquad (6.7)$$

A second, more conservative criterion was defined as:

$$q_{stab} = 0.10\,S^{-1.3}\,\sqrt{g\,\sigma_z^3} \qquad (6.8)$$

where the coefficient $m = 0.10$ was selected manually in a way that data points belonging to q_{stab} (bold green diamonds) plot above the threshold line. Equations (6.7) and (6.8) are used to predict unit discharge q_{stab} for a given S and σ_z or, vice versa, the step-pool geometry can be designed for a given q and S. How σ_z relates to the step-pool geometries (e.g., to the step height H and step spacing L) is addressed in Section 6.8.6.

6.8   Step-pool geometry

The geometry of artificial step-pool sequences is analyzed herein. The parameters step height H, drop height H_d, residual depth or scour pool depth H_{res}, and step spacing L_d are defined according to Figure 3.9a. Step height H is the vertical distance between step crest and the deepest point in the scour hole and drop height H_d is the net difference in between two subsequent steps. Step spacing L_d is the predefined distance between the step crests, L is the actual step length ($L \leq L_d$ for small q and $L \approx L_d$ for large q), and l_1 is the distance from the step crest to the deepest point in the scour pool. Typical dimensionless parameters describing the step-pool geometry, i.e, relative steepness H/H_d or step height-to-block size ratio H/D_{eq} are presented in Section 6.8.1 and 6.8.2, respectively. Step height and step length were compared with literature (Section 6.8.4), a novel empirical relation was developed to estimate step height in artificial step-pool systems (Section 6.8.4), and implications on the uncertainty regarding step height are provided (Section 6.8.5). Finally, the roughness parameter σ_z was related to the step height H which is important to link reach-scale bed roughness to the geometry of artificial step-pool systems (Section 6.8.6).

6.8.1   Relative steepness

Relative steepness of the step-pool units is defined as $c = H/(S\,L_d)$ with H = step height, S = bed slope, and L_d = step length. If the step expands to the downstream step, the drop height equals $H_d = S\,L_d$ and the steepness ratio becomes $c = H/H_d$. A relative steepness of $c = 1$ indicates a stair-case step-pool sequence with $H_{res} = 0$, whereas $H_d = H_{res}$ if $c = 2$.

Figure 6.38 shows c as a function of q and the corresponding histogram evaluated for all experiments. Relative steepness increased with increasing q because step height increased while the drop height was constant. According to Abrahams *et al.* (1995), $1 < c < 2$ are commonly observed in self-organizing step-pool systems as flow resistance is maximized for this range. Steepness ratios $c > 2$ were common in artificial step-pool systems, which is attributed to the highly optimized geometry leading to deeper scour pools in comparison with self-organizing step-pool systems. According to Figure 6.38b, 90% of the steps had steepness ratios in between $1.1 \leq c \leq 2.6$ with a mean of $c = 1.8$.

Apparently, the data presented herein were obtained from stable step-pool units which have not experienced step failure. The risk of step failure related to scouring, which occur-
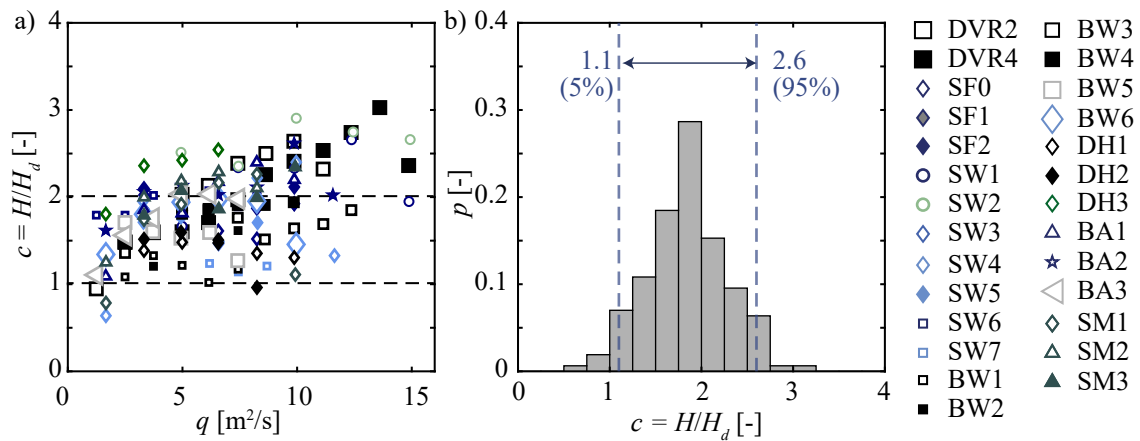
Figure 6.38 a) Relative steepness $c = H/H_d$ as a function of unit discharge q, dashed lines: criteria by Abrahams *et al.* (1995), b) histogram of c, dashed lines indicate the 5th- and 95th-percentiles, parameters according to Table 6.3

red in 45% of all step failures (Section 6.4.7), increases with increasing steepness ratio. It is recommended to design step-pool sequences with steepness ratios $1.1 < c < 2.6$. Scour protection measures may be required for $c > 1.8$ (e.g., PYR+SP, Figure 4.11e).

6.8.2 Step height-to-block size ratio

Similarly to the steepness ratio presented in the previous section, the ratio between step height and step-forming block diameter $e = H/D_{eq}$ provides insights regarding step failure. The risk of step failure due to scouring increases with increasing H/D_{eq}. Figure 6.39 shows that e generally increased with q. The 5% and 95%-percentiles were used to quantify minimum and maximum estimates of e resulting in $0.6 < H/D_{eq} < 1.5$ and a mean around $H/D_{eq} \approx 1$. According to Chin (1999) and Ashida *et al.* (1984), the ratio between drop height and particle size is $H_d/D \approx 1.0$ to 1.2 in natural step-pool streams. Step height was compared herein instead of drop height, which amounts to approximately $H = 2 H_d$ (Figure 6.38). Consequently, ratios $H_d/D \leq 0.75$ were observed in artificial step-pool sequence, which is lower compared to natural step-pool systems. In artificial step-pool systems, a bimodal sediment mixture is used with larger step-forming blocks. On the contrary, natural step-pool systems contain more widely graded bed material in which the size of the step-forming blocks are smaller but also more variable.

The parameter $e = H/D_{eq}$ should be considered as a reference for step-pool geometry. It is recommended to avoid step-pool sequences with ratios $e > 1.5$ as the likelihood of step failure related to scouring increases. Scour protection measures are recommended for $e > 1.0$ (e.g., PYR+SP configuration, Figure 4.11e).
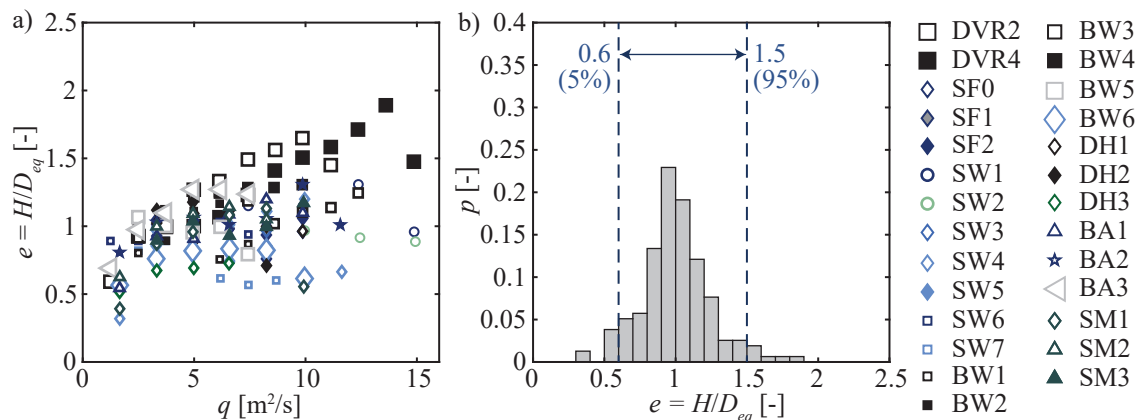
Figure 6.39 a) Step height to step-forming block diameter ratio $e = H/D_{eq}$ as a function of unit discharge q, b) histogram of e, dashed lines indicate the 5th- and 95th-percentiles, parameters according to Table 6.3

6.8.3 Comparison with literature

This section compares step geometry with literature. Step height H, step length L, and the distance to the deepest point in the scour pool l_1 are compared with existing relations for step-pool systems, artificial check-dam sequences, or single drop structures summarized in Table 6.4 indicating the investigated structure type and the parameter range. The most promising approach is adapted to develop a novel equation to estimate H for artificial step-pool sequences.

Step height

Step height H is defined as the distance between the step crest and the deepest point in the scour pool and is the sum of the drop height and the scour depth $H = H_d + H_{res}$ (Figure 3.9). Figure 6.40 compares the measured H_{meas} and calculated step height H_{calc} with the approaches detailed in Table 6.4. Step height was highly underestimated using the approach of Maxwell and Papanicolaou (2001). Equation (3.5) originates from flume data for a self-organizing step-pool system with a less organized step-pool geometry compared to artificial step-pool units leading to smaller H. Furthermore, the GSD in a self-organizing step-pool system is more evenly graded, i.e., all grain fractions are present, whereas the artificial step-pool system has a more bimodal sediment mixture (Section 2.4.5). The larger grain fractions of the bed material in self-organizing step-pool systems sustain higher discharges leading to smaller scour depths, i.e., step heights.

The approach of Thomas *et al.* (2000) underestimates large step heights $H \geq 1.5$ m emerging at high discharges. Similarly to the equations of Maxwell and Papanicolaou

Table 6.4 Overview of existing empirical relations (H = step height, L = step spacing, l_1 = distance to deepest point in scour, Sed = sediment supply considered)

	Data type	Eq. for		Parameter range	Sed
		H	L, l_1		
Kotoulas (1967)	Artificial drop structure, flume data	(3.22)	(3.24)	$5 < (q^{1/2}\Delta h^{1/4})/d_{90} < 25$	yes
Lenzi et al. (2003)	Check-dams & bed sills, field & flume data	(3.26)	-	$S = 0.02\text{-}0.16$	no
Marion et al. (2006)	Check-dam sequences, flume & field data	(3.21)	-	$S = 0.05\text{-}0.14, \sigma_g \approx 1.5\text{-}6$	yes
Maxwell and Papanicolaou (2001)	Step-pool system, flume data	(3.5)	(3.6)	$S = 0.03\text{-}0.07,$ $W/d_{84} = 5\text{-}15,$ $h/d_{84} = 0.5\text{-}2$	no
Thomas et al. (2000)	Step-pool system, field data	(3.12)	(3.13)	$S = 0.02\text{-}0.08, d_{50} \approx$ 55 mm, $D_{eq} \approx 550$ mm	no
Volkart (1972)	Check-dam sequence, flume data	(3.14)	(3.16)	$S = 0.006\text{-}0.07,$ $d_m = 1\text{-}3$ mm	yes

(2001), Equation (3.12) resulted from a self-organizing step-pool system. The median grain diameter $d_{50} \approx 55$ mm of the bed material was larger than the $d_{50} = 35$ to 41 mm used in this study. Moreover, the step-forming blocks were smaller with $D_{eq} \approx 0.55$ m compared to $D_{eq} \approx 1.5$ m used herein. Consequently, the step-forming blocks were mobilized earlier leading to smaller step heights, which was most pronounced at high discharges.

Step height was generally overestimated by Volkart (1972), who investigated check-dam sequences in a flume. Herein, only Equation (3.14) for CW conditions was applied because the sediment concentrations $C_s = 0.34$ to 0.67% of the present study were much higher compared to Volkart (1972) with $C_s \leq 0.134\%$ leading to unreasonable results. The overestimation of H is attributed to the auxiliary blocks placed in between the steps. These large blocks were not present in the study of Volkart (1972) leading to larger scour depths (i.e., step heights). The large step-forming blocks were partly or fully mobilized at a certain flow stage in the present study potentially lowering the step crest and therewith reducing the overall step height. On the contrary, the check-dam crests do not adjust to the flow and remain at the same position throughout the experiments. Moreover, the check-dam crests were clearly defined in comparison with the irregular step crest in artificial step-pool units due to differences in block shape and placement. As a consequence, the emerging jet is more compact in the well defined check-dam systems potentially leading to deeper scour depths.

The relation of Marion *et al.* (2006) was developed for a sequence of bed sills in a flume as well as field data of artificial drop structures. Marion *et al.* (2004) observed interference of the scour with the downstream sill for ratios $L/H_e < 15$, with $H_e = 3/2\,h_c$ = energy head, which was the case for more than 94% of the data points in the present study. Equation (3.21) contains the parameter a = morphological jump height which equals drop height ($a = H_d$) in case the scour extends to the downstream step, which was generally the case in artificial step-pool sequences. The data of the present study comply with the indicated application range with $0.08 < a/H_e < 1.4$. Overall, small step heights $H \lesssim 2$ m were slightly overestimated but the largest step heights $H \gtrsim 2$ m were underestimated. The underestimation for small H may be related to the assumption $a = H_d$ which may not be the case for small step heights where the scour did not expand to the downstream step. The overestimation may be explained by the presence of auxiliary blocks limiting the scour extent.

Figure 6.40e compares the results with the equation proposed by Lenzi *et al.* (2003), which was developed for single grade-control structures mainly from field data. Step
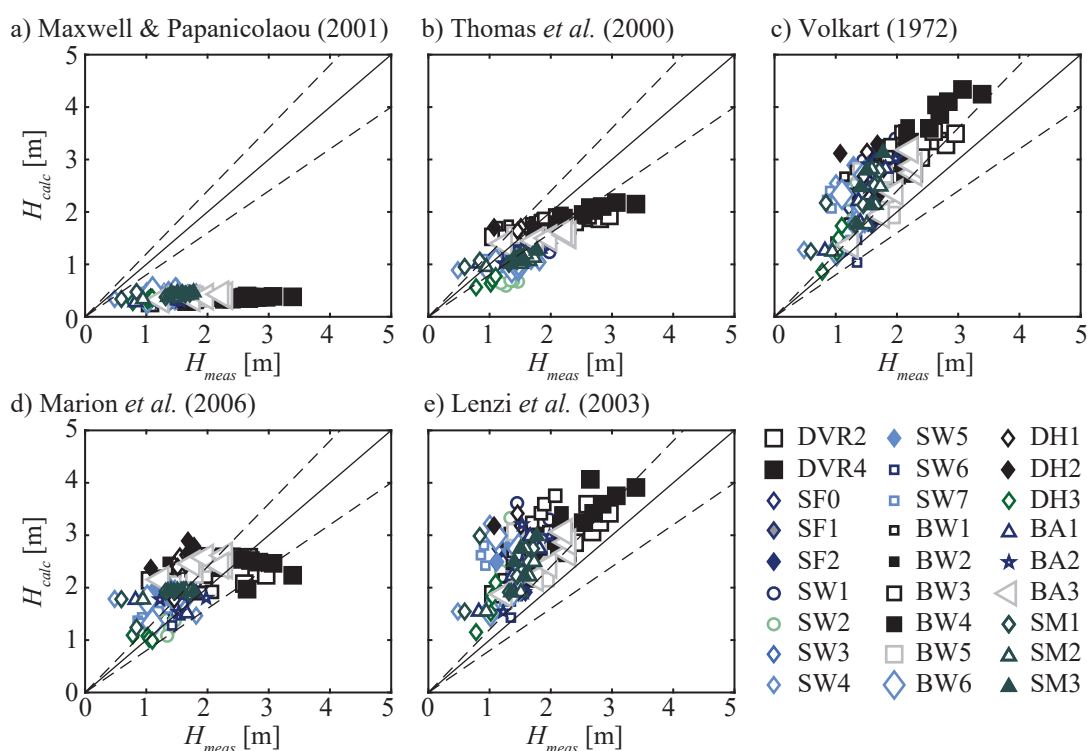
Figure 6.40 Comparison of measured H_{meas} and calculated step height H_{calc} for the corresponding approaches; solid line: perfect agreement, dashed lines: ±20%; experiment designation according to Table 4.9

height was generally overestimated and the scatter was rather large. Equation (3.26) accounts for the hydraulic load applied in terms of critical flow depth and for the drop height for single drop structures. The interference with a downstream sill is not accounted for explaining the overestimation, which may be amplified by the auxiliary blocks in the pools of the artificial step-pool systems.

Equation (3.22) of Kotoulas (1967) was developed to estimate the scour depth at a single drop structure. For the data of the present study, step height was multiplied by 0.84 as the jet was generally submerged by the downstream flow. Clearly, the step height is heavily overestimated using d_{90} of the base material as bed grain size (Figure 6.41a), even though the application range $4.2 < q^{1/2}\Delta h^{1/4}/d_{90} < 16$ is met for most data points. On the one hand, the scour pool in a single drop structure fully develops as there is no interference with a downstream sill. On the other hand, the artificial step-pool units contain auxiliary blocks in the pools decreasing scour depths. Using the equivalent grain diameter of the auxiliary blocks $D_{eq,aux}$ as a grain roughness parameter improves the prediction substantially despite the violation of the application range with $0.9 < q^{1/2}\Delta h^{1/4}/d_{90} < 3.3$. However, the scatter is rather high compared to the approaches previously presented in Figure 6.40 particularly for step heights $H < 2.5$ m.

Overall, the approaches developed for self-organizing step-pool sequences like Maxwell *et al.* (2001) or Thomas *et al.* (2000) underestimated step height mainly due to less-organized natural step-pool systems containing widely graded bed material. On the contrary, experiment for single drop structure like Kotoulas (1967) or Lenzi *et al.* (2003) overestimated step height because the interference with a downstream sill was not accounted
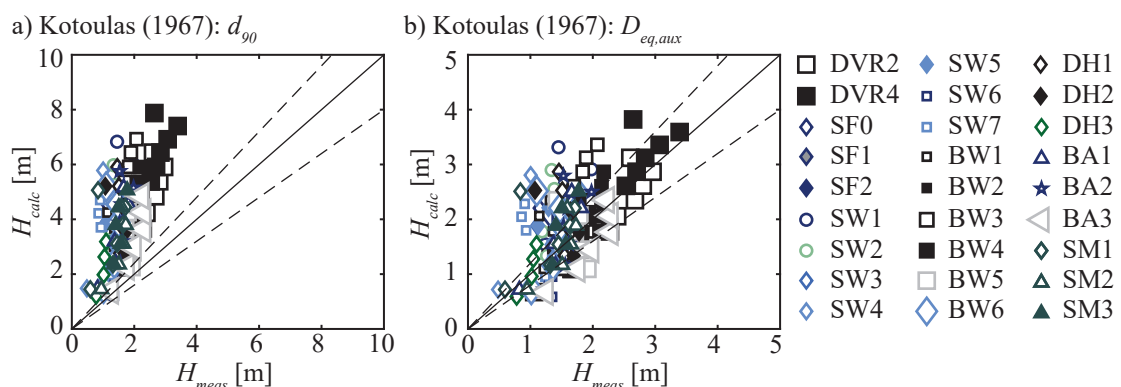

Figure 6.41 Comparison of measured H_{meas} and calculated step height H_{calc} for the approach of Kotoulas (1967) using a) d_{90} of the base material, b) D_{eq} of the auxiliary blocks; solid line: perfect agreement, dashed lines: ±20%; legend according to Figure 6.40

for and because of the presence of auxiliary blocks in artificial step-pool systems limited scour depth. The approaches developed for check-dam sequences like Volkart (1972) or Marion *et al.* (2006) performed best but still overestimated step height due to the absence of auxiliary blocks and the rigid, more clearly defined crests in check-dam sequences. The approach of Volkart (1972) was considered for further analysis and was recalibrated with the present data in Section 6.8.4.

Step length

Figure 6.42 compares the measured and calculated step length L with Equation (3.6) by Maxwell and Papanicolaou (2001) and Equation (3.13) by Thomas *et al.* (2000). The step length was systematically overestimated by the approach of Maxwell and Papanicolaou (2001) primarily because step length was defined as the step-to-step spacing L_d in natural streams, thus, not allowing treads (i.e., regions neither belonging to a step nor to a pool unit). Furthermore, interference of the downstream step in artificial step-pool sequences may have led to a decrease in step length. This geometrical interference was found to be relevant for $L_d/H_e < 15$ where H_e is the critical energy head (Marion *et al.* 2004). Within the scope of the present study, this range was $1.8 < L_d/H_e < 12.8$ for $q = 3$ to 15 m^2/s and $L_d = 6.7$ to 18.7 m indicating that geometrical interference was relevant.

The approach of Thomas *et al.* (2000), which is based on field data, predicts step length considerably well. Therein, the step length was referred to as pool length indicating that the actual step length L was considered and not the step-to-step spacing L_d as in Maxwell
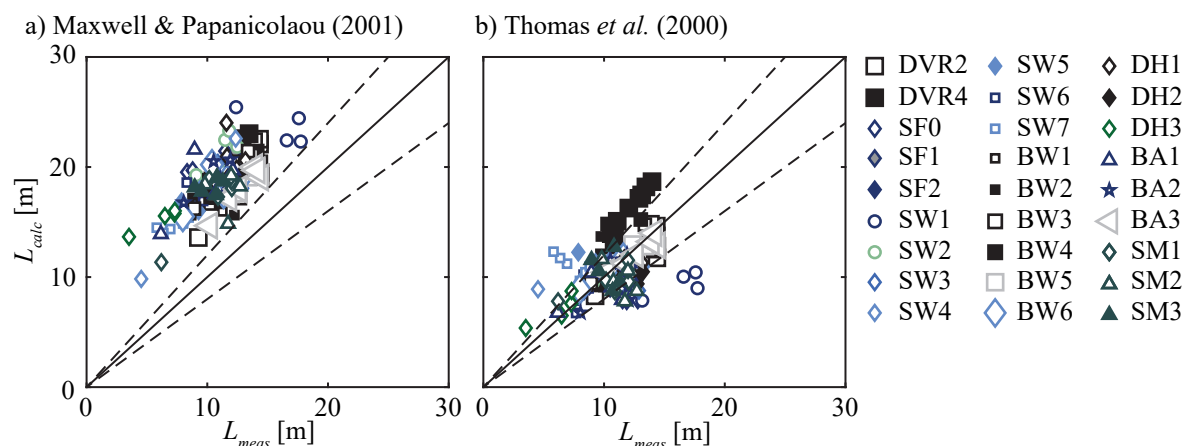

Figure 6.42 Measured and calculated step length L with a) Equation (3.6) by Maxwell and Papanicolaou (2001) and b) Equation (3.13) by Thomas *et al.* (2000); solid line: perfect agreement, dashed lines: ±20%

and Papanicolaou (2001). The equation originates from field data and is recommended for the design of „vortex weirs", which are single drop structure consisting of large boulders built in channels with bed slopes $S < 0.01$. They also found a good agreement between step or pool spacing in natural streams and pool spacing of these vortex weirs even though the vortex weirs were implemented in streams with an order of magnitude smaller bed slopes.

Distance to maximum scour depth

Figure 6.43 compares the distance from the step crest to the deepest point in the scour pool l_1 with Equations (3.16) and (3.24) developed by Volkart (1972) and Kotoulas (1967), respectively. The former was developed for a check-dam sequence and the latter for a single drop structure. Volkart (1972) predicts l_1 well for small values of $l_{1,meas} < 4$ m but tends to overestimate the distance for larger $l_{1,meas}$. Similarly, the maximum scour depth is generally located closer to the step crest in case of a single drop structure. The scatter is rather high for both approaches, nevertheless, the approach by Volkart (1972) may be used to estimate the location of the deepest point in the scour hole.
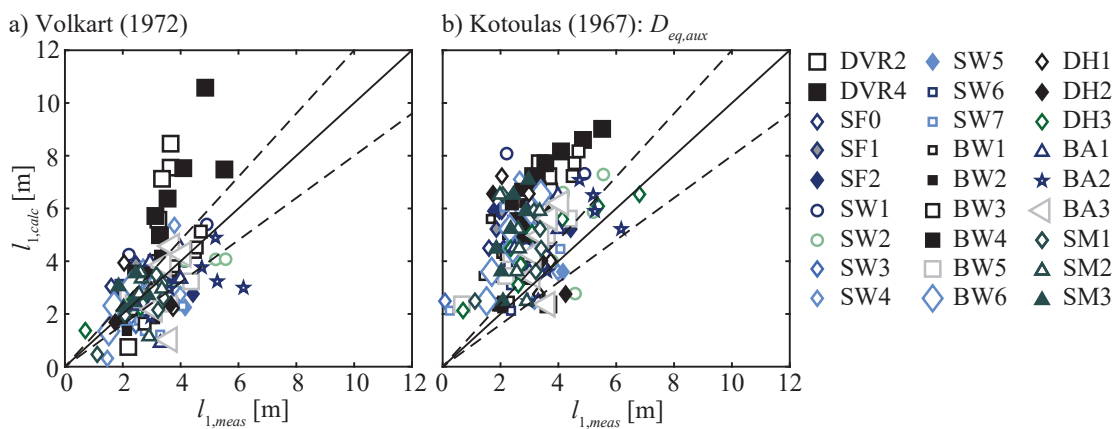

Figure 6.43 Measured and calculated distance to maximum scour depth l_1 with a) Equation (3.16) by Volkart (1972) and b) Equation (3.24) by Kotoulas (1967) using the diameter of the auxiliary blocks $D_{eq,aux}$; solid line: perfect agreement, dashed lines: $\pm 20\%$

6.8.4 Empirical relations for step height

Two novel empirical relations were developed to estimate mean step height H as a function of unit discharge q, bed slope S, step spacing L_d, and the characteristic grain diameter d_{84} of the base material while differentiating clear-water (CW) and sediment feed (SF) conditions. Therefore, the structure of Equation (3.14) by Volkart (1972) was

used and the coefficients were fitted to the artificial step-pool data of the present study. The coefficients b_1 to b_4 were selected to obtain a dimensional consistent equation, yielding:

$$H = b_1 \frac{q^{b_2}\, S^{b_3}\, L_d^{b_4}}{d_{84}^{(\frac{3}{2}b_2 + b_4 - 1)}\, (s-1)\, g^{(\frac{1}{2}b_2)}} \tag{6.9}$$

First, the data corresponding to CW conditions ($n_{CW} = 132$) were used for the regression analysis resulting in $b_{1,CW} = 2.23$, $b_2 = 2/5$, $b_3 = 11/12$, and $b_4 = 3/4$, leading to:

$$H = 2.23 \frac{q^{2/5}\, S^{11/12}\, L_d^{3/4}}{d_{84}^{7/20}\, (s-1)\, g^{1/5}} \qquad (\text{R}^2 = 0.782) \tag{6.10}$$

This equation is only applicable to the following conditions:

$$0.3 \leq \frac{q^{1/2}\, S\, L_d^{1/4}}{d_{84}\, g^{1/4}} \leq 1.8 \tag{6.11}$$

The data for SF conditions ($n_{SF} = 39$) were used in a second regression analysis following Equation (6.9) but using the previously determined exponents $b_2 = 2/5$, $b_3 = 11/12$, and $b_4 = 3/4$ while only allowing b_1 to adjust resulting in $b_{1,SF} = 2.00$. It indicates that step height was reduced by approximately 10% compared to CW conditions. The following relation is proposed to estimate step height H_s in channels with SF:

$$H_s = 0.90\, H \qquad (\text{R}^2 = 0.752) \tag{6.12}$$

The sediment supply rates ranged between 10 and 20% of the estimated TC with Equation (2.43) by Rickenmann (1990). Herein, the decrease in step height H did not depend on the sediment feed rate $q_{s,in}$, however, $q_{s,in} \gg 20\%$ TC may lead to a further decrease in step height. The average values of step height were used in the regression analysis and the step height of a single step may vary substantially as discussed in Section 6.8.5.

Figure 6.44 compares the measured step height H_{meas} with the calculated step height H_{calc} separately for CW and SF experiments. The RMSE was 0.22 and 0.27 m and the mean absolute prediction error was $|\text{PE}| = 11.9$ and 11.6% for CW and SF conditions, respectively. The majority of the step heights were predicted within the ±20% PE range but step height was overestimated by up to 50 to 60% for small step heights $H < 1.5$ m presumably because the step spacing L_d and not the actual step length L was used in the
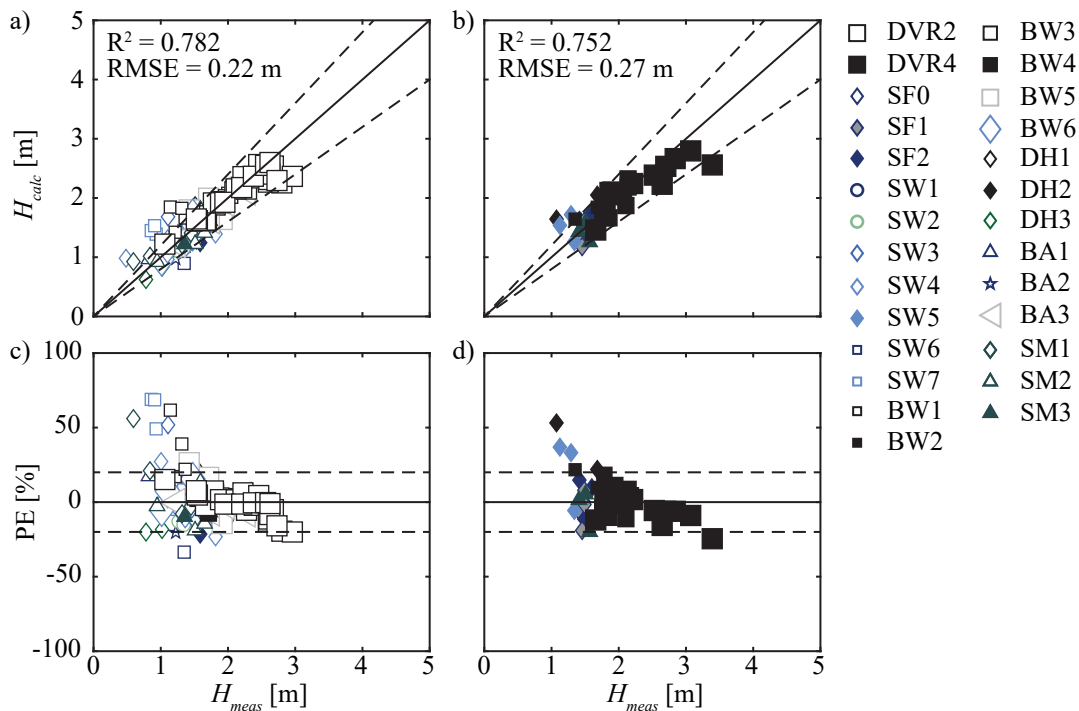
Figure 6.44 Comparison of measured H_{meas} and calculated step height H_{calc} using a) Equation (6.10) for CW experiments with the corresponding PE in c) and b) Equation (6.12) for SF experiments with the corresponding PE in d); solid lines indicate perfect agreement and dashed lines PE = ±20%; parameters see Table 6.3

equation. Nevertheless, the use of L_d is more straight forward as L is not known a priori. Note that the first two intervals with $qS \leq 0.2$ m^2/s were conducted with CW conditions also in the series with sediment supply explaining the filled markers in the CW data set.

Knowledge of step height (i.e., scour pool depth) is crucial for the design of artificial step-pool sequences, particularly for the foundation depth of bank protection measures. These novel approaches allow to estimate the mean step height H with prediction errors below 20%. However, Equations (6.10) and (6.12) predict mean step height but individual step height varied substantially, which is discussed in the following section.

6.8.5 Individual step height

Equations (6.10) and (6.12) predict the mean step height H in artificial step-pool systems. However, the individual step height H_{ind} considerably deviated from H. Figure 6.45 shows the histogram of H_{ind}/H with mean $\mu = 1.0$ and standard deviation $\sigma = 0.19$. In particular the maximum step height H_{max} is decisive for the bank protection foundation depths. Moreover, the step height was 4.9 ±3.9% (i.e. maximum ~10%) higher during peak flow compared to the final step height measured when hydrographs were applied

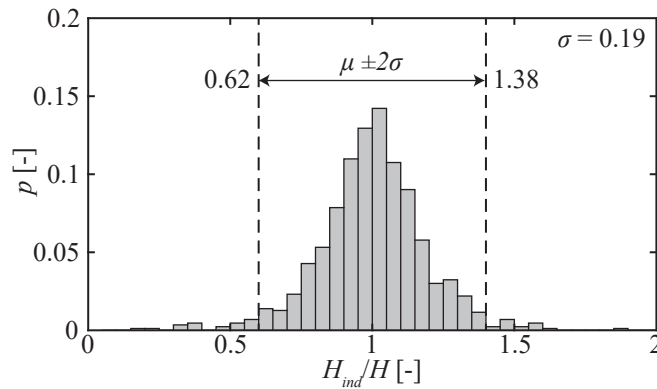**Figure 6.45** Histogram of the ratio between the individual step height and the mean step height H_{ind}/H, μ = expected value, σ = standard deviation

(Figure 6.18). It is recommended to add approximately $2\,\sigma$ to the mean step height H plus the increase of step height during peak flow of 10% to estimate the maximum step height, yielding:

$$H_{max} \approx 1.5\,H \tag{6.13}$$

An additional safety factor may be applied for the bank protection foundation depth.

6.8.6 Relating bed roughness to step height

The bed roughness parameter σ_z is key to estimate the mean flow velocity (Section 6.3.2) but also to assess bed stability of artificial step-pool channels (Section 6.7). However, σ_z is not known a priori when designing artificial step-pool sequences. The design procedure requires to relate σ_z to the step-pool geometry, i.e., to the step height H. Figure 6.46a shows σ_z as a function of mean step height H. A linear regression analysis resulted in:

$$\sigma_z = 0.50\,d_{84} + 0.26\,H \qquad (R^2 = 0.762) \tag{6.14}$$

A positive linear relation between σ_z and H makes sense as large step heights result in a large standard deviation from the mean bed elevation. Bed roughness becomes $\sigma_z = 0.50\,d_{84}$ in case step-pool units are lacking (i.e., $H = 0$ m), which agrees with flume and field data from literature (Aberle and Smart 2003; Zimmermann 2010; Nitsche *et al.* 2012; Chen *et al.* 2020). For instance, Chen *et al.* (2020) correlated σ_z with d_{84} and found a linear relation $\sigma_z = 0.40\,d_{84}$ for plane-bed reaches. Moreover, Nitsche *et al.* (2012) conducted field measurements and found $d_{84} = 0.22$ m corresponding to 0.45 $\sigma_z = 0.10$ m in the plane-bed Riedbach Stream ($S = 0.04$, $W = 6.5$ m).

According to Figure 6.46b, σ_z is predicted with PE smaller than $\pm 20\%$. Equation (6.14) is essential for the design procedure, i.e., when applying the stability diagram (Figure 6.37) and predicting bed roughness σ_z for a given combination of S and q. It enables converting σ_z into step height H, which determines the geometry of the artificial step-pool sequences.
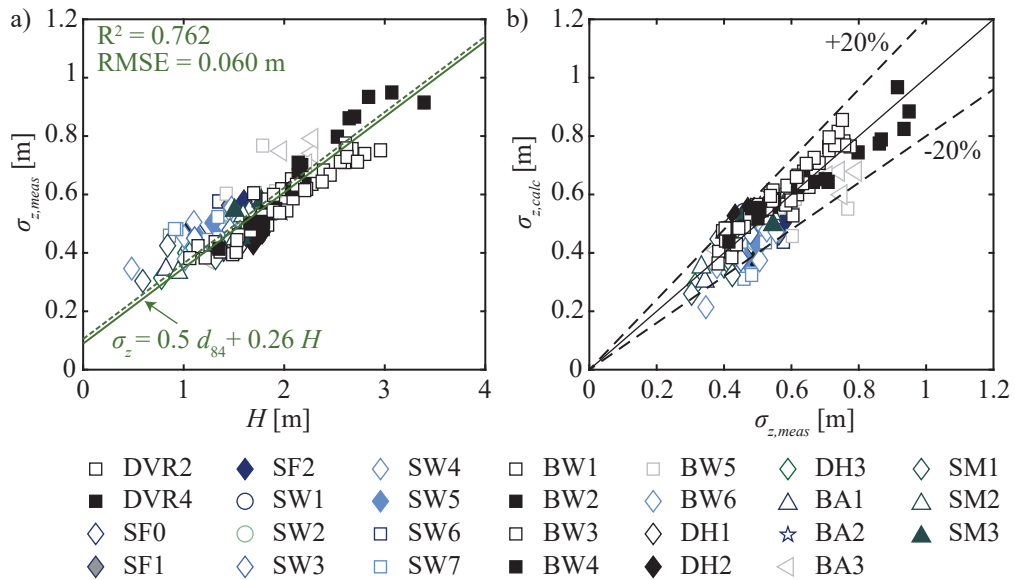

Figure 6.46 a) Relation between step height H and bed roughness parameter σ_z (solid green line: $d_{84} = 0.18$ m and dashed green line: $d_{84} = 0.21$ m), b) measured vs predicted σ_z; solid black line: perfect agreement, dashed lines: $\pm 20\%$ PE; parameters are indicated in Table 6.3

7 Implications for practitioners

7.1 Outline

This section summarizes the most important results regarding the design and stability of artificial step-pool systems. The investigated step-pool geometry is presented providing recommendations regarding the block arrangement. A design procedure is described in which drop height, step spacing, step height, and the size of the step-forming blocks are determined. A computational example is presented to demonstrate the application of the proposed design aid and remarks on bank protection measures are summarized. Finally, limitations and uncertainties regarding the design of artificial step-pool sequences are discussed.

7.2 General remarks and application range

Bed slope S, channel width W, design discharge Q, unit discharge $q = Q/W$, and the characteristic grain diameter of the base material d_{84} are input parameters for the design procedure. The lowercase d refers to the grain diameter of the base material and the uppercase letter D to the diameter of the step-forming blocks. The resulting design parameters are the step-forming block diameter D_{eq}, drop height H_d, step spacing L_d, step heights H and H_s for clear-water (CW) and sediment feed (SF) conditions, respectively (Figure 7.1). The design aid was developed for the following parameter ranges:

- Bed slope $\quad\quad\quad\quad\quad\quad\quad\quad\quad\quad\quad\quad$ S $\quad\quad\quad$ = 0.04 ... 0.08
- Normalized step spacing $\quad\quad\quad\quad\quad\quad$ L_d/W $\quad$ = 0.8 ... 3.1
- Normalized drop height $\quad\quad\quad\quad\quad\quad\quad$ H_d/D_{eq} = 0.3 ... 0.8
- Relative step-forming block diameter $\quad$ D_{eq}/d_{84} = 6.7 ... 10.6
- Froude number $\quad\quad\quad\quad\quad\quad\quad\quad\quad\quad$ F $\quad\quad\quad$ = 0.53 ... 1.16
- Aspect ratio $\quad\quad\quad\quad\quad\quad\quad\quad\quad\quad\quad$ W/h $\quad\quad$ = 1.7 ... 16.1
- Dimensionless bed shear stress $\quad\quad\quad\quad$ θ_D $\quad\quad$ = 0.017 ... 0.083
- Sediment feed rate $\quad\quad\quad\quad\quad\quad\quad\quad\quad$ $q_{s,in}$ $\quad$ ≤ 20% transport capacity (TC)

More information regarding the experimental setup of the artificial step-pool system is detailed in Section 4.4. All experiments were conducted in a rectangular, straight channel. The effects of bank inclination and stream course (e.g., stream bends) were not investigated

and require thorough consideration in the planning of artificial step-pool sequences. All measures are given in prototype scale using a scale factor $\lambda = 20$. This is done mainly for illustration as the design approach uses non-dimensional equations.

7.3   Step-pool geometry

A sketch of the investigated step-pool geometry is illustrated in Figure 7.1. The BASE configuration consisted of two step-forming block layers with a horizontal overlap of approximately half a block length ($\approx 1/2\, D_a$ with $D_a = a$-axis length of step-forming blocks). Auxiliary blocks were placed in between the steps with the purpose of reducing the scour extent and depth. The first set of auxiliary blocks was placed approximately one block diameter $L_{A1} = D_{eq}$ downstream of the block in the upper block row. These first row auxiliary blocks were of category B1 (Table 4.6) with a mean block weight $M_B = 3.8\,\text{t}$ (2.4 to 4.8 t). The second row of auxiliary blocks was placed approximately $L_{A2} \approx 0.5\, L_d$ downstream of the upper row of step-forming blocks. This second row of auxiliary blocks were of category B2 with $M_B = 5.4\,\text{t}$ (4.8 to 6.4 t). Note that Table 4.5 summarizes the number of step-forming and auxiliary blocks which were used depending on channel width.

Additionally to the BASE configuration, pyramidal steps (PYR) and pyramidal steps with scour protection (PYR+SP) were investigated (Figure 7.1d,e). The steps were supplemented with a block row in the upstream (marked in blue) reducing an early tilting
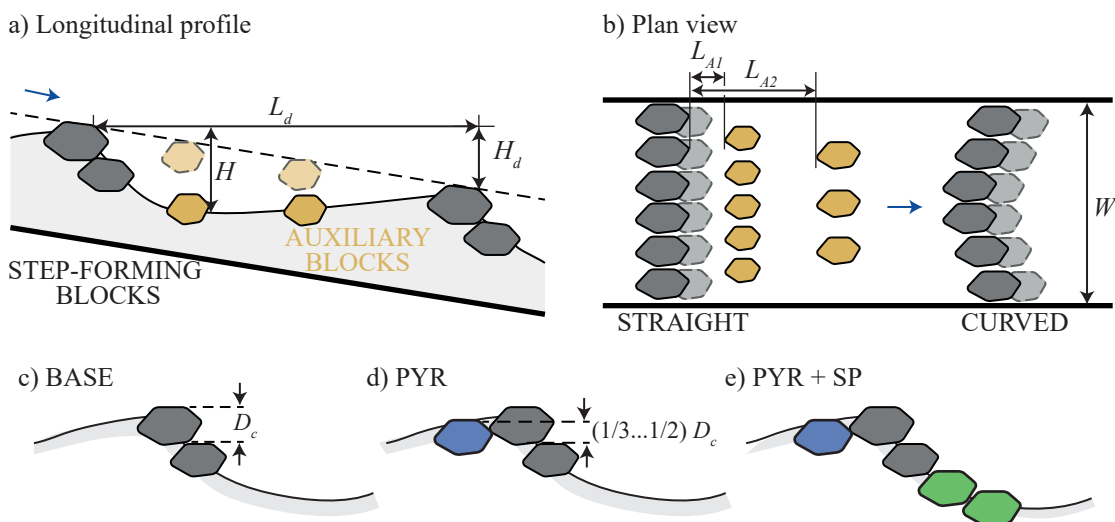

Figure 7.1 Step-pool geometry with $H_d =$ drop height, $H =$ step height, $L_d =$ step spacing, $L_{A1} =$ distance to first auxiliary blocks, $L_{A2} =$ distance to second auxiliary blocks, $W =$ channel width, $D_c = c$-axis length of step-forming blocks; a) longitudinal profile, b) plan view, c) base configuration (BASE), d) pyramidal steps (PYR), and c) pyramidal steps with scour protection (PYR+SP)

and two block rows at the step toes (marked in green) reducing failure due to scouring. These configurations were more stable compared to the BASE configuration but featured higher block placement densities (Section 6.6.6). It is recommended to either use the PYR or PYR+SP geometry.

Jamming (i.e., the interlocking of the step-forming blocks with each other and the channel banks) was attained by a tight placement of the step-forming blocks, firmly attached to each other, forming channel-spanning force chains. In case of a jammed state, the applied force is not only transmitted to the ground but also into the channel banks leading to an increase in stability. In artificial step-pool sequences, jamming was attained by a curved step shape in plan view in wide channels (CUR, Figure 7.1b) or by ensuring a tight (straight) placement of the step-forming blocks in narrow channels. However, even though jamming effects are important regarding step stability, it is worth mentioning that step stability increased rather by few discharge increments (i.e., by ~20 to 30%) and by far not by an order of magnitude.

7.4   Design procedure

The design procedure for artificial step-pool sequences takes advantage of different bed adjustment mechanisms occurring in steep streams. According to these mechanisms, the channel bed adjusts to an increase in discharge either by an increase in bed roughness (i.e., increase in scour depth), by a decrease in bed slope, or both (Aberle 2000; Weichert *et al.* 2009). An increase in bed roughness leads to a more pronounced energy dissipation, thus, balancing the additional energy imposed on the system. A decrease in bed slope occurs when the larger grains are mobilized, as they can no longer resist the increase in bed shear stress, resulting in a smaller bed slope.

These mechanisms have proven to occur rather subsequently than simultaneously in artificial step-pool systems (Section 6.7). The system initially adjusts by scouring (i.e., increasing bed roughness) until a critical condition is reached, leading to the destruction of one or more step(s). Either the step-forming blocks tilt into the downstream pool (tilting, Section 6.4) or the entire step glides into the pool as the step toe is destabilized by scouring (scouring, Section 6.4). Consequently, the system adapts by decreasing its bed slope.

The stability diagram (Figure 7.2) relates bed slope S and the applied unit discharge q to bed roughness σ_z, where the latter two are combined as $q^* = q/(g\,\sigma_z^3)^{1/2}$. The diagram was originally developed for self-organizing step-pool systems but this study de-
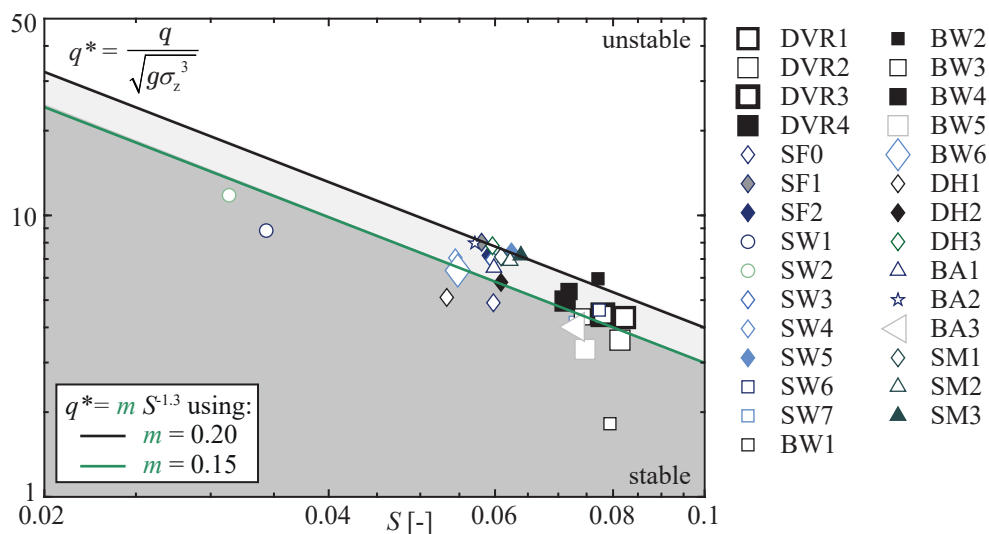
Figure 7.2 Stability diagram for artificial step-pool sequences showing data of all experiments for the maximum discharge sustained by the system ($q = q_{stab}$); experiment designation: Table 6.3

monstrated its applicability to artificial step-pool systems (Section 6.7.2). It predicts bed roughness σ_z for a steep stream with bed slope S and discharge q. In the present study, an empirical relation was developed to relate σ_z to the step height H enabling the prediction of H for a given q and S. Step height H, in turn, is a function of the step spacing L_d (and q, S, and d_{84}) described by Equation (6.10) presented in Section 6.8.4. Consequently, the step spacing L_d is selected in a way to obtain the required step height H. The step-pool system geometry is fully determined when knowing L_d and H.

However, knowing H, L_d, and $H_d = S L_d$ does not suffice to determine the system's stability. The step-forming block size has to be chosen to withstand the design discharge. The design procedure presents a Shields criterion to determine the required block size. Moreover, threshold values are provided for the scour depth-related parameters H/H_d and H/D to avoid step failure related to scouring. The design procedure is divided into four main steps:

1. The required bed roughness $\sigma_{z,req}$ is determined using the stability diagram.

2. The geometric parameters H, L_d and H_d are estimated.

3. Mean flow velocity v and the applied bed shear stress θ_D are calculated.

4. The step-forming blocks are selected large enough to withstand the applied bed shear stress.

Table 7.1 provides an overview of all parameters required during the four steps of the design procedure, which is detailed in the following.

Table 7.1 Overview of parameters used in the design procedure for the different design steps

Step	Parameter		Definition	Remarks
1	$m = 0.15$	$[0.15 ... 0.20]$	$q^* = m\, S^{-1.3}$ $\to$ Eq. (7.1)	m small: higher H_d (larger D_{eq}) required
2	$c = 1.8$	$[1.1 ... 2.6]$	$H/H_d < c$ $\to$ Eq. (7.2)	c small: step failure due to scouring is less likely
4	$b = 0.56$	$[0.43 ... 0.69]$	$\theta_D = b\, \theta_c$ $\to$ Eq. (7.8)	b small: more conservative regarding block stability
	$a_1 = 6$		$a_1 < D_{eq}/d_{84}$ $\to$ Eq. (7.11)	a_1 small: blocks entrained (use larger blocks)
	$a_2 = 11$		$D_{eq}/d_{84} < a_2$ $\to$ Eq. (7.11)	a_2 large: blocks sink in (consider filter layer)
	$e = 1.0$	$[1.0 ... 1.5]$	$H/D_{eq} < e$ $\to$ Eq. (7.12)	e small: more conservative regarding step stability

Step 1: Required bed roughness

The required bed roughness $\sigma_{z,req}$ is estimated for a given unit discharge q and bed slope S considering the stability diagram. Therein, data points corresponding to stable conditions plot below or in the vicinity of the indicated threshold lines described by the relation $q^* = m\, S^{-1.3}$ (Figure 7.2). The parameter $m = 0.20$ originates from self-organizing step-pool data developed by Aberle (2000) and $m = 0.15$ from a regression analysis using the artificial step-pool data of this study. Using these thresholds defined by Equations (3.11) and (6.7), solving for σ_z, yields:

$$\sigma_{z,req} = \left(\frac{q}{q^* \sqrt{g}} \right)^{2/3} = \left(\frac{q}{m\, S^{-1.3}\, \sqrt{g}} \right)^{2/3} \tag{7.1}$$

This estimate $\sigma_{z,req}$ represents the required bed roughness of the step-pool system to dissipate the energy imposed on the systems by a given combination of S and q. The system can only evolve towards this state if the steps are stable enough to maintain a constant bed slope, i.e., the bed only adjusts by scouring. For example, if D_{eq} was selected too small, the steps collapse prior to reaching the design step height. According to Figure 7.2, most of the experiments, and particularly those with sediment feed (SF) conditions (filled markers), plot in between the stability lines defined by $m = 0.15$ and 0.20. The least stable experiments SW1, SW2, DH1, and BW1 plotting below the line defined by $m = 0.15$ all failed gradually (Table 6.3). The step geometry was not selected ideally (e.g., D_{eq} too

small, L_d and H too large) in these cases leading to a step failure prior to reaching the required bed roughness $\sigma_{z,req}$.

It is recommended to use $m = 0.15$ in the design procedure. However, as this parameter is sensitive regarding drop height H_d and step spacing L_d (Step 2), a sensitivity analysis is required by repeating the design procedure for different values of m as in the computational example presented below (Section 7.5, Table 7.2). Using $m = 0.20$ predicts a lower bound for bed roughness required for a certain q and S. As a consequence, it also predicts a lower bound for H_d but potentially leads to a less stable system because the choice of the step-forming block diameter D_{eq} depends on the drop height H_d (Step 4). Large drop heights require larger step-forming blocks to avoid failure due to scouring.

Step 2: Determine step height and spacing

The second step relates the previously determined bed roughness $\sigma_{z,req}$ to the required drop height H_d:

$$H_d = \left(\frac{(\sigma_{z,req} - 0.5\, d_{84})\, d_{84}^{7/20}\, (s - 1)\, g^{1/5}}{0.52\, q^{2/5}\, S^{1/6}} \right)^{4/3} \qquad (7.2)$$

with $s = \rho_s/\rho =$ relative sediment density and $g =$ gravitational acceleration. Step spacing L_d, step heights H and H_s for clear-water (CW) and sediment feed (SF) conditions, respectively, and bed roughness parameter $\sigma_{z,Hs}$ corresponding to H_s are determined with Equations (7.3) to (7.5):

$$L_d = \frac{H_d}{S}; \qquad L_{d,min} = W \qquad (7.3)$$

$$H = 2.23 \frac{q^{2/5}\, S^{11/12}\, L_d^{3/4}}{d_{84}^{7/20}\, (s - 1)\, g^{1/5}}; \qquad H_s = 0.90\, H \qquad (7.4)$$

$$\sigma_{z,Hs} = 0.50\, d_{84} + 0.26\, H_s \qquad (7.5)$$

Note that Equation (7.2) resulted from combining Equations (7.3) to (7.5), representing the condition $\sigma_{z,H_s} = \sigma_{z,req}$. Minimum step spacing $L_{d,min}$ should not be smaller than one channel width, i.e., $L_{d,min}/W \geq 1$, approximately corresponding to the minimum $L_d/W = 0.8$ investigated in the present study. This ratio L_d/W was found to be larger than unity in self-organizing step-pool systems (Equations (3.1) and (3.2), Chin 1999; Okazaki *et al.* 2006, respectively). Moreover, a minimum step spacing is required for the step-pool geometry investigated herein corresponding to approximately two times the *a*-axis of the auxiliary blocks.

To avoid step failure due to scouring at discharges smaller than the design discharge, the relative steepness ratio H/H_d is compared to the threshold parameter c:

$$\frac{H}{H_d} \leq c \qquad (7.6)$$

Relative steepness ratios were in the range of $1.1 < H/H_d < 2.6$ in artificial step-pool experiments (Figure 6.38) indicating that these ratios represent stable conditions. It is recommended to only allow relative steepness ratios $c \leq 1.8$. For $1.8 < c \leq 2.6$ it is recommended to use the PYR+SP geometry to reduce the risk of step failure due to scouring.

Step 3: Hydraulics

The stability assessment of the step-forming blocks requires knowledge of the applied bed shear stress, estimated from flow depth, which is calculated from the reach-averaged flow velocity. The experimental data showed that mean flow velocity was well predicted with the approach of Aberle and Smart (2003) (Figure 6.5a,d). Knowing bed roughness $\sigma_{z,Hs}$ allows to determine the reach-averaged flow velocity:

$$v = 0.96 \, g^{0.20} \, S^{0.20} \, q^{0.60} \, \sigma_{z,Hs}^{-0.40} \qquad (7.7)$$

The mean flow depth h is estimated with $h = q/v$, which will be used to obtain the bed shear stress θ_D in the subsequent Step 4. Alternatively, the mean flow velocity can be estimated with Equations (6.2) and (6.3) using block size and step height as bed roughness parameters, respectively. However, Equation (7.7) has the highest accuracy. The reach-averaged flow conditions should be subcritical (i.e., $F < 1$) to ensure the emergence of hydraulic jumps, which are highly efficient in dissipating energy.

Step 4: Step-forming block size

The step-forming block diameter D_{eq} is determined based on the critical Shields parameter. The bed shear stress θ_D, calculated with Equation (4.8), should not exceed a reduced critical bed shear stress θ_c:

$$\theta_D \leq b \, \theta_c \qquad (7.8)$$

with $b = 0.56 \pm 0.13$ and θ_c = critical Shields parameter (Equation (2.42), Lamb *et al.* 2008). Note that b accounts for the reduction of θ_c observed in artificial step-pool systems

(Figure 6.35): according to the Shields concept, the step-forming blocks are mobilized at $\theta_D/\theta_c \approx 1$. However, this is only the case for a bed entirely covered with grains of size D_{eq}. In the case of artificial step-pool sequences, the block exposure is typically larger resulting in a lower threshold for incipient motion. Resolving Equation (7.8) for D_{eq} yields:

$$D_{eq} \geq \frac{h\,S}{(s-1)\,b\,\theta_c} = \frac{h\,S}{(s-1)\,b\,(0.15\,S^{0.25})} \tag{7.9}$$

Flow depth h is used instead of the hydraulic bed radius R_b to estimate the bed shear stress as it represents the maximum shear stress exerted on the bed, i.e., the bank shear stress is neglected (Section 2.3). It is recommended to estimate the step-forming block diameter for a range of $b = 0.56 \pm 0.13$ to get a range for D_{eq}. Note that the b-axis of the step-forming blocks is well approximated by the equivalent spherical diameter D_{eq}. Subsequently, the block weight M_B is determined by:

$$M_B = \frac{D_{eq}^3\,\rho_s\,\pi}{6} \tag{7.10}$$

with ρ_s = sediment density. Using $b = 0.43$ is more conservative leading to higher step-forming block diameters D_{eq}. For example, applying $b = 0.43$ is recommended in situations with high damage potential, in case a tight placement of the blocks leading to jamming of the step-forming blocks and the banks is not possible, or in cases where CW conditions are expected (e.g., downstream of a bedload retention structure). Vice versa, $b = 0.69$ is suitable in case of a low damage potential, short test reaches, or occasionally when using the PYR+SP configuration.

It is reasonable to assume critical conditions at the step crest, as the reach-averaged flow is subcritical ($F < 1$) leading to the oscillation between supercritical flow over the steps and subcritical flow in the pools. However, using the critical flow depth h_c to estimate the step-forming grain diameter with Equation (7.9) leads to smaller values for D_{eq}, which does not represent conservative conditions.

Two additional criteria need to be satisfied to avoid step failures at discharges smaller than the design discharge: i) D_{eq}/d_{84} and ii) H/D_{eq}. First, the ratio between step-forming block diameter and characteristic grain diameter of the base material should comply with:

$$a_1 < \frac{D_{eq}}{d_{84}} < a_2 \tag{7.11}$$

According to Raudkivi and Ettema (1982), who investigated the stability of bimodal sediment mixtures (Section 2.4.5), direct erosion of the large fraction is expected for $D_{eq}/d_{84} \leq 6$. Moreover, for $D/d_{84} \geq 17$, the large step-forming blocks may sink into the base material. The ratio investigated in the present study was $6.7 \leq D_{eq}/d_{84} \leq 10.6$. Thus, it is recommended to use $a_1 = 6$ and $a_2 = 11$ in the design procedure. Note that a filter layer is recommended between the step-forming blocks (or auxiliary blocks) and the base material if $11 \leq a_2 < 17$. Second, the step height-to-block size ratio H/D_{eq} should not be too large to avoid step failure due to scouring:

$$\frac{H}{D_{eq}} < e \tag{7.12}$$

with e representing the threshold parameter. According to the experimental data, this parameter was $0.6 < e < 1.5$ for the investigated step-pool systems (Figure 6.39) indicating stable conditions. However, scour protection (e.g., geometry PYR+SP, Figure 7.1e) is recommended for $e \geq 1.0$.

7.5 Design example

The design procedure for artificial step-pool sequences is illustrated using a design example with the following boundary conditions (Figure 7.3):

- Bed slope $\qquad\qquad\qquad\qquad S \;\; = 0.065$
- Channel width $\qquad\qquad\quad W \; = 8 \text{ m}$
- Design discharge $\qquad\quad\;\; Q \;\; = 40 \text{ m}^3/\text{s}, \;\; q = 5 \text{ m}^2/\text{s}$
- Grain diameter of base material $\; d_{84} = 0.25 \text{ m}$

The PYR step-pool geometry is selected consisting of three block rows arranged in pyramid shape. The required bed roughness is estimated with Equation (7.1) and $m = 0.15$ leading to $\sigma_{z,req} = 0.45$ m. The resulting drop height, calculated with Equation (7.2), is $H_d = 0.79$ m corresponding to a step spacing of $L_d = 12.1$ m, a step height $H = 1.41$ m and $H_s = 1.27$ m with CW and SF conditions, respectively, using Equations (7.3) to (7.4). Per definition, the bed roughness calculated with Equation (7.5) equals $\sigma_{z,Hs} = \sigma_{z,req} = 0.45$ m. The minimum required step spacing ($L_d/W \geq 1$) is satisfied with $L_d/W = 1.5$ and also the relative steepness $H/H_d = 1.8$ is in line with the recommendations. The reach-averaged mean flow velocity is calculated with Equation (7.7) yielding $v = 3.2$ m/s, $h = 1.6$ m,
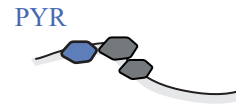
DESIGN PROCEDURE

Boundary conditions and step geometry
> Define bed slope, width, design discharge, base material properties
> Select step-pool geometry (PYR or PYR+SP recommended)

BASE   PYR   PYR + SP
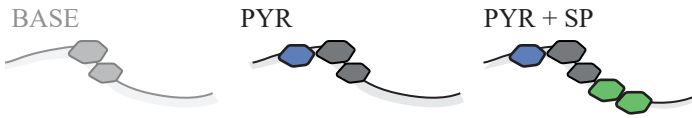
$S = 0.065$, $W = 8$ m
$Q = 40$ m³/s, $q = 5$ m²/s
$d_{84} = 0.25$ m

PYR

Step 1: Required bed roughness

Eq. (7.1) $\sigma_{z,req} = \left(\dfrac{q}{m\, S^{-1.3} \sqrt[3]{g}} \right)^{2/3}$ $m = 0.15\ [0.15 \ldots 0.20]$ $\sigma_{z,req} = 0.45$ m

Step 2: Determine step height and step spacing

Eqs. (7.3) to (7.5):

$L_d = H_d\, /\, S$

$H = 2.23 \dfrac{q^{2/5}\, S^{11/12}\, L_d^{3/4}}{d_{84}^{7/20}\, (s-1)\, g^{1/5}}$

$H_s = 0.90\, H$

$\sigma_{z,Hs} = 0.50\, d_{84} + 0.26\, H_s$

Eq. (7.2):

$H_d = \left(\dfrac{(\sigma_{z,req} - 0.5 d_{84})\, d_{84}^{7/20}\, (s-1)\, g^{1/5}}{0.52\, q^{2/5}\, S^{1/6}} \right)^{4/3}$
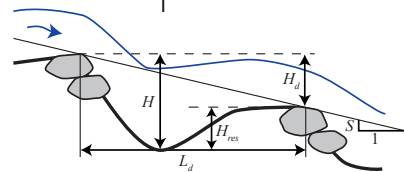
$H_d = 0.79$ m
$H = 1.41$ m $H_s = 1.27$ m
$\sigma_{z,Hs} = \sigma_{z,req} = 0.45$ m

> Check minimum step spacing: $L_d / W \geq 1$

$L_d = 12.1$ m
$L_d / W = 1.5$ (ok)

> Check steepness ratio: Eq. (7.6): $H/H_d \leq c$
                                                 $c = 1.8\ [1.1 \ldots 2.6]$

$H/H_d = 1.8$ (~ok)

⚠ $c > 1.8$: consider scour protection (PYR+SP)

Step 3: Hydraulics

Eq. (7.7): $v = 0.96\, g^{0.20}\, S^{0.20}\, q^{0.60}\, \sigma_{z,Hs}^{-0.40}$ $h = q/v$

$v = 3.2$ m/s, $h = 1.6$ m

> Check flow conditions: $F < 1$ $F = 0.80$ (ok)

Step 4: Step-forming block size

Eq. (7.9): $D_{eq} = \dfrac{hS}{(s-1)\, b\, (0.15\, S^{0.25})}$ $b = 0.56\ [0.43 \ldots 0.69]$ $D_{eq} = 1.47$ m

Eq. (7.10): $M_B = \dfrac{D_{eq}^3\, \rho_s\, \pi}{6}$ $M_B = 4.4$ t

> Bimodal mixtures: Eq. (7.11): $a_1 < D_{eq}/d_{84} < a_2$ $D_{eq}/d_{84} = 5.8$
                                                                                (~ok)
⚠ $a_2 > 11$: consider filter layer $a_1 = 6$
                                            $a_2 = 11$

> Step height to block size ratio: Eq. (7.12): $H/D_{eq} < e$ $H/D_{eq} = 0.96$ (ok)
                                                             $e = 1.0\ [1.0 \ldots 1.5]$

⚠ $e > 1.0$: consider scour protection (PYR+SP)

Figure 7.3 Overview of design procedure applied to a design example

and $F = 0.80$. Equation (7.9) and $b = 0.56$ are used to determine the step-forming block diameter $D_{eq} = 1.47$ m (i.e., mean block weight $M_B = 4.4$ t). The ratio $D_{eq}/d_{84} = 5.8$ is slightly lower than recommended and a larger diameter D_{eq} may be chosen, particularly if sediment-starved conditions are expected making the exposure of step-forming blocks to the flow more likely (see Section 6.6.1). The ratio $H/D_{eq} = 0.96$ complies with the recommendations.

A sensitivity analysis is conducted by repeating the design procedure using $m = 0.15$ and 0.20 and $b = 0.69$ and 0.43 because m and b are sensitive regarding H_d and D_{eq}, respectively (Table 7.2). Choosing $m = 0.15$ results in a larger drop height H_d and step spacing L_d compared to $m = 0.20$. A higher step spacing results in a lower block placement density. Using the less conservative estimates for $b = 0.69$ is not recommended without scour protection measures as it results in small block diameter D_{eq} leading to high H/D_{eq} ratios (dark red, Table 7.2) increasing the risk of step failure due to scouring. Using $m = 0.20$ and $b = 0.69$ to 0.56 results in low $D_{eq}/d_{84} = 4.4$ to 5.4 potentially leading to an entrainment of the step-forming blocks (light red, Table 7.2). A lower boundary for drop height $H_d = 0.56$ m results when using $m = 0.20$. A small step spacing L_d is associated with a high block placement density but a smaller required block size. The blocks may be entrained in case D/d_{84} becomes too small. It is worth emphasizing that the uncertainty in the required block size is large. The recommended block weight computed with $b = 0.56$ varies approximately by a factor of ± 2 by using the full range of parameter b. The inherent heterogeneity of steep streams, the complexity of these systems, and the randomness during failure do not allow a more precise estimate for the block weight M_B.

Table 7.2 Sensitivity analysis for the design procedure (conditions violating design parameter are bold, corresponding parameter set is colored in red

m	b	H_d	L_d	H	H/H_d	F	D_{eq}	M_B	D_{eq}/d_{84}	H/D_{eq}
[-]	[-]	[m]	[m]	[m]	[-]	[-]	[m]	[t]	[-]	[-]
0.15	0.43	0.79	12.1	1.4	1.8	0.80	1.91	9.7	7.7	0.73
	0.56						1.47	4.4	5.9	1.00
	0.69						1.19	2.4	**4.8**	**1.18**
0.20	0.43	0.55	8.4	1.1	2.0	0.90	1.77	7.7	7.1	0.60
	0.56						1.36	3.5	**5.4**	0.78
	0.69						1.10	1.9	**4.4**	0.97

7.6   Remarks on bank protection

The above presented design procedure is based on experiments in a straight channel with rectangular smooth sidewalls. As steep mountain streams do not necessarily fulfill these boundary conditions, attention has to be paid to channel bends and to the shape of the channel banks. Theoretically, the bed shear stress decreases in the vicinity of inclined rough banks. However, the connection between step-forming blocks and banks, which is crucial for stability increasing jamming effects, represent potential weak spots in channels with incised banks.

Bank protection measures are required to avoid bank erosion potentially triggering an abrupt system failure. The foundation depth primarily depends on the expected scour depths but also reach-scale channel bed incision has to be considered. Furthermore, bed forms such as alternate bars inducing horizontally oscillating flow may lead to a higher hydraulic stress on the banks but also locally on the steps. Scour depth estimation and bed morphology is shortly discussed in the following.

Scour depth estimation

The mean step height is estimated during the design process for both clear-water (CW) and sediment feed (SF) conditions (H and H_s, respectively). The scour depth is defined as the difference between step height and drop height $H_{res} = H - H_d$ (Figure 7.3). The step height H for CW conditions is decisive regarding the required foundation depths of the bank protection measures. However, maximum height of individual steps $H_{max} = 1.5\,H$ is substantially higher than mean step height H (Section 6.8.5), which has to be considered for the bank protection design.

Bed morphology

The channel banks and bed may experience a higher hydraulic load in case of the formation of alternate bar structures, particularly for small flow depths and in wide channels, i.e. low aspect ratios. Therefore, the regime theory presented in Figure 7.4 is recommended to assess bed morphology. The indicated point represents the conditions of the design example presented above. The boundary conditions should be selected in a way to avoid the formation of alternate bars. If alternate bars are expected, bank protection may be reinforced to prevent bank erosion.
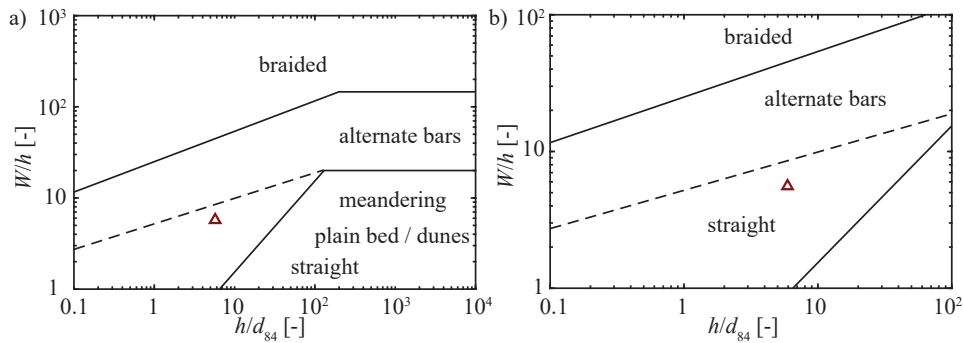
Figure 7.4 Regime theory diagram adapted from Weichert (2006) with criteria by da Silva (1991) and Zarn (1997), marker indicates conditions for the design example; b) presents a zoom in on a)

7.7   Limitations and uncertainties

The above presented design scheme is a useful tool for practitioners to design artificial step-pool systems. Nevertheless, it is crucial to be aware of uncertainties due to the heterogeneity of these systems and the randomness during failure. The most important aspects are:

- The design procedure requires an estimate for d_{84} of the base material. Determining the grain size distribution (GSD) in steep streams is difficult owing to the heterogeneity but also to the size of the largest grain size fraction (i.e., boulders) complicating data acquisition. Applying the design procedure to a range of d_{84} rather than a single estimate is recommended.

- An integral system failure may be triggered by an initial failure of a single step leading to an upstream migrating erosion pattern (i.e., abrupt failure). The decrease in reach-averaged bed slope depends on the location of this initial step failure, on the reach length, but also on the timing of the step failure during a flood hydrograph. The stream bed incision after a high-intensity flood is much more pronounced if the step failure occurs during the ascending limb or peak flow compared to a failure during the receding limb of the hydrograph.

- The uncertainty regarding the step-forming block weight corresponds approximately to a factor of ±2 (Table 7.2).

- The experiments were conducted in a straight channel and the increase in bed shear stress in bends was not considered.

- The prediction error of the mean step height was below ±20%. Nevertheless, step height of individual steps was up to 50% higher compared to the mean step height. Consequently, an appropriate safety factor is required regarding the foundation depth of the bank protection.

- Artificial step-pool sequences are not necessarily suitable for all kinds of boundary conditions. Note that exceeding the indicated bed slopes (i.e., dimensionless bed shear stresses) requires careful considerations regarding step-forming block stability. Moreover, a continuous bed protection of the entire pool with large boulders may be required (e.g., artificial step-pool sequence in Maira Stream, Switzerland, Section 3.4.5).

8 Conclusions and outlook

The step-pool morphology is typical in steep streams with bed slopes exceeding ~4%. The near-critical flow regime attributed to the alternating supercritical flow over the steps and subcritical flow in the pools leads to the emergence of hydraulic jumps, which are highly efficient in dissipating energy. Using artificial step-pool sequences as bed stabilization works, imitating the natural step-pool morphology, represents a promising alternative to the rigid concrete drop structures. The overall goal of the present study was to improve the understanding of the processes shaping these step-pool systems. Part A investigated the effect of macrorough sidewalls on flow resistance and bed stability addressing fundamental processes of self-organizing step-pool systems. Part B focused on bed stability and failure mechanisms of artificial step-pool systems compiling the main results into a design aid for practitioners. Therefore, physical flume experiments were conducted at the Laboratory of Hydraulics, Hydrology and Glaciology (VAW), ETH Zurich. The main conclusions are presented separately for Part A and B in the following sections.

8.1 Conclusions Part A

Steep mountain streams have macrorough sidewalls induced by large boulders, vegetation, or logs protruding into the flow. Part A addressed the effect of these macrorough sidewalls on flow resistance and bed stability, untangling hydraulic and granular effects. The main findings regarding research questions A1 and A2 (Section 1.3) are summarized in the following:

A1: *Sidewall friction*: The generalized Einstein Johnson's sidewall correction procedure was successfully modified to account for sidewall friction induced by macrorough elements in steep rough channels (Section 5.3.4). Sidewall friction accounted for 10 to 70% of the total shear stress in the experiments with a fixed rough bed without step-pool units. In the mobile bed experiments, where step-pool units were present, macrorough sidewall friction accounted for 5 to 40% of total shear as the step-pool morphology induced more flow resistance compared to the fixed rough bed experiments.

A2: *Hydraulic and granular effects*: The increase in bed stability was fully explained by hydraulic effects at least in moderately rough sidewall experiments with relative sidewall roughness $\sigma_w/W_m \leq 0.035$. However, granular effects became important

in the roughest sidewall experiments ($\sigma_w/W_m > 0.035$) as the steps preferentially formed in the narrowing sections upstream of the roughness elements. These configurations also sustained higher bed shear stress indicating that grain-sidewall interlocking considerably increases step stability (Section 5.5).

Part A provides novel insights into the processes shaping the typical step-pool morphology in steep streams with macrorough sidewalls thereby contributing to a better understanding of these systems.

8.2   Conclusions Part B

Part B investigated artificial step-pool sequences representing a nature-based bed stabilization work for flood control and restoration projects. All measures are indicated in prototype scale because Part B aims at providing recommendations for practitioners. The research questions B1 to B5 (Section 1.3) are addressed in the following:

B1: *Failure mechanisms:* The most prominent failure mechanisms in artificial step-pool systems (Section 6.4) were tilting of the upper row blocks (46%) and scouring due to an undermining of the steps (45%). Step failure was related to internal erosion processes (5%), direct entrainment (3%), and pool filling (1%). In comparison with self-organizing step-pool systems, scouring was also very frequent while tilting of the upper row blocks was an additional main driver for step destruction. Step burial rarely occurred and failure by collision was never observed. Step failure potentially triggered a progressive upstream erosion (PUE) pattern leading to the destruction of all steps located upstream of the initial step failure (Section 6.4.2). Consequently, bed slope decreased considerably leading to bed incision particularly in the upstream part of the test reach. This pattern was also observed in self-organizing step-pool systems (Section 5.2) but the decrease in slope was assumed to be smaller owing to the widely graded sediment mixture containing more large boulders (i.e., a higher density of the large, step-forming blocks).

B2: *Self-stabilizing character:* Artificial step-pool systems were prone to an abrupt system failure associated with a considerable decrease in bed slope ($\Delta S = -0.01$ to -0.02) in a short time period (<20 minutes) severely incising the bed (Section 6.4.5). Approximately 70% of the experiments showed an abrupt failure while only 30%

failed gradually (Table 6.3). Consequently, a self-stabilizing mechanism was not achieved as the step-forming blocks were buried (or transported) and did not reorganize into a system comparable with the initial, highly organized step-pool sequence. The decrease in bed slope depended on whether the step failed during peak flow or later during the receding limb of the hydrograph. Furthermore, a higher block placement density (Section 6.6.8) may also lead to a less pronounced decrease in bed slope, i.e., to a more gradual failure mode or more pronounced self-stabilizing character of the system.

B3: *Hydrograph shape:* Experiments with exactly the same step-pool geometry were investigated with stationary conditions, hydrographs, and hydrographs with intermittent periods of low discharge (Section 6.5). The steps sustained comparable discharges and attained similar maximum Shields ratios (Figure 6.16). Moreover, once the steps failed, an upstream migrating erosion pattern was observed independent of the discharge regime. In stationary experiments, the final step height was reached after 45 minutes while in unsteady experiments, the major changes occurred during the peak flow (~20 minutes) and approximately 10 and 20 minutes before and after (Figure 6.18). As hydrographs led to 4.9 ±3.7% higher step heights, the impinging angle of the jet might have an effect on step height but it did not trigger step destruction at lower discharges. Low stationary flow conditions in between hydrographs did not alter the channel bed (Figure 6.19). To conclude, both stationary conditions and hydrographs are suitable to evaluate bed stability, failure mechanisms, and geometric relations of step-pool systems as long as the peak duration of the hydrograph is not too short (i.e., ≥15 to 20 minutes).

B4: *Sediment supply:* Sediment supply experiments sustained higher discharges and bed shear stress mainly attributed to differences in scour depth, block exposure, and jamming effects (Section 6.6.1) confirming the hypotheses. The step height decreased by ~10% in sediment supply experiments (Section 6.8.4) making step failures related to scouring less likely to occur. Moreover, sediment-starved conditions fostered internal erosion of the base material leading to water flow through the steps. The related exposure of the uppermost row of step-forming blocks made tilting more likely to occur (Figure 6.11). The largest grains of the base mixture may promote jamming effects as they interlock in between the step-forming blocks

creating stable force chains. Overall, clear-water experiments represent conservative conditions regarding bed stability. However, all sediment supply experiments showed an abrupt failure in case of overload (Table 6.3). The increase in flow velocity related to smaller step heights (i.e., lower bed roughness and higher bed shear stresses) led to the mobilization of auxiliary blocks in between steps increasing the scour depth (Figure 6.23).

B5: *Structural stability:* The effect of various parameters on the structural stability was addressed in Section 6.6. Block weight proved to have the largest effect on step stability (Section 6.6.5). Channels with milder slopes sustained higher unit discharges but no differences were observed regarding bed shear stress (Section 6.6.3). Channel width, base material, and step spacing did not significantly alter the system's stability. Jamming of the step-forming blocks, attained by either placing the blocks tightly next to each other or by a curved step shape in plan view, led to an increase in stability. However, the jamming ratio W/D_{eq} was found to be of minor importance in artificial step-pool systems as jamming was externally imposed on the system. Step stability increased with using pyramid-shaped steps with and without scour protection blocks located in the vicinity of the step toes (Section 6.6.6).

These findings were compiled into a design procedure for artificial step-pool sequences (Chapter 7) allowing to determine the required step-pool geometry, i.e., drop height, step spacing, and step height for a given design discharge and bed slope. Additionally, empirical relations are provided to estimate reach-averaged flow velocity and bed shear stress allowing conclusions on the required step-forming block size. Overall, the presented design guidelines represent a strong tool for practitioners planning artificial step-pool systems for grade-control and restoration projects.

8.3   Outlook

The present work contributes to a better understanding of processes in steep streams with both natural and artificial step-pool sequences. Nevertheless, many questions still remain unanswered owing to the complexity of these systems. The subsequent question regarding *self-organizing step-pool systems* may be addressed in the future:

- *Sidewall roughness parameter:* A sidewall correction procedure was proposed to quantify the effect of macrorough sidewalls on bed shear stress. However, a concise

procedure to estimate the sidewall roughness parameter σ_w in the field is lacking. A standardization procedure to determine σ_w may decrease the uncertainty.

The following points related to the *artificial step-pool systems* are perceived important and require further research:

- *Block placement density:* The present study focused on step-pool systems with low to moderate placement densities. Further experiments are required to quantify the effect of the step-pool sequences with high placement densities (i.e., $\lambda_D > 0.5$) for higher bed slopes and unit discharges.

- *Bank inclination:* The artificial step-pool experiments were conducted in a rectangular channel. It remains unclear, how bank inclination affects the stability of artificial step-pool sequences. The connection between step-forming blocks and banks may be challenging to obtain for inclined banks.

- *Stream curvature:* The experiments were conducted in a straight flume. However, the stream may be curved leading to a local increase in bed shear stress at the outer bank. Flume experiments with a step-pool system in stream bends would allow to quantify the local increase in shear stress permitting an indication on the required weight of the step-forming blocks at the outer banks.

- *Numerical modeling*: Numerical modeling of 3D hydrodynamics and morphodynamics in steep mountain streams is extremely challenging and has hardly been addressed, yet. There is a strong need for an improvement of these models to improve the bed stability assessment in steep mountain streams.

- *High resolution 3D flow field*: High resolution 3D flow velocity measurements in step-pool channels are rare and studies investigating the flow field in artificial step-pool systems lack entirely. A high resolution flow field and the associated bed shear stresses would improve the prediction of the structural stability of artificial step-pool systems. Moreover, such data are useful for the validation of numerical models.

- *Ecological relevance:* The present study primarily focused on design guidelines with respect to structural stability and did not consider ecological aspects. It remains unclear to what extent the habitat quality and availability for fish and other aquatic

organisms improves when using step-pool systems in restoration projects. Monitoring studies are required to assess the impact on habitat quality and availability in artificial step-pool systems.

- *Field measurements:* Only few artificial step-pool case studies exist and field data is generally lacking. It is of great importance to conduct a (long-term) monitoring of artificial step-pool systems to quantify the bed elevations changes but also to assess bed stability during floods.

Notation

Symbols

Roman letters

A	Area (m^2)
A_D	Area of boulder perpendicular to reference plane (m^2)
A_L	Area of boulder projected on the reference plane (m^2)
C	Chézy roughness coefficient
C_D	Drag coefficient (-)
C_L	Lift coefficient (-)
C_s	Sediment concentration $C_s = q_s/((\rho_s - \rho)\,q)$ (-)
c	Relative steepness, steepness ratio (-)
c_i	Coefficients (-)
D	Grain diameter of the coarse fraction, step-forming blocks (m)
D_a	Grain diameter corresponding to a-axis (m)
D_b	Grain diameter corresponding to b-axis ($\approx D_{eq}$) (m)
D_c	Grain diameter corresponding to c-axis (m)
D_{eq}	Equivalent spherical diameter (m)
d_i	Characteristic grain diameter for which $i\%$ is finer, base material (m)
d_m	Mean grain size diameter (m)
F	Froude number (-)
F_B	Buoyancy force (N)
F_D	Drag force (N)
F_G	Gravity force (N)
F_L	Lift force (N)
f	Darcy-Weisbach friction factor (-)
g	Gravitational acceleration (m^2/s)
H	Step height (m)
H_d	Drop height (m)
H_e	Energy head $H_e = 3/2\,h_c$
H_{res}	Residual depth, scour depth (m)
H_s	Step height with sediment supply (m)

H_t	Horizontal scour depth of check dam sequence relative to initial flat channel bed (m)
h	Flow depth (m)
h_c	Critical flow depth $h_c = (q^2/g)^{1/3}$ (m)
k	Hydraulic roughness (m)
L	Step length (m)
L_{A1}, L_{A2}	Distance from step crest to auxiliary blocks A1, A2 (m)
L_d	Step crest to step crest spacing = step spacing (m)
L_p	Pool length (m)
L_t	Distance between two check dams parallel to the bed (m)
L_{tot}	Length of the test reach in Part A (m)
l	Roughness element length (m)
l_1	Distance to the deepest point in pool (m)
l_2	Total scour length in single drop structures (m)
l_t	Distance to deepest point in scour parallel to the bed for a check dam sequence (m)
M_B	Mean block weight (kg)
m_i	Coefficients (-)
n	Number or frequency of a certain quantity (-)
n_M	Manning roughness coefficient (-)
p_{Pear}	Pearson's correlation coefficient (-)
Q	Water discharge (m³/s)
q	Unit water discharge (m²/s)
q^{**}	Dimensionless unit discharge $q^{**} = q/\sqrt{g\,S\,d_{84}^3}$ (-)
q_{ini}	Unit water discharge at which sediment supply started (m²/s)
q_s	Unit gravimetric sediment transport rate (kg/(sm))
$q_{s,v}$	Unit volumetric sediment transport rate (m²/s)
$q\,S$	Unit stream power (m²/s)
R	Hydraulic radius (m)
Re	Reynolds number (-)
Re_{*d}	Particle Reynolds number (-)
r	Roughness element thickness (m) or relative sediment density ρ_s/ρ (-)

r_q	Relative increase in discharge compared to previous interval (-)
S	Bed slope (-)
S_f	Energy slope (-)
SI	Sorting index $SI = 0.5(d_{84}/d_{50} + d_{50}/d_{16})$ (-)
S_{st}	Step slope (-)
s	Roughness element spacing (m)
T	Scour water depth in an individual drop structure (m)
T'	Scour water depth for submerged case (m)
t_{peak}	Duration of peak discharge during hydrographs (h)
t_{stat}	Duration of the stationary intervals in Part B (h)
t_{tot}	Total hydrograph duration (h)
u_*	Shear velocity (m/s)
v	Reach-averaged flow velocity (m/s)
v_f	Velocity of failure at which step-forming blocks start sliding (m/s)
v^{**}	Dimensionless flow velocity $v^{**} = v/\sqrt{g\,S\,d_{84}}$ (-)
W	Channel (flume) width (m)
W_m	Mean channel width (m)
x	Longitudinal direction parallel to the flume bottom (m)
y	Transversal direction (m)
z	Vertical direction perpendicular to flume bottom (m)

Greek letters

α	Angle of reference plane compared to horizontal plane ($\circ$)
Δq	Unit discharge increment (m^2/s)
$\Delta(qS)$	Stream power increment (m^2/s)
ΔS	Decrease in bed slope ($\Delta S = S_{ini} - S$) (-)
Δx_{NAR}	Length of NAR region upstream of roughness elements [m]
Δz	Reach-averaged bed elevation changes (m)
θ	Dimensionless shear stress (-)
θ_D	Dimensionless shear stress using D_{eq} for normalization (-)
Λ	Step wavelength (m)
λ	Froude scale factor (-)
$\lambda_{D_{eq}}$	Block placement density (-)

λ_{M_B} Block weight density (t/m^2)

μ Coefficient of static friction $\mu = \tan \psi$ (-)

ν Kinematic viscosity of water (m^2/s)

ρ Water density (kg/m^3)

ρ_s Sediment density (kg/m^3)

$\rho_{s,bulk}$ Bulk sediment density (kg/m^3)

$\Sigma Q_{s,out}$ Cumulative sediment outflow (kg)

σ_g Geometrical standard deviation $\sigma_g = \sqrt{d_{84}/d_{16}}$ (-)

σ_w Standard deviation of the bank variations (m)

σ_z Standard deviation of the bed elevations (m)

τ Boundary shear stress (N/m^2)

ϕ Tilting angle (°)

ψ Angle of repose (°)

Subscripts

b   bed

c   critical

calc   calculated

dep   deposition

ds   downstream

eq   equilibrium, equivalent

ero   erosion

in   inflow

ini   initial

M   model scale

m   mean

max   maximum

meas   measured

min   minimum

out   outflow

P   prototype scale

ref   reference

req	required
rot	rotated
s	sediment
sub	submerged
us	upstream
w	sidewall (bank)

Abbreviations

CA	Catchment area
CI	Confidence interval
CW	Clear-water
DEM	Digital elevation model
DL	Descending limb
DoD	DEM of differences
DVR	Discharge variation regime
EoP	End of Pool
EoS	End of Step
FDM	Flow depth method
FL	Filter layer
FOEN	Federal Office for the Environment
FR	Fixed rough bed
FS	Fixed smooth bed
GCP	Ground control point
GEJ	Generalized Einstein-Johnson
GSD	Grain size distribution
HRM	Hydraulic radius method
HSR	Hochschule für Technik Rapperswil
HYD	Discharge regime with hydrographs
HYD+LQ	HYD regime with intermittent periods of low flow
HYD+SF	HYD regime with sediment feed
LDS	Laser distance sensor
MID	Magnetic-inductive flow meter

MR	Mobile rough bed
NAR	Narrow region
NRF	Normal recirculating flow
PE	Prediction error
PER	Percentile
PUE	Progressive upstream erosion
RAF	Reattachment flow
RI	Recurrence interval
RMS	Root mean square
RMSE	Root mean square error
SF	Sediment feed
SfM	Structure from Motion
SGF	Square-grooved flow
STAT	Stationary discharge regime
TC	Transport capacity
ToS	Top of Step
UDS	Ultrasonic distance sensor
VAW	Laboratory of Hydraulics, Hydrology and Glaciology
VPE	Variable power equation
WID	Wide region
WSE	Water surface elevation

Literaturverzeichnis

Aberle, J. (2000). Untersuchung der Rauheitsstruktur zur Bestimmung des Fliesswiderstandes in Gebirgsbächen unter Klarwasserabfluss. *PhD Thesis*, Universität Fridericiana zu Karlsruhe (TH) [in German].

Aberle, J.; Smart, G. (2003). The influence of roughness structure on flow resistance on steep slopes. *Journal of Hydraulic Research*, 41(3): 259–269. https://doi.org/10.1080/00221680309499971.

Abrahams, A.; Li, G.; Atkinson, J. (1995). Step-pool streams: Adjustment to maximum flow resistance. *Water Resources Research*, 31(10): 2593–2602. https://doi.org/10.1029/95wr01957.

Adachi, S. (1964). On the Artificial Strip Roughness. *Bulletins - Disaster Prevention Research Institute, Kyoto University*: 1–20. http://hdl.handle.net/2433/123743.

Aigner, D.; Bollrich, G.; Carstensen, D.; Diersch, H.J.; Horlacher, H.B.; Martin, H.; Pohl, R. (2015). Technische Hydromechanik 4. *Verlag Bauwesen, Berlin, Germany* [in German].

Ashida, K.; Bayazit, M. (1973). Initiation of motion and roughness of flows in steep channels. *IAHR Proceeding 15th Congress, Istanbul, Turkey*: 475–484.

Ashida, K.; Egashira, S.; Ando, N. (1984). Generation and geometric features of step-pool bed forms. *Bulletin of the Disaster Prevention Research Institute, Kyoto University* [Japanese with English abstract].

Badoux, A.; Andres, N.; Turowski, J. (2013). Damage costs due to bedload transport processes in Switzerland. *Natural Hazards and Earth System Sciences*, 14: 4188–4222. https://doi.org/10.5194/nhessd-1-4181-2013.

Bathurst, J. (1982). Theoretical aspects of flow resistance: 443–462. In: R. Hey; J. Bathurst; C. Thorne (eds.) Gravel-Bed Rivers. *John Wiley and Sons*.

Bathurst, J. (1987). Critical conditions for bed material movement in steep, boulder-bed streams. *Erosion and Sedimentation in the Pacific Rim, Proceeding of the Corvallis Symposium, IAHS Publication*, 5: 309–318.

Beffa, C. (2016). Blaues Kolloquium: Stufen-Becken am Steinbach. https://www.fluvial. ch/pub/VAW-Kolloquium_2016_Stufen-Becken.pdf [in German].

beffa tognacca GmbH (2020). Stabilität stark strukturierter Sohlen: Resultate Feldmess- kampagne Ticino-Verzasca. *Technical Report*, beffa tognacca GmbH [unpublished, in German].

Benda, L.; Hassan, M.; Church, M.; May, C. (2005). Geomorphology of Steepland Head- waters: The transition From Hillslopes to Channels. *Journal of the American Wa- ter Resources Association*, 41(4): 835–851. https://doi.org/10.1111/j.1752-1688.2005. tb03773.x.

Bezzola, G. (2021). Flussbau-Skript, Fassung 2021, ETH Zurich [in German].

Bezzola, G.R. (2002). Fliesswiderstand und Sohlenstabilität natürlicher Gerinne unter be- sonderer Berücksichtigung des Einflusses der relativen Überdeckung. *VAW-Mitteilung 172* (H.E. Minor, ed.). Laboratory of Hydraulics, Hydrology and Glaciology, ETH Zu- rich, Switzerland. https://doi.org/10.3929/ethz-a-004288999 [in German].

Boes, R.; Hager, W. (2003). Two-phase flow characteristics of stepped spillways. *Journal of Hydraulic Engineering*, 129(9). https://doi.org/10.1061/(asce)0733-9429(2003)129: 9(661).

Bray, D.; Davar, K. (1987). Resistance to flow in gravel-bed rivers. *Canadian Journal of Civil Engineering*, 14: 77–86. https://doi.org/10.1139/l87-010.

Buffington, J.; Montgomery, D.R. (1997). A systematic analysis of eight decades of inci- pient motion studies, with special reference to gravel-bedded rivers. *Water Resources Research*, 33(8): 1993–2029. https://doi.org/10.1029/96wr03190.

Campbell, C. (2003). A problem related to the stability of force chains. *Granular Matter*, 5: 129–134. https://doi.org/10.1007/s10035-003-0138-6.

Chanson, H. (1994). Hydraulics of skimming flows over stepped channels and spill- ways. *Journal of Hydraulic Research*, 32(3): 445–460. https://doi.org/10.1080/ 00221689409498745.

Chartrand, S.; Jellinek, M.; Whiting, P.; Stamm, J. (2011). Geometric scaling of step-pools in mountain streams: Observations and implications. *Geomorphology*, 129: 141–151. https://doi.org/10.1016/j.geomorph.2011.01.020.

Chartrand, S.; Whiting, P. (2000). Alluvial Architecture in Headwater Streams with Special Emphasis on Step-pool Topography. *Earth Surf Processes Landforms*, 25: 583 – 600. https://doi.org/10.1002/1096-9837(200006)25:6<583::AID-ESP92>3.0.CO;2-3.

Chen, X.; Hassan, M.A.; An, C.; Fu, X. (2020). Roughness Correlations: Meta-Analysis of Roughness Measures in Gravel Bed Rivers. *Water Resources Research*, 56(8). https://doi.org/10.1029/2020WR027079.

Chin, A. (1989). Step pools in stream channels. *Progress in Physical Geography: Earth and Environment*, 13(3): 391–407. https://doi.org/10.1177/030913338901300304.

Chin, A. (1999). The morphologic structure of step-pools in mountain streams. *Geomorphology*, 27: 191–204. https://doi.org/10.1016/s0169-555x(98)00083-x.

Chin, A.; Anderson, S.; Collison, A.; Ellis-Sugai, B.; Haltiner, J.; Hogervorst, J.; Kondolf, G.; O'Hirok, L.; Purcell, A.; Riley, A.; Wohl, E. (2009). Linking Theory and Practice for Restoration of Step-Pool Streams. *Environmental Management*, 43: 645–661. https://doi.org/10.1007/s00267-008-9171-x.

Chin, A.; O'Dowd, A.P.; Mendez, P.; Valesco, K.; Florsheim, J.L.; Laurencio, L.R.; Leventhal, R.D. (2021). Toward natural approaches in restoration: Experiments of co-evolving physical and biological structures in a self-organizing step-pool channel. *River Research and Applications*, 37(10): 1480–1493. https://doi.org/10.1002/rra.3851.

Chin, A.; Wohl, E. (2005). Toward a theory for step pools in stream channels. *Progress in Physical Geography*, 29(3): 275–296. https://doi.org/10.1191/0309133305pp449ra.

Church, M.; Zimmermann, A. (2007). Form and stability of step-pool channels: Research progress. *Water Resources Research*, 43. https://doi.org/10.1029/2006wr005037.

Colebrook, C. (1939). Turbulent flow in pipes with particular reference to the transition region between the smooth and rough pipe laws. *Proceedings of the Institution of Civil Engineers*, 12(8): 393–422. https://doi.org/10.1680/ijoti.1939.13150.

Comiti, F.; Andreoli, A.; Lenzi, M. (2005). Morphological effects of local scouring in step-pool streams. *Earth Surface Processes and Landforms*, 30: 1567–1581. https://doi.org/10.1002/esp.1217.

Comiti, F.; Cadol, D.; Wohl, E. (2009a). Flow regimes, bed morphology, and flow resistance in self-formed step-pool channels. *Water Resources Research*, 45. https://doi.org/10.1029/2008wr007259.

Comiti, F.; Mao, L. (2012). Gravel-bed Rivers: Processes, Tools, Environments. Chap. 26: Rececnt Advances in the Dynamics of Steep Channels: 353–377. In: *John Wiley & Sons, Ltd.*.

Comiti, F.; Mao, L.; Lenzi, M.; Siligardi, M. (2009b). Artificial steps to stabilized mountain rivers: A post-project ecological assessment. *River Research and Applications*, 25(5): 639–659. https://doi.org/10.1002/rra.1234.

Crowe, J. (2002). An experimental study of the step-pool bed form. *PhD Thesis*, Johns Hopkins University, Baltimore.

Curran, J.C.; Wilcox, P.R. (2005). Characteristic dimensions of the step-pool bed configuration: An experimental study. *Water Resources Research*, 41. https://doi.org/10.1029/2004wr003568.

Curran, J.H.; Wohl, E.E. (2003). Large woody debris and flow resistance in step-pool channels, Cascade Range, Washington. *Geomorphology*, 51: 141–157. https://doi.org/10.1016/s0169-555x(02)00333-1.

da Silva, A. (1991). Alternate bars and related alluvial processes. *PhD Thesis*, Queens University, Kingston Ontario, Canada.

Downing, J.; Cole, J.; Duarte, C.; Middelburg, J.; Melack, J.; Prairie, Y.; Kortelainen, P.; Striegl, R.G.; McDowell, W.; Tranvik, L. (2012). Global abundance and size distribution of streams and rivers. *Inland Waters*, 2(4): 229–236. https://doi.org/10.5268/IW-2.4.502.

Einstein, H.A. (1934). Der hydraulische oder Profil-Radius. *Schweizer Bauzeitung*, 103(8): 89–91. https://www.e-periodica.ch/digbib/view?pid=sbz-002:1934:103::108#1077 [in German].

Fenton, J.; Abbot, J. (1977). Initial movement of grains on a stream bed: the effect of realtive protrusion. *Proceedings of the Royal Society of London*, Ser. A(352): 523–537. https://doi.org/10.1098/rspa.1977.0014.

Ferguson, R. (2007). Flow resistance equations for gravel- and boulder-bed streams. *Water Resources Research*. https://doi.org/10.1029/2006wr005422.

Ganz, T.F. (2003). Entstehung und Entwicklung von Abflussinstabilitäten bei Absturztreppen. *PhD Thesis*, Universität Innsbruck [in German].

Gaudio, R.; Marion, A.; Bovolin, V. (2000). Morphological effects of bed sills in degrading rivers. *Journal of Hydraulic Research*, 38(2): 89–96. https://doi.org/10.1080/00221680009498344.

GEOPRAEVENT AG (2022). Felsüberwachung und Murgang-Alarmsystem Bondo (Rock monitoring and debris flow alarm system Bondo). https://www.geopraevent.ch/project/bergsturz-und-murgangueberwachung-bondoval-bondasca/ [accessed on April 24, 2022].

Golly, A.; Turowski, J.; Badoux, A.; Hovius, N. (2019). Testing models of step formation against observation of channel steps in a steep mountain stream. *Earth Surface Processes and Landforms*, 44: 1390–1406. https://doi.org/10.1002/esp.4582.

Grant, G.; Swanson, F.; Wolman, M. (1990). Pattern and origin of stepped-bed morphology in high-gradient streams, Western Cascades, Oregon. *GSA Bulletin*, 1102(3). https://doi.org/10.1130/0016-7606(1990)102<0340:paoosb>2.3.co;2.

Guo, J. (2015). Sidewall and non-uniformity corrections for flume experiments. *Journal of Hydraulic Research*, 53(2): 218–229. https://doi.org/10.1080/00221686.2014.971449.

Hassan, M.A.; Zimmermann, A.E. (2012). Channel Response and Recovery to Changes in Sediment Supply. Chap. 33: 464–473. In: Gravel-Bed Rivers. *John Wiley & Sons, Ltd*. https://doi.org/10.1002/9781119952497.ch33.

Hayward, J. (1980). Hydrology and stream sediments in a mountain catchment. *Tussock Grasslands & Mountain Lands Institute, Lincoln College*.

Heller, V. (2011). Scale effects in physical hydraulic engineering models. *Journal of Hydraulic Research*, 49(3): 293–306. https://doi.org/10.1080/00221686.2011.578914.

Hohermuth, B.; Weitbrecht, V. (2018). Influence of Bed-Load Transport on Flow Resistance of Step-Pool Channels. *Water Resources Research*, 54: 5567–5583. https://doi.org/10.1029/2017wr021523.

HSR (2017). Hochwasserschutz und Längsvernetzung Sperre Sandweidli (Flood protection and longitudinal connectivity - Sandweidli check dam). *Technical report 3600304*, Institut für Bau und Umwelt (IBU), Hochschule für Technik Rapperswil (HSR).

Johnson, J. (1942). The Importance of Considering Side-wall Friction in Bed-load Investigations. *Civil Engineering*, 12: 329–332.

Judd, H. (1964). A study of bed characteristics in relation to flow in rough- high-gradient natural channels. *PhD Thesis*, Utah State University, Logan.

Kaspar, P. (2017). Stabilität künstlicher Stufen-Becken Systeme (Stability of artificial step-pool systems). *Master Thesis*, VAW, ETH Zurich [unpublished in German].

Keulegan, G. (1938). Laws of turbulent flow in open channels. *Journal of Research of the National Bureau of Standards*, 21: 707–741. https://doi.org/10.6028/jres.021.039.

Kotoulas, D. (1967). Das Kolkproblem unter besonderer Berücksichtigung der Faktoren Zeit und Geschiebemischung im Rahmen der Wildbachverbauung (Scouring problems under consideration of time and sediment mixture within the scope of grade-control measures in torrents). *Schweizerische Anstalt für für das Forstliche Versuchswesen*, 43.

Laboratorium 3D (2022). Sohlenstabilisierung der Maira bei Promontogno durch ein Stufen-Becken System. https://laboratorium3d.ch/portfolio_page/sohlenstabilisierung-der-maira/?lang=de [accessed June 12, 2022].

Lamb, M.; Dietrich, W.; Venditti, J. (2008). Is the critical Shields stress for incipient sediment motion dependent on channel-bed slope? *Journal of Geophysical Research*, 113. https://doi.org/10.1029/2007jf000831.

Lamb, M.P.; Brun, F.; Fuller, B.M. (2017). Direct measurements of lift and drag force on shallowly submerged cobbles in steep streams: Implications for flow resistance and sediment transport. *Water Resources Research*, 53: 7607–7629. https://doi.org/10.1002/2017WR020883.

Lane, E.W. (1955). Design of Stable Channels. *Trans. ASCE*, 120: 1234–1279. https://doi.org/10.1061/taceat.0007188.

Lange, R. (2019). Stabilität künstlicher Stufen-Becken-Systeme (Stability of artificial step-pool sequences. *Master Thesis*, VAW, ETH Zurich [unpublished in German].

Lenzi, M. (2001). Step-pool evolution in the Rio Cordon, Northeastern Italy. *Earth Surface Processes and Landforms*, 26: 991–1008. https://doi.org/10.1002/esp.239.abs.

Lenzi, M. (2002). Stream bed stabilization using boulder check dams that mimic step-pool morphology features in Northern Italy. *Geomorphology*, 45: 243–260. https://doi.org/10.1016/s0169-555x(01)00157-x.

Lenzi, M.; Comiti, F. (2003). Local scouring and morphological adjustments in steep channels with check-dam sequences. *Geomorphology*, 55: 97–109. https://doi.org/10.1016/s0169-555x(03)00134-x.

Lenzi, M.; D'Agostino, V.; Billi, P. (1999). Bedload transport in the instrumented catchment of the Rio Cordon Part I: Analysis of bedload records, conditions and threshold of bedload entrainment. *Catena*, 36: 171–190. https://doi.org/10.1016/S0341-8162(99)00016-8.

Lenzi, M.; Mao, L.; Comiti, F. (2004). Magnitude-frequency analysis of bed load data in an Alpine boulder bed stream. *Water Resources Research*, 40. https://doi.org/10.1029/2003wr002961.

Lenzi, M.; Mao, L.; Comiti, F. (2006). When does bedload transport begin in steep boulder-bed streams? *Hydrological Processes*, 20: 322–345. https://doi.org/10.1002/hyp.6168.

Lenzi, M.; Marion, A.; Comiti, F. (2003). Local scouring at grade-control structures in alluvial mountain rivers. *Water Resources Research*, 39(7). https://doi.org/10.1029/2002wr001815.

Lenzi, M.; Marion, A.; Comiti, F.; Gaudio, R. (2002). Local scouring in low and high gradient streams at bed sills. *Journal of Hydraulic Research*. https://doi.org/10.1080/00221680209499919.

Leonardi, S.; Orlandi, P.; Smalley, R.; Djenidi, L.; Antonia, R. (2003). Direct numerical simulations of turbulent channel flow with transverse square bars on one wall. *Journal of Fluid Mechanics*, 491: 229–238. https://doi.org/10.1017/s0022112003005500.

Leopold, L.; Maddock, T. (1953). The hydraulic geomtry of stream channels and some physiographic implications. *U.S.G.S Prof. Paper*, 252. https://doi.org/10.3133/pp252.

Li, Z.; Komar, P. (1986). Laboratory Measurements of Pivoting Angles for Applications to Selective Entrainment of Gravle in a Current. *Sedimentology*, 33: 413–423. https://doi.org/10.1111/j.1365-3091.1986.tb00545.x.

Little, W.; Mayer, P. (1972). The role of sediment gradation on channel armoring. *ERC-0672*, Environmental Resources Center, Georgia Inst. of Technology.

Liu, C.K.; Kline, S.; Johnston, J. (1966). An experimental study of turbulent boundary layers on rough walls. *Report, Department of Mechanical Engineering, Standford University*, MD-15.

Maager, F.; Hohermuth, B.; Boes, R.; Weitbrecht, V. (2022a). Bed stability of step-pool channels with macrorough sidewalls. *Water Resources Research* [under review].

Maager, F.; Hohermuth, B.; Weitbrecht, V.; Boes, R. (2019). Influence of block arrangement on stability of man-made step-pool sequences in steep mountain streams. *Proc. Proceedings of the 38th IAHR World Congress, September 1-6, 2019, Panama City, Panama*. https://doi.org/10.3850/38wc092019-0646.

Maager, F.; Hohermuth, B.; Weitbrecht, V.; Boes, R. (2020). Effect of bank roughness on step-pool systems in steep channels. *Proc. Proceedings of the10th Conference on Fluvial Hydraulics - River Flow 2020, July 6-17, 2020, Delft, The Netherlands (online)*. https://doi.org/10.1201/b22619-69.

Maager, F.; Hohermuth, B.; Weitbrecht, V.; Boes, R. (2022b). Effect of discharge variations and sediment supply on the scour development and stability of artificial step-pool

sequences. *Proc. Proceedings of the 39th IAHR World Congress, June 19-24, 2022, Granada, Spain.*

Maager, F.; Hohermuth, B.; Weitbrecht, V.; Boes, R. (2022c). Effect of Macrorough Sidewalls on Flow Resistance in Steep Rough Channels. *Water Resources Research*, 58. https://doi.org/10.1029/2021wr031490.

Marion, A.; Lenzi, M.; Comiti, F. (2004). Effect of sill spacing and sediment size grading on scouring at grade-control structures. *Earth Surface Processes and Landforms*. https://doi.org/10.1002/esp.1081.

Marion, A.; Tregnaghi, M.; Tait, S. (2006). Sediment supply and local scouring at bed sills in high-gradient streams. *Water Resources Research*. https://doi.org/10.1029/2005wr004124.

Maxwell, A.; Papanicolaou, A. (2001). Step-pool morphology in high-gradient streams. *International Journal of Sediment Research*, 16(3): 380–390.

Maxwell, A.; Papanicolaou, A.; Hotchkiss, R.; Barber, M.; Schafer, J. (2001). Step-pool morphology in high-gradient countersunk culverts. *Transportation Research Record*, 1743(1): 49–56. https://doi.org/10.3141/1743-07.

Meile, T.; Boillat, J.L.; Schleiss, A.J. (2011). Flow resistance caused by large-scale bank roughness in a channel. *Journal of Hydraulic Engineering*, 137(12): 1588–1597. https://doi.org/10.1061/(asce)hy.1943-7900.0000469.

Meyer-Peter, E.; Müller, R. (1948). Formulas for bed-load transport. *Second Meeting IAHSR, Appendix 2, Stockholm*, (3): 39–64 [in German].

Milzow, C.; Molnar, P.; McArdell, B.W.; Burlando, P. (2006). Spatial organization in the step-pool structure of a steep mountain stream (Vogelbach, Switzerland). *Water Resources Research*, 42. https://doi.org/10.1029/2004wr003870.

Mizuyama, T. (1977). Bedload Transport in Steep Channels. *PhD Thesis*, Kyoto University, Kyoto.

Molnar, P.; Densmore, A.; McArdell, B.; Turowski, J.; Burlando, P. (2010). Analysis of changes in the step-pool morphology and channel profile of a steep mountain stream fol-

lowing a large flood. *Geomorphology*, 124: 85–94. https://doi.org/10.1016/j.geomorph.
2010.08.014.

Monaghan, M.T.; Robinson, C.T.; Spaak, P.; Ward, J. (2005). Macroinvertebrate diversity
in fragmented Alpine streams: implications for freshwater conservation. *Aquat. Sci.*,
67: 454–464. https://doi.org/10.1007/s00027-005-0787-0.

Montgomery, D.; Buffington, J. (1997). Channel-reach morphology in mountain draina-
ge basins. *GSA Bulletin*, 109(5): 596–611. https://doi.org/10.1130/0016-7606(1997)
109<0596:crmimd>2.3.co;2.

Mooney, D.M.; Holmquist-Johnson, C.L.; Broderick, S. (2007). Rock ramp design gui-
delines. *Technical Report*, US Bureach of Reclamation.

Morgan, J.A.; Brogan, D.J.; Nelson, P.A. (2017). Application of Structure-from-Motion
photogrammetry in laboratory flumes. *Geomorphology*, 276: 125–143. https://doi.org/
10.1016/j.geomorph.2016.10.021.

Neill, C. (1967). Mean-velocity criterion for scour of coarse uniform bed-material. *Proc.
Proc. 12th Congress int. Assoc. Hydraulic. Res.*: 46–54.

Nitsche, M.; Rickenmann, D.; Kirchner, J.; Turowski, J.; Badoux, A. (2012). Macrorough-
ness and variations in reach-averaged flow resistance in steep mountain streams. *Water
Resources Research*, 48. https://doi.org/10.1029/2012wr012091.

Nitsche, M.; Rickenmann, D.; Turowski, J.; Badoux, A.; Kirchner, J. (2011). Evaluation
of bedload transport predictions using flow resistance equations to account for macro-
roughness in steep mountain streams. *Water Resources Research*, 47. https://doi.org/
10.1029/2011wr010645.

Okazaki, T.; Gonda, Y.; Nishii, Y.; Kawabe, H. (2006). Characteristics of Step-Pool Mor-
phology in the Mountain Streams of Japan. *Disaster Mitigation of Debris Flows, Slope
Fialures and Landslides*.

Palucis, M.; Lamb, M. (2017). What controls channel form in steep mountain streams?
Geophysical Research Letter, 44: 7245–7255. https://doi.org/10.1002/2017gl074198.

Perry, A.; Schofield, W.; Joubert, P. (1969). Rough wall turbulent boundary layers. *Journal of Fluid Mechanics*, 37(2): 383–413. https://doi.org/10.1017/s0022112069000619.

Peterson, D.; Mohanty, P. (1960). Flume studies of flow in steep, rough channels. *Am. Soc. Civ. Eng. J. Hydraulic Div.*, 85: 55–76. https://doi.org/10.1061/jyceaj.0000543.

Piton, G.; Recking, A. (2019). Steep bedload-laden flows: Near critical? *Journal of Geophysical Researach Earth Surface*. https://doi.org/10.1029/2019jf005021.

Powell, D. (2014). Flow resistance in gravel-bed rivers: Progress in research. *Earth-Science Reviews*, 136: 301–338. https://doi.org/10.1016/j.earscirev.2014.06.001.

Rainato, R.; Mao, L.; Garcia-Rama, A.; Picco, L.; Cesca, M.; Vianello, A.; Preciso, E.; Scussel, G.; Lenzi, M. (2017). Three decades of monitoring in the Rio Cordon instrumented basin: Sediment budget and temporal trend of sediment yield. *Geomorphology*, 291: 45–56. https://doi.org/10.1016/j.geomorph.2016.03.012.

Rainato, R.; Mao, L.; Picco, L. (2020). The effects of low-magnitude flow conditions on bedload mobility in a steep mountain stream. *Geomorphology*, 367. https://doi.org/10.1016/j.geomorph.2020.107345.

Raudkivi, A.; Ettema, R. (1982). Stability of armour layers in rivers. *Proc. ASCE J. of Hydr. Div*, 108(HY9): 1047–1057. https://doi.org/10.1061/jyceaj.0005903.

Recking, A.; Leduc, P.; Liébault, F.; Church, M. (2012). A field investigation of the influence of sediment supply on step-pool morphology and stability. *Geomorphology*, 139-140: 53–66. https://doi.org/10.1016/j.geomorph.2011.09.024.

Richardson, K.; Carling, P. (2021). Morphology and origin of alluvial step-pools: A sysnthesis of experimental and field data from formative flows. *Earth-Science Reviews*, 222. https://doi.org/10.1016/j.earscirev.2021.103823.

Rickenmann, D. (1990). Bedload transport capacity of slurry flows at steep slopes. *PhD Thesis*, Laboratory of Hydraulics, Hydrology and Glaciology (VAW), ETH Zurich.

Rickenmann, D. (2016). Methods for the quantitative assessment of channel processes in torrents (steep streams). ISBN 978-1-138-02961-3. 1 edn. *CRC Press/Balkema*.

Rickenmann, D.; Recking, A. (2011). Evaluation of flow resistance in gravel-bed rivers through a large field data set. *Water Resources Research*, 47. https://doi.org/10.1029/2010wr009793.

Saletti, M.; Hassan, M.A. (2020). Width variations control the development of grain structuring in steep step-pool dominated streams: insight from flume experiments. *Earth Surface Processes and Landforms*, 45(6). https://doi.org/10.1002/esp.4815.

Saletti, M.; Molnar, P.; Zimmermann, A.; Hassan, M.; Church, M. (2015). Temporal variability and memory in sediment transport in anexperimental step-pool channel. *Water Resources Research*, 51: 9325–9337. https://doi.org/10.1002/2015WR016929.

Shields, A. (1936). Anwendungen der Ähnlichkeitsmechanik und der Turbulenzforschung auf die Geschiebebewegung. *Versuchsanstalt für Wasser- und Schiffbau, Berlin*, Mitt. Nr. 87.

Simonett, S.; Weitbrecht, V. (2011). Bed load transport in a physical scale model of two merging mountain streams: 275–286. In: P. Rowinski (ed.) Experimental Methods in Hydraulic Research. https://doi.org/10.1007/978-3-642-17475-9_20.

Smith, D.P.; Kortman, S.; Caudillo, A.M.; Kwan-Davis, R.L.; Wandke, J.; Klein, J.W.; Gennaro, M.; Bogdan, M.; Vannerus, P. (2020). Controls on large boulder mobility in an 'auto-naturalized' constructed step-pool river: San Clemente Reroute and Dam Removal Project, Carmel River, California, USA. *Earth Surface Processes and Landforms*, 45(9): 1990–2003. https://doi.org/10.1002/esp.4860.

Strahler, A. (1957). Quantitative analysis of watershed geomorphology. *T. Am. Geophys. Union*, 38: 913–920. https://doi.org/10.1029/tr038i006p00913.

swisstopo (2020). Maps of Switzerland. Federal Office for Topography (swisstopo). https://map.geo.admin.ch/ (accessed April 4, 2020).

SWV (2021). KOHS-Wasserbautagung 2021 - Schutzkonzepte und ihre Bauten am Lebensende - was nun? https://www.swv.ch/detail/kohs-wasserbautagung-2021.

Tamagni, S. (2013). Unstructured block ramps. *VAW-Mitteilung 223* (R.M. Boes, ed.). Laboratory of Hydraulics, Hydrology and Glaciology, ETH Zurich, Switzerland.

Thomas, D.; Abt, S.; Musseter, R.; Harvey, M. (2000). A Design Procedure for Sizing Step-Pool Structures. *Proc. Proceedings of ASCE Joint Conference on Water Resource Engineering and Water Resources Planning and Management*. https://doi.org/10.1061/40517(2000)340.

Thompson, S.; Campbell, P. (1979). Hydraulics of a large channel paved with boulders. *Journal of Hydraulic Engineering*, 17: 341–354. https://doi.org/10.1080/00221687909499577.

Tschopp, J.; Bisaz, E. (1972). Profundidad de Erosion al Pie de un Vertedero para la Aplicacion de Correccion de Arroyos en Quembradas Epinados. *V. Congreso Latinoamericano de hidraulica, IAHR*.

Turowski, J.; Badoux, A.; Leuzinger, J.; Hegglin, R. (2013). Large floods, alluvial overprint, and bedrock erosion. *Earth Surface Processes and Landforms*, 38: 947–958. https://doi.org/10.1002/esp.3341.

Turowski, J.; Yager, E.M.; Badoux, A.; Rickenmann, D.; Molnar, P. (2009). The impact of exceptional events on erosion, bedload transport and channel stability in a step-pool channel. *Earth Surface Processes and Landforms*, 34: 1661–1673. https://doi.org/10.1002/esp.1855.

Vanoni, V.A.; Brooks, N.H. (1957). Laboratory studies of the roughness and suspended load of alluvial streams. *Report E-68*, CalTech, Pasadena, CA..

VAW (2014). Schwemmholzrückhalt Chlewigen, Kleine Schliere (Wood retention in Chlewigen, Kleine Schliere Streams). *Technical Report 4300*, Laboratory of Hydraulics, Hydrology and Glaciology (VAW), ETH Zurich [unpublished, in German].

VAW (2015). Stufen-Becken-Abfolge, Betelriedgraben (Step-pool sequences, Betelriedgraben Stream). *Technical Report 4319*, Laboratory of Hydraulics, Hydrology and Glaciology (VAW), ETH Zurich [unpublished, in German].

VAW (2018). Untersuchung zum dynamischen Verhalten von traversensystemen (Investigation on the dynamics of check-dam sequences). *Technical Report*, Laboratory of Hydraulics, Hydrology and Glaciology (VAW), ETH Zurich [unpublished, in German].

Volkart, P. (1972). Die Stabilisierung von Flussläufen mittels einer Folge von Querschwellen. *VAW-Mitteilung 6* (D. Vischer, ed.). Versuchsanstalt für Wasserbau, Hydrologie und Glaziologie (VAW), ETH Zürich, Switzerland [in German].

Waldon, M.G. (2004). Estimation of Average Stream Velocity. *Journal of Hydraulic Engineering*, 130(11): 1119–1122. https://doi.org/10.1061/(asce)0733-9429(2004)130: 11(1119).

Wang, Z.; Melching, C.S.; Duan, X.; Yu, G. (2009). Ecological and Hydraulic Studies of Step-Pool Systems. *Journal of Hydraulic Engineering*, 135(9): 705–717. https://doi.org/10.1061/(asce)0733-9429(2009)135:9(705).

Weichert, R. (2006). Bed morphology and stability of steep open channels. *VAW-Mitteilung 192* (H.E. Minor, ed.). Laboratory of Hydraulics, Hydrology and Glaciology, ETH Zurich, Switzerland.

Weichert, R.; Bezzola, G.; Minor, H.E. (2008). Bed morphology and gerneration of step-pool channels. *Earth Surface Processes and Landforms*, 33: 1678–1692. https://doi.org/10.1002/esp.1639.

Weichert, R.; Bezzola, G.; Minor, H.E. (2009). Bed erosion in steep open channels. *Journal of Hydraulic Research*, 47(3): 360–371. https://doi.org/10.1080/00221686.2009.9522007.

Whittaker, J. (1987). Sediment transport in step-pool streams. Chap. 18: 545–79. In: C. Thorne; J. Bathurst; R. Hey (eds.) *John Wiley & Sons Ltd.*.

Whittaker, J.; Jäggi, M. (1982). Origin of step-pool systems in mountain streams. *J. Hydraul. Div. Am. Soc. Civ. Eng.*, 108: 758–773. https://doi.org/10.1061/jyceaj.0005873.

Wilcox, A.; Wohl, E.; Comiti, F.; Mao, L. (2011). Hydraulic, morphology and energy dissipation in an alpine step-pool channel. *Water Resources Research*, 47. https://doi.org/10.1029/2010wr010192.

Wilcox, A.C.; Nelson, J.M.; Wohl, E.E. (2006). Flow resistance dynamics in step-pool channels: 2. Partitioning between grain, spill, and woody debris resistance. *Water Resources Research*, 42. https://doi.org/10.1029/2005wr004278.

Wilcox, A.C.; Wohl, E. (2007). Field measurements of three-dimensional hydraulic in a step-pool channel. *Geomorphology*, 83: 215–231. https://doi.org/10.1016/j.geomorph. 2006.02.017.

Wohl, E.; Grodek, T. (1994). Channel bed-steps along Nahal Yael, Negev desert, Israel. *Geomorphology*, 9: 117–126. https://doi.org/10.1016/0169-555x(94)90070-1.

Wohl, E.; Madsen, S.; MacDonald, L. (1997). Characteristics of log and clast bed-steps in step-pool streams of northwestern Montana, USA. *Geomorphology*, 20: 1–10. https://doi.org/10.1016/s0169-555x(97)00021-4.

Wooldridge, C.; Hickin, E. (2002). Step-pool and cascade morphology, Mosquito Creek, British Columbia: a test of four analytical techniques. *Canadian Journal of Earth Sciences*, 39: 493–503. https://doi.org/10.1139/e01-087.

Wu, S.; Rajaratnam, N. (1996). Submerged flow regimes of rectangular sharp-crested weirs. *Journal of Hydraulic Engineering*. https://doi.org/10.1061/(asce) 0733-9429(1996)122:7(412).

Yu, G.; Wang, Z.; Zhang, K.; Duan, X.; Chang, T. (2010). Restoration of an incised mountain stream using artificial step-pool system. *Journal of Hydraulic Research*, 48(2): 178–187. https://doi.org/10.1080/00221681003704186.

Zarn, B. (1992). Lokale Gerinneaufweitung - eine Massnahme zur Sohlenstabilisierung der Emme bei Utzenstorf (Local channel widening - a bed stabilization measure in the Emme River near Utzenstorf). *VAW-Mitteilung 118* (D. Vischer, ed.). Laboratory of Hydraulics, Hydrology and Glaciology, ETH Zurich, Switzerland, 98–103 [in German].

Zarn, B. (1997). Einfluss der Flussbettbreite auf die Wechselwirkung zwischen Abfluss, Morphologie und Geschiebetransportkapazitat (Influence of channel width on the interaction of discharge, morphology, and bed-load transport capacity). *VAW-Mitteilung 154* (D. Vischer, ed.). Laboratory of Hydraulics, Hydrology and Glaciology, ETH Zurich, Switzerland [in German].

Zhang, C.; Xu, M.; Hassan, M.; Chartrand, S.; Wang, Z. (2018). Experimental study on the stability and failure of individual step-pool. *Geomorphology*, 311: 51–62. https://doi.org/10.1016/j.geomorph.2018.03.023.

Zimmermann, A. (2009). Experimental investigations of step-pool channel formation and stability. *PhD Thesis*, The University of British Columbia, Canada [unpublished].

Zimmermann, A. (2010). Flow resistance in steep streams: An experimental study. *Water Resources Research*, 46. https://doi.org/10.1029/2009wr007913.

Zimmermann, A.; Church, M. (2001). Channel morphology, gradient profiles and bed stresses during flood in a step-pool channel. *Geomorphology*, 40: 311–327. https://doi.org/10.1016/s0169-555x(01)00057-5.

Zimmermann, A.; Church, M.; Hassan, M.A. (2008). Identification of steps and pools from stream longitudinal profile data. *Geomorphology*, 102: 395–406. https://doi.org/10.1016/j.geomorph.2008.04.009.

Zimmermann, A.; Church, M.; Hassan, M.A. (2010). Step-pool stability: Testing the jammed state hypothesis. *Journal of Geophysical Research*, 115. https://doi.org/10.1029/2009jf001365.

A Appendix

A.1 Methods

A.1.1 Mean-flow velocity estimation

According to Waldon (2004), the harmonic mean time-of-travel t_{HM} passing a fixed point x relates to:

$$t_{HM} = \frac{1}{\int_{t=0}^{\infty} \frac{1}{t} p_x(t) \, dt}$$ (A.1)

where $p_x(t)$ is the normalized temporal profile with unit area at location x and equals the temporal probability distribution function. The average tracer velocity can be obtained by dividing the travel distance $\Delta x = x_i - x_{i-1}$ by the difference of the harmonic mean time-of-travel $\Delta t_{HM} = t_{HM,i} - t_{HM,i-1}$ between cross-sections x_{i-1} and x_i.

$$v(x_{i-1} \rightarrow x_i) = \frac{\Delta x}{\Delta t_{HM}}$$ (A.2)

The tracer temporal profiles were pre-processed prior to calculating the harmonic mean tracer time-of-travel. The base signal, averaged over the initial 5 s, was subtracted and a moving-average filter with 0.1 s window length was applied. An automatized algorithm was used to determine the start and end position of the signal. The start position was defined as the first local minimum occurring right before the global maximum arrived. The end position was defined as the first point of the descending limb of the signal falling below two times the standard deviation of the base signal. All erroneous conductivity
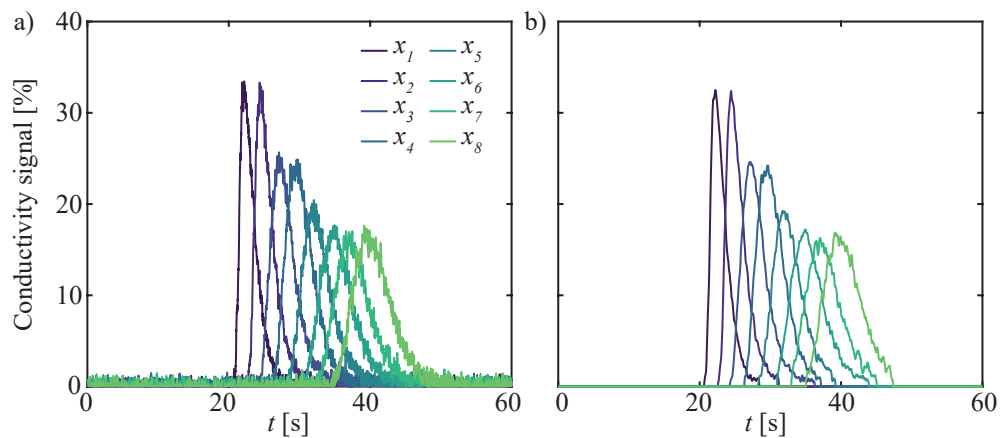
Figure A.1 Temporal profiles of the conductivity measurements at cross-sections x_i, a) raw signal (base signal subtracted), b): after pre-processing

measurements, e.g., with peaks not being fully captured, were excluded from the analysis. An example of the raw and the pre-processed temporal profiles at cross-sections x_i is illustrated in Figure A.1.

A total of 21 to 27 velocity estimates v_{ij} were obtained for conductivity measurements at seven to eight cross-sections, respectively (e.g., $v_{12}(x_1 \rightarrow x_2)$, $v_{13}(x_1 \rightarrow x_3)$, ... , $v_{78}(x_7 \rightarrow x_8)$). Three measurement, i.e., salt solution injections, resulted in 63 to 81 velocity estimates being averaged to obtain the reach-averaged flow velocity v. Figure A.2 shows the velocity estimates v_{ij} located in between the corresponding measurement positions x_i and x_j. This plot enables the detection of potential acceleration or deceleration within the test section. The standard deviation of all velocity estimates σ_v was calculated to quantify the uncertainty.
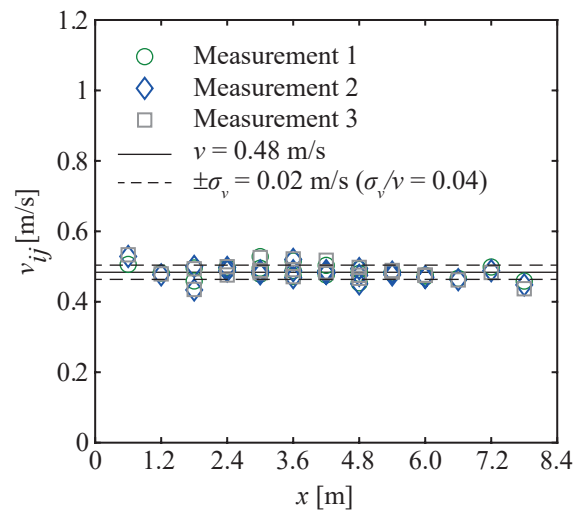
Figure A.2 Example of velocity estimates v_{ij} in longitudinal direction x, with reach-averaged flow velocity v, standard deviation of velocity estimates σ_v, and distance between two conductivity measurement positions Δx

A.1.2   Sediment outflow - correction procedure

The measurements of the cumulative sediment outflow ΣQ_s is disturbed by the water jet impinging on the sediment captured in the filter basket exerting little additional force. Measurements show that the weight of the sediment in the filter basket decreases as discharge is approaching zero at the end of an experiment (Figure A.3) being physically impossible because sediment cannot leave the filter basket. However, this additional force is proportional to the discharge and to the amount of sediment captured in the filter basket and a correction procedure can be applied. Therefore, the differences ΔQ_s between the

cumulative sediment weight right at the end of each interval but still at maximum discharge $\Sigma Q_s(Q_{max})$ (i.e., blue circles in Figure A.3) and after discharge was decreased to zero $\Sigma Q_s(Q_0)$ (i.e., black diamonds in Figure A.3).
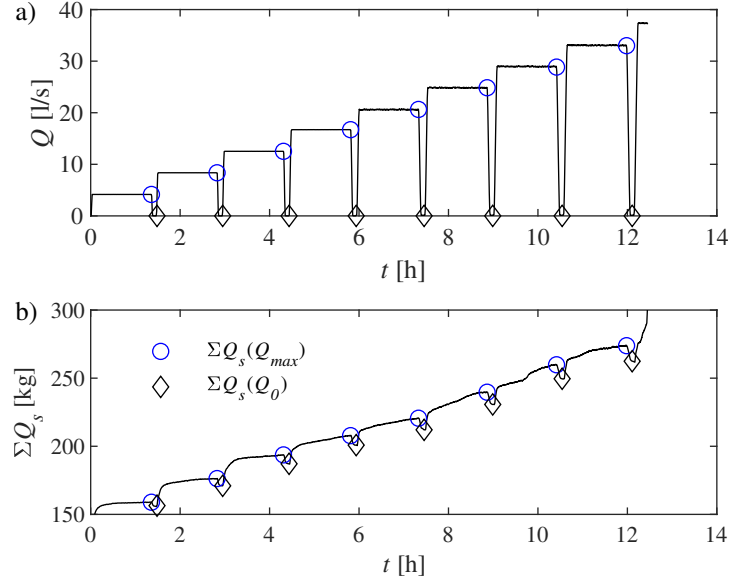
Figure A.3 Time series of an experimental test run with steady flow conditions, a) discharge Q, b): cumulative sediment outflow ΣQ_s, cumulative sediment outflow at maximum discharge at the end of each interval $Q_s(Q_{max})$ and after decreasing discharge to zero $Q_s(Q_0)$

Figure A.4 shows that the differences ΔQ_s induced by the jet impinging on the filter basket increases with discharge Q. The errorbars represents the standard deviation of the measured sediment outflow during the corresponding discharge. A nonlinear regression was conducted and the following fit was obtained with $R^2 = 0.997$ (option A):

$$\Delta Q_s = 0.61\, Q^{0.8} \tag{A.3}$$

However, this option A only accounts for the discharge and not for the initial amount of sediment inside the filter basket $\Sigma Q_{s,ini}$. Thus, a multiple linear regression (option B, Equation A.4) and a multiple nonlinear regression (option C, Equation A.5) were conducted accounting for the sediment captured in the filter basket at the beginning of each interval.

$$\Delta Q_s = 0.3141\, Q + 0.0077\, \Sigma Q_{s,ini} \tag{A.4}$$

$$\Delta Q_s = 0.7330\, Q^{0.7416} + 0.0063\, \Sigma Q_{s,ini} \tag{A.5}$$
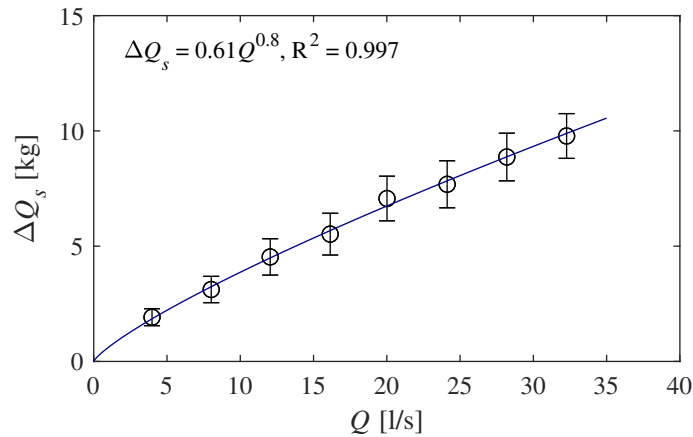
Figure A.4 Differences in sediment outflow ΔQ_s caused by the impinging jet altering the measurements as a function of discharge Q

Figure A.5 shows the measured and predicted values of ΔQ_s for data with an empty filter basket and data with a filter basket initially filled with sediment ($\Sigma Q_{s,ini} \neq 0 \, \text{kg}$) for regression options A, B, and C. Option C performs best for both empty and initially filled filter basket and is therefore chosen to correct the sediment output data. The buoyancy correction was applied after correcting for the effect caused by the impinging jet.
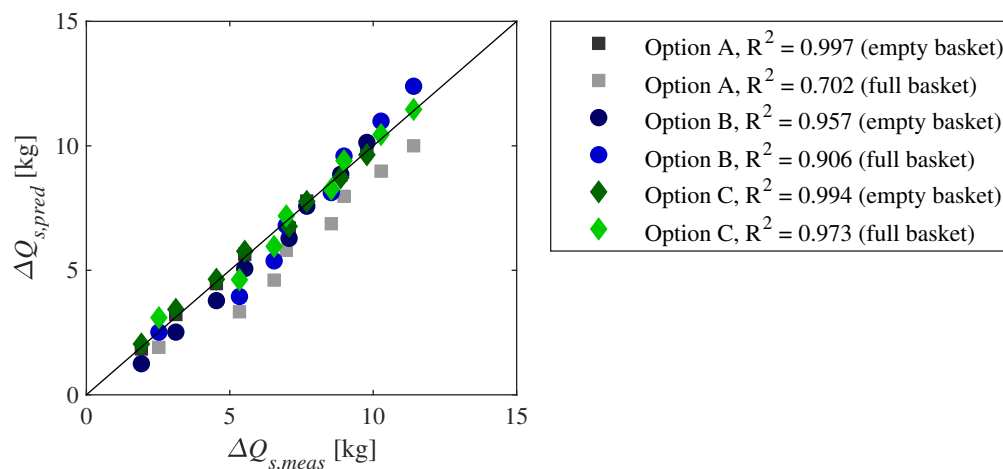
Figure A.5 Validation of the regression analysis showing the measured $\Delta Q_{s,meas}$ and the predicted $\Delta Q_{s,pred}$ for option A (Equation A.3), option B (Equation A.4), and option C (Equation A.5)

A.2 Self-organizing step-pool sequences

A.2.1 Bed elevation changes of self-organizing step-pool experiments
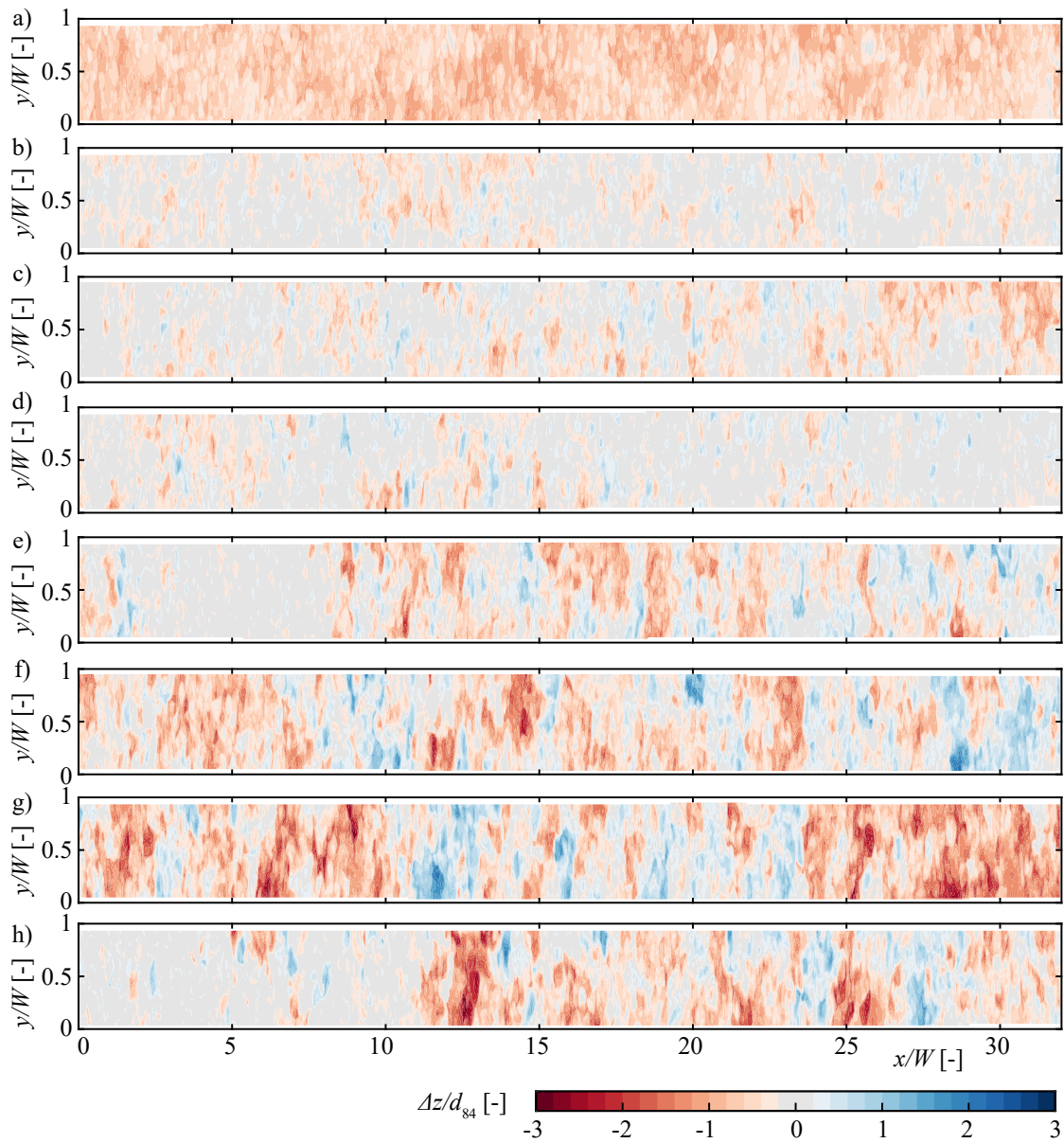
Figure A.6 Bed elevation changes of experiment "0" with smooth sidewalls and $\Delta q = 0.01$ m^2/s after a) $q = 0.01$ m$^2/s$, b) $q = 0.02$ m^2/s, c) $q = 0.03$ m^2/s, d) $q = 0.04$ m^2/s, e) $q = 0.05$ m^2/s, f) $q = 0.06$ m^2/s, g) $q = 0.07$ m^2/s, h) $q = 0.08$ m^2/s was applied (difference to previous interval)
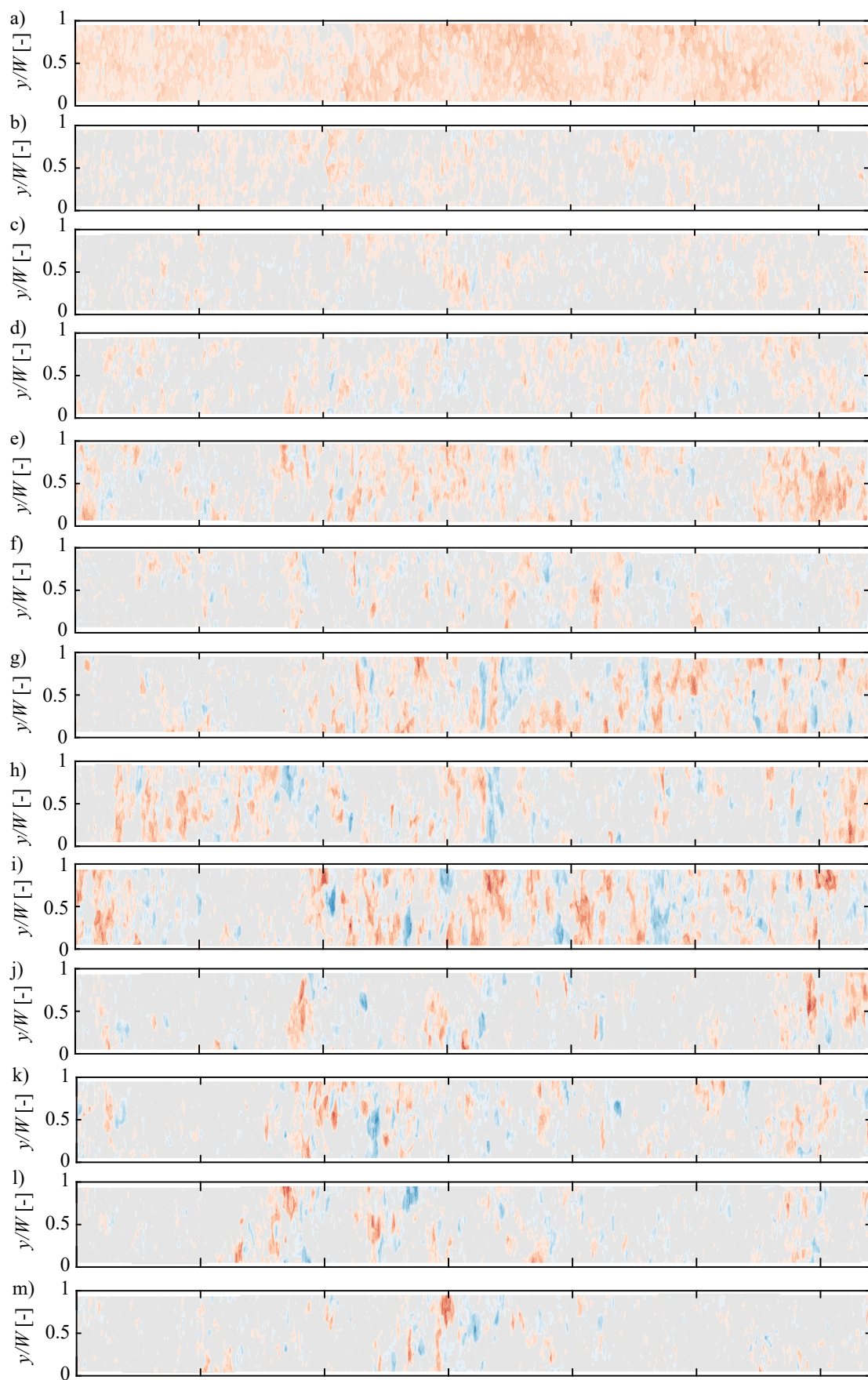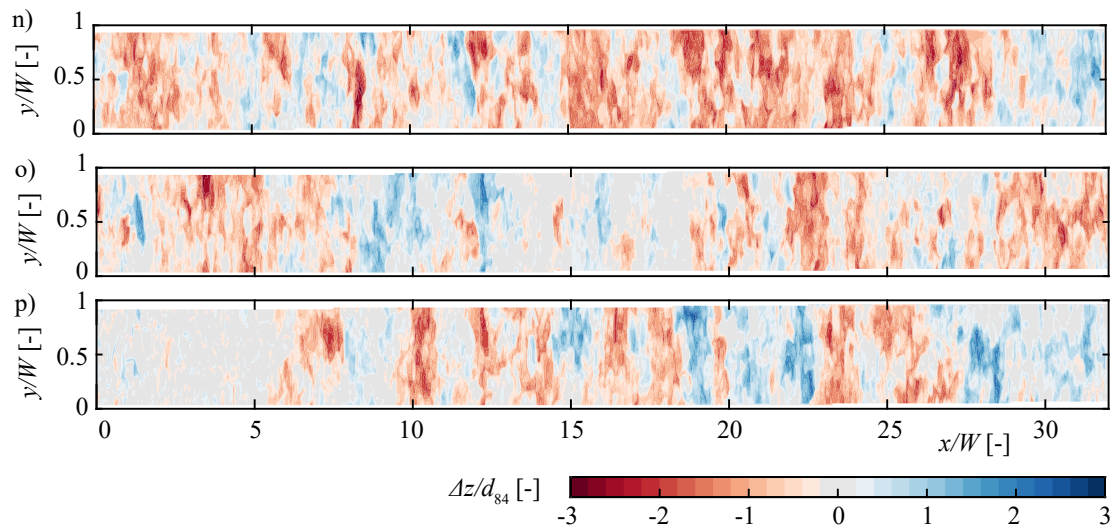
Figure A.7 Bed elevation changes of experiment "0 (rep)" with smooth sidewalls and $\Delta q = 0.005$ m^2/s after a) $q = 0.005$ m^2/s, b) $q = 0.010$ m^2/s, c) $q = 0.015$ m^2/s, d) $q = 0.020$ m^2/s, e) $q = 0.025$ m^2/s, f) $q = 0.030$ m^2/s, g) $q = 0.035$ m^2/s, h) $q = 0.040$ m^2/s, i) $q = 0.045$ m^2/s, j) $q = 0.050$ m^2/s, k) $q = 0.055$ m^2/s, l) $q = 0.060$ m^2/s, m) $q = 0.065$ m^2/s, n) $q = 0.070$ m^2/s, o) $q = 0.075$ m^2/s, and p) $q = 0.080$ m^2/s was applied (difference to previous interval)
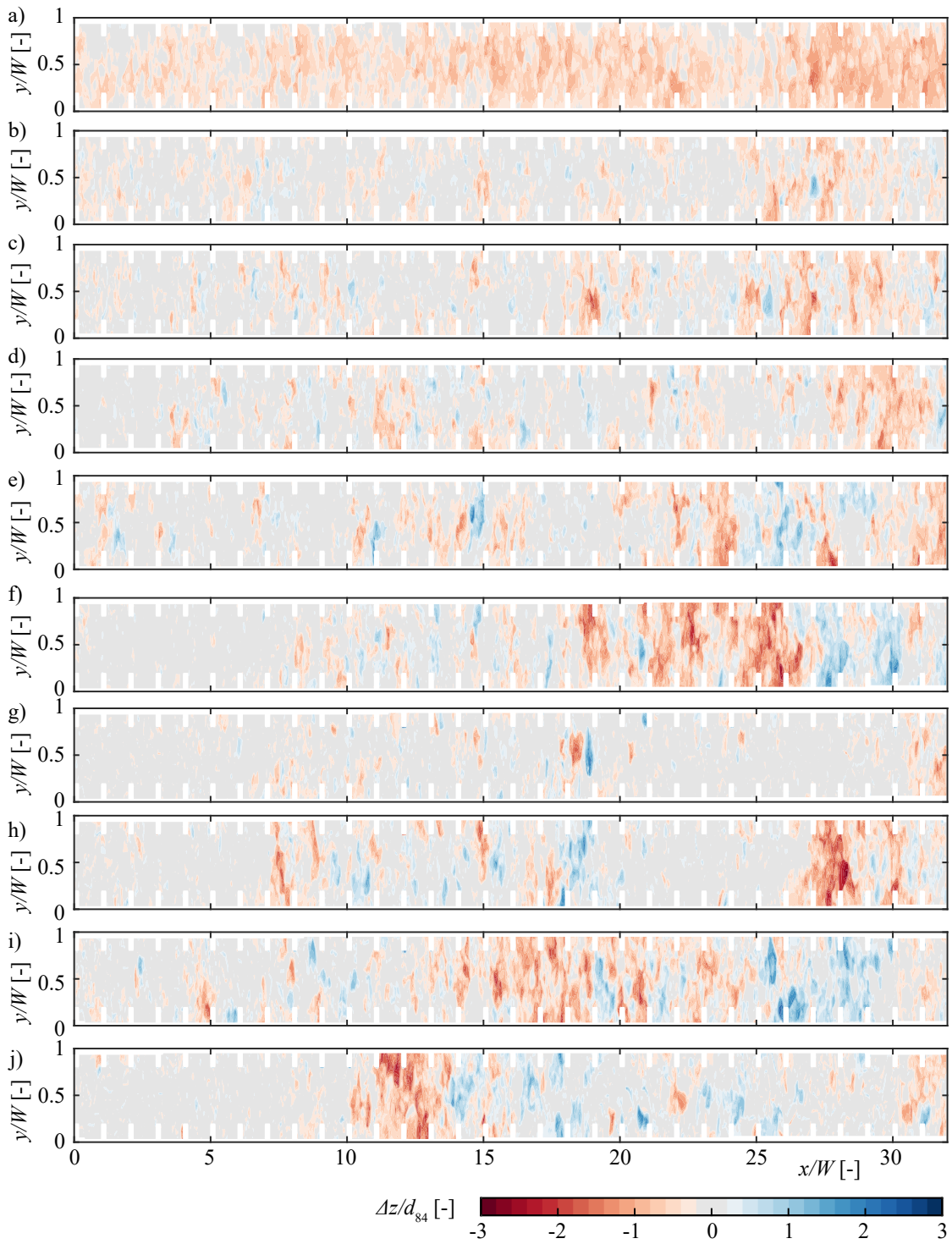
Figure A.8 Bed elevation changes of experiment RR25 after a) $q = 0.01$ m^2/s, b) $q = 0.02$ m^2/s, c) $q = 0.03$ m^2/s, d) $q = 0.04$ m^2/s, e) $q = 0.05$ m^2/s, f) $q = 0.06$ m^2/s, g) $q = 0.07$ m^2/s, h) $q = 0.08$ m^2/s, i) $q = 0.09$ m^2/s, j) $q = 0.10$ m^2/s was applied (difference to previous interval)
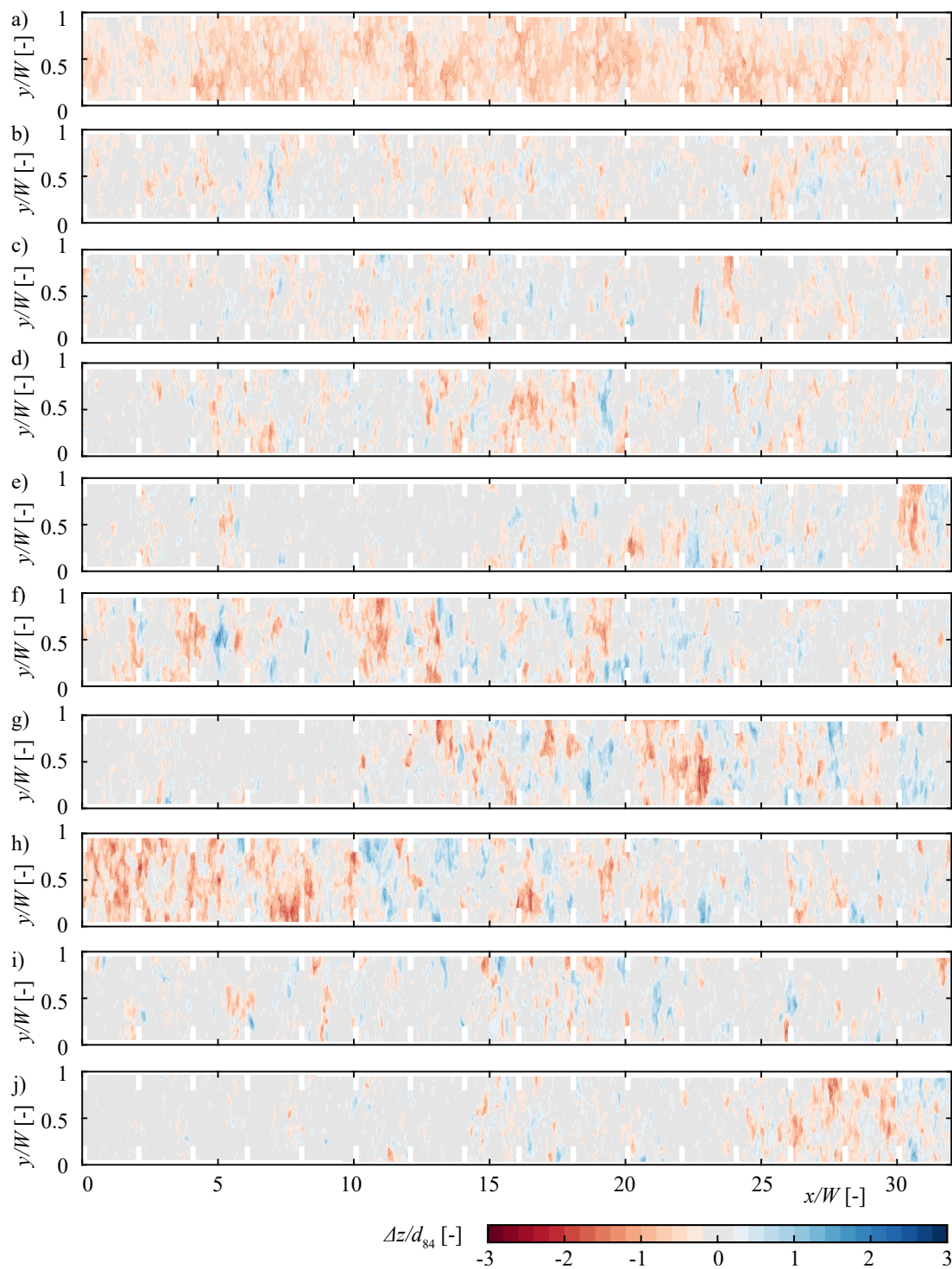
Figure A.9 Bed elevation changes of experiment RR55 after a) $q = 0.01$ m$^2/s$, b) $q = 0.02$ m^2/s, c) $q = 0.03$ m^2/s, d) $q = 0.04$ m^2/s, e) $q = 0.05$ m^2/s, f) $q = 0.06$ m^2/s, g) $q = 0.07$ m^2/s, h) $q = 0.08$ m^2/s, i) $q = 0.09$ m^2/s, j) $q = 0.10$ m^2/s was applied (difference to previous interval)
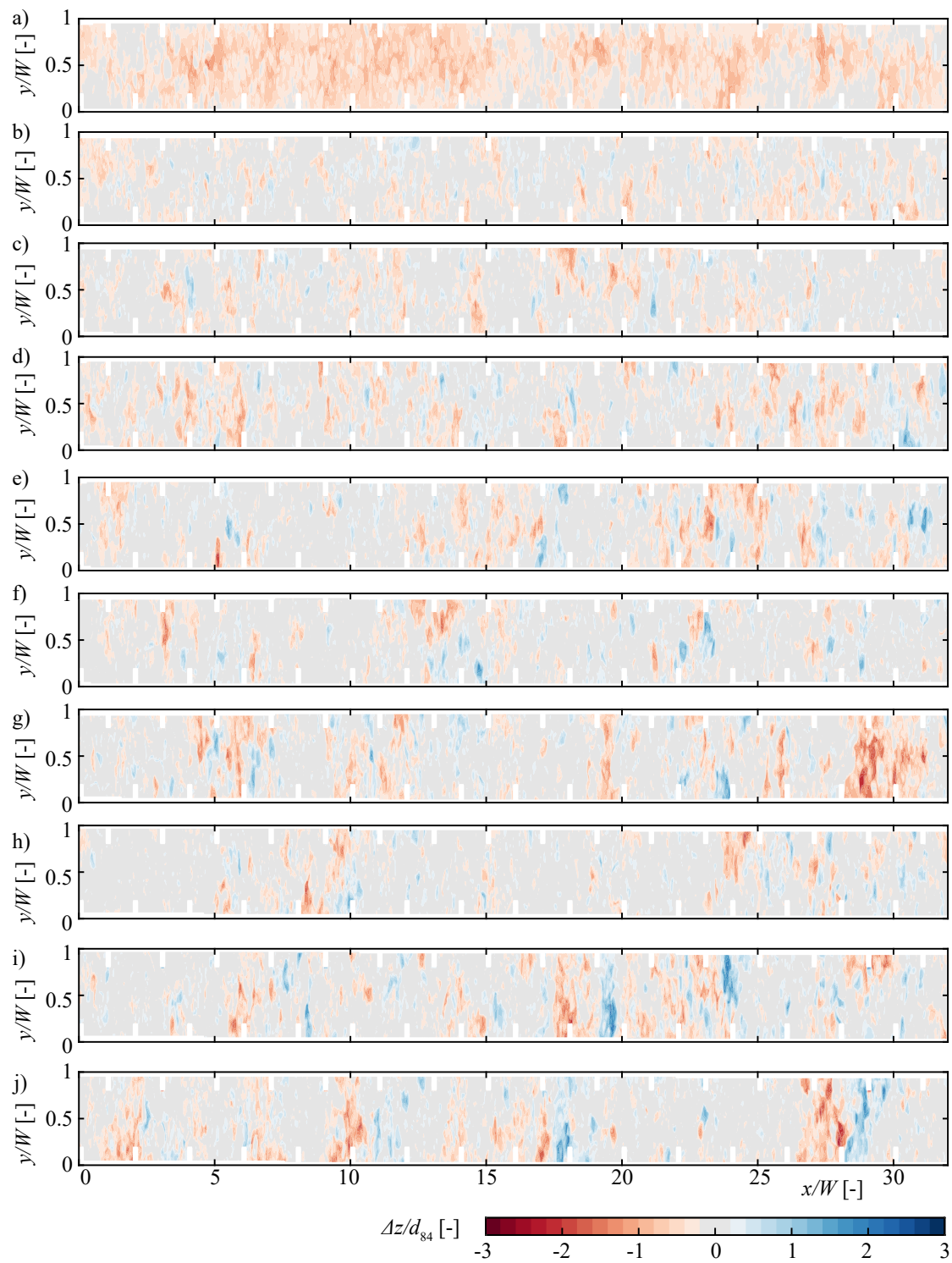
Figure A.10 Bed elevation changes of experiment RR55A after a) $q = 0.01$ m^2/s, b) $q = 0.02$ m^2/s, c) $q = 0.03$ m^2/s, d) $q = 0.04$ m^2/s, e) $q = 0.05$ m^2/s, f) $q = 0.06$ m^2/s, g) $q = 0.07$ m^2/s, h) $q = 0.08$ m^2/s, i) $q = 0.09$ m^2/s, j) $q = 0.10$ m^2/s was applied (difference to previous interval)
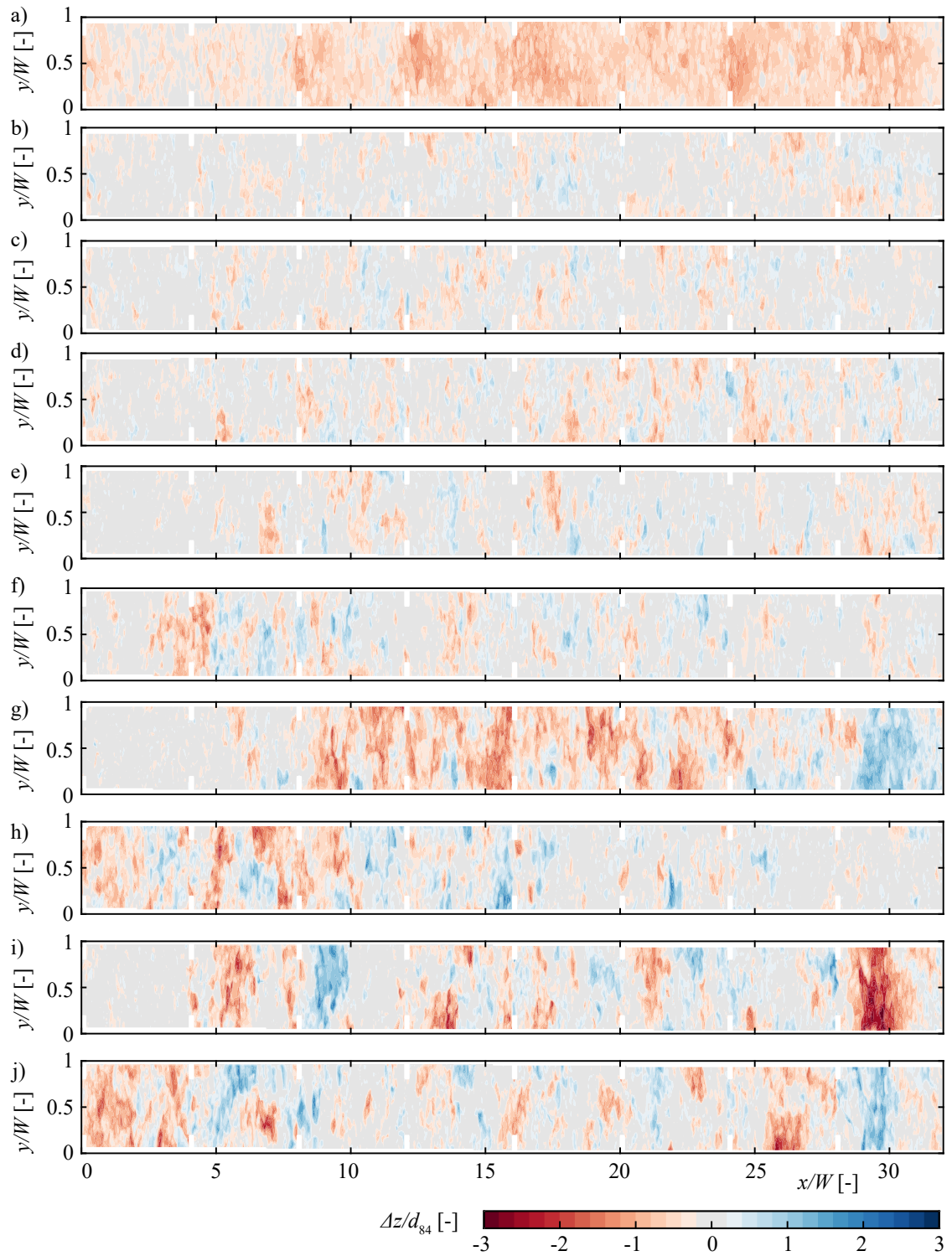
Figure A.11 Bed elevation changes of experiment RR115 after a) $q = 0.01$ m^2/s, b) $q = 0.02$ m^2/s, c) $q = 0.03$ m^2/s, d) $q = 0.04$ m^2/s, e) $q = 0.05$ m^2/s, f) $q = 0.06$ m^2/s, g) $q = 0.07$ m^2/s, h) $q = 0.08$ m^2/s, i) $q = 0.09$ m^2/s, j) $q = 0.10$ m^2/s was applied (difference to previous interval)
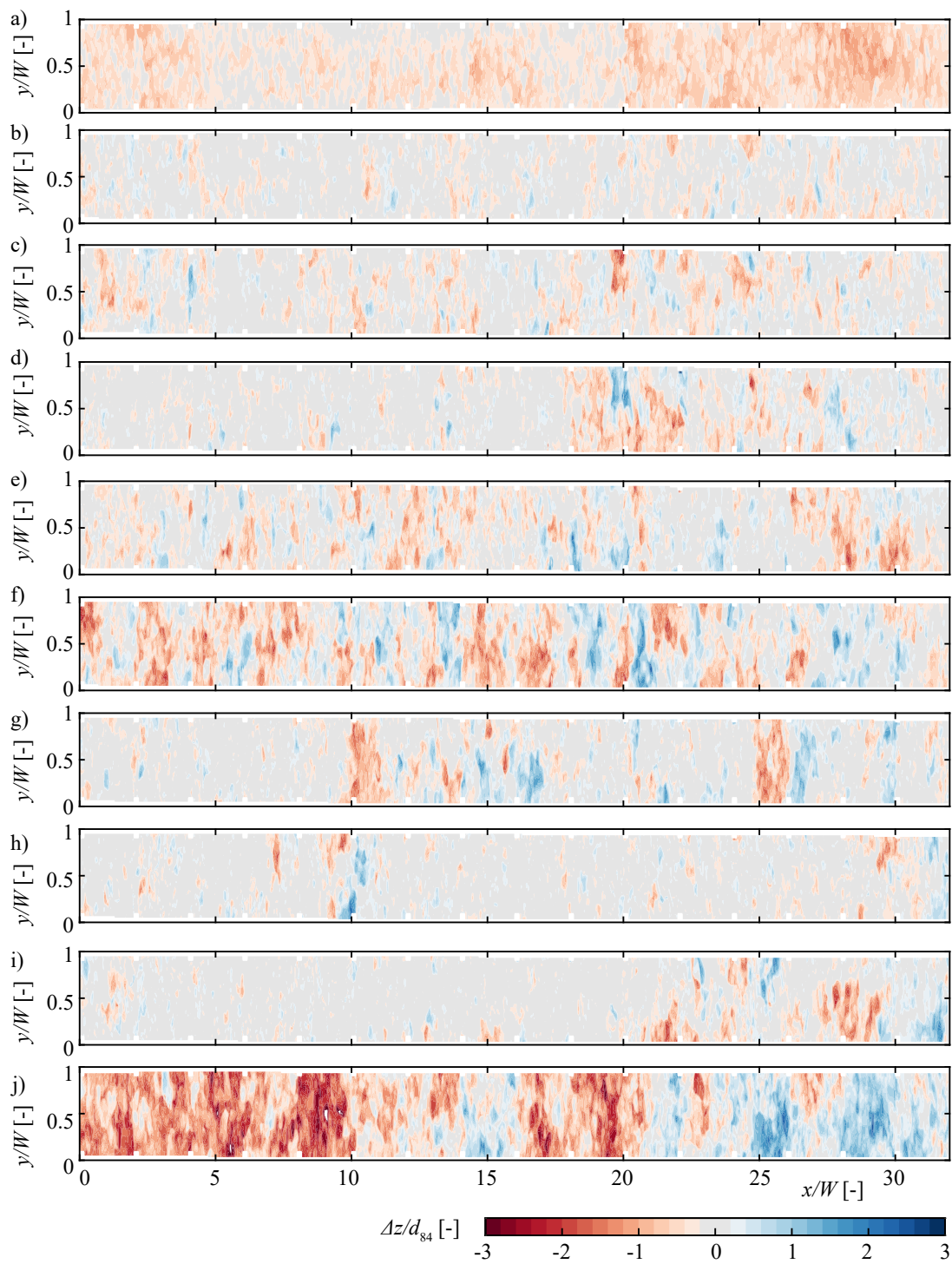
Figure A.12 Bed elevation changes of experiment R55 after a) $q = 0.01$ m^2/s, b) $q = 0.02$ m^2/s, c) $q = 0.03$ m^2/s, d) $q = 0.04$ m^2/s, e) $q = 0.05$ m^2/s, f) $q = 0.06$ m^2/s, g) $q = 0.07$ m^2/s, h) $q = 0.08$ m^2/s, i) $q = 0.09$ m^2/s, j) $q = 0.10$ m^2/s was applied (difference to previous interval)
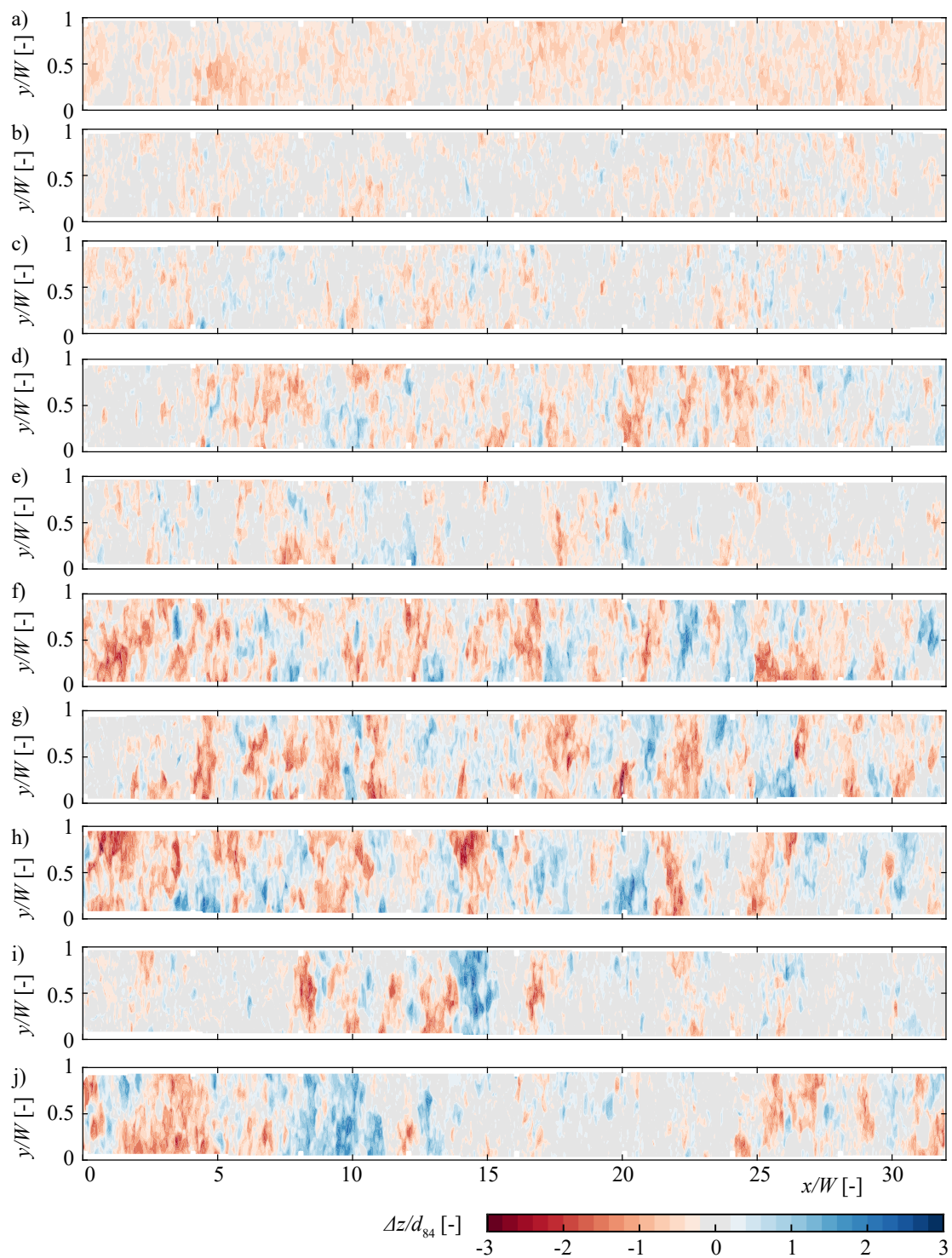
Figure A.13 Bed elevation changes of experiment R115 after a) $q = 0.01$ m^2/s, b) $q = 0.02$ m^2/s, c) $q = 0.03$ m^2/s, d) $q = 0.04$ m^2/s, e) $q = 0.05$ m^2/s, f) $q = 0.06$ m^2/s, g) $q = 0.07$ m^2/s, h) $q = 0.08$ m^2/s, i) $q = 0.09$ m^2/s, j) $q = 0.10$ m^2/s was applied (difference to previous interval)
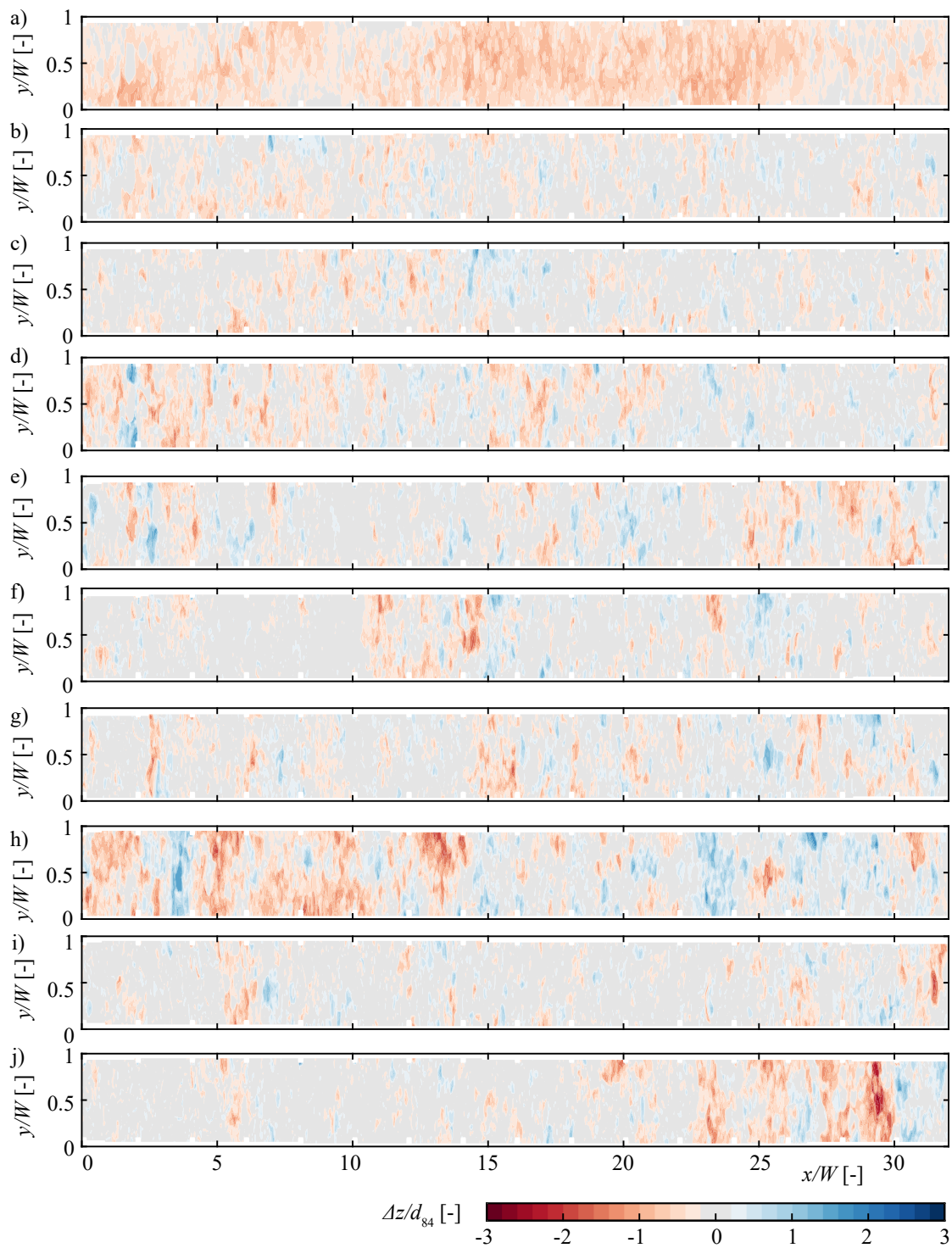
Figure A.14 Bed elevation changes of experiment R55 after a) $q = 0.017$ m^2/s, b) $q = 0.033$ m^2/s, c) $q = 0.050$ m^2/s, d) $q = 0.067$ m^2/s, e) $q = 0.083$ m^2/s, f) $q = 0.100$ m^2/s, g) $q = 0.117$ m^2/s, h) $q = 0.133$ m^2/s, i) $q = 0.150$ m^2/s, j) $q = 0.167$ m^2/s was applied (difference to previous interval)
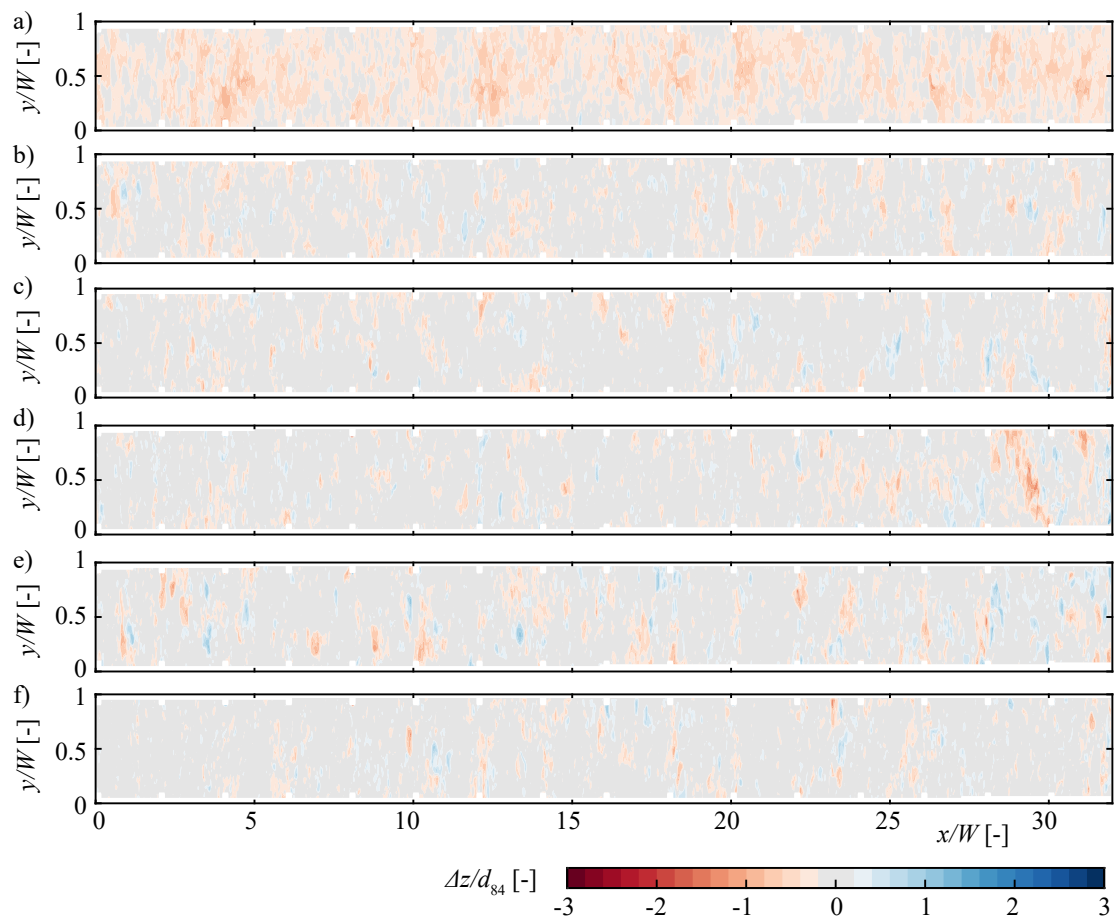
Figure A.15 Bed elevation changes of experiment R55 after a) $q = 0.025$ m^2/s, b) $q = 0.050$ m^2/s, c) $q = 0.750$ m^2/s, d) $q = 0.100$ m^2/s, e) $q = 0.125$ m^2/s, f) $q = 0.150$ m^2/s was applied (difference to previous interval)
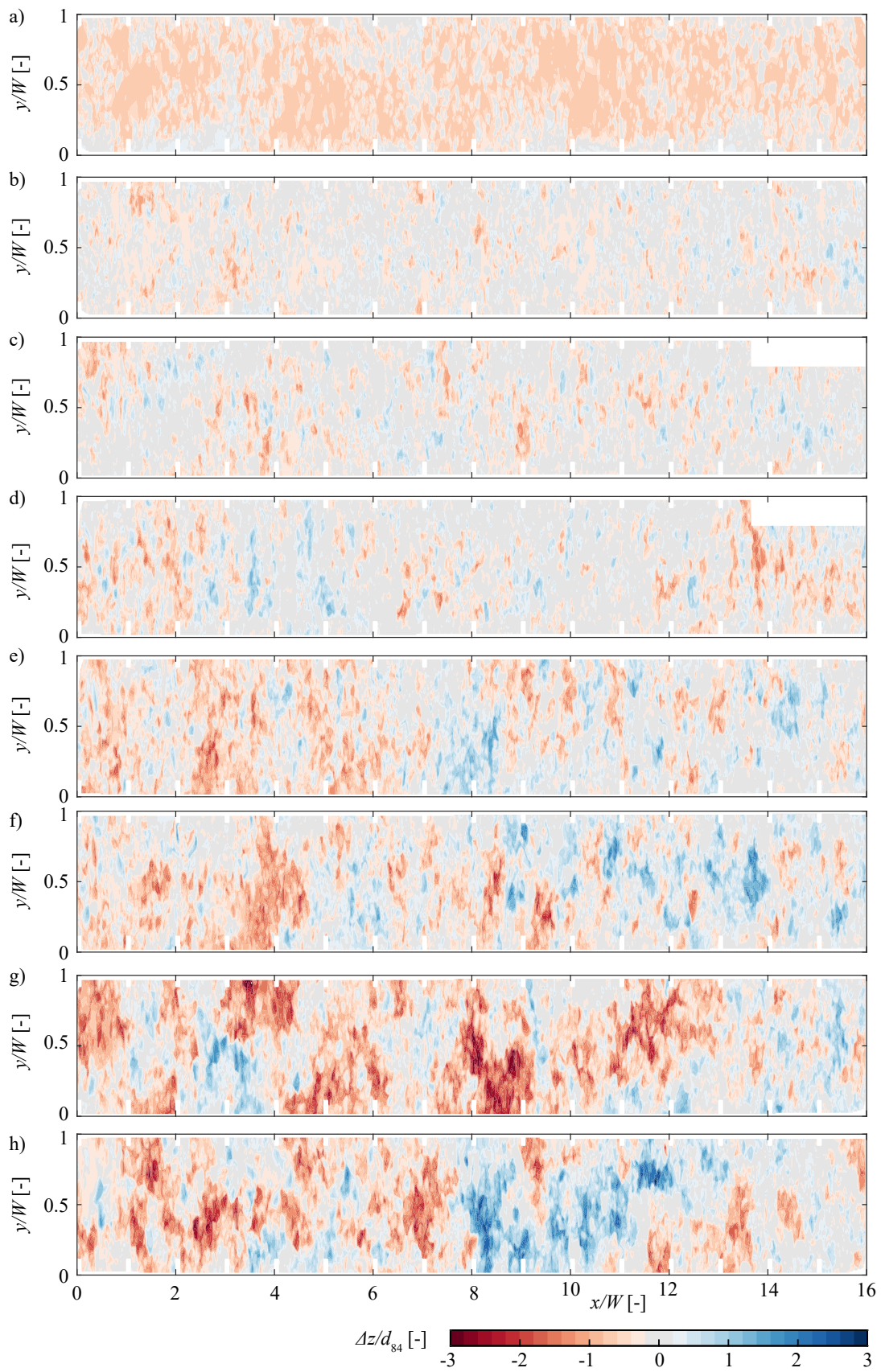
Figure A.16 Bed elevation changes of experiment RR55 in the channel with $W = 0.6$ m after a) $q = 0.01$ m^2/s, b) $q = 0.02$ m^2/s c) $q = 0.3$ m^2/s, d) $q = 0.04$ m^2/s, e) $q = 0.05$ m^2/s, f) $q = 0.06$ m^2/s, g) $q = 0.07$ m^2/s, h) $q = 0.08$ m^2/s was applied (difference to previous interval)

A.3 Artificial step-pool sequences

A.3.1 Step-forming blocks

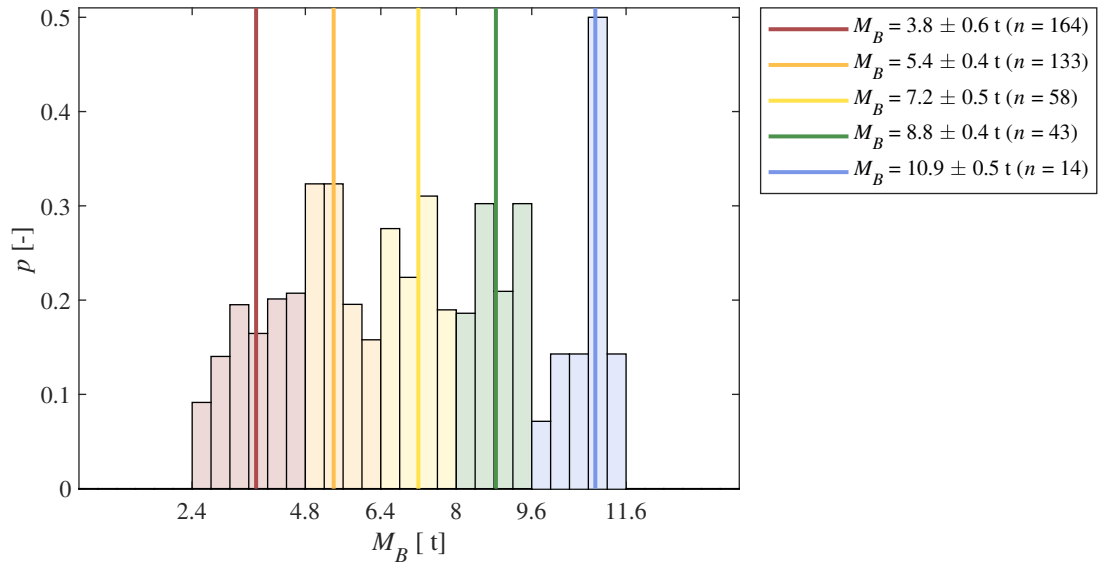Figure A.17 shows the weight distribution of the step-forming blocks used in this study.

Figure A.17 Weight distribution of step-forming blocks used in this study (see Figure 4.12, Table 4.6)

A.3.2 Hydrographs in steep mountain streams

Herein, various unsteady hydrographs are presented which were either measured or estimated for Erlenbach, Betelriedgraben, and Kleine Schliere streams.

Erlenbach

Figure A.18 shows four flood events between 1984 and 2010 measured at Erlenbach stream in Switzerland (Turowski *et al.* 2009, 2013). Erlenbach stream has a rather small $CA = 0.7$ km^2. The flood events have a RI = 30 to 50 years. The flood duration was approximately two hours and the peak arrived after $t_p = 20$ to 30 minutes, thus after t_p/t_{tot} = 1/6 to 1/4 with t_{tot} = total duration.
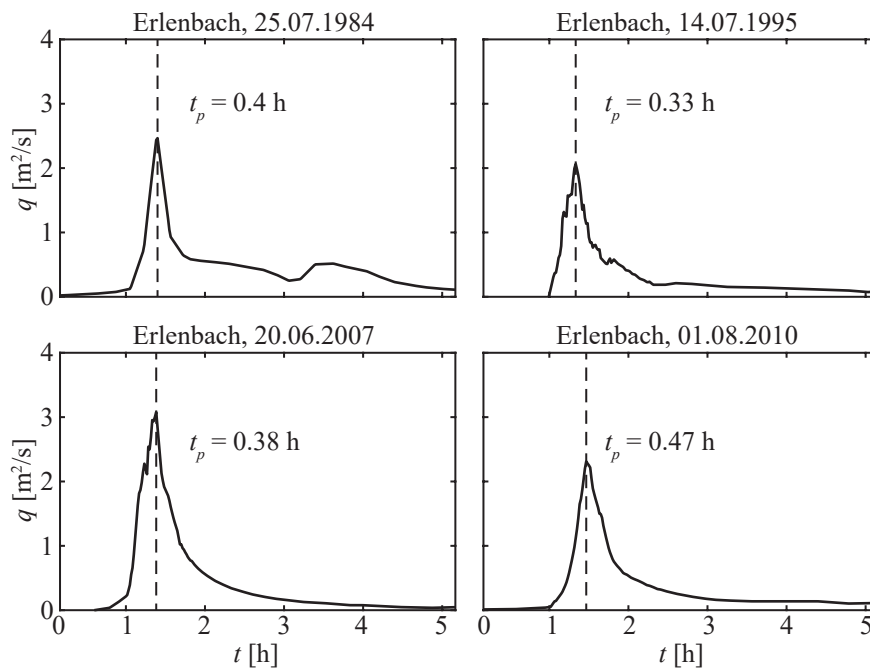

Figure A.18 Hydrographs of four flood events measured in Erlenbach stream, Switzerland (adapted from Turowski *et al.* 2009, 2013)

Betelriedgraben

Figure A.19 shows the estimated hydrographs of flood events with RI = 100 to 300 years in Betelriedgraben stream in Switzerland with a $CA = 12$ km^2 (VAW 2015). The generated triangular-shaped hydrographs were used in laboratory tests to investigate stability of an artificial step-pool sequence. A total duration of approximately $t_{tot} = 3$ and 4 h was estimated with the peak arriving after $t_p = 1.1$ and 1.4 h corresponding to 1/3 of the total duration. Herein, the sediment hydrograph q_s is presented with the sediment peak

occurring simultaneously with the water discharge peak. The maximum feed rates were q_s = 300 to 360 kg/(sm).
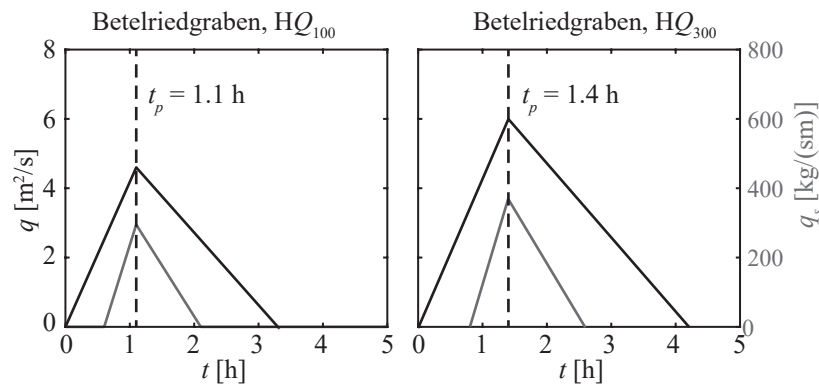

Figure A.19 Estimated hydrographs for flood events with return period of 100 and 300 years at Betelriedgraben, Switzerland (adapted from VAW 2015)

Kleine Schliere

The Kleine Schliere stream in Switzerland has a rather large CA = 21 km^2. Similarly to the Betelriedgraben stream, two synthetic hydrographs are presented for flood events with RI = 100 and 300 years, respectively. The total duration of the triangular-shaped hydrographs with an inflexion point in the descending limb was approximately t_{tot} = 6 h. The peak arrived after t_p = 1.7 to 1.8 h corresponding to around 1/4 of the total duration t_{tot}. Furthermore the sediment supply rates are presented which range between q_s = 180 and 290 kg/(sm).
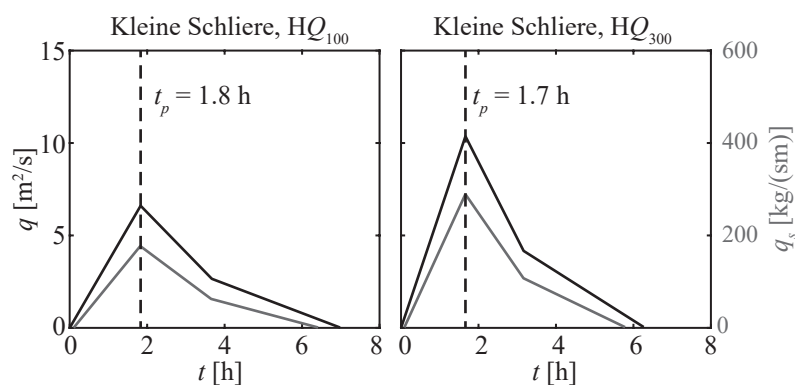

Figure A.20 Estimated hydrographs for flood events with RI = 100 and 300 years at Kleine Schliere, Switzerland (adapted from VAW 2014)

A.3.3 Check dam sequences - scour depth

Concrete check dam sequences in the Kleine Schliere stream were investigated performing physical experiments (VAW 2018). Preliminary stationary tests were conduced and Figure A.21 shows the scour depth H_t (defined in Figure 3.9b) as a function of transport capacity (TC), normalized with scour depth under CW conditions $H_t(\text{TC} = 0)$. The scour depth decrease was most pronounced in experiment with TC<0.25. Note that a rather linear decrease was observed in experiment with uniform grains $d = 0.34$ m.
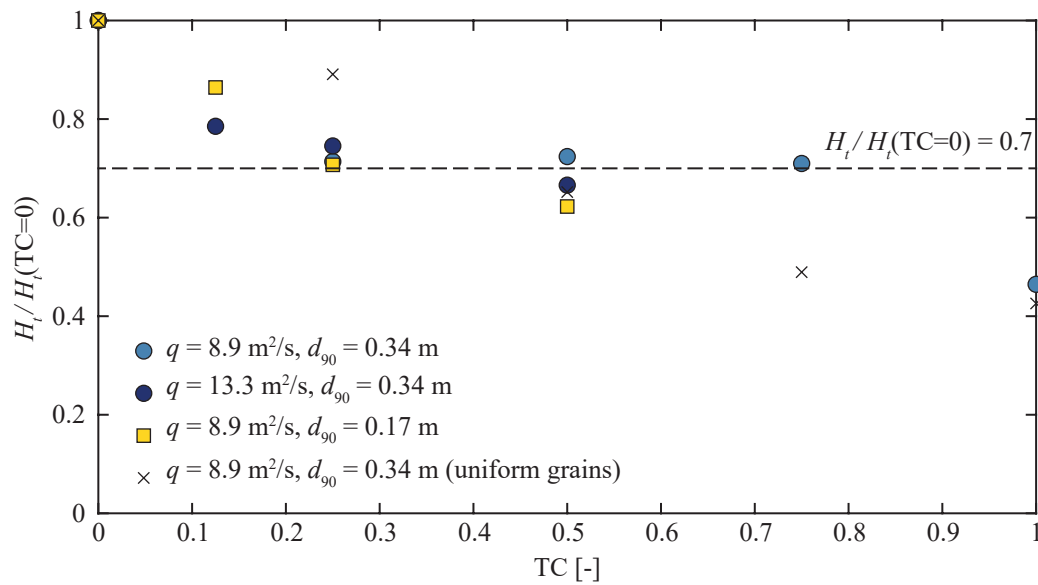

Figure A.21 Effect of transport capacity (TC) on scour depth H_t (according to Figure 3.9b) of a check dam sequence investigated in the laboaratory for bed slope $S = 5\%$ (VAW 2018)